Asymptotics with Numerical Relativity: Gravitational Memory, BMS Frames, and Nonlinearities

Thesis by
Keefe Edward Alden Mitman

In Partial Fulfillment of the Requirements for the
Degree of
Doctor of Philosophy

CALIFORNIA INSTITUTE OF TECHNOLOGY
Pasadena, California

2024
Defended May 3rd, 2024

Keefe Edward Alden Mitman
ORCID: 0000-0003-0276-3856

ACKNOWLEDGMENTS

Thank you to Saul Teukolsky, my advisor, for providing support and guidance throughout my entire PhD and encouraging my independence as a researcher.

Thank you to Leo Stein, for the many fruitful physics discussions that we have had over the years and for continuously showing me how to be a successful researcher.

Thank you to Mark Scheel, for teaching me the foundations of numerical relativity and helping me develop and improve my various code frameworks.

Thank you to Nils Deppe, for supporting the next stage of my academic career.

Thank you to the members of the Simulating eXtreme Spacetimes collaboration, especially Michael Boyle, Dante Iozzo, Matt Giesler, Lorena Magaña Zertuche, Jordan Moxon, Vijay Varma, and Jooheon Yoo, for the productive conversations.

Thank you to my many other collaborators, especially Will Farr, Alexander Grant, Maximiliano Isi, Neev Khera, Macarena Lagos, Harrison Siegel, and Hengrui Zhu.

Thank you to the other members of my thesis committee, Katerina Chatziioannou, Yanbei Chen, and Alan Weinstein, for your interest and support in this work.

Thank you to JoAnn, for not only all of your indispensable administrative work, but also for the fun and spontaneous chats that we have had throughout Cahill.

Thank you to my friends for the many unforgettable memories.

Finally, thank you to my parents for their continuous encouragement and my partner, Emma Gomez, for always believing in me and keeping me balanced.

ABSTRACT

With the recent commencement of the LIGO-Virgo-KAGRA (LVK) Collaboration's fourth observing run, the field of gravitational-wave physics is uniquely poised to collect even more accurate data from compact binary coalescences. Consequently, we will soon be able to perform more stringent tests of general relativity (GR). Because GR must, in some regime, be violated—either because the Universe is described by an alternative theory or because of the emergence of quantum effects—these tests of GR are crucial for unveiling new physics. Performing such tests, however, requires that our understanding of GR and gravitational waves is reliable. And, while there are many tools for unraveling Einstein's equations, the only one that is robust in every regime of GR is numerical relativity (NR): a means for computing accurate solutions to Einstein's equations with supercomputers.

In this thesis, I highlight some recent and impactful advancements that have been incorporated into NR simulations of binary black holes. In particular, I show how a more robust procedure for calculating the radiative data at future null infinity from NR simulations, called Cauchy-characteristic evolution (CCE), produces waveforms that exhibit a not-yet observed prediction of GR colloquially referred to as memory. This phenomenon corresponds to the permanent net displacement that two observers will experience due to the passage of transient gravitational radiation. Memory is of particular interest in the testing GR and theory communities because of its relation to asymptotic symmetries and scattering amplitude calculations in particle physics. With these contemporary CCE waveforms, I provide explicit methods to calculate the various memory effects and I also comment on their relative magnitudes and detectability in the near future. Apart from this, I also demonstrate the importance of controlling the BMS freedoms of these waveforms, i.e., their frame freedom at future null infinity, for building waveform models as well as for extracting physics, such as GR's nonlinearities, from the ringdown phase of binary black hole mergers.

As we start to enter the next phase of high-precision gravitational-wave astronomy, correctly modeling gravitational waves with NR simulations will play a crucial role in pushing Einstein's theory of relativity to its limits. It is the aim of this thesis to illustrate the importance of combining gravitational-wave theory and NR to not only improve our understanding of black holes and gravitational waves, but also further our prospects for unveiling the true nature of gravity within our universe.

PUBLISHED CONTENT AND CONTRIBUTIONS

[1] K. Mitman et al., Phys. Rev. Lett. **130**, 081402 (2023) 10.1103/PhysRevLett.130.081402,
K.M. conceived the framework, performed the calculations, ran the numerical evolutions, and wrote the manuscript.

[2] J. Yoo et al., Phys. Rev. D **108**, 064027 (2023) 10.1103/PhysRevD.108.064027,
K.M. conceived the framework, ran the numerical evolutions, constructed the waveforms for the surrogate, and wrote portions of the manuscript.

[3] K. Mitman et al., Phys. Rev. D **106**, 084029 (2022) 10.1103/PhysRevD.106.084029,
K.M. conceived the framework, performed the calculations, ran the numerical evolutions, and wrote the manuscript.

[4] K. Mitman et al., Phys. Rev. D **103**, 024031 (2021) 10.1103/PhysRevD.103.024031,
K.M. conceived the framework, performed the calculations, ran the numerical evolutions, and wrote the manuscript.

[5] K. Mitman et al., Phys. Rev. D **104**, 024051 (2021) 10.1103/PhysRevD.104.024051,
K.M. conceived the framework, performed the calculations, ran the numerical evolutions, and wrote the manuscript.

[6] K. Mitman, J. Moxon, M. A. Scheel, S. A. Teukolsky, M. Boyle, N. Deppe, L. E. Kidder, and W. Throwe, Phys. Rev. D **102**, 104007 (2020) 10.1103/PhysRevD.102.104007,
K.M. conceived the framework, performed the calculations, ran the numerical evolutions, and wrote the manuscript.

TABLE OF CONTENTS

Chapter 1

INTRODUCTION

One of the main objectives of physics research is to characterize the behavior of our universe with mathematical theories whose predictions match the data that we collect from our real-world experiments. Currently, however, we lack a theory that unifies our best theory of gravity—Einstein's theory of general relativity (GR) [1]—with the theory that we use to explain the physics of the microscopic realm— quantum mechanics [2]. Because of this, there is hope that if we can observe the way in which our universe ties gravity and quantum mechanics together, e.g., through the coalescence of two black holes, then this data may help show us a path to the long-sought-after theory of "quantum gravity". Nonetheless, to understand if such data is truly evidence for this type of coupling, we must first be certain that we have accurate and robust solutions to Einstein's equations for the types of phenomena that we are observing. Otherwise how can we be certain that the data that we have seen is really evidence of something that cannot be explained by GR? With the recent and important detection of a gravitational wave produced by a binary black hole merger, GW150914 [3, 4], the possibility of obtaining data that has the potential to disagree with Einstein's theory of GR became a reality and ushered in the pivotal and incredibly exciting era of gravitational wave astronomy.

This thesis, which focuses on obtaining correct solutions to Einstein's equations for the coalescence of two black holes and the gravitational waves that they produce with numerical simulations, aims to contribute to this ongoing effort to test GR and reveal fundamental information about how gravity in our universe works.

1.1 General Relativity

Formulated by Einstein in 1915 [1], general relativity is currently our best theory at explaining how the interaction of "gravity" seems to work within our universe. Fundamentally, Einstein's theory of GR states that gravity is a geometric effect and can be understood as the curvature of "spacetime"—a four-dimensional fabric that our universe is comprised of. It also says that this spacetime curvature is influenced by the presence of energy, which through the energy-momentum relation $E^2 = (mc^2)^2+(pc)^2$ [5] can also be related to the presence of matter and momentum. For example, when the Earth orbits the Sun, Einstein's theory says that the two are

interacting not through some force, but instead through the warping of the spacetime that they each induce with their individual energies, i.e., their masses and momenta. Their motion with respect to each other is simply because of their perpetual falling and their inherent need to follow the straightest path within this curved geometry. The same can be said of light, which although has no mass, has momentum and thus can also move through the curved geometry and warp the spacetime while doing so.

Mathematically, the curvature of the fabric of spacetime is encoded in a variable called the spacetime metric $g_{\mu\nu}$. It describes the path along which objects travel via the infinitesimal line element $ds^2 = g_{\mu\nu}dx^\mu dx^\nu$, where dx^μ corresponds to some infinitesimal displacement through the spacetime manifold and the index μ represents the four spacetime coordinates. Einstein's equations, i.e., GR, state that the way the metric responds to the presence of energy in spacetime is via

$$G_{\mu\nu} = \frac{8\pi G}{c^4} T_{\mu\nu}, \tag{1.1}$$

where $G_{\mu\nu}$ is the Einstein tensor and is a function of the metric $g_{\mu\nu}$ and $T_{\mu\nu}$ is the stress-energy tensor and describes the energy, mass, and momentum that are present in the spacetime. In the remainder of this thesis, I will use units with $G = c = 1$.

1.2 Asymptotically Flat Spacetimes

While there are many spacetime geometries that are physically meaningful in the context of GR, the simplest and most relevant to current observational experiments are those which are "asymptotically flat". Roughly speaking, these spacetimes are those in which the spacetime curvature vanishes at large distances from some region, so that at these large distances the metric instead resembles that of Minkowski, i.e., "flat", spacetime. What makes this feature useful is that, because of this similarity to Minkowski spacetime in the asymptotic limit, extracting physics at the boundary of asymptotically flat spacetimes is much more straightforward than if that boundary had some nontrivial curvature. But the boundary of asymptotically flat spacetimes, which is called "asymptotic infinity", is still not as simple as the more familiar bulk of Minkowski spacetime. In particular, Refs. [6, 7] showed that the symmetries of asymptotic infinity are not the usual Poincaré symmetries [8], but are instead an infinite collection of transformations with a much more rich and complex structure.

These extra symmetries, at least for the part of asymptotic infinity that is the (future) asymptotic limit of null rays, i.e., null infinity, can be understood through the following thought experiment. Imagine you have a collection of observers that are surrounding some kind of event, say a binary black hole merger. If these observers

know their relative positions, then a single observer could simply move to the position of their peer and receive the same information at the same time. However, if we push these observers to future null infinity, then they are infinitely far away from each other and are thus causally disconnected, meaning we can freely translate each observer on this celestial sphere without changing the underlying physics. So, instead of having only four spacetime translations as symmetries of our spacetime, at future null infinity we have an infinite number of such translations: one for each point on the two-sphere. These extra symmetry transformations, which extend the usual Poincaré spacetime translations, are referred to as supertranslations. They are important because, thanks to Noether's theorem [9], their existence implies that there are extra conservation laws at null infinity that control how certain observables, e.g., gravitational waves, evolve with respect to certain sources, e.g., orbiting masses.

1.3 Gravitational Waves

Like the orbit of astrophysical objects, bending of light, and existence of black holes, Einstein's theory of GR also predicts the existence of gravitational waves (GWs)—ripples in the fabric of spacetime [1, 10]. In their most simple form, GWs can be understood as perturbations of the spacetime metric about some background metric

$$g_{\mu\nu} = \eta_{\mu\nu} + h_{\mu\nu}, \tag{1.2}$$

where $\eta_{\mu\nu}$ is the metric of the background, e.g., that of Minkowski spacetime, and $h_{\mu\nu}$ is a small perturbation representing the GW. By inserting Eq. (1.2) into Eq. (1.1), taking $\eta_{\mu\nu}$ to be the metric describing Minkowski spacetime, and setting $T_{\mu\nu} = 0$, one readily finds that, in Lorenz gauge [11], Einstein's equations yield

$$\Box \bar{h}_{\mu\nu} = 0, \tag{1.3}$$

where $\Box \equiv \nabla_\alpha \nabla^\alpha$ and $\bar{h}_{\mu\nu} \equiv h_{\mu\nu} - \frac{1}{2}\eta_{\mu\nu}\bar{h}$ is the "trace reverse" of $h_{\mu\nu}$ with $\bar{h} = h^\mu{}_\mu$. Clearly Eq. (1.3) exhibits solutions of the form

$$\bar{h}_{\mu\nu} = A_{\mu\nu} \exp\left(i k_\alpha x^\alpha\right), \tag{1.4}$$

where $A_{\mu\nu}$ is a complex tensor independent of time and k_α is a real null vector. Consequently, Eq. (1.4) can be viewed as a wave-like solution which propagates along null rays. Or, put more simply, Eq. (1.4) illustrates that, to first order in perturbation theory, GR predicts ripples in the curvature of spacetime, i.e., GWs.

What is lacking about this linear description, however, is that it fails to capture the full nonlinearity of GR, which is a fundamental part of the theory. In particular,

through the conservation of energy and momentum, one can readily intuit that the sources of GWs are those with mass multipole moments equal to or higher than the quadrupole moment. But, because GWs are waves and therefore carry energy away from their source, this means that GWs must have a mechanism that enables them to affect the spherically symmetric part of their source's mass. This mechanism is exactly the back reaction that stems from the nonlinearity of GR, i.e., the fact that GWs can interact with themselves to fundamentally change various properties of the spacetime, not just the usual ripple-like behavior predicted by the linear theory.

In the broader context of asymptotically flat spacetimes in full nonlinear GR, GWs can more formally be understood as perturbations about the angular part of some background metric. In particular, by working with the Bondi coordinates (u, r, θ, ϕ) of Refs. [6, 7] where $u \equiv t - r$ is the retarded time, one can write the metric for an arbitrary spacetime as

$$ds^2 = -Ue^{2\beta}du^2 - 2e^{2\beta}dudr + r^2 h_{AB}\left(d\theta^A - \mathcal{U}^A du\right)\left(d\theta^B - \mathcal{U}^B du\right), \tag{1.5}$$

where capital Latin indices range over (θ, ϕ) and U, β, $\mathcal{U}^A$, and h_{AB} are functions of the Bondi coordinates. The four gauge conditions that have been enforced are

$$g_{rr} = 0, \tag{1.6a}$$

$$g_{rA} = 0, \tag{1.6b}$$

for simplicity, and

$$\partial_r \det\left(h_{AB}\right) = 0 \tag{1.6c}$$

to ensure that r corresponds to the luminosity distance. Then, to make Eq. (1.5) uniquely correspond to the metric of asymptotically flat spacetimes, one must impose extra conditions that control the falloff behavior of the various functions appearing in Eq. (1.5). While there is no preferred method for choosing these falloff conditions, there are certain choices that one can make that are more natural than others, e.g., those which lead to spacetimes with GWs, but not those that have infinite energy. The conditions that were considered in Refs. [6, 7] and what we will use throughout

this thesis lead to the following metric function expansions in powers of $1/r$:

$$\beta = \frac{\beta_0}{r} + \frac{\beta_1}{r^2} + O\left(r^{-3}\right), \tag{1.7a}$$

$$U = 1 - \frac{2m}{r} + O\left(r^{-2}\right), \tag{1.7b}$$

$$\mathcal{U}^A = \frac{U^A}{r^2} - \frac{1}{r^3}\left[-\frac{2}{3}N^A + \frac{1}{16}D^A\left(C_{BC}C^{BC}\right) + \frac{1}{2}C^{AB}D^C C_{BC}\right] + O\left(r^{-4}\right), \tag{1.7c}$$

$$h_{AB} = q_{AB} + \frac{C_{AB}}{r} + O\left(r^{-2}\right), \tag{1.7d}$$

where the various coefficients on the right-hand sides are functions of $\left(u, \theta^A\right)$ only, and $q_{AB}\left(\theta^A\right)$ is the metric on the two-sphere, i.e., in the usual spherical coordinates $q_{AB}\left(\theta, \phi\right) dx^A dx^B = d\theta^2 + \sin^2\theta d\phi^2$. Of the many functions appearing in Eqs. (1.7), the one encoding information about the spacetime's GWs is the "shear" (or "strain") tensor C_{AB}, since this is the component that corresponds to outgoing null rays that are transverse to future null infinity, i.e., what one would expect of the radiation of a spin-2 field such as GR, as illustrated through Eq. (1.4).

From this formalism, the importance of the nonlinearity of GR can then be made apparent through the following. If one inserts Eq. (1.5) into Eq. (1.1) with $T_{\mu\nu} = 0$, examines the resulting equation for the (u, u) component of the spacetime metric and the r^{-2} coefficient of the asymptotic expansion, and takes the spherically symmetric contribution to this equation, then they readily recover the Bondi mass loss formula

$$\frac{d}{du}m(u) = -\frac{1}{4\pi}\oint_{S^2}|N|^2 d\Omega, \tag{1.8}$$

where $m(u)$ is the Bondi mass of the spacetime and N is related to the norm of the "news" tensor $N_{AB} \equiv \partial_u C_{AB}$. Eq. (1.8) shows that, for C_{AB} being the part of the metric related to GWs, if there is some nonzero GW radiating in the spacetime, i.e., $N \neq 0$, then there must be a corresponding loss in the spacetime's Bondi mass. Therefore, GWs not only propagate over some background metric, but because of GR's nonlinearity they also carry away energy (and momentum/angular momentum) and thus influence the background metric in a nontrivial and interesting way.

1.4 Gravitational Memory Effects

Another peculiar feature of GWs is that, apart from their intuitive carrying of energy (and momentum/angular momentum), they also permanently change the spacetime that they propagate through. This phenomenon is called the memory effect and was first realized in 1974 when Zel'dovich and Polnarev successfully calculated

the gravitational radiation produced by two objects on hyperbolic trajectories [12]. Working with Einstein's equations in linearized GR, they found that, because the stress-energy tensor exhibits a net change between early and late times due to the change in the mass distribution of the flyby objects, the gravitational-wave strain will also exhibit a net change. Later, in 1985, Braginsky and Grischuk elaborated upon this result and named this net change phenomenon the "memory effect" [13]. Following this, in 1987 Braginsky and Thorne found a simple equation for the memory for scattering scenarios in terms of the four-momentum of the ingoing and outgoing massive particles [14]. It says rather simply that for a system of N particles, the net change in the gravitational-wave strain between early and late times is

$$\Delta h_{ij}^{\mathrm{TT}} = \frac{4}{r}\Delta \sum_{A=1}^{N} \frac{M_A}{\sqrt{1-v_A^2}} \left(\frac{v_A^i v_A^j}{1 - v_A \cos\theta_A} \right)^{\mathrm{TT}}, \tag{1.9}$$

where r is the distance between the observer and the source, M_A is the mass of particle A, $\vec{v}_A$ is the velocity with v_A^i the i^{th} component and v_A the norm, θ_A is the angle between $\vec{v}_A$ and the observer, and the Δ before the sum on the right-hand side refers to the difference in this sum evaluated for the outgoing and ingoing particles.

After these early works, it was largely thought the memory effect was understood. This opinion, however, was completely overturned in 1991 when Christodoulou found that gravitational waves themselves will also source a certain type of memory, through a subtle, but non-negligible nonlinear interaction with themselves [15].[1] Christodoulou obtained this result by working with null hypersurface equations and asymptotic limits to obtain an equation relating the gravitational-wave strain to the flux of radiation through each point on the celestial two-sphere. A year later in 1992, Thorne realized that Christodoulou's finding was equivalent to that of Ref. [14], but with the massive particles being replaced by null gravitons, i.e.,

$$\Delta h_{ij}^{\mathrm{TT}} = \frac{4}{r} \int \frac{dE}{d\Omega'} \left(\frac{\xi^{i'} \xi^{j'}}{1 - \cos\theta'} \right)^{\mathrm{TT}} d\Omega', \tag{1.10}$$

where E is the energy of the radiation, $\xi^{i'}$ is a unit vector pointing from the source toward $d\Omega'$, and θ' is the angle between $\xi^{i'}$ and the observer [18].

What makes memory effects so tantalizing, apart from their unique nature, however, is their intimate connection to the BMS group. In particular, Eqs. (1.9) and (1.10) turn out to both be parts of a conservation law at future null infinity that stems

[1] This discovery was also realized by Payne as well as Blanchet and Damour in Refs. [16, 17].

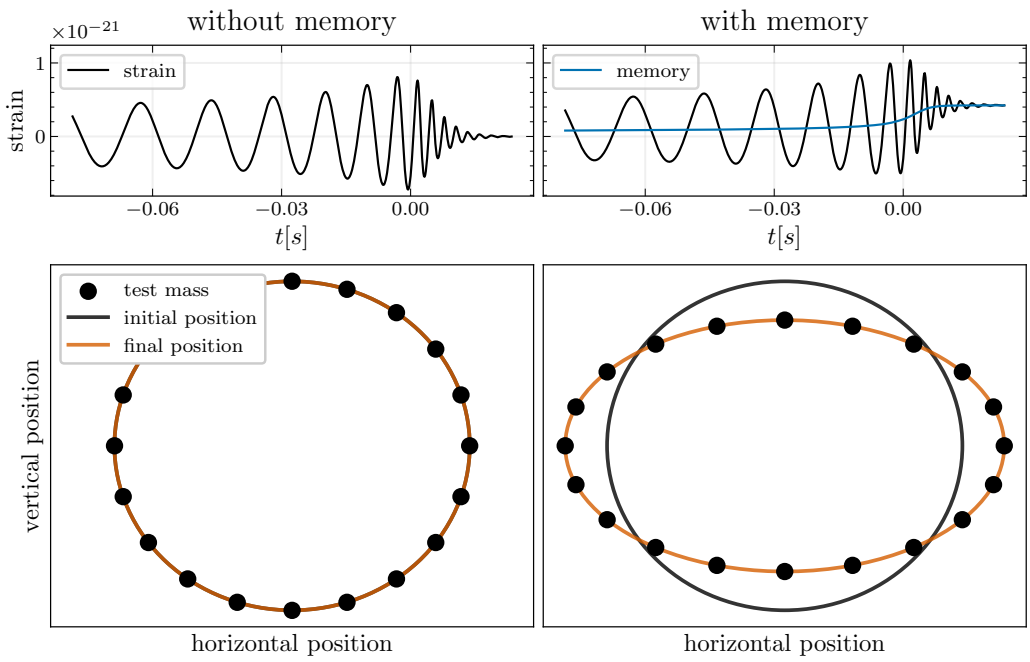

Figure 1.1: *Top Left*: A gravitational wave sourced by a binary black hole merger without memory. *Top Right*: Identical to the top left panel, but now with memory. The time-dependent growth of the memory is shown in blue. *Bottom Left (Right)*: The initial and final positions of a series of test particles after the passage of a gravitational wave without (with) memory.

from the supertranslation symmetries. Specifically, if one carries out the procedure before Eq. (1.8) without the last step, i.e., not taking the spherically symmetric part, and integrates in time they instead find

$$\mathrm{Re}\left[\eth^2\bar{\sigma}\right] = m + \int_{-\infty}^{u} |\dot{\sigma}|^2 du, \tag{1.11}$$

where $\eth$ is a certain angular operator and σ is the gravitational-wave shear, which is related to the gravitational-wave strain via $\sigma \equiv \bar{h}/2$. From this equation, one can then readily see that if there is a net change in the Bondi mass aspect m or a net change in the energy flux, i.e., the second term on the right-hand side, then there will also be a net change in the gravitational-wave strain. In fact, a net change in the Bondi mass aspect corresponds to the effect found by Zel'dovich and Polnarev, i.e., Eq. (1.9), while a net change in the energy flux corresponds to the effect found by Christodoulou, i.e., Eq. (1.10). Because of this more modern interpretation of memory through the supertranslation conservation law, memory effects appearing in the charge-like component of this conservation law are typically called "ordinary",

while those in the flux component are called "null" [19]. Ordinary memory is sourced by unbound objects, e.g., hyperbolic black holes, while null memory is primarily sourced by bound objects, e.g., binary black hole mergers. An example of the null memory sourced by a realistic binary black hole merger is shown in Fig. 1.1.

But the story does not simply end here. In particular, in 2014 memory effects received a burst of new attention from the high-energy theory community when the relationship between memory and asymptotic symmetries, i.e., the BMS group, was explicitly stated in Refs. [20–22], even though this relationship between the two has been effectively understood since, e.g., Refs. [23–27]. What grabbed the theory community's interest, however, was not simply this connection, but rather the infrared triangle that was found to connect soft theorems from particle physics to memory effects and asymptotic symmetries [22, 28, 29]. This connection was exciting because soft theorems are inherently useful for studying the quantum gravity $\mathcal{S}$-matrix and thus play a large role in constructing a quantum theory of gravity. So, the fact that these quantum gravity soft theorems could be connected to not only the asymptotic symmetries of our universe, but also the memory, which can be observed with GW detectors, was an astonishing realization and possible step toward probing the quantum nature of gravity. Ever since, there has been a large increase in the number of people studying what is now called "celestial holography", i.e., working with the holographic principle, e.g., the AdS/CFT correspondence, to try to formulate a quantum theory of gravity (see Ref. [30] for a review).

1.5 Numerical Relativity

While the infrared connection between memory effects, asymptotic symmetries, and soft theorems is an exciting one and is perhaps the way in which we will probe the quantum nature of gravity, to utilize memory effects to study our universe we first have to detect them. And, even before that, we need to know what they look like. Currently, our most promising means for observing memory effects is through the detection of loud GW events with a large enough signal-to-noise ratio (SNR) to see the subdominant memory signal. Thus, to know what the memory should look like, we need to know what the memory content in a gravitational-wave signal emitted by, say, a binary black hole merger, looks like. Unfortunately, because Einstein's theory of GR is a highly nonlinear theory, working this out with pen and paper turns out to be practically impossible. Instead, we need to rely on supercomputers to solve Einstein's equations for the problem of two coalescing black holes.

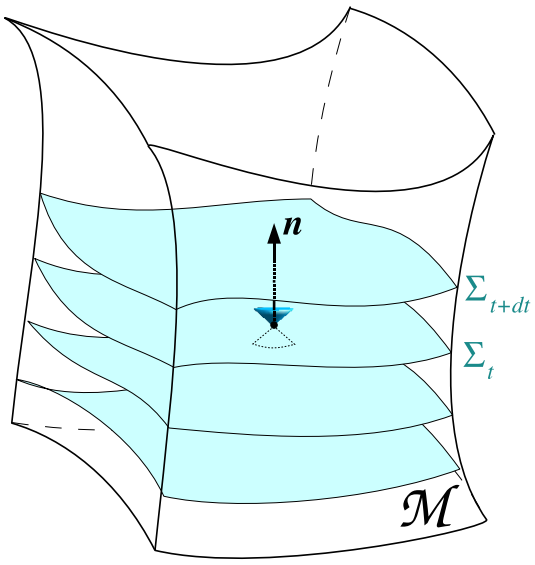

Figure 1.2: Foliation of a spacetime manifold $\mathcal{M}$ by spacelike hypersurfaces $\{\Sigma_t\}_{t\in\mathbb{R}}$; **n** represents the normal vector to the hypersurface Σ_t. Credit: Ref. [31].

In numerical relativity, this task of solving what a complex spacetime looks like is often broken down into two parts: constructing initial data for the spacetime and evolving the initial data using Einstein's equations. To do so requires computing the value of the spacetime metric $g_{\mu\nu}$ at each point in spacetime. Typically, this task is simplified by instead computing the metric on foliations of the spacetime, i.e., non-intersecting, three-dimensional leaves Σ_k which have a timelike normal vector n^a and can be labeled by some time coordinate t_k. Then, on each leaf Σ_k one only needs to compute the induced metric $g_{ij}^{(k)}$ and the extrinsic curvature $K_{ij}^{(k)}$, which measures how the normal n^a to each leaf changes from point to point on the leaf. An illustration of such a spacetime foliation is provided in Fig. 1.2.

With this foliation, Einstein's equations can be written as two sets of equations: constraint equations and evolution equations. The constraint equations control whether or not the spacetime, on a single leaf, is a solution to Einstein's equations. Consequently, they only need to be solved on the first leaf, i.e., as a part of the initial data construction, to provide initial values of g_{ij} and K_{ij} for the remaining evolution equations. The evolution equations then, as their name suggests, are used to evolve each leaf and thus compute the spacetime throughout the entire foliation. Following this, one can then extract the gravitational wave at future null infinity—a reasonable proxy for the location of Earth—by taking the gravitational wave to be the $1/r$ component of the angular part of the metric, i.e., the C_{AB} term in Eq. (1.7d).

Despite a vast amount of work from numerous numerical relativity groups, it took nearly four decades until the first successful binary black hole merger simulation was run in 2005 [32]. Part of why running such a black hole simulation proved to be so challenging is because, even though Einstein's equations are covariant, i.e., coordinate-independent, successfully implementing them in numerical relativity requires coordinates that enable stable numerical evolution [32, 33]. Nonetheless, since the breakthrough in 2005, a number of numerical relativity groups have implemented codes for solving Einstein's equations (see Ref. [34] for a review), with the most robust code being the Spectral Einstein Code (SpEC) [35], which was created by the Simulating eXtreme Spacetimes (SXS) Collaboration [36] and is heavily relied upon for the majority of the work presented in the thesis.

1.6 Cauchy-Characteristic Evolution

After numerical relativity groups figured out how to simulate the coalescence of binary black holes in GR, it then became possible to provide predictions for the gravitational waves that future detectors would observe. In particular, after solving for the spacetime metric on each of the leaves in the entire spacetime foliation, the gravitational-wave strain at future null infinity could then be computed by fitting the angular part of the metric, at various radial points, to polynomials in $1/r$ and extracting the strain as the leading $1/r$ component. This procedure, which is used by nearly every numerical relativity group, is called "extrapolation" as it uses data local to the simulated spacetime to extrapolate to radial points infinitely far away. One issue with this procedure, however, is that by doing so one never actually solves Einstein's equations on the null rays that connect the simulated spacetime volume to future null infinity.[2] Consequently, if there is any physics sourced during the propagation of the GW signal to future null infinity, e.g., gravitational memory, the extrapolation procedure will not capture it. Consequently, one can instead imagine running a simulation after the usual Cauchy simulation, which uses the metric resulting from the Cauchy simulation as initial data for an evolution of various radially compactified null hypersurfaces that connect the finite volume of the Cauchy simulation to future null infinity. Conducting such an evolution would then simulate Einstein's equations across the entirety of spacetime.[3]

[2] Note that most simulations simulate a finite spacetime volume because the smaller the volume, the simpler and faster the simulation is.

[3] An even better solution than this is to run this null hypersurface evolution in conjunction with the Cauchy simulation and simultaneously feed information back and forth between the two simulations. This is called Cauchy-characteristic matching (CCM) [37].

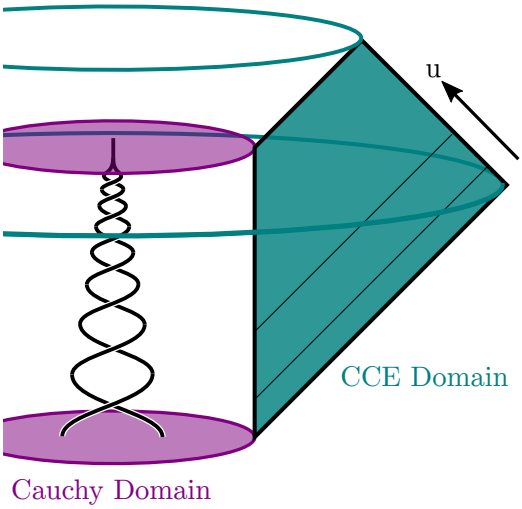

Figure 1.3: An illustration of CCE compared to a finite-volume Cauchy evolution. Notice that the CCE domain extends the finite-volume Cauchy domain all the way to future null infinity (the side of the blue domain labeled by u). Credit: Ref. [48].

This procedure is called Cauchy-characteristic evolution (CCE). It was first theorized in 1996 and was later implemented in simulations of binary black hole mergers in 2009 using the finite-difference Pitt Null code [38–42]. In 2014, an improved version of CCE using spectral methods was incorporated into the SpEC code [43–45]. And, finally, in 2020 and 2021 an even more improved version of CCE that enabled the extraction of the Weyl scalars was developed by Ref. [46] and incorporated into the SpECTRE code [47] by Ref. [48]. This version of CCE is the most advanced version and is what will be used throughout the work that is presented in this thesis. An illustration of the independent spacetime domains that are evolved by CCE and a Cauchy evolution to obtain waveforms at future null infinity is shown in Fig. 1.3.

In Refs. [40, 49, 50], it was found that unlike the extrapolation procedure, CCE was not only able to resolve the memory effect, but it also did so in a manner that is consistent with the supertranslation conservation law, i.e., Eq. (1.11). This will be the focus of Chapters 2 and 3. One issue that arose with CCE waveforms, however, was that because they contained memory effects, they could not be easily compared to post-Newtonian waveforms (see Ref. [51] for a review), which had information about the entire past history of the binary's coalescence and therefore predicted larger values for the memory [49]. Fortunately, this "issue" turned out to instead be a subtlety regarding the frame freedom such waveforms have at future null infinity

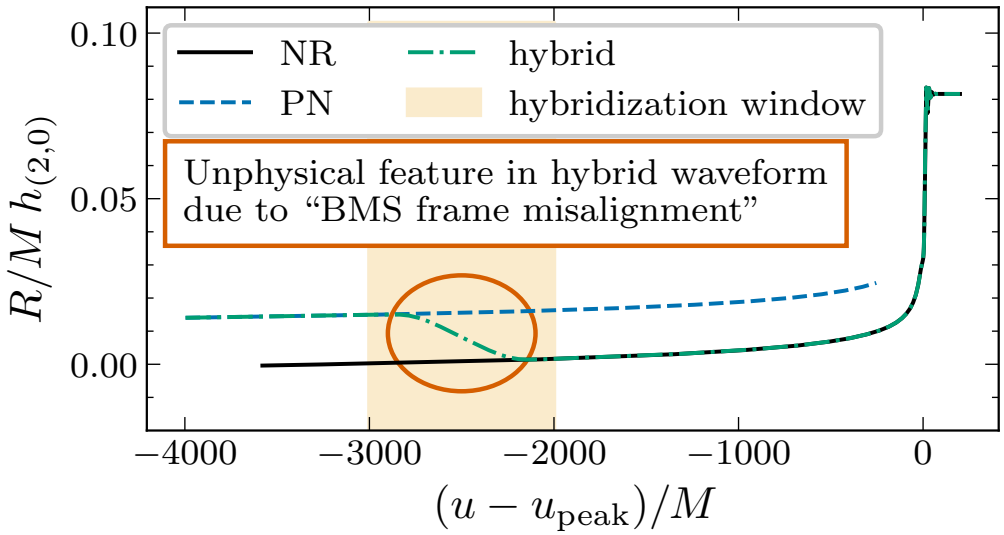

Figure 1.4: Comparing the $(2, 0)$ mode of a PN waveform (dashed, blue) and a NR waveform (solid, black), as output by CCE. The two waveforms are in different BMS frames—e.g., they differ by a supertranslation—so the hybridized waveform (dot-dashed, green), which is a smooth blending of the PN and NR waveforms, exhibits an unphysical feature in the hybridization window (orange).

because of the nontrivial symmetry group, i.e., the BMS group [52, 53].

1.7 BMS Frame Fixing

Because of the rich number of symmetries possessed by future null infinity, i.e., the BMS group, whenever one studies gravitational radiation they must also consider the frame freedom that such data possesses. As an example, consider first the more familiar Poincaré symmetries exhibited by Minkowski space. For a system in such a spacetime, to study that system in a meaningful way, one must first specify the specific frame, i.e., the coordinate system, that the system is in. This is because whether or not such a system is in its, e.g., center-of-mass frame can produce rather different interpretations of the radiation that the system is emitting. Consequently, this frame freedom plays an important role when comparing data across different waveform models, because there is no guarantee that the data from each model will be in the same frame. This issue is typically resolved by fixing the frame of one model to match that of the other. For systems that exhibit the Poincaré symmetries, this frame-fixing procedure is fairly straightforward. In particular, because there are only ten Poincaré freedoms, one can fix the Poincaré frame by mapping to the

center-of-mass frame, and choosing meaningful time and spatial axes.

For systems living at future null infinity and exhibiting the BMS symmetries, like the gravitational radiation emitted by a binary black hole merger, this process of fixing the BMS frame is more involved. This is because, unlike the Poincaré group, the BMS group is an infinite-dimensional group with no obvious canonical frame and more complicated coordinate transformations. Nonetheless, Refs. [52, 53] established meaningful BMS frames that can be used to fix the BMS freedom of waveforms at future null infinity, like those produced by CCE. This topic will be the main focus of Chapters 4 and 5. Effectively, what Refs. [52, 53] realized was that, like Poincaré frames which can be defined by the value of certain Poincaré charges, i.e., the momentum charge, the BMS frame of data at future null infinity can also be defined by certain BMS charges. Furthermore, they found that BMS charges that should be used are those which naturally fall out of the BMS conservation laws, like the Bondi mass aspect appearing in Eq. (1.11). This novel result enabled not only the robust analysis of NR waveforms, but also the construction of highly accurate waveform models that can be used by gravitational-wave detectors to study GR and measure the characteristics of GW-emitting sources. An example of a problem that can arise due to waveforms being in different BMS frames is shown in Fig. 1.4.

1.8 Waveform Modeling

Once a waveform has been produced by a simulation of some black hole coalescence, it can be used to compare against observations made by gravitational-wave detectors. However, because NR simulations are computationally expensive and therefore fairly slow to run, there is often a need to build models of the waveforms output by NR to speed up the analysis of real-world data. These waveform models typically come in two types: phenomenological models which aim to model the overall features of the waveform by make certain assumptions about how the data seems to behave [54–59], and surrogate models which aim to model the NR waveform data directly [60–68]. As should be clear, because surrogate models are trained on real NR data, they have a better chance at reproducing NR waveforms, which are our current best solutions to Einstein's equations for the astrophysical events that our detectors can observe.

A gravitational-wave surrogate model works via the following. First, given some waveforms in a consistent BMS frame for some series of parameters, e.g., mass ratio or spins, decompose the waveform data into smoothly varying pieces. For example, rather than modeling the waveform itself, which can be oscillatory in time, one can

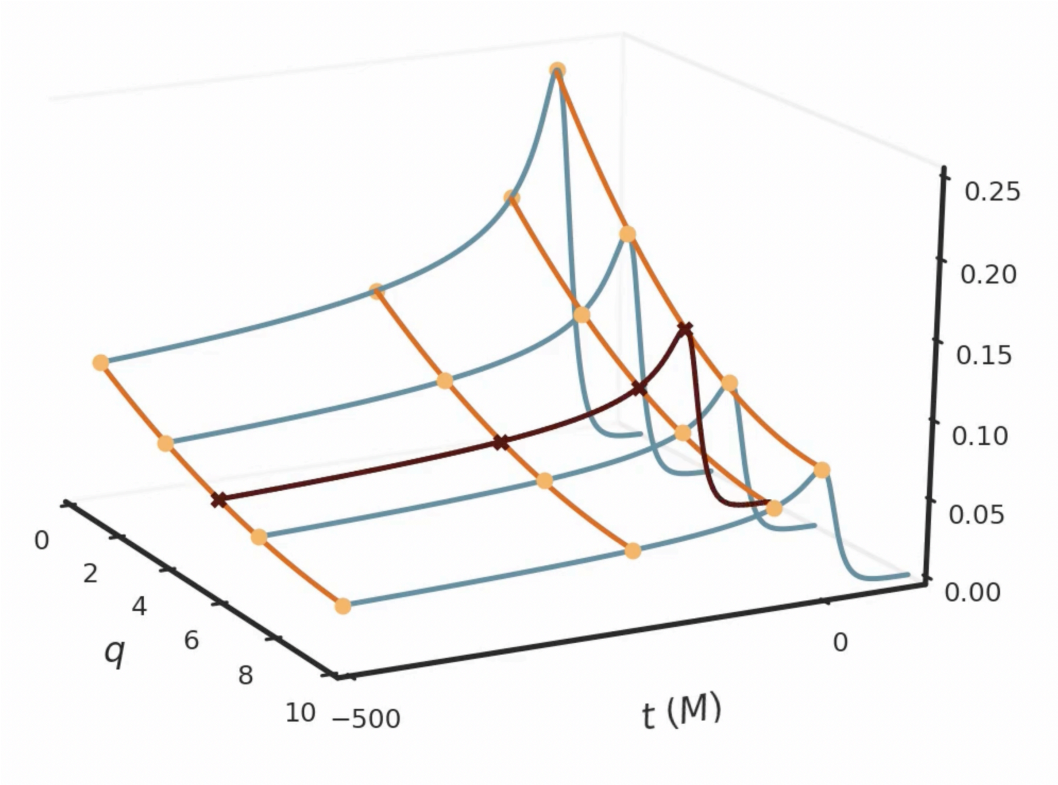

Figure 1.5: Demonstration of the gravitational-wave surrogate modeling procedure. Each blue curve corresponds to a training amplitude (as a function of time t), which is associated with a mass ratio q in the training parameter space. The orange points represent the interpolant points, with the red curves being the actual interpolants. The black curve corresponds to the evaluation of the surrogate model at a point not in the training parameter space, e.g., a waveform prediction. Credit: V. Varma.

instead model the amplitude and phase, which should be smooth functions of time and should vary smoothly over parameter space. Next, choose basis functions to model each of the smooth data pieces that were extracted from the input waveforms. This is typically performed using an iterative routine, i.e., at each iteration, use the waveform from the training set which has the largest projection error onto the basis as a new basis element for the next iteration. Once this procedure has converged, which usually takes ~10 iterations, one then has a set of basis functions (that are functions of time) that can be used to fit the waveform data pieces. Following this, build a basis of interpolants across parameter space at certain times that is the same size as the number of temporal basis functions. Finally, with these interpolants one can then solve a linear system of equations to obtain the coefficients of the temporal

basis functions and then compute the waveform at any point in parameter space [60]. An illustration of how the surrogate modeling procedure works is shown in Fig. 1.5. In Chapter 6 I will present the state-of-the-art gravitational-wave surrogate model for aligned-spin binary black hole waveforms that contain memory effects.

1.9 Black Hole Ringdowns

Another way to model gravitational waves, besides using surrogate models, that is particularly interesting from a testing-GR standpoint is trying to understand the "ringdown" of the remnant black hole after the progenitor black holes have merged. When two black holes merge, they form a highly perturbed remnant black hole that rings down to an equilibrium state by emitting energy via gravitational waves. Because this process can be viewed as some perturbation acting on an isolated black hole geometry, it turns out that this problem can be solved using black hole perturbation theory [69]. In particular, when solving Einstein's equations in this perturbed geometry, one finds that the equations are not only separable, but also yield a relatively simple set of solutions at first order that describe a set of discrete frequencies at which the black hole can ring. These are called quasi-normal modes (QNMs) and only depend on the mass and spin of the remnant black hole. Therefore, they can be used test GR by seeing if the observed frequencies match those that are predicted by black hole perturbation theory in the context of GR [70, 71].

More specifically, first-order black hole perturbation theory states that the strain emitted by a ringing black hole can be modeled as

$$h = \sum_{\ell,|m|\leq\ell,n,p\in[-1,+1]} A_{(\ell,m,n,p)} e^{-i\omega_{(\ell,m,n,p)}t}, \tag{1.12}$$

where ℓ and m are the angular indices, n is the overtone number and can be thought of as a radial index that corresponds to the lifetime of each QNM, $p = \mathrm{sgn}\,(m\mathrm{Re}\,[\omega])$ describes whether the QNM phase front is co-rotating ($p = +$) or counter-rotating ($p = -$) with the black hole, $A_{(\ell,m,n,p)}$ is the complex amplitude of the QNM, and $\omega_{(\ell,m,n,p)}$ is the complex frequency of the QNM. With this, one can then test GR by, e.g., fitting a NR waveform with this QNM model, computing the amplitudes for each QNM frequency, and seeing if these amplitudes agree with those measured from real-world data. However, one main challenge with this fitting procedure is that, a priori, it is not known what QNMs are really present in the NR data. Thus, fitting NR waveforms needs to be carried out with care to ensure that the fits are physically meaningful and that other, nonlinear content in the NR waveform is not being fit away by these simple and numerous linear QNM predictions.

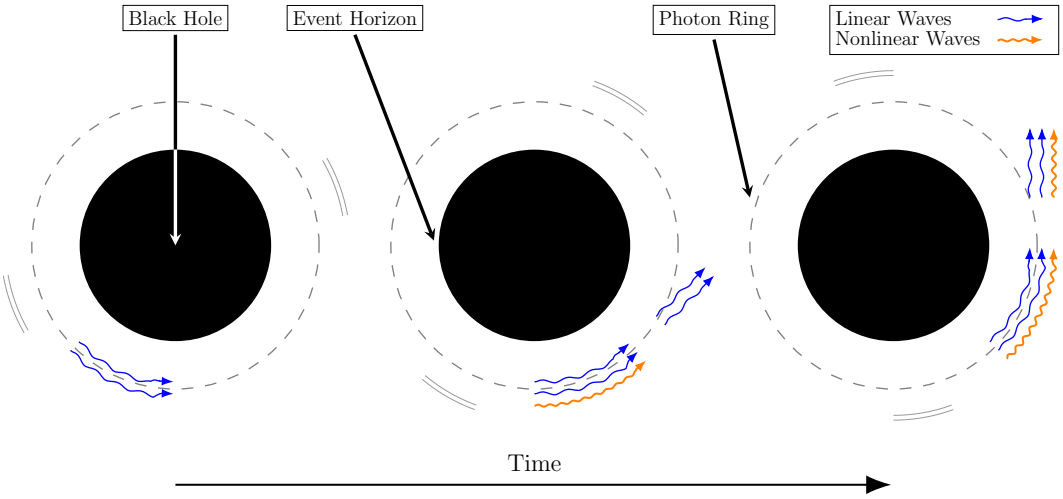

Figure 1.6: Cartoon showing how two linear QNMs (blue) can interact with each other near the black hole light ring and produce a nonlinear QNM (orange) that escapes from the black hole to future null infinity. Credit: L. C. Stein.

This turns out to be a real challenge in NR data analyses because the waveforms produced by NR simulations are not solutions to the linearized Einstein's equations, but are instead solutions to the fully nonlinear set of equations. As a result, in the ringdown of these waveforms it is expected (and has been shown [72, 73]) that there should be nonlinear features of GR that are mixed in with the linear QNMs. This is because black hole perturbation theory, at some arbitrary order, looks like

$$\mathcal{T}\psi = \mathcal{S}, \tag{1.13}$$

where $\mathcal{T}$ is the Teukolsky operator, i.e., the linearized Einstein equations, ψ is the perturbation to the remnant black hole, and $\mathcal{S}$ is some source term that vanishes for linear perturbations in vacuum [69]. So, at second order, $\mathcal{S}$ will instead be some nontrivial source, which is a function of the first-order perturbation, than can source non-negligible, higher-order contributions to the ringdown phase of NR waveforms. A cartoon showing how ringdown nonlinearities can be sourced is shown in Fig. 1.6. The exact form of these higher-order ringdown contributions and their presence in NR waveforms will be examined in Chapter 7.

1.10 Thesis Outline

The rest of this thesis is organized as follows.

Chapter 2 presents the NR waveforms computed using CCE and provides an explicit calculation of the BMS balance laws that can be used to study the memory content,

as well as other features, of NR waveforms. This work was published in Ref. [49].

Chapter 3 illustrates how existing NR waveforms that do not contain memory effects can be corrected to contain such phenomena using the BMS balance laws of Ref. [49]. This work was published in Ref. [50].

Chapter 4 provides a method to constrain the BMS freedoms of NR waveforms at future null infinity by minimizing the error between NR and PN waveforms as a function of a finite-dimensional BMS transformation applied to the NR system. This work was published in Ref. [52].

Chapter 5 provides an improved method for fixing the BMS frame compared to Ref. [52] which explicitly relies on BMS charges and is thus much faster than numerical optimization. This work was published in Ref. [53].

Chapter 6 builds a surrogate model that models the waveforms produced by CCE. It is trained on binary black hole merger simulations with mass ratios $q \leq 8$ and dimensionless spins that are aligned with the orbital angular momentum with magnitudes $\chi_{1,2} \leq 0.8$. This work was published in Ref. [68].

Chapter 7 shows that ringdown predictions from second-order perturbation theory can be found in the ringdown of NR waveforms and exhibit the expected behavior of a second-order perturbation. This work was published in Ref. [72].

References

[1] A. Einstein, Sitzungsberichte der Königlich Preussischen Akademie der Wissenschaften, 844 (1915).

[2] M. Born and P. Jordan, Z. Phys. **34**, 858 (1925) 10.1007/BF01328531.

[3] B. P. Abbott et al. (LIGO Scientific, Virgo), Phys. Rev. Lett. **116**, 061102 (2016) 10.1103/PhysRevLett.116.061102.

[4] B. P. Abbott et al. (LIGO Scientific, Virgo), Phys. Rev. Lett. **116**, 241102 (2016) 10.1103/PhysRevLett.116.241102.

[5] M. PLANCK, Verhandlungen der deutschen physikalischen Gesellschaft, 136.

[6] H. Bondi, M. G. J. van der Burg, and A. W. K. Metzner, Proc. Roy. Soc. Lond. A **269**, 21 (1962) 10.1098/rspa.1962.0161.

[7] R. K. Sachs, Proc. Roy. Soc. Lond. A **270**, 103 (1962) 10.1098/rspa.1962.0206.

[8] H. Minkowski, Mathematische Annalen **68**, 472 (1910).

[9] E. Noether, ger, Nachrichten von der Gesellschaft der Wissenschaften zu Göttingen, Mathematisch-Physikalische Klasse **1918**, 235 (1918).

[10] A. Einstein, Sitzungsberichte der Königlich Preussischen Akademie der Wissenschaften, 688 (1916).

[11] L. Lorenz, The London, Edinburgh, and Dublin Philosophical Magazine and Journal of Science **34**, 287 (1867) 10.1080/14786446708639882.

[12] Y. B. Zel'dovich and A. G. Polnarev, Sov. Astron. **18**, 17 (1974).

[13] V. B. Braginsky and L. P. Grishchuk, Sov. Phys. JETP **62**, 427 (1985).

[14] V. B. Braginsky and K. S. Thorne, Nature **327**, 123 (1987) 10.1038/327123a0.

[15] D. Christodoulou, Phys. Rev. Lett. **67**, 1486 (1991) 10.1103/PhysRevLett.67.1486.

[16] P. N. Payne, Phys. Rev. D **28**, 1894 (1983) 10.1103/PhysRevD.28.1894.

[17] L. Blanchet and T. Damour, Phys. Rev. D **46**, 4304 (1992) 10.1103/PhysRevD.46.4304.

[18] K. S. Thorne, Phys. Rev. D **45**, 520 (1992) 10.1103/PhysRevD.45.520.

[19] L. Bieri and D. Garfinkle, Phys. Rev. D **89**, 084039 (2014) 10.1103/PhysRevD.89.084039.

[20] J. Winicour, Class. Quant. Grav. **31**, 205003 (2014) 10.1088/0264-9381/31/20/205003.

[21] É. É. Flanagan and D. A. Nichols, Phys. Rev. D **92**, [Erratum: Phys.Rev.D 93, 049905 (2016)], 084057 (2015) 10.1103/PhysRevD.92.084057.

[22] A. Strominger and A. Zhiboedov, JHEP **01**, 086 (2016) 10.1007/JHEP01(2016)086.

[23] E. T. Newman and R. Penrose, J. Math. Phys. **7**, 863 (1966) 10.1063/1.1931221.

[24] R. P. Geroch and J. Winicour, J. Math. Phys. **22**, 803 (1981) 10.1063/1.524987.

[25] A. Ashtekar and M. Streubel, Proc. Roy. Soc. Lond. A **376**, 585 (1981) 10.1098/rspa.1981.0109.

[26] T. Dray and M. Streubel, Class. Quant. Grav. **1**, 15 (1984) 10.1088/0264-9381/1/1/005.

[27] M. Ludvigsen, Gen. Rel. Grav. **21**, 1205 (1989) 10.1007/BF00763308.

[28] S. Weinberg, Phys. Rev. **140**, B516 (1965) 10.1103/PhysRev.140.B516.

[29] A. Strominger, JHEP **07**, 152 (2014) 10.1007/JHEP07(2014)152.

[30] S. Pasterski, M. Pate, and A.-M. Raclariu, in Snowmass 2021 (Nov. 2021).

[31] E. Gourgoulhon, (2007).

[32] F. Pretorius, Phys. Rev. Lett. **95**, 121101 (2005) 10.1103/PhysRevLett.95.121101.

[33] F. Pretorius, Class. Quant. Grav. **22**, 425 (2005) 10.1088/0264-9381/22/2/014.

[34] U. Sperhake, Class. Quant. Grav. **32**, 124011 (2015) 10.1088/0264-9381/32/12/124011.

[35] *The Spectral Einstein Code*, https://www.black-holes.org/code/SpEC.html.

[36] *Simulating eXtreme Spacetimes*, https://www.black-holes.org/.

[37] N. T. Bishop, R. Gomez, L. Lehner, B. Szilagyi, J. Winicour, and R. A. Isaacson, "Cauchy characteristic matching", in *Black Holes, Gravitational Radiation and the Universe: Essays in Honor of C.V. Vishveshwara*, edited by B. R. Iyer and B. Bhawal (Jan. 1998), pp. 383–408, 10.1007/978-94-017-0934-7_24.

[38] N. T. Bishop, R. Gomez, L. Lehner, and J. Winicour, Phys. Rev. D **54**, 6153 (1996) 10.1103/PhysRevD.54.6153.

[39] N. T. Bishop, R. Gomez, L. Lehner, M. Maharaj, and J. Winicour, Phys. Rev. D **56**, 6298 (1997) 10.1103/PhysRevD.56.6298.

[40] C. Reisswig, N. T. Bishop, D. Pollney, and B. Szilagyi, Class. Quant. Grav. **27**, 075014 (2010) 10.1088/0264-9381/27/7/075014.

[41] C. Reisswig, N. T. Bishop, D. Pollney, and B. Szilagyi, Phys. Rev. Lett. **103**, 221101 (2009) 10.1103/PhysRevLett.103.221101.

[42] M. C. Babiuc, B. Szilagyi, J. Winicour, and Y. Zlochower, Phys. Rev. D **84**, 044057 (2011) 10.1103/PhysRevD.84.044057.

[43] C. J. Handmer and B. Szilagyi, Class. Quant. Grav. **32**, 025008 (2015) 10.1088/0264-9381/32/2/025008.

[44] C. J. Handmer, B. Szilágyi, and J. Winicour, Class. Quant. Grav. **32**, 235018 (2015) 10.1088/0264-9381/32/23/235018.

[45] C. J. Handmer, B. Szilágyi, and J. Winicour, Class. Quant. Grav. **33**, 225007 (2016) 10.1088/0264-9381/33/22/225007.

[46] J. Moxon, M. A. Scheel, and S. A. Teukolsky, Phys. Rev. D **102**, 044052 (2020) 10.1103/PhysRevD.102.044052.

[47] N. Deppe, W. Throwe, L. E. Kidder, N. L. Vu, K. C. Nelli, C. Armaza, M. S. Bonilla, F. Hébert, Y. Kim, P. Kumar, G. Lovelace, A. Macedo, J. Moxon, E. O'Shea, H. P. Pfeiffer, M. A. Scheel, S. A. Teukolsky, N. A. Wittek, et al., *SpECTRE v2024.04.12*, 10.5281/zenodo.10967177, version 2024.04.12, Apr. 2024, 10.5281/zenodo.10967177.

[48] J. Moxon, M. A. Scheel, S. A. Teukolsky, N. Deppe, N. Fischer, F. Hébert, L. E. Kidder, and W. Throwe, Phys. Rev. D **107**, 064013 (2023) 10.1103/PhysRevD.107.064013.

[49] K. Mitman, J. Moxon, M. A. Scheel, S. A. Teukolsky, M. Boyle, N. Deppe, L. E. Kidder, and W. Throwe, Phys. Rev. D **102**, 104007 (2020) 10.1103/PhysRevD.102.104007,

[50] K. Mitman et al., Phys. Rev. D **103**, 024031 (2021) 10.1103/PhysRevD.103.024031,

[51] L. Blanchet, Living Rev. Rel. **17**, 2 (2014) 10.12942/lrr-2014-2.

[52] K. Mitman et al., Phys. Rev. D **104**, 024051 (2021) 10.1103/PhysRevD.104.024051,

[53] K. Mitman et al., Phys. Rev. D **106**, 084029 (2022) 10.1103/PhysRevD.106.084029,

[54] S. Khan, F. Ohme, K. Chatziioannou, and M. Hannam, Phys. Rev. D **101**, 024056 (2020) 10.1103/PhysRevD.101.024056.

[55] A. Nagar, G. Riemenschneider, G. Pratten, P. Rettegno, and F. Messina, Phys. Rev. D **102**, 024077 (2020) 10.1103/PhysRevD.102.024077.

[56] G. Pratten et al., Phys. Rev. D **103**, 104056 (2021) 10.1103/PhysRevD.103.104056.

[57] S. Ossokine et al., Phys. Rev. D **102**, 044055 (2020) 10.1103/PhysRevD.102.044055.

[58] S. Akcay, R. Gamba, and S. Bernuzzi, Phys. Rev. D **103**, 024014 (2021) 10.1103/PhysRevD.103.024014.

[59] H. Estellés, M. Colleoni, C. García-Quirós, S. Husa, D. Keitel, M. Mateu-Lucena, M. d. L. Planas, and A. Ramos-Buades, Phys. Rev. D **105**, 084040 (2022) 10.1103/PhysRevD.105.084040.

[60] S. E. Field, C. R. Galley, J. S. Hesthaven, J. Kaye, and M. Tiglio, Phys. Rev. X **4**, 031006 (2014) 10.1103/PhysRevX.4.031006.

[61] J. Blackman, S. E. Field, C. R. Galley, B. Szilágyi, M. A. Scheel, M. Tiglio, and D. A. Hemberger, Phys. Rev. Lett. **115**, 121102 (2015) 10.1103/PhysRevLett.115.121102.

[62] J. Blackman, S. E. Field, M. A. Scheel, C. R. Galley, D. A. Hemberger, P. Schmidt, and R. Smith, Phys. Rev. D **95**, 104023 (2017) 10.1103/PhysRevD.95.104023.

[63] J. Blackman, S. E. Field, M. A. Scheel, C. R. Galley, C. D. Ott, M. Boyle, L. E. Kidder, H. P. Pfeiffer, and B. Szilágyi, Phys. Rev. D **96**, 024058 (2017) 10.1103/PhysRevD.96.024058.

[64] V. Varma, S. E. Field, M. A. Scheel, J. Blackman, L. E. Kidder, and H. P. Pfeiffer, Phys. Rev. D **99**, 064045 (2019) 10.1103/PhysRevD.99.064045.

[65] V. Varma, S. E. Field, M. A. Scheel, J. Blackman, D. Gerosa, L. C. Stein, L. E. Kidder, and H. P. Pfeiffer, Phys. Rev. Research. **1**, 033015 (2019) 10.1103/PhysRevResearch.1.033015.

[66] T. Islam, V. Varma, J. Lodman, S. E. Field, G. Khanna, M. A. Scheel, H. P. Pfeiffer, D. Gerosa, and L. E. Kidder, Phys. Rev. D **103**, 064022 (2021) 10.1103/PhysRevD.103.064022.

[67] J. Yoo, V. Varma, M. Giesler, M. A. Scheel, C.-J. Haster, H. P. Pfeiffer, L. E. Kidder, and M. Boyle, Phys. Rev. D **106**, 044001 (2022) 10.1103/PhysRevD.106.044001.

[68] J. Yoo et al., Phys. Rev. D **108**, 064027 (2023) 10.1103/PhysRevD.108.064027,

[69] W. H. Press and S. A. Teukolsky, Astrophys. J. **185**, 649 (1973) 10.1086/152445.

[70] M. Isi, M. Giesler, W. M. Farr, M. A. Scheel, and S. A. Teukolsky, Phys. Rev. Lett. **123**, 111102 (2019) 10.1103/PhysRevLett.123.111102.

[71] M. Isi, W. M. Farr, M. Giesler, M. A. Scheel, and S. A. Teukolsky, Phys. Rev. Lett. **127**, 011103 (2021) 10.1103/PhysRevLett.127.011103.

[72] K. Mitman et al., Phys. Rev. Lett. **130**, 081402 (2023) 10.1103/PhysRevLett.130.081402,

[73] M. H.-Y. Cheung et al., Phys. Rev. Lett. **130**, 081401 (2023) 10.1103/PhysRevLett.130.081401.

Chapter 2

COMPUTATION OF DISPLACEMENT AND SPIN GRAVITATIONAL MEMORY IN NUMERICAL RELATIVITY

K. Mitman, J. Moxon, M. A. Scheel, S. A. Teukolsky, M. Boyle, N. Deppe, L. E. Kidder, and W. Throwe, Phys. Rev. D **102**, 104007 (2020) 10.1103/PhysRevD.102.104007,

2.1 Abstract

We present the first numerical relativity waveforms for binary black hole mergers produced using spectral methods that show both the displacement and the spin memory effects. Explicitly, we use the SXS Collaboration's SpEC code to run a Cauchy evolution of a binary black hole merger and then extract the gravitational wave strain using SpECTRE's version of a Cauchy-characteristic extraction. We find that we can accurately resolve the strain's traditional $m = 0$ memory modes and some of the $m \neq 0$ oscillatory memory modes that have previously only been theorized. We also perform a separate calculation of the memory using equations for the Bondi-Metzner-Sachs charges as well as the energy and angular momentum fluxes at asymptotic infinity. Our new calculation uses only the gravitational wave strain and two of the Weyl scalars at infinity. Also, this computation shows that the memory modes can be understood as a combination of a memory signal throughout the binary's inspiral and merger phases, and a quasinormal mode signal near the ringdown phase. Additionally, we find that the magnetic memory, up to numerical error, is indeed zero as previously conjectured. Lastly, we find that signal-to-noise ratios of memory for LIGO, the Einstein Telescope (ET), and the Laser Interferometer Space Antenna (LISA) with these new waveforms and new memory calculation are larger than previous expectations based on post-Newtonian or Minimal Waveform models.

2.2 Introduction

As has been understood since the early 1970s [1–4], when gravitational waves (GWs) pass through the arms of a GW detector, a persistent physical change to the corresponding region of spacetime is induced as a result of the transient radiation. Originally, this effect, which is referred to as the *memory effect* or just *memory*, was found by studying the fly-by behavior of two compact astrophysical objects that

travel to asymptotic infinity as $t \to +\infty$ on timelike paths [1]. Later, it was realized that the memory effect also occurs when null radiation travels to asymptotic null infinity as $r, t \to +\infty$ at a fixed Bondi time $u \equiv t - r$ [3]. Originally, these two unique contributions to memory were called *linear memory* and *nonlinear memory*[1] because of the order of the metric's perturbative expansion that was used to calculate each of the independent memory contributions.

Recently, the memory effect was realized to be the element needed to extend the Poincaré conservation laws to the infinite number of proper Bondi-Metzner-Sachs (BMS) conservation laws [5–8], which correspond to the various BMS and extended BMS transformations [9–17], i.e., supertranslations, superrotations, and superboosts.[2] Unlike the ten Poincaré conservation laws, which equate the change in the Poincaré charges to the corresponding energy and momentum fluxes, the BMS conservation laws state that the change in the BMS charges minus the corresponding fluxes[3] is exactly the memory effect, i.e.,

$$\text{Change in BMS charges} - \text{BMS fluxes} = \text{Memory}. \tag{2.2}$$

Early studies of gravitational memory focused on the type of memory corresponding to supertranslations and supermomentum, which is called *displacement memory*. We follow [6] and [7] and refer to the other memory effects, which are related to superrotations and superboosts, as the *spin* and the *center-of-mass* (CM) memory effects. While the displacement memory is the most prominent in the strain of a gravitational wave, the spin and CM memory effects can most easily be noticed in the time integral of the strain. Physically, displacement memory is related to a change in a GW detector's arm length [1–4], while the spin memory relates to the relative time delay that would be acquired by counter-orbiting objects, e.g., the particle beams in the Large Hadron Collider or a freely falling Sagnac interferometer [6]. The CM memory, by contrast, corresponds to the relative time delay that would be acquired

[1] Also known as *Christodoulou memory* [3, 4].

[2] Formally, superrotations and superboosts, which are the two types of super-Lorentz transformations, can be realized as the $|m| \geq 2$ elements of the Virasoro algebra (an extension of the more common Möbius transformations, i.e., $PL(2, \mathbb{C})$), just as supertranslations can be viewed as the $l \geq 2$ spherical harmonics. These super-Lorentz transformations, though, which form the extended BMS group, do not preserve asymptotic flatness.

[3] Often, the BMS conservation law is written as

$$\text{Change in BMS charges} - \text{BMS fluxes} = 0, \tag{2.1}$$

where the "BMS flux" is understood to have two contributions: "hard" and "soft," with the hard contribution being the flux in Eq. (2.2) and the soft contribution being the memory in Eq. (2.2).

by objects on antiparallel paths [7]. As an example, for two particles bouncing back and forth in a Fabry-Perot cavity, if a gravitational wave propagates at an angle through the cavity, then the particles will acquire a relative time delay given by the CM memory.

Furthermore, because the various memory effects are now known to be calculable from BMS flux-balance laws, both of the previous classifications of linear and nonlinear contributions have been renamed to be more indicative of what they represent. Instead, the two contributions to each of the three memory effects are now referred to as the *ordinary memory* and the *null memory*. Moreover, the modern nomenclature also avoids potential confusion about which types of terms should be included in each memory effect because whether a particular effect appears linearly or nonlinearly varies with the perturbation theory that is being considered [18]. As one might expect, for the most common sources of observable GW radiation, i.e., binary black holes (BBHs), the displacement memory is the most prominent, followed by the spin memory, and then the center-of-mass memory [7].

Over the past few years, there have been many studies of whether current or future GW detectors could measure the displacement and the spin memory effects [19–24]. These previous studies, however, used approximations of the memory since earlier calculations of the memory in a BBH merger have, until now, been incomplete. For one, the waveforms produced by numerical simulations using extrapolation techniques have been unable to resolve the primary $m = 0$ memory modes and have also failed to produce the expected memory in certain oscillatory $m \neq 0$ memory modes.[4] Apart from this, previous calculations of memory have used post-Newtonian (PN) approximations or have tried to compute an effective memory using the available numerical waveforms through various kinds of postprocessing techniques [19, 22, 26, 27].

So far, PN approximations have been computed for the modes contributing to the displacement memory through 3PN order, through 2.5PN order for the spin memory, and even through 3PN for the CM memory [7, 19, 20]. However, the memory effect is predominantly accumulated during the merger phase of a BBH coalescence, in which most of the system's energy and angular momentum are radiated by GWs. Because PN theory cannot capture the merger phase of a BBH coalescence, we must

[4] While the strain $(2, 0)$ mode, which is the primary contributor to the displacement memory, has been resolved previously [25], the code used in this work was much more computationally expensive and thus could not easily run longer simulations required to accurately resolve the other memory effects.

instead use numerical relativity (NR) simulations to calculate the displacement, spin, and CM memory effects.

As already mentioned, previous numerical relativity simulations have been unable to extract the three unique memory effects for a variety of reasons [19]. For one, numerical relativity simulations of BBH mergers typically compute the strain on concentric finite-radius spheres and then extrapolate the strain to future null infinity using a collection of fits. While this procedure is adequate for computing the main strain modes, it unfortunately does not produce waveforms that accurately resolve the modes responsible for illustrating the various memory effects. As a result, even though approximate calculations of the memory in the strain can be performed using waveforms that have been computed thus far, they will nonetheless be incomplete since they fail to include the next-order memory contributions from the fluxes induced by the memory modes themselves. Furthermore, many of these postprocessing computations of the memory use only the primary waveform modes—often just the $(2, 2)$ mode—instead of every mode. This is because, before this work, there has not been a method for fully computing the memory from every mode of a waveform.[5]

As a part of this study, we present the first successful resolution of the modes that contain memory by using the Simulating eXtreme Spacetimes (SXS) Collaboration's older and newer codes, `SpEC` [28] and `SpECTRE` [29]. Explicitly, we use Cauchy-characteristic extraction (CCE) to evolve a world tube produced by a Cauchy evolution to asymptotic infinity, where we extract many observables, most importantly the strain [30]. With CCE, we find that we can resolve many of the $m = 0$ and $m \neq 0$ modes that contribute to the displacement and spin memories. Through this, we observe that not only do CCE waveforms surpass extrapolated waveforms in terms of resolving the displacement memory, but they also exhibit a spin memory that is roughly twice as much as what is seen in the extrapolated waveforms [20]. Furthermore, we compare the displacement and spin memory modes to the memory computed from the numerical waveforms using the new memory equations presented in this paper. We find that the two agree exceptionally well, which implies that the CCE waveforms obey the BMS flux-balance laws to a rather high degree of accuracy. We also briefly discuss the CM memory's formulation in Sec. 2.3.2.3 and

[5] In [22] a procedure using the result of [4] was presented for computing just the displacement memory using all of the modes of a strain waveform. However, this method was only used on extrapolated waveforms, which exhibit no displacement memory, and thus fails to accurately capture the "memory of the memory", i.e., the memory induced by the memory modes.

its presence in our numerical results in Appendix 2.C.

2.2.1 Overview

We organize our computations and results as follows. Using Einstein's field equations, we compute expressions for the displacement and spin memory in Secs. 2.3.1 and 2.3.2, which are valid in asymptotically flat spacetimes. Moreover, we write these expressions in terms of the observables that are explicitly produced by SXS's CCE. We also provide a few brief comments on the CM memory in Sec. 2.3.2.3, but not a complete mathematical expression. Following this, in Sec. 2.4.1, we describe certain aspects of CCE and outline the choices that we make to produce memory results that agree with post-Newtonian theory. Note, we explore the features of CCE further in Sec. 2.4.8. Continuing to our numerical results, in Sec. 2.4.2, we then illustrate how well our extracted observables comply with the BMS flux-balance laws that we compute in Sec. 2.3.2. Next, in Secs. 2.4.3, 2.4.4, and 2.4.5, we present the results for five numerical simulations covering combinations of equal and unequal masses, spinning and nonspinning, and precessing and nonprecessing, whose parameters are outlined in the introduction of Sec. 2.4. We not only show the success of CCE in resolving the modes that express memory effects, but also compare them to the memory that is expected according to our calculations in Sec. 2.3.2. Furthermore, in Sec. 2.4.6, we show that during ringdown, the most prominent memory modes can be accurately modeled as a sum of the null memory contribution and the corresponding quasinormal modes (QNMs) of the remnant BH. Finally, in Sec. 2.4.7, with these results we then compute signal-to-noise ratios (SNRs) for LIGO, ET, and LISA and thus provide estimates on the measurability of both the displacement and the spin memory effects. We also provide computations of the Bondi mass aspect and the Bondi angular momentum aspect in Appendixes 2.A and 2.B in terms of the strain and the Weyl scalars Ψ_2 and Ψ_1. Appendix 2.C gives an informal presentation of a mode of the strain that exhibits the CM memory effect.

2.2.2 Conventions

We set $c = G = 1$. When working with complex dyads, following the work of Moxon *et al.* [30], we use

$$q_A = -(1, i \sin\theta) \text{ and } q^A = -(1, i \csc\theta), \tag{2.3}$$

and denote the round metric on the two-sphere as q_{AB}. The complex dyad obeys the following properties

$$q_A q^A = 0,\ q_A \bar{q}^A = 2,\ q_{AB} = \frac{1}{2}(q_A \bar{q}_B + \bar{q}_A q_B). \tag{2.4}$$

We built spin-weighted fields with the dyads as follows. For a tensor field $W_{A\cdots D}$, the function

$$W = W_{A\cdots BC\cdots D} q^A \cdots q^B \bar{q}^C \cdots \bar{q}^D \tag{2.5}$$

with m factors of q and n factors of $\bar{q}$ has spin-weight $s = m - n$. We raise and lower spins using the differential spin-weight operators $\eth$ and $\bar{\eth}$,

$$\eth W = (D_E W_{A\cdots BC\cdots D}) q^A \cdots q^B \bar{q}^C \cdots \bar{q}^D q^E, \tag{2.6a}$$

$$\bar{\eth} W = (D_E W_{A\cdots BC\cdots D}) q^A \cdots q^B \bar{q}^C \ldots \bar{q}^D \bar{q}^E. \tag{2.6b}$$

Here, D_A is the covariant derivative on the two-sphere. The $\eth$ and $\bar{\eth}$ operators in spherical coordinates are then

$$\eth W(\theta,\phi) = -(\sin\theta)^{+s}(\partial_\theta + i \csc\theta \partial_\phi) \left[(\sin\theta)^{-s} W(\theta,\phi)\right], \tag{2.7a}$$

$$\bar{\eth} W(\theta,\phi) = -(\sin\theta)^{-s}(\partial_\theta - i \csc\theta \partial_\phi) \left[(\sin\theta)^{+s} W(\theta,\phi)\right]. \tag{2.7b}$$

Thus, when acting on spin-weighted spherical harmonics, these operators produce

$$\eth({}_sY_{\ell m}) = +\sqrt{(\ell - s)(\ell + s + 1)}\, {}_{s+1}Y_{\ell m}, \tag{2.8a}$$

$$\bar{\eth}({}_sY_{\ell m}) = -\sqrt{(\ell + s)(\ell - s + 1)}\, {}_{s-1}Y_{\ell m}. \tag{2.8b}$$

As a result, for $f(\theta,\phi)$ an arbitrary spin-weight 0 function, the spherical Laplacian D^2 is then given by

$$D^2 f(\theta,\phi) = \eth\bar{\eth} f(\theta,\phi) = \bar{\eth}\eth f(\theta,\phi). \tag{2.9}$$

Last, for our comparisons to PN computations, we use the polarization convention that coincides with Kidder [31], rather than Blanchet [32], since most PN calculations of the memory make this choice as well [19, 20].

2.3 Description of Memory

We now review the mathematical formulation of the memory effects and extend previous results to be more relevant for calculations in numerical relativity.

2.3.1 Bondi Framework

We begin by reviewing a few of Einstein's equations for the asymptotically flat Bondi-Sachs metric to obtain relationships between conserved charge quantities and memory-contributing terms. We closely follow the work of Flanagan and Nichols [33], but we only consider a vacuum spacetime. We extend their results by computing the memory contribution to the gravitational wave strain, i.e., the quantity that is extracted in numerical relativity and currently measured by GW detectors.

Consider retarded Bondi coordinates, $(u, r, \theta^1, \theta^2)$, near future null infinity, where $u \equiv t - r$. For such a system, the metric of arbitrary asymptotically flat spacetimes can be written in the form

$$\begin{aligned} ds^2 = &-Ue^{2\beta}du^2 - 2e^{2\beta}dudr \\ &+ r^2\gamma_{AB}(d\theta^A - \mathcal{U}^A du)(d\theta^B - \mathcal{U}^B du), \end{aligned} \tag{2.10}$$

where $A, B \in \{1, 2\}$ are coordinates on the two-sphere, and U, β, $\mathcal{U}^A$, and γ_{AB} are functions of u, r, and θ^A. Here we apply the four gauge conditions

$$g_{rr} = 0,\ g_{rA} = 0,\ \text{and}\ \det(\gamma_{AB}) = \det(q_{AB}), \tag{2.11}$$

where $g_{\mu\nu}$ is the metric of four-dimensional spacetime. We now expand these metric functions as series in $1/r$ to relevant orders, which gives

$$U = 1 - \frac{2m}{r} - \frac{2\mathcal{M}}{r^2} + O(r^{-3}), \tag{2.12}$$

$$\beta = \frac{\beta_0}{r} + \frac{\beta_1}{r^2} + \frac{\beta_2}{r^3} + O(r^{-4}), \tag{2.13}$$

$$\begin{aligned} \mathcal{U}^A = \frac{U^A}{r^2} + \frac{1}{r^3}\Big[&-\frac{2}{3}N^A + \frac{1}{16}D^A(C_{BC}C^{BC}) \\ &+ \frac{1}{2}C^{AB}D^C C_{BC}\Big] + O(r^{-4}), \end{aligned} \tag{2.14}$$

$$\gamma_{AB} = q_{AB} + \frac{C_{AB}}{r} + \frac{D_{AB}}{r^2} + \frac{E_{AB}}{r^3} + O(r^{-4}), \tag{2.15}$$

where the various coefficients on the right-hand sides are functions of (u, θ^A) only, and $q_{AB}(\theta^A)$ is the metric on the two-sphere, i.e., $q_{AB}(\theta, \phi) = d\theta^2 + \sin^2\theta\, d\phi^2$ in ordinary spherical coordinates. The three most important functions above are: the Bondi mass aspect m, the Bondi angular momentum aspect N^A, and the shear tensor C_{AB}, whose retarded time derivative is the Bondi news tensor $N_{AB} \equiv \partial_u C_{AB}$. The Bondi mass aspect is related to the supermomentum charge while the angular

momentum, once a few extra terms are included,[6] corresponds to the super-Lorentz charges [8]. Applying the gauge conditions in Eq. (2.11) produces the constraints

$$q^{AB}C_{AB} = 0, \tag{2.16}$$

$$D_{AB} = \frac{1}{4}q_{AB}C_{CD}C^{CD} + \mathcal{D}_{AB}, \tag{2.17}$$

$$E_{AB} = \frac{1}{2}q_{AB}C_{CD}\mathcal{D}^{CD} + \mathcal{E}_{AB}, \tag{2.18}$$

where $\mathcal{D}_{AB}$ and $\mathcal{E}_{AB}$ are two arbitrary traceless tensors.

Finally, we consider Einstein's equations. By computing the $O(1/r^2)$ terms of the uu part of the evolution equation for the Bondi mass aspect, we find

$$\dot{m} = -\frac{1}{8}N_{AB}N^{AB} + \frac{1}{4}D^A D^B N_{AB}. \tag{2.19}$$

Equation (2.19) is identical to the central result of [9], which outlines the link between a system's news and mass loss.[7] If we integrate and reorder this equation, we obtain

$$\frac{1}{4}D^A D^B C_{AB} = m + 4\pi\mathcal{E}, \tag{2.20}$$

where

$$\mathcal{E} = \frac{1}{32\pi}\int N_{AB}N^{AB}du \tag{2.21}$$

is just the energy that is radiated per unit solid angle. Equation (2.20) represents one of the two BMS flux-balance laws that we will examine. The first term corresponds to the memory appearing in the shear. The second term, which relates to the ordinary memory contribution, can be understood as the change in a BMS charge—specifically, the supermomentum charge. The third term, which can be viewed as the null memory contribution, is a flux—specifically, an energy flux. We now repeat the calculation performed above, but for the angular momentum aspect.

Computing the $O(1/r^2)$ terms of the uA part of the evolution equation for the angular momentum aspect produces an equation similar to that of Eq. (2.19),

$$\begin{aligned}\dot{N}_A = D_A m + \frac{1}{4}D_B D_A D_C C^{BC} - \frac{1}{4}D^2 D^B C_{AB} \\ + \frac{1}{4}D_B(C_{AC}N^{BC}) + \frac{1}{2}C_{AC}D_B N^{BC}.\end{aligned} \tag{2.22}$$

[6] Extra terms are needed because the angular momentum aspect cannot explicitly be related to one of the conserved BMS charges; see Sec. 2.3.1 for a further explanation.

[7] The reason why the $D^A D^B N_{AB}$ term was not important in [9] is because they integrated their version of Eq. (2.19) over the sphere, which kills this term because its $\ell = 0, 1$ modes are zero.

However, the terms in this equation cannot as clearly be classified as "memory-like," "ordinary-like," and "null-like," analogous to those appearing in Eq. (2.19) or (2.20). Therefore, before we compute the memory, we must first rewrite Eq. (2.22) in terms of the function $\widehat{N}_A$, which can be thought of as an angular momentum that corresponds to the conserved super-Lorentz charges. We henceforth call $\widehat{N}_A$ the angular momentum aspect rather than N_A. According to Flanagan and Nichols's [33] Eq. (3.11), $\widehat{N}_A$ is

$$\begin{aligned}\widehat{N}_A \equiv N_A - uD_A m \\ - \frac{1}{16} D_A (C_{BC} C^{BC}) - \frac{1}{4} C_{AB} D_C C^{BC}.\end{aligned} \tag{2.23}$$

Using Eq. (2.22) in the retarded time derivative of Eq. (2.23) produces the result

$$\begin{aligned}\partial_u \widehat{N}_A &= \frac{1}{4}(D_B D_A D_C C^{BC} - D^2 D^B C_{AB}) \\ &\quad + \frac{1}{4} D_B (C_{AC} N^{BC}) + \frac{1}{2} C_{AC} D_B N^{BC} \\ &\quad - \frac{1}{8} D_A (C_{BC} N^{BC}) - \frac{1}{4} N_{AB} D_C C^{BC} \\ &\quad - \frac{1}{4} C_{AB} D_C N^{BC} - u D_A \dot{m} \\ &= \frac{1}{4}(D_B D_A D_C C^{BC} - D^2 D^B C_{AB}) \\ &\quad - \Big[(\frac{3}{8} N_{AB} D_C C^{BC} - \frac{3}{8} C_{AB} D_C N^{BC}) \\ &\quad - (\frac{1}{8} N^{BC} D_B C_{AC} - \frac{1}{8} C^{BC} D_B N_{AC}) \Big] \\ &\quad - u D_A \dot{m}.\end{aligned} \tag{2.24}$$

For the second equality, we have used

$$N^{BC} D_A C_{BC} = N^{BC} D_B C_{AC} + N_{AB} D_C C^{BC}, \tag{2.25}$$

$$C^{BC} D_A N_{BC} = C^{BC} D_B N_{AC} + C_{AB} D_C N^{BC}. \tag{2.26}$$

Finally, using the angular momentum aspect, we may write the evolution equation (2.22) as

$$\begin{aligned}\frac{1}{4}(D_B D_A D_C C^{BC} - D^2 D^B C_{AB}) \\ = \partial_u (\widehat{N}_A + 8\pi \mathcal{J}_A) + u D_A \dot{m},\end{aligned} \tag{2.27}$$

where

$$\dot{\mathcal{J}}_A \equiv \frac{1}{64\pi}\Big[(3N_{AB}D_C C^{BC} - 3C_{AB}D_C N^{BC}) - (N^{BC}D_B C_{AC} - C^{BC}D_B N_{AC})\Big] \tag{2.28}$$

is the retarded time derivative of the angular-momentum radiated per unit solid angle. Akin to Eq. (2.20), we have written Eq. (2.27) so that the first, second, and third terms on the right-hand side of the equation correspond to the memory that can be found in the shear as well as the ordinary and null memory contributions. As we will show next, Eq. (2.20) produces the displacement memory while its counterpart, Eq. (2.27), produces the recently discovered spin memory. While we do not present an explicit equation for the CM memory effect, Eq. (2.20) can be shown to contain terms that relate to the CM memory (see Sec. 2.3.2.3 for more explanation).

2.3.2 Computation of Memory

Consider a spacetime in which the flux of energy and angular momentum to future null infinity vanishes before some early retarded time u_1, so that the news tensor N_{AB} and the stress-energy tensor vanish there as well. Further, assume that sometime thereafter there is emission of gravitational waves, and that these fluxes again vanish for times after some $u_2 > u_1$. The displacement memory is the effect that a pair of freely falling, initially comoving observers will then be able to observe a nonzero change in their relative position. This change is determined by changes to the spacetime of order $1/r$ and is given by a function known as the *memory tensor*,

$$\Delta C_{AB} \equiv C_{AB}(u_2) - C_{AB}(u_1). \tag{2.29}$$

Here, we use the notation $\Delta f \equiv f(u_2) - f(u_1)$ where f is some function of Bondi time.

We now write the memory tensor as the sum of an electric and a magnetic component. Motivated by how one may write a vector field on the two-sphere as the sum of a gradient ("electric") and a curl ("magnetic")[8], we have

$$\Delta C_{AB} = (D_A D_B - \frac{1}{2}q_{AB}D^2)\Delta\Phi + \epsilon_{C(A}D_{B)}D^C\Delta\Psi, \tag{2.30}$$

where $\Delta\Phi \equiv \Phi(u_2) - \Phi(u_1)$ and $\Delta\Psi \equiv \Psi(u_2) - \Psi(u_1)$ are scalar functions that represent the electric and magnetic components of the displacement memory and ϵ_{AB} is just the Levi-Civita tensor on the two-sphere.

[8] i.e., $V_A = D_A\Phi + \epsilon_{AB}D^B\Psi$.

Because our Cauchy-characteristic extraction extracts the strain h, we now rewrite the BMS flux-balance laws, i.e., Eqs. (2.20) and (2.27), in terms of this observable. Using the complex dyad introduced previously in Sec. 2.2.2, we construct the strain as a spin-weight -2 quantity:

$$h \equiv \frac{1}{2}\bar{q}^A \bar{q}^B C_{AB} = \sum_{\ell \geq 2} \sum_{|m| \leq \ell} h_{\ell m} \, {}_{-2}Y_{\ell m}(\theta, \phi). \tag{2.31}$$

Here we are only considering the $1/r$ part of the strain. Generally the strain is computed using the full metric at asymptotic infinity—namely, $h \equiv \frac{1}{2}\bar{q}^A \bar{q}^B \gamma_{AB}$. However, the $1/r$ part of the strain is the only observable component at future null infinity and thus all we need to consider.

We now use Eqs. (2.20) and (2.27) to compute the memory ΔJ. But, to simplify this work we first write the memory in terms of its electric and magnetic components, i.e., $\Delta J = \Delta J^{(E)} + \Delta J^{(B)}$, where

$$\begin{aligned}
\Delta J^{(E)} &\equiv \frac{1}{2}\bar{q}^A \bar{q}^B \Delta C^{(E)}_{AB}(\Delta\Phi) \\
&= \frac{1}{2}\bar{q}^A \bar{q}^B \left[(D_A D_B - \frac{1}{2} q_{AB} D^2) \Delta\Phi \right] \\
&= +\frac{1}{2}\bar{\eth}^2 \Delta\Phi, \qquad (2.32a) \\
\Delta J^{(B)} &\equiv \frac{1}{2}\bar{q}^A \bar{q}^B \Delta C^{(B)}_{AB}(\Delta\Psi) \\
&= \frac{1}{2}\bar{q}^A \bar{q}^B \left[\epsilon_{C(A} D_{B)} D^C \Delta\Psi \right] \\
&= -\frac{1}{2} i \bar{\eth}^2 \Delta\Psi. \qquad (2.32b)
\end{aligned}$$

We reserve the letter J to represent observables that we calculate using functions extracted from our simulations, such as the strain h, the news $\dot{h}$, or the Weyl scalars.

2.3.2.1 Electric Memory

The electric component of the memory is the piece that arises from the scalar function $\Delta\Phi$. Using Eq. (2.30), the memory term in Eq. (2.20) becomes

$$\begin{aligned}
\frac{1}{4} D^A D^B \Delta C_{AB} &= \frac{1}{8}(D^4 - 2D^A \left[D_A, D_B\right] D^B) \Delta\Phi \\
&= \frac{1}{8}(D^4 + 2D^A q_{AB} D^B) \Delta\Phi \\
&= \frac{1}{8} D^2 (D^2 + 2) \Delta\Phi \\
&= \mathfrak{D} \Delta\Phi, \qquad (2.33)
\end{aligned}$$

where

$$\mathfrak{D} \equiv \frac{1}{8} D^2 (D^2 + 2). \tag{2.34}$$

In computing Eq. (2.33) we have used the fact that $[D_A, D_B] D^B = -q_{AB} D^B$ on the two-sphere and used symmetry/antisymmetry to remove the dependence on the magnetic term $\Delta\Psi$. We act on Eq. (2.33) with $\mathfrak{D}^{-1}$ to obtain an expression for $\Delta\Phi$. But, because $\mathfrak{D}$ maps the $\ell = 0, 1$ modes to zero, $\mathfrak{D}^{-1}$'s action on these modes is ambiguous. Therefore, to avoid this complication we construct $\mathfrak{D}^{-1}$ so that it maps the $\ell = 0, 1$ modes to zero. Note that this choice has no effect on the strain since it is a spin-weight -2 function, and will thus be independent of these modes. By acting on Eq. (2.33) with $\mathfrak{D}^{-1}$ and combining the result with the expression from Eq. (2.20), we then obtain

$$\Delta\Phi = \mathfrak{D}^{-1} \left[\Delta m + 4\pi \left(\frac{1}{32\pi} \int_{u_1}^{u_2} N_{AB} N^{AB} \, du \right) \right]. \tag{2.35}$$

Using

$$C_{AB} = \frac{1}{2} \left(q_A q_B h + \bar{q}_A \bar{q}_B \bar{h} \right), \tag{2.36}$$

which follows from the symmetric, trace-free condition of the shear tensor, we find that we may write Eq. (2.35) as

$$\Delta\Phi = \mathfrak{D}^{-1} \left[\Delta m + 4\pi \left(\frac{1}{16\pi} \int_{u_1}^{u_2} \dot{h} \dot{\bar{h}} \, du \right) \right]. \tag{2.37}$$

Thus, the electric component of the memory can readily be found by combining the results of Eqs. (2.32a) and (2.35),

$$\Delta J^{(E)} = \frac{1}{2} \bar{\eth}^2 \mathfrak{D}^{-1} \left[\Delta m + \frac{1}{4} \int_{u_1}^{u_2} \dot{h} \dot{\bar{h}} \, du \right], \tag{2.38}$$

with the Δm term as the ordinary contribution and the $\dot{h}\dot{\bar{h}}$ term as the null contribution. Equation (2.38) could also be written with $\eth^{-2}$ since this operator is equivalent to $\frac{1}{8}\bar{\eth}^2 \mathfrak{D}^{-1}$ when acting on spin-weight 0 functions. But, we choose to use $\mathfrak{D}$ for numerical purposes. At this point, it remains to compute the Bondi mass aspect in terms of the strain and the Weyl scalar Ψ_2. As is shown in Appendix 2.A, by Eq. (2.65), the result one obtains is

$$m = -\mathrm{Re} \left[\Psi_2 + \frac{1}{4} \dot{h} \bar{h} \right], \tag{2.39}$$

where Re denotes the real part.

2.3.2.2 Magnetic Memory

To compute the magnetic memory, we use Eq. (2.27) and proceed in a similar manner to the above calculation of the electric memory. By replacing C_{AB} with ΔC_{AB}, Eq. (2.27) can be written as

$$\begin{aligned}&\frac{1}{4}(D_B D_A D_C \Delta C^{BC} - D^2 D^B \Delta C_{AB}) \\ &\quad = \Delta\Big[\partial_u(\widehat{N}_A + 8\pi\mathcal{J}_A) + u D_A \dot{m}\Big].\end{aligned} \tag{2.40}$$

Using Eq. (2.30) in Eq. (2.40) and making use of the identity $D_A[D^4, D^A]\Delta\Psi = D^2(2D^2{+}1)\Delta\Psi$, which follows from $D_A[D^4, D^B]f(\theta,\phi) = D_A D^B(2D^2{+}1)f(\theta,\phi)$, we obtain

$$\frac{1}{4}(D_B D_A D_C \Delta C^{BC} - D^2 D^B \Delta C_{AB}) = \epsilon_{AC} D^C \mathfrak{D}\Delta\Psi, \tag{2.41}$$

Note that the electric component $\Delta\Phi$ vanishes because of various commutation relations similar to the one above. Therefore, we have the relation

$$\epsilon_{AC} D^C \mathfrak{D}\Delta\Psi = \Delta\left[\partial_u(\widehat{N}_A + 8\pi\dot{\mathcal{J}}_A) + u D_A \dot{m}\right]. \tag{2.42}$$

If we now contract Eq. (2.42) with the function $\epsilon^{AB} D_B$, since $\epsilon^{AB} = \frac{1}{2} i(q^A \bar{q}^B - \bar{q}^A q^B)$, we obtain

$$\begin{aligned}\mathfrak{D} D^2 \Delta\Psi &= \Delta\epsilon^{AB} D_B\left[\partial_u(\widehat{N}_A + 8\pi\dot{\mathcal{J}}_A) + u D_A \dot{m}\right] \\ &= \Delta\mathrm{Im}\left[\eth\partial_u(\widehat{\overline{N}} + 8\pi\overline{\mathcal{J}})\right],\end{aligned} \tag{2.43}$$

where Im denotes the imaginary part and

$$\widehat{N} \equiv q_A \widehat{N}^A \quad \text{and} \quad \mathcal{J} \equiv q_A \mathcal{J}^A. \tag{2.44}$$

Note that the Bondi mass aspect term drops out because of the commutativity of the covariant derivatives when acting on a scalar function and the antisymmetry of the Levi-Civita tensor. Consequently, by acting on Eq. (2.43) with $\mathfrak{D}^{-1}D^{-2}$ and using Eq. (2.28) we have

$$\Delta\Psi = \mathfrak{D}^{-1}D^{-2}\Delta\mathrm{Im}\left[\eth\partial_u(\widehat{\overline{N}} + 8\pi\overline{\mathcal{J}})\right] \tag{2.45a}$$

$$\begin{aligned}&= \mathfrak{D}^{-1}D^{-2}\Delta\mathrm{Im}\Big\{\eth(\partial_u\widehat{\overline{N}}) + \frac{1}{8}\eth\bar{q}^A \\ &\qquad\Big[(3N_{AB}D_C C^{BC} - 3C_{AB}D_C N^{BC}) \\ &\qquad\quad - (N^{BC}D_B C_{AC} - C^{BC}D_B N_{AC})\Big]\Big\}.\end{aligned} \tag{2.45b}$$

Expressing the angular momentum flux quantities on the right-hand side in terms of the observable h gives

$$N_{AB}D_C C^{BC} = \mathrm{Re}\big[q_A \dot{h}\bar{\eth}\bar{h}\big], \tag{2.46a}$$
$$C_{AB}D_C N^{BC} = \mathrm{Re}\big[q_A h\bar{\eth}\dot{\bar{h}}\big], \tag{2.46b}$$
$$N^{BC}D_B C_{AC} = \mathrm{Re}\big[q_A \dot{\bar{h}}\bar{\eth}h\big], \tag{2.46c}$$
$$C^{BC}D_B N_{AC} = \mathrm{Re}\big[q_A \bar{h}\bar{\eth}\dot{h}\big], \tag{2.46d}$$

Thus, by combining everything together and using the result of Eq. (2.32b), we find

$$\Delta J^{(B)} = \frac{1}{2}i\bar{\eth}^2\mathfrak{D}^{-1}D^{-2}\Delta\mathrm{Im}\Big\{\bar{\eth}(\partial_u\widehat{N}) + \frac{1}{8}\Big[\eth(3h\bar{\eth}\dot{\bar{h}} - 3\dot{h}\bar{\eth}\bar{h} + \dot{\bar{h}}\bar{\eth}h - \bar{h}\bar{\eth}\dot{h})\Big]\Big\}. \tag{2.47}$$

Next, we need the angular momentum aspect in terms of the strain and the Weyl scalar Ψ_1. As is shown in Appendix 2.B, by Eq. (2.79b), the result one obtains is

$$\mathrm{Im}\Big[\bar{\eth}(\partial_u\widehat{N})\Big] = \mathrm{Im}\left\{2\bar{\eth}\dot{\Psi}_1 - \frac{1}{4}\bar{\eth}\left[\partial_u(\bar{h}\eth h)\right]\right\}. \tag{2.48}$$

As is illustrated by either Eq. (2.45a) or (2.47), the magnetic component of the memory is the total derivative with respect to retarded time of some scalar function, whereas the electric component of the memory contains terms that are either net changes, i.e., the Δm term, or retarded time integrals, i.e., the $\dot{h}\dot{\bar{h}}$ term. Consequently, since the magnetic memory does not have such terms, one might presume that the magnetic memory vanishes, i.e., that the net change in the magnetic component of the strain is zero. Currently, this is unknown [18, 33–35]. But, it *is* known that the retarded time integral of the magnetic memory does not vanish; this is what we refer to as the spin memory effect. We explore the conjectured vanishing feature of the magnetic memory in Sec. 2.4.4 and the spin memory in Sec. 2.4.5.

Equipped with both Eqs. (2.38) (the electric memory) and (2.47) (the magnetic memory), we may now compute the electric and magnetic memory contributions to the strain by expressing each of these functions as a sum over spin-weighted spherical harmonics and acting with the inverse operators accordingly,

$$D^{-2}Y_{\ell m} = [-\ell(\ell+1))]^{-1}Y_{\ell m}, \tag{2.49a}$$
$$\mathfrak{D}^{-1}Y_{\ell m} = \left[\frac{1}{8}(\ell-1)\ell(\ell+1)(\ell+2)\right]^{-1}Y_{\ell m}. \tag{2.49b}$$

We thus obtain the spin-weighted spherical harmonic representation of the memory

$$\Delta J(\theta,\phi) = \sum_{\ell\geq 2}\sum_{|m|\leq\ell} \Delta J_{\ell m}\, {}_{-2}Y_{\ell m}(\theta,\phi), \tag{2.50}$$

which we can use to compare the memory modes to those of the CCE extracted strain produced in our various numerical relativity simulations.

2.3.2.3 CM Memory

Finally, we now illustrate how one can realize that Eq. (2.38) contains terms contributing to the CM memory. According to Eq. (2.42), we have

$$\partial_u \Delta\widehat{N}_A = \frac{1}{8}\epsilon_{AC} D^C \mathfrak{D}\Delta\Psi - 8\pi\Delta\dot{\mathcal{J}}_A - uD_A\Delta\dot{m}. \tag{2.51}$$

If we then contract this equation with D^A and take the real part of the entire equation, we obtain

$$\begin{aligned}\partial_u \mathrm{Re}(\bar{\eth}\widehat{N}) &= -8\pi\mathrm{Re}(\bar{\eth}\dot{\mathcal{J}}) - uD^2\dot{m} \\ &= -8\pi\mathrm{Re}(\bar{\eth}\dot{\mathcal{J}}) - \partial_u(uD^2 m) + D^2 m,\end{aligned} \tag{2.52}$$

since the Bondi mass aspect term is a purely real quantity. By rearranging this equation and then entering the results back into the ordinary part of Eq. (2.38), we obtain

$$\begin{aligned}\Delta J^{(E)}_{\text{ordinary}} = \frac{1}{2}\bar{\eth}^2\mathfrak{D}^{-1}\Delta\Big\{&(m+u\dot{m}) + \\ &\partial_u D^{-2}\mathrm{Re}\left[\bar{\eth}(\widehat{N}+8\pi\mathcal{J})\right]\Big\}.\end{aligned} \tag{2.53}$$

When written in this manner, it is now clear how the ordinary part of the electric memory can be realized as containing terms involving the retarded time derivative of the real part of the super-Lorentz charges, which are a part of the $\widehat{N}$ term, and the angular momentum flux. Even though this is somewhat trivial since we have simply changed the Bondi mass aspect by a function that is zero, Eq. (2.53) nonetheless illustrates how the ordinary part of the electric memory can be broken up into not only a displacement contribution (the first two terms), but also the time derivative of a CM contribution (the terms with the ∂_u in front of them). To obtain the full expression for the CM memory, the remaining component that is needed is the null contribution, which can, in principle, be extracted from the energy flux. Joining this component with the ordinary CM memory contribution in Eq. (2.53) gives the full expression for the CM memory in terms of its ordinary and null parts. We explore the CM memory further with numerical results in Appendix 2.C.

2.4 Results

We now compute the electric and magnetic components of the memory for various binary black hole simulations run using the code SpEC. Each of these merger simulations corresponds to an entry in the public SXS Catalog [28] and collectively encompasses both equal and unequal masses, spinning and nonspinning black holes, and configurations that are either precessing or nonprecessing. We provide the main parameters of these simulations in Table 2.1.

Table 2.1: Primary parameters of the various BBH mergers analyzed in this paper. We use the mass and effective spin values that are obtained at the simulation's relaxation time [28]. While these are the runs that we show in this paper, many others have been used to understand and refine our conclusions. The spin vectors of 1389 are $\chi_1 = (-0.2917, +0.2005, -0.3040)$ and $\chi_2 = (-0.01394, +0.4187, +0.1556)$.

SXS:BBH:	Classification	M_1/M_2	$\chi_{\rm eff}$	$N_{\rm orbits}$
1155	Nonspinning	1.000	$+2.617 \times 10^{-5}$	40.64
0554	Nonspinning	2.000	$+4.879 \times 10^{-5}$	19.25
1412	Spinning	1.630	$+1.338 \times 10^{-1}$	145.1
1389	Precessing	1.633	-1.293×10^{-1}	140.4
0305	GW150914	1.221	-1.665×10^{-2}	15.17

Each simulation produces a GW strain computed by Regge-Wheeler-Zerilli (RWZ) extraction at a series of spheres of finite radius and then extrapolates the strain to future null infinity [28]. This is the strain that can be found in the SXS Catalog. Like Pollney and Reisswig [25], we find, however, that this method for constructing the strain does not seem to be able to resolve the memory. Consequently, we instead compute the strain using CCE.

Fortunately, each of our BBH simulations also produces the metric and its derivatives on a series of world tubes, where each world tube is a coordinate two-sphere dragged through time that provides the inner boundary conditions for the CCE module from the code SpECTRE [29, 30]. We use this CCE module to explicitly compute the strain h at future null infinity. Note that we use the variable h to represent the strain thus obtained from CCE, while the variable J has been reserved for the strain computed from the BMS flux-balance laws. These should be identical in the absence of numerical error. Furthermore, unlike earlier implementations of CCE that exhibited the resolution of the strain $(2, 0)$ mode [25], the SpECTRE CCE module computes the strain directly, like [36]. Consequently, there is no need to compute the news

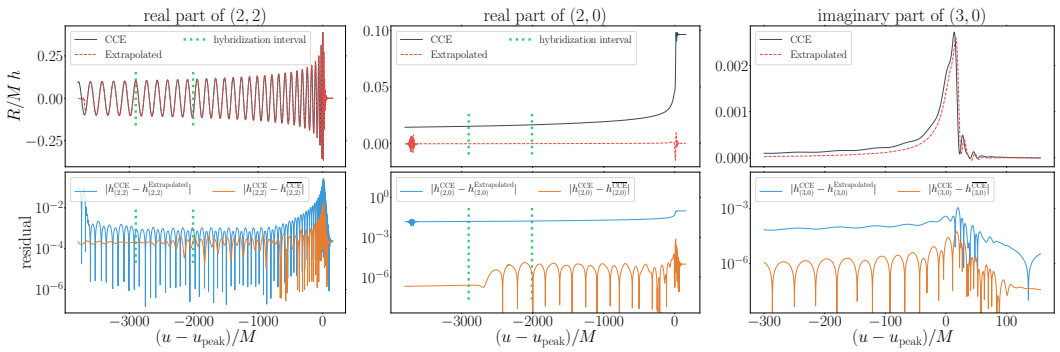

Figure 2.1: Comparison of the strain computed by CCE versus RWZ extraction followed by extrapolation to future null infinity, for several spin-weight -2 spherical harmonic modes of the SXS simulation SXS:BBH:0305. On each plot, we show the interval over which the hybridization between CCE and PN is performed, i.e., before this interval the waveform is purely from a post-Netwonian calculation while after this interval the waveform is purely from numerical computations. In the bottom row of each plot we provide the residuals and an estimate of the error in the CCE waveform, $|h^{\rm CCE}_{(\ell,m)} - h^{\overline{\rm CCE}}_{(\ell,m)}|$, where $h^{\rm CCE}_{(\ell,m)}$ is the highest resolution waveform of SXS:BBH:0305 and $h^{\overline{\rm CCE}}_{(\ell,m)}$ is the next highest resolution waveform for the same binary system. We align the waveforms in both time and phase around $u_{\rm peak}$, which is where the L^2 norm of the strain achieves its maximum. See Table 2.1 for the parameters of SXS:BBH:0305.

first and then integrate it with respect to retarded time, which could introduce errors from the choice of integration constants.

Within the SXS Catalog, most of the BBH simulations follow only a few tens of binary orbits. PN computations of memory, however, include effects that are obtained by integrating over the waveform starting at $u \to -\infty$. Accordingly, we hybridize the numerical strain obtained from CCE with a PN waveform corresponding to the same BBH merger (see Sec. 2.4.8) using the python packages `GWFrames` and `Post-Newtonian` [37, 38]. When using `Post-Newtonian`, we also modified the code to include memory terms up to 3PN order. With this scheme, we find that we can resolve the traditional and most prominent $m = 0$ memory modes, as well as other $m \neq 0$ modes that exhibit both the displacement and spin memory effects.

Last, it should be noted that we primarily use the python package `scri` to perform our analysis [39–42].

2.4.1 CCE vs Extrapolation

We first compare the strain that we compute using two distinct extraction methods: (1) RWZ extraction followed by extrapolation to future null infinity and (2) CCE plus a PN hybridization. In Fig. 2.4.1. we compare three different spin-weight -2 spherical harmonic modes of the strain for the numerical simulation SXS:BBH:0305, which is a simulation of GW150914 (see Table 2.1). We compare the $(2,2)$, $(2,0)$, and $(3,0)$ modes from CCE/PN hybrids to those from extrapolated RWZ waveforms. Each one of these modes corresponds to the most prominent mode for the strain as well as the electric and magnetic memory (see Secs. 2.4.3 and 2.4.4). We also show an estimate of the error in the CCE waveform $|h^{\mathrm{CCE}}_{(\ell,m)} - h^{\overline{\mathrm{CCE}}}_{(\ell,m)}|$, where $h^{\mathrm{CCE}}_{(\ell,m)}$ is the highest resolution waveform available for SXS:BBH:0305 and $h^{\overline{\mathrm{CCE}}}_{(\ell,m)}$ is the next highest resolution. While there is also some numerical error that comes from the Cauchy-characteristic extraction, we find that these errors are of order 10^{-10} and thus negligible in comparison to the Cauchy evolution's resolution error. Consequently, for all the plots in this paper, we only present the error that comes from the Cauchy evolution.

As can be seen in the plots in Fig 2.4.1, the CCE and extrapolated waveforms coincide well for the $(2,2)$ mode. However, the extrapolation method fails to capture the memory contribution to the $(2,0)$ electric memory mode, but does recover the quasinormal mode ringdown near the peak of the waveform. Curiously, the extrapolated waveform *does* contain nontrivial contributions to the imaginary part of the $(3,0)$ magnetic memory mode, but does not determine the time integral of the mode, which is the main contribution to the spin memory, accurately ($\sim$50% of the values seen in CCE for the runs we studied). Thus, the importance of using CCE can readily be seen: while previous extrapolation-based extraction schemes cannot accurately resolve memory effects, the current implementation of SpECTRE's CCE can.

2.4.2 Checking the Flux-balance Laws

As shown in Sec. 2.3.2, using Eqs. (2.38) and (2.47), one can compute the memory $\Delta J(\theta,\phi)$, which is the change in the strain between the retarded times corresponding to the nonradiative[9] regimes that exist before and after the passage of radiation. However, the flux-balance laws—Eqs. (2.20) and (2.27)—from which the memory effects are computed should be true for any given retarded time. This version of

[9] A BBH coalescence is never truly nonradiative at future infinity; here we assume that future infinity is approximately nonradiative at both early and late retarded times.

these BMS flux-balance laws is called the finite time version, rather than the global version. Thus, to see if our Cauchy-characteristic extraction is performing as we expect it to for the strain as well as the Weyl scalars Ψ_1 and Ψ_2, we can compare the strain h as obtained from CCE to the "flux-balance strain,"

$$\begin{aligned} J &\equiv \sum_{\ell\geq 2}\sum_{|m|\leq\ell} J_{\ell m}\, {}_{-2}Y_{\ell m}(\theta,\phi) \\ &= \sum_{\ell\geq 2}\sum_{|m|\leq\ell} (J^{(E)}_{\ell m} + J^{(B)}_{\ell m})\, {}_{-2}Y_{\ell m}(\theta,\phi), \end{aligned} \tag{2.54}$$

where $J^{(E)}_{\ell m}$ and $J^{(B)}_{\ell m}$ take on the same functional form as the spin-weighted spherical harmonic decompositions of $\Delta J^{(E)}$ and $\Delta J^{(B)}$ coming from Eqs. (2.38) and (2.47), but are now also functions of the retarded time u, i.e., the operator Δ from Eqs. (2.38) and (2.47) is removed. Put differently, we wish to check the consistency of

$$h = J^{(E)} + J^{(B)} \tag{2.55}$$

up to the error of the corresponding Cauchy evolution.

In Fig. 2.4.2, we compare the strain obtained from CCE to the strain computed from the BMS charges and fluxes. As in the comparison shown in Fig 2.4.1, we show results for the $(2,2)$, $(2,0)$ and $(3,0)$ modes for the same NR simulation as before: SXS:BBH:0305. As can be seen, the two coincide with each other rather well, with the $(2,2)$ mode being the best, followed by the $(2,0)$ mode, and then the $(3,0)$ mode. Most important, though, one can observe through the $(2,0)$ and $(3,0)$ modes that the memory primarily comes from the null contribution, while the ordinary contribution appears to only capture the quasinormal mode behavior. Nevertheless, this is perhaps as expected because the majority of the simulations in the SXS Catalog experience little to no supertranslations or super-Lorentz transformations [43]. Consequently, there will be little to no BMS charges for the radiation to carry to future null infinity, which will make the contribution from the ordinary memory small compared to that of the null memory, i.e.,

$$\Delta J^{(E)} \approx +\frac{1}{8}\bar{\eth}^2\mathfrak{D}^{-1}\left[\int_{u_1}^{u_2} \dot{h}\dot{\bar{h}}\, du\right], \tag{2.56a}$$

$$\begin{aligned} \Delta J^{(B)} \approx &+\frac{1}{16} i\bar{\eth}^2\mathfrak{D}^{-1}D^{-2}\Delta\mathrm{Im} \\ &\left[\eth(3h\bar{\eth}\dot{\bar{h}} - 3\dot{h}\bar{\eth}\bar{h} + \dot{\bar{h}}\bar{\eth}h - \bar{h}\bar{\eth}\dot{h})\right]. \end{aligned} \tag{2.56b}$$

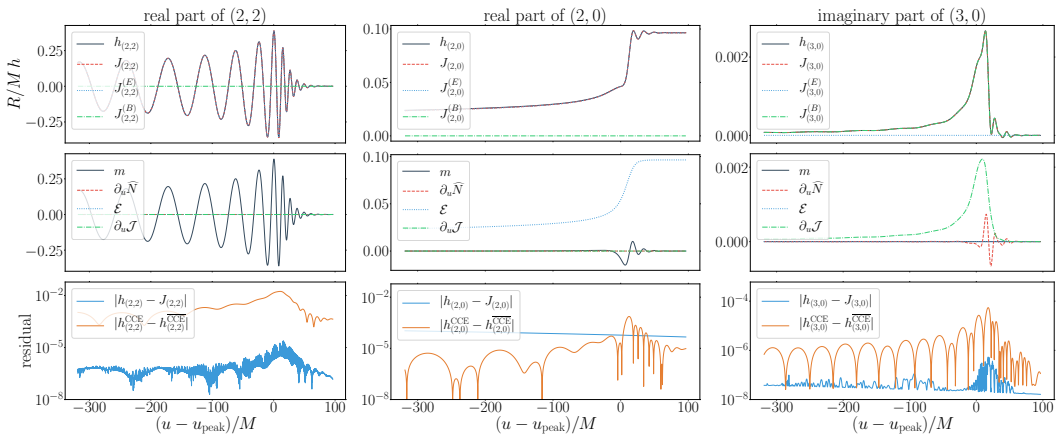

Figure 2.2: Comparison of the strain extracted using CCE from SXS simulation SXS:BBH:0305 versus the strain computed using the BMS flux-balance laws, Eqs. (2.38) and (2.47), without the Δ operator. Each column shows a particular spin-weight -2 mode. The top row shows the extracted strain (black/solid), the strain computed from the BMS flux-balance laws (red/dashed), and its corresponding electric (blue/dotted) and magnetic (green/dashed/dotted) components coming from Eqs. (2.38) and (2.47). The middle row shows the contributions from the mass aspect (black/solid), the angular momentum aspect (red/dashed), the energy flux (blue/dotted), and the angular momentum flux (green/dashed/dotted). Because the energy flux contribution to the electric component of the strain is an integral over retarded time, we are free to change the electric component by a constant. We take this angle-dependent constant to be the final value of the extracted strain.

In this work, our primary objective is to provide a statement on the measurability of the memory rather than any other phenomenon, such as quasinormal modes. Thus, we need to consider the function that represents the instantaneous memory effect as a function of time. As can be seen in Fig. 2.4.2 and as was just discussed, the observable that serves as a reasonable proxy for this is the null contribution to the flux-balance strain. Therefore, in the following sections, we will only examine the null contribution to the flux-balance strain and henceforth refer to this contribution as the system's overall memory. We represent the memory as a function of time as

$$\Delta J(u) \equiv \sum_{\ell \geq 2} \sum_{|m| \leq \ell} \Delta J_{\ell m}(u)\, {}_{-2}Y_{\ell m}(\theta, \phi). \tag{2.57}$$

From an observational standpoint, a GW observatory will only be able to measure the complete memory mode, i.e., a superposition of memory and quasinormal modes. Thus, to measure the memory effect, one needs to be able to filter the quasinormal mode frequencies so that only the frequencies corresponding to the memory remain.

As we thoroughly explore in Sec. 2.4.7, performing such a postprocessing analysis of LIGO observations should indeed be feasible, thereby allowing for the measurement of the memory induced by a GW within an interferometer. As a result, since the null memory contribution contains no quasinormal mode contribution, this is a fair proxy for what LIGO would see once the quasinormal modes have been filtered out of the strain memory modes.

Note that we are free to change the null contributions to the electric and spin memories by constants, since they depend on certain energy and angular momentum fluxes that are computed by performing retarded time integrals. The need for these angle-dependent constants is a result of not knowing the past history of the numerical waveforms. Unless stated otherwise, we choose these constants so that the flux-balance strain has the same initial value as the CCE/PN hybrid strain.

2.4.3 Electric Memory Modes

We now analyze the main memory modes obtained from numerical relativity by comparing them to PN theory and $\Delta J(u)$ via the functional forms of Eqs. (2.56a) and (2.56b), i.e., Eqs. (2.38) and (2.47) but without the contribution coming from the negligible ordinary memory.[10] According to Favata [19, 26, 27], the bulk of the electric memory should be in the real component of the nonoscillatory $(2, 0)$ mode, with other contributions primarily persisting in the other ℓ = even, $m = 0$ modes. But, as was also noted by Favata, there may be memory contributions from $m \neq 0$ oscillatory modes, e.g., the $(3, \pm 1)$ modes. Consequently, we examine results for not only the usual $m = 0$ memory modes, but also a few of the potential $m \neq 0$ oscillatory memory modes. We begin by first illustrating the agreement between our $(2, 0)$ mode and what is expected according to PN theory.

For this PN comparison, we consider SXS:BBH:0305. As in Fig. 2.4.1, in Fig. 2.4.3, we show the agreement between CCE and PN in the top plot and provide a rough estimate of the numerical error in the bottom plot. As expected, the numerical waveform and the PN waveform coincide well during the inspiral, but then diverge from one another as the binary system approaches the merger phase.

Next, to illustrate the variation of the memory across various BBH parameters, we examine an equal mass and nonspinning system: SXS:BBH:1155. We again find that the main memory modes are the $m = 0$ modes, with both of the $(2, 0)$

[10] While the ordinary contribution to the strain is not negligible, seeing as it contains information about the quasinormal modes, the memory part of this contribution can indeed be considered to be negligible, as we argued through the results shown in Fig. 2.4.2.

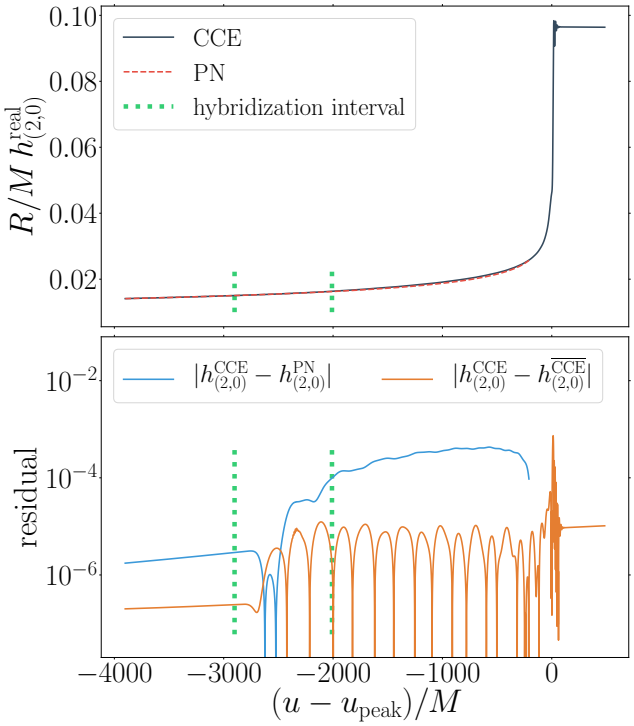

Figure 2.3: Comparison between the $(2,0)$ mode obtained from numerical relativity to that which is computed using PN theory. For reference, in the bottom plot we provide an estimate of the error in the CCE waveform, $|h^{\rm CCE}_{(2,0)} - h^{\overline{\rm CCE}}_{(2,0)}|$, where $h^{\rm CCE}_{(2,0)}$ refers to the highest resolution waveform of SXS:BBH:0305 and $h^{\overline{\rm CCE}}_{(2,0)}$ refers to the next highest resolution. The reason why the hybrid and the PN waveform are not identical before the hybridization interval is because there is numerical error that is introduced when aligning the two waveforms.

and $(4,0)$ modes taking on values that are larger than the corresponding numerical error. However, the other $m = 0$ modes acquire values that are smaller than can be resolved at this run's numerical resolution. Moreover, we find that both of the $(2,0)$ and $(4,0)$ modes coincide rather well with the instantaneous memory from Eqs. (2.56a) and (2.56b), as illustrated in Fig. 2.4.3.

For the other types of binary black hole systems that we examined, the results are very similar to what we have presented thus far except for the following observations. For a nonequal mass, nonspinning system we find that the total accumulated memory is not as large as that occurring in an equal mass system of the same total mass. Furthermore, for a spinning system, we find that the total accumulated memory is constant as a function of spin for antialigned spins, but increases with the total spin for aligned spin systems, which agrees with Ref. [25]. Also, for a precessing

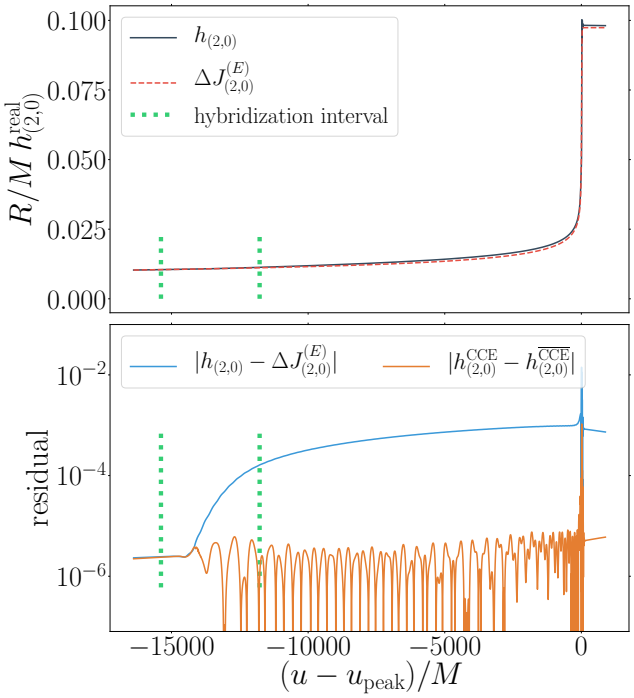

Figure 2.4: Comparison of the $(2, 0)$ mode with the memory for an equal mass, nonspinning system (SXS:BBH:1155, see Table 2.1).

system, we observe mode mixing which causes the electric memory to leak into certain unexpected modes, such as the $(2, 1)$ and $(3, 0)$ modes. Last, we find that for nonequal mass systems there appears to be memory accumulated in the $(3, \pm 1)$ modes, which serves as an example of memory being accumulated in one of the oscillatory modes. We illustrate this effect using SXS:BBH:0554 in Fig. 2.4.3. Although this memory is indeed resolvable relative to numerical error, the value acquired is roughly a third of the total memory that is found in the $(4, 0)$ mode and is thus inconsequential when compared to the $(2, 0)$ mode's memory, which is nearly two orders of magnitude more than the $(4, 0)$ mode's.

Finally, we present Table 2.2 which contains the memory computed using Eqs. (2.56a) and (2.56b) and the memory accumulated in the strain modes, with rough estimates of the corresponding numerical error obtained by comparing the two highest resolution waveforms.

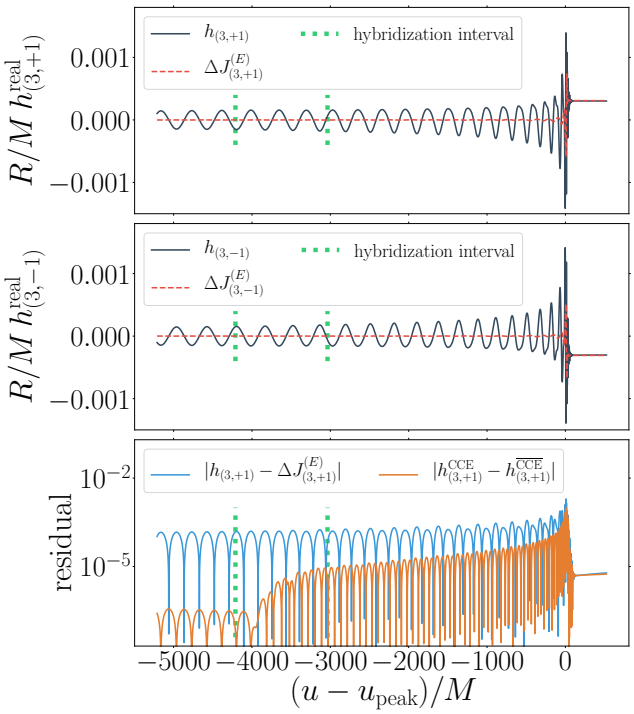

Figure 2.5: Comparison of the $(3, \pm 1)$ modes with the memory for an nonequal mass, nonspinning system (SXS:BBH:0554, see Table 2.1).

Table 2.2: Memory values that are obtained by combining Eqs. (2.56a) and (2.56b) and those obtained from the overall net change in the extracted strain memory modes. Again, the error that we provide in the final column is simply the residual between the two highest resolution waveforms.

SXS:BBH:	$h_{(2,0)}(u_{\rm final})$	$\Delta J_{(2,0)}(u_{\rm final})$	Error
0305	9.00×10^{-2}	8.97×10^{-2}	1.02×10^{-5}
1155	9.14×10^{-2}	9.06×10^{-2}	5.60×10^{-6}
0554	7.16×10^{-2}	7.11×10^{-2}	6.91×10^{-6}
1412	9.34×10^{-2}	9.13×10^{-2}	2.48×10^{-4}
1389	6.83×10^{-2}	6.67×10^{-2}	5.42×10^{-3}

SXS:BBH:	$h_{(4,0)}(u_{\rm final})$	$\Delta J_{(4,0)}(u_{\rm final})$	Error
0305	1.61×10^{-3}	1.46×10^{-3}	4.71×10^{-5}
1155	1.63×10^{-3}	1.54×10^{-3}	2.44×10^{-6}
0554	8.35×10^{-4}	7.18×10^{-4}	1.48×10^{-5}
1412	1.30×10^{-3}	1.31×10^{-3}	9.51×10^{-6}
1389	7.71×10^{-4}	7.10×10^{-4}	2.69×10^{-4}

2.4.4 Magnetic Memory Modes

There has been much speculation regarding whether the magnetic part of the displacement memory vanishes, i.e., if $\Delta J^{(B)} = 0$ [18, 33–35].[11] As proved by Bieri and Garfinkle [18], at linear order, the magnetic part vanishes provided that the news vanishes: $\dot{h} \to 0$ for $u \to +\infty$. We similarly find that our nonlinear expression as the magnetic memory in terms of the strain's $1/r$ part, i.e., Eq. (2.47), also is zero for cases with vanishing news. Unfortunately, confirming that the magnetic component of the memory vanishes in complete generality is not as analytically simple; so, we instead turn to the results of our numerical computations of the magnetic memory.

Unlike the electric memory, which as illustrated earlier is primarily amassed during just the merger phase of a BBH system's coalescence, the magnetic memory as a function of time also acquires meaningful contributions throughout the system's inspiral phase. These contrasting accumulation rates are because of the electric memory's relation to the binary system's energy flux, while the magnetic memory, by contrast, is instead related to the angular momentum flux. As a result, we find that to study accurate magnetic memory effects and observe reasonable agreement between the strain spin memory modes and the spin memory computed from the flux-balance laws, i.e., by calculating $\int \Delta J^{(B)}(u)\, du$, we need to examine numerical simulations with roughly 100 orbits or more. Unfortunately, such simulations are fairly sparse in the SXS Catalog. But as outlined in Table. 2.1, there are a few of these $\sim$100 orbit mergers that we examine now.

By computing the magnetic memory using Eq. (2.56b), we find that the maximum value of magnetic memory as a function of the angle in the sky for SXS:BBH:1412 is

$$R/M \ \max\left(|\Delta J^{(B)}|(\theta,\phi)\right) = 2.31 \times 10^{-7} \pm 2.60 \times 10^{-2}.$$

It is often speculated that a superkick system[12] may be the best candidate for producing magnetic memory [35]. For the superkick waveform SXS:BBH:0963,[13] we

[11] While the magnetic memory $\Delta J^{(B)}$ may indeed vanish, this does not mean that $J^{(B)}(u)$—the magnetic component of the strain— or even $\Delta J^{(B)}(u)$—the magnetic memory as a function of time—must be zero, but rather that their overall net change is zero.

[12] A system with initially antiparallel spins in the orbital plane.

[13] The relevant parameters of this system are

$$\begin{aligned} M_1/M_2 &= 1.0, \quad N_{\rm orbits} = 19, \\ \chi_1^{\rm initial} &= (+0.18, -0.78, -1.2\times10^{-3}), \\ \chi_2^{\rm initial} &= (-0.16, +0.78, +1.2\times10^{-3}). \end{aligned} \tag{2.58}$$

find

$$R/M \ \max\left(|\Delta J^{(B)}|(\theta,\phi)\right) = 9.37\times10^{-5} \pm 1.75\times10^{-2}.$$

Therefore, the magnetic memory is consistent with zero [18, 33–35].

Because the magnetic memory effect for each system we have looked at is much smaller than the corresponding numerical error, we believe that we are most likely overestimating the magnetic memory's numerical uncertainty. While the magnetic component of the memory appears to be zero, we expect the spin memory, i.e., the retarded time integral of the magnetic memory, to take on some nonzero final value in a manner similar to that of the electric memory. Because of this, we only provide one example of a magnetic memory mode and reserve a more exhaustive presentation for the nonzero spin memory, which we examine in Sec. 2.4.5.

From earlier comparisons with PN approximations [20], we expect the primary magnetic memory contributions to be from the imaginary part of the ℓ = odd, $m = 0$ modes, with the most pronounced mode being the $(3,0)$ mode. In Fig. 2.6 we compare the most prominent strain magnetic memory mode to the computed magnetic memory. Notice, not unlike the electric memory, the magnetic memory tends to act as the average of the more oscillatory strain. While the $(3,0)$ mode may seem to be poorly resolved near the system's merger phase, this is merely a consequence of examining SXS's ∼100 orbit runs, whose available numerical resolutions tend to be poorer than the other runs in the SXS Catalog. One can easily observe this by examining the $(3,0)$ mode shown in Fig. 2.4.1, which shows this mode for SXS:BBH:0305: a run with a much more accurate and precise Cauchy evolution.

2.4.5 Spin Memory Modes

We now evaluate the spin memory $\int \Delta J^{(B)}(u)\,du$, which we compute by taking the time integral of Eq. (2.56b). Because the spin memory, as with the magnetic memory, corresponds to the angular momentum flux, we expect the spin memory to closely resemble the electric memory, but with a considerably larger build-up during inspiral. As we show in Fig. 2.7, this is the case as nearly the same amount of spin memory is accumulated throughout the system's inspiral phase as there is in the merger phase. Further, like the electric memory and its $(4,0)$ mode, we find that we can also resolve the next most prominent spin memory mode—namely, the $(5,0)$ mode—to within numerical error, but not the other $m = 0$ modes.

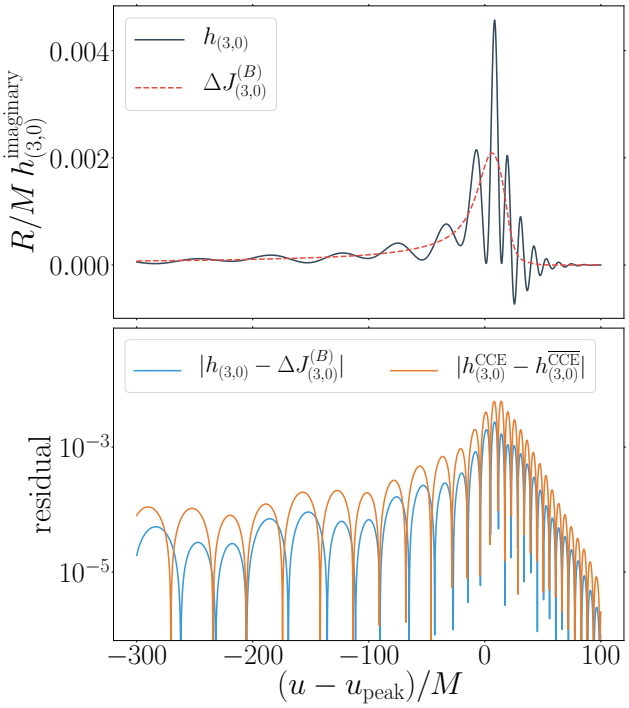

Figure 2.6: Comparison of imaginary part of the $(3,0)$ mode with the magnetic memory for a $N_{\rm orbit} \approx 150$ system (SXS:BBH:1412, see Table 2.1).

Last, we present Table 2.3, which is of the same form as Table 2.2, but contains the values of the spin memory computed by integrating Eq. (2.56b) and the spin memory found in the retarded time integral of the strain modes.

2.4.6 Fitting Ringdown to QNMs

We now investigate the oscillatory ringdown part of the $(2,0)$ and $(3,0)$ modes, which otherwise correspond to the electric and magnetic memory. We wish to explain the ringdown part of these modes with perturbation theory, i.e., by fitting them to the expected quasinormal modes. As was recently explored by Giesler *et al.* [44], once a BBH system has merged into a single black hole, the resulting black hole ringdown is well described by a *linear* superposition of quasinormal modes even from as early as the peak of the waveform, provided that the overtones are included. These quasinormal modes can be used to find the mass and spin angular momentum of the final black hole [44–46]. Thus far, though, only the $(2,2)$ mode has been thoroughly examined. Consequently, while we do not attempt to estimate the final black hole's characteristics using our fits to the $(2,0)$ and $(3,0)$ modes, we nonetheless present the accuracy of our fits, saving the parameter estimation and analysis for a future work.

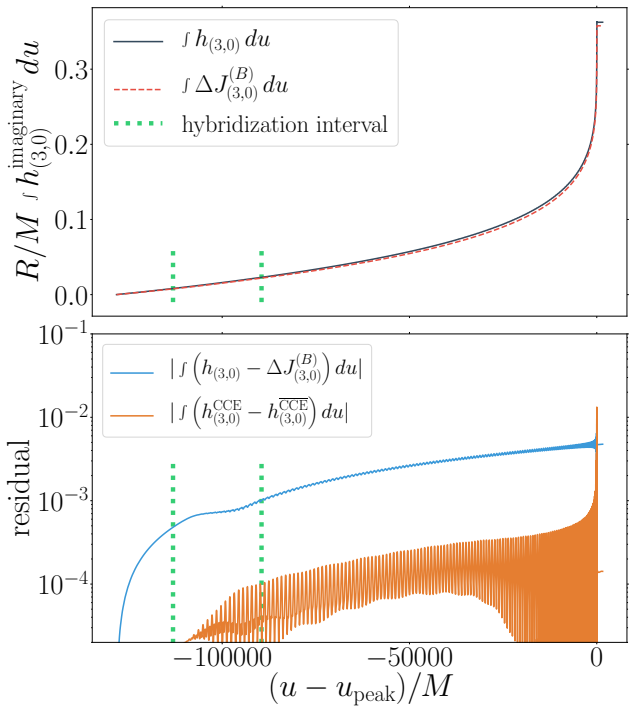

Figure 2.7: Comparison of the retarded time integral of the imaginary part of the $(3,0)$ mode with the spin memory for a $N_{\rm orbit} \approx 150$ system (SXS:BBH:1412, see Table 2.1).

Table 2.3: Spin memory values obtained by computing the retarded time integral of Eq. (2.56b) and those obtained from the overall net change in the retarded time integral of the extracted strain spin memory modes. Again, the error that we provide in the final column is simply the residual between the two highest resolution waveforms.

SXS:BBH:	$\int^{u_{\rm final}} h_{(3,0)}(u)\,du$	$\int^{u_{\rm final}} \Delta J^{(B)}_{(3,0)}(u)\,du$	Error
0305	4.05×10^{-1}	3.61×10^{-1}	7.24×10^{-5}
1155	4.32×10^{-1}	3.55×10^{-1}	1.53×10^{-4}
0554	3.28×10^{-1}	2.85×10^{-1}	1.21×10^{-5}
1412	3.62×10^{-1}	3.58×10^{-1}	1.42×10^{-4}
1389	2.79×10^{-1}	2.88×10^{-1}	4.13×10^{-2}

SXS:BBH:	$\int^{u_{\rm final}} h_{(5,0)}(u)\,du$	$\int^{u_{\rm final}} \Delta J^{(B)}_{(5,0)}(u)\,du$	Error
0305	8.56×10^{-4}	9.53×10^{-4}	1.22×10^{-5}
1155	1.09×10^{-3}	1.03×10^{-3}	5.85×10^{-6}
0554	1.80×10^{-4}	2.15×10^{-4}	1.70×10^{-5}
1412	7.06×10^{-4}	7.46×10^{-4}	1.39×10^{-6}
1389	3.12×10^{-4}	3.64×10^{-4}	6.92×10^{-5}

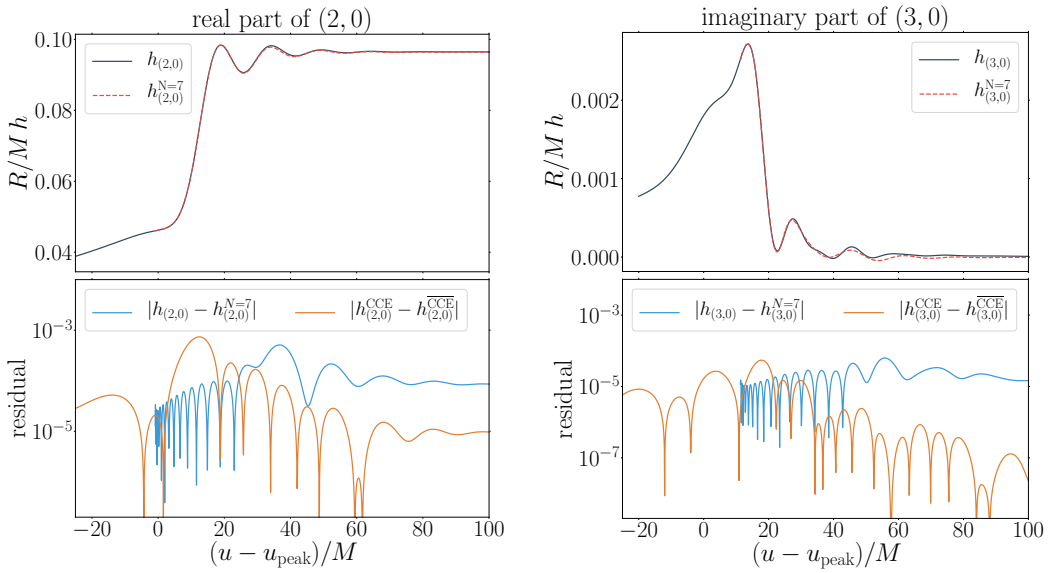

Figure 2.8: Comparison between the numerical relativity waveform and the $N = 7$ "QNM + memory" model for the primary electric and magnetic memory modes of SXS:BBH:0305. We start the QNM model at $u_0 \approx 0\,M$ for the $(2,0)$ mode and at $u_0 \approx 10\,M$ for the $(3,0)$ mode. The top row shows the strain and its corresponding fit, while the bottom row shows the residual. We also show an estimate of the error in the CCE waveform, $|h^{\rm CCE}_{(\ell,m)} - h^{\overline{\rm CCE}}_{(\ell,m)}|$, where $h^{\rm CCE}_{(\ell,m)}$ refers to the highest resolution waveform of SXS:BBH:0305 and $h^{\overline{\rm CCE}}_{(\ell,m)}$ refers to the next highest resolution.

Like previous work on quasinormal modes [47–50], we model the radiation occurring during ringdown as a sum of damped sinusoids with complex frequencies $\omega_{lmn} = \omega_{lmn}(M_f, \chi_f)$ which can be computed by using perturbation theory [51]. But, because the strain now exhibits memory effects that are not captured by the usual quasinormal mode expression, we instead perform a superposition of the memory and the quasinormal modes:

$$h^N_{lm} = \Delta J(u) + \sum_{n=0}^{N} C_{lmn} e^{-i\omega_{lmn}(u-u_0)} \quad u \geq u_0, \tag{2.59}$$

where N is the number of overtones used in our fitting and u_0 is a specifiable "start time" for the model, with any times that occur before u_0 not being included in the fits. Recall that in this paper we approximate $\Delta J(u)$ with only the null memory, ignoring the ordinary memory; this may introduce some error in our fits to Eq. (2.59). However, since the ordinary part's contribution is fairly minor—roughly 0.3% that of the null part's contribution—our fits to the QNMs should be reasonably accurate. Further, because the QNM expressions tend to zero as $u \to +\infty$, rather than making

the strain and the memory be equal at their initial values, we instead make them coincide at the time $u_{\rm final}$. With our adjusted waveforms, we then fit Eq. (2.59) to the $(2,0)$ and $(3,0)$ modes.

We construct fits for the simulation SXS:BBH:0305. We find the mismatch

$$\mathcal{M} = 1 - \frac{\langle h_{\ell m}, h^N_{\ell m}\rangle}{\sqrt{\langle h_{\ell m}, h_{\ell m}\rangle \langle h^N_{\ell m}, h^N_{\ell m}\rangle}}. \tag{2.60}$$

between our fits and the memory modes are minimized for $u_0 \approx 0\,M$ for the $(2,0)$ mode, while an initial time of $u_0 \approx 10\,M$ is needed to minimize the mismatch for the $(3,0)$ mode. We believe that the $(3,0)$ mode likely needs a larger value of u_0 because the error in that mode is larger than that of the $(2,0)$ mode, so the magnetic memory is not as accurate and thus the QNM model needs to start further on in the ringdown phase to minimize the effect of this inaccuracy. In Fig. 2.4.6 we present the fit results for the simulation SXS:BBH:0305 at the optimal fit times u_0 as found by minimizing the corresponding mismatch between the strain and the fit. The final mismatches for these modes are then

$$\begin{aligned}\mathcal{M}\big(\mathrm{Re}(h_{2,0})\big) &= 4.01 \times 10^{-7},\\ \mathcal{M}\big(\mathrm{Im}(h_{3,0})\big) &= 6.57 \times 10^{-4}.\end{aligned}$$

2.4.7 Signal-to-Noise Ratios

We now investigate the measurability of the memory by calculating the signal-to-noise ratios for the displacement and spin memory effects in a few of the current and planned GW detectors. We compute the SNR ρ using

$$\rho = \sqrt{4 \int_{f_{\rm min}}^{f_{\rm max}} \frac{|\tilde{h}(f)|^2}{S_n(f)}\, df}, \tag{2.61}$$

where $\tilde{h}(f)$ is the Fourier transform in frequency of the detector response $h(u)$ (see Eq. (2.62)), $S_n(f)$ is the noise power-spectral density (PSD), and $f_{\rm min}$ and $f_{\rm max}$ are frequency limits that are regulated by the chosen PSD. We construct $h(u)$ as

$$\begin{aligned}h(t) = {}& F_+(\theta,\phi,\psi) h_+(u,\iota,\phi_0)\\ &+ F_\times(\theta,\phi,\psi) h_\times(u,\iota,\phi_0),\end{aligned} \tag{2.62}$$

where F_+ and $F_\times$ are the antenna response patterns,

$$F_+ = \frac{1}{2}\left(1+\cos^2\theta\right)\cos(2\phi)\cos(2\psi) - \cos\theta\sin(2\phi)\sin(2\psi), \tag{2.63a}$$

$$F_\times = \frac{1}{2}\left(1+\cos^2\theta\right)\cos(2\phi)\sin(2\psi) + \cos\theta\sin(2\phi)\cos(2\psi), \tag{2.63b}$$

with θ and ϕ being the spherical coordinates relative to the observatory's axes and ψ the angle between the two usual polarization components h_+ and $h_\times$ and the observatory's two axes. The angles ι and ϕ_0 are the spherical coordinates relative to the BBH's source frame. While these angles could take on a variety of values, to simplify our computations we choose the values that maximize the SNR for the respective memory observables.

We examine SNRs for LIGO, the Einstein Telescope,[14] and LISA using the simulation SXS:BBH:0305, which for the values $M = 65\,M_\odot$ and $R = 410\,\mathrm{Mpc}$ resembles the first event that was observed by LIGO: GW150914 [52]. When computing the LISA SNRs, though, we instead use the mass $M = 10^5\,M_\odot$ to mimic the mass of supermassive black hole binaries, which places the memory signal near the bucket of the LISA noise curve. For LIGO SNRs, we use the updated Advanced LIGO sensitivity design curve, while for the ET and LISA SNRs we use the the sensitivity curve approximations that are shown in Eq. (19) of [53] and Eq. (1) of [54]. For our SNRs, we only examine the primary electric and magnetic modes because the other modes' contributions are negligible. Furthermore, we find that it is important to only consider the null memory when computing SNRs, rather than the strain, because the QNM frequencies in the strain can contaminate and thus obscure the memory SNRs, as is illustrated in Fig. 2.9. In other words, the $h_{(2,0)}$ mode contains higher frequencies due to QNM oscillations than the $\Delta J_{(2,0)}$ mode, which just describes the growth of the memory, and will thus yield a larger memory SNR than the true memory SNR.

In Table 2.4, we present the results that we find for these orientation-optimized SNRs. Alongside the SNRs for the $(2,0)$ and $(3,0)$ modes, we also provide the SNR for the $(2,2)$ mode computed using the same orientation that was chosen for the specific memory mode.

[14] Specifically, the single-interferometer configuration (ET-B).

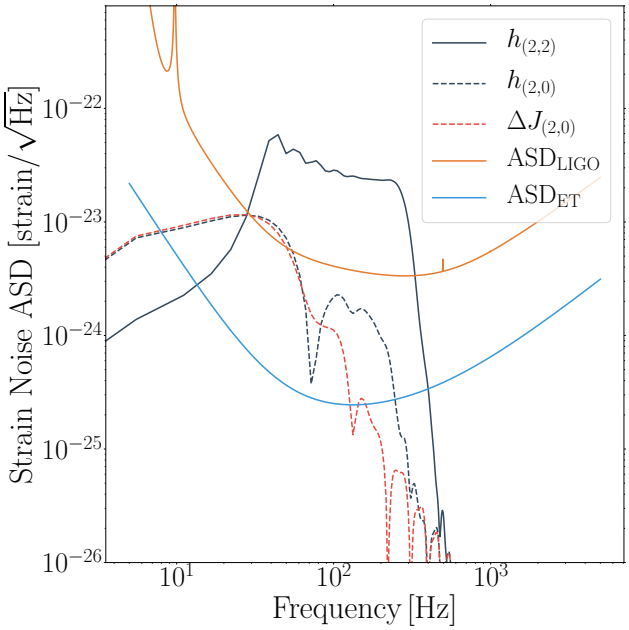

Figure 2.9: Both of LIGO's and the Einstein Telescope's (ET) amplitude spectral densities (ASD) compared to the strain $(2,2)$ (black/solid) and $(2,0)$ (black/dashed) modes as well as the memory's $(2,0)$ mode (red/dashed).

Table 2.4: LIGO, ET, and LISA SNRs for the most prominent electric and magnetic memory modes from SXS:BBH:0305. The LIGO and ET SNRs are for a total mass of $M = 65\,M_\odot$, while for LISA we use $M = 10^5\,M_\odot$.

Detector	$\Delta h_{(2,0)}$	$h_{(2,2)}$	$\Delta h_{(3,0)}$	$h_{(2,2)}$
LIGO	$2.12 \times 10^{+0}$	$2.03 \times 10^{+1}$	6.36×10^{-2}	$5.06 \times 10^{+1}$
ET-B	$3.48 \times 10^{+1}$	$3.14 \times 10^{+2}$	$1.05 \times 10^{+0}$	$7.83 \times 10^{+2}$
LISA	$1.44 \times 10^{+2}$	$2.98 \times 10^{+2}$	$3.16 \times 10^{+0}$	$7.49 \times 10^{+2}$

The SNRs that we find are larger, even if only slightly, than previous calculations that have taken advantage of either PN or postprocessing methods. Because of this, we conclude that the memory effect will most likely only be measured in future observatories or by stacking signals recorded by LIGO for ~100 events, which should take about five years [21, 23].

2.4.8 Cauchy-Characteristic Extraction

Finally, we discuss some of the important features of SpECTRE's Cauchy-characteristic extraction that need to be dealt with to successfully extract memory effects. As has been remarked by Favata and others [19, 20, 27], as well as in Fig. 2.4.1, numerical relativity simulations that employ Reggi-Wheeler-Zerilli perturbative extraction or

Newman-Penrose (NP) extraction have so far been unable to resolve the $m = 0$ modes, which contain the majority of the memory effect induced by a BBH merger. Currently, the reason for this issue is not known. Fortunately, though, Cauchy-characteristic extraction [55] can succeed.

Unlike the RWZ and NP extraction schemes, CCE takes the finite-radius world tube information created by a Cauchy evolution as the inner boundary data for an evolution of Einstein's field equations on hypersurfaces constructed by constant retarded time. Consequently, gravitational waves can then be computed directly from Einstein's equations at future null infinity. Further, since SpECTRE's CCE extracts the strain independently of the news, unlike previous works that have used CCE [25], there is no need to integrate the news with respect to retarded time, which introduces ambiguities because of an unknown integration constant.

Despite the improved precision of the CCE waveforms, there is a degree of freedom in the procedure that needs to be dealt with. The characteristic evolution within CCE allows one field, the strain h, to be (almost) freely chosen on the initial null hypersurface, and the choice of that field then influences the waveform at future null infinity. Consequences of this choice manifest as transient effects that appear at early retarded times. We can eliminate these effects by choosing a late enough transition time when hybridizing the CCE strain with the PN waveform. The transient effects caused by the choice of h on the initial null hypersurface were previously explored in [56]. For this paper, we choose initial data to match the value and first radial derivative of h from the Cauchy data on the world tube, using the simple ansatz

$$h(u = 0, r, \theta^A) = \frac{A(\theta^A)}{r} + \frac{B(\theta^A)}{r^3}. \tag{2.64}$$

The two coefficients $A(\theta^A)$ and $B(\theta^A)$ are fixed by the Cauchy data on the world tube. The form of Eq. (2.64) is chosen to maintain regularity of the characteristic system, which requires a careful choice of gauge and initial data in which the $\propto 1/r^2$ part vanishes at future null infinity.

As we illustrate in Fig. 2.4.8, the initial behavior of the $(2, 0)$ mode of the strain is dependent upon the choice of the world tube radius that one makes: a smaller radius results in the strain becoming more negative once the junk passes. Similar to the junk radiation seen around $-3700\,M$ in Fig. 2.4.8, the initial transient radiation in CCE is a result of numerical relativity not possessing a complete past history of the binary system's evolution. Fortunately, we find that we can remedy this junk effect by constructing a numerical relativity and PN hybrid, which starts at a time that

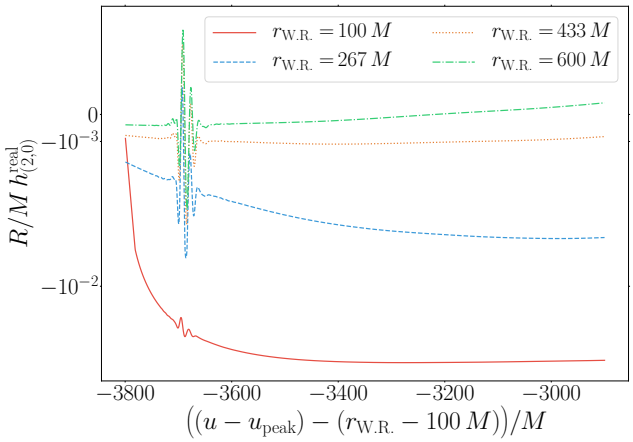

Figure 2.10: The strain $(2,0)$ mode computed using CCE world tubes of various radii $r_{\rm W.R.}$, for the simulation SXS:BBH:0305. We have added a time translation so that waveforms for every $r_{\rm W.R.}$ begin at the same time. We show only the beginning of the waveform, and the values here are much smaller than the overall scale of the $(2,0)$ mode as seen, e.g., in Fig. 2.4.3.

corresponds to 4 times the worldtube radius, e.g., $u \approx 400\,M$ for $r_{\rm W.R.} = 100\,M$, and extends throughout $\sim$ % of the numerical waveform. For the results we presented earlier, we chose to hybridize the second smallest world tube radius waveform, seeing as this waveform produced the best agreement between the strain and the BMS flux-balance strain.

2.5 Conclusion

When a binary black hole merger emits radiation that propagates through spacetime toward asymptotic infinity, persistent physical changes known as memory effects occur. These changes are induced as a consequence of BMS flux-balance laws that extend the Poincaré balance laws. Because these BMS flux-balance laws physically relate to supertranslations, -rotations, or -boosts, these changes are called displacement, spin, or center-of-mass memories. Measuring these memory effects will be an important test of Einstein's theory of general relativity. However, computing the memory produced in a binary black hole merger requires numerical relativity. Before this work, studying memory using numerical relativity has been challenging because many of the memory contributions to the metric could not be properly resolved.

Using a collection of energy and angular momentum flux equations, we computed the memory that is induced in vacuum spacetimes as a function of the radiated strain,

thereby allowing for the complete calculation of both the electric and magnetic components of the memory effect. We then verified that the strain and the two Weyl scalars from SpECTRE's Cauchy-characteristic extraction obey the two BMS flux-balance equations that we used to calculate the memory. While performing this check, we saw that the primary contribution to the memory comes from the null contribution, because the simulations in the SXS Catalog tend to experience no supertranslations or super-Lorentz transformations. We derived an expression for the null memory contribution that depends on every one of the strain modes and on some of the Weyl scalars. We compared this expression with the well-understood $m = 0$ memory modes of the strain, for many simulations of BBH mergers spanning a variety of input parameters. Overall, this new expression for the memory effect agrees with the strain very well, and our comparison works even for the conjectured oscillatory $m \neq 0$ memory modes. Furthermore, we found that the magnetic component of the memory, which is believed to be zero, indeed vanishes to the precision of the corresponding Cauchy simulation.

In addition, we found that we can rather accurately model the various memory modes as the combination of a memory signal during the inspiral and merger phases and a quasinormal mode signal during the ringdown phase. Our best fits to the two primary electric and magnetic memory modes offer the possibility that memory modes could participate in constraining the remnant black hole's mass and spin. However, the extent to which the inclusion of the memory modes can improve parameter estimation remains a subject for a future investigation.

Last, we found that the memory SNRs for LIGO, the Einstein Telescope, and LISA are slightly better than previous expectations. Consequently, memory should be observable with future detectors or once a big enough catalog of merger events is obtained by LIGO.

During the past few years, the memory effect was shown to be equivalent to Weinberg's soft theorem through a Fourier transform in time [5, 6], thus forming a curious connection between memory, asymptotic symmetries, and soft theorems. Because of this, memory can perhaps serve as an important physical realization of these abstractly formulated results, and thus may one day help realize the holographic structure of quantum gravity in arbitrary four-dimensional spacetimes.

2.6 Acknowledgments

We thank Matt Giesler for many useful conversations. Computations were performed on the Wheeler cluster at the California Institute of Technology (Caltech), which is supported by the Sherman Fairchild Foundation and by Caltech. This work was supported in part by the Sherman Fairchild Foundation and by NSF Grants No. PHY-1708212, No. PHY-1708213, and No. OAC-1931266 at Caltech and NSF Grants No. PHY-1912081 and No. OAC-1931280 at Cornell.

2.A Bondi Mass Aspect

As was shown in Sec. 2.3.2.1, the ordinary contribution to the electric component of the memory is a function of the Bondi mass aspect m. Consequently, to compute the electric memory from numerical relativity waveforms, one needs to know the Bondi mass aspect in terms of the strain and the Weyl scalar Ψ_2. Using the results that were obtained by Moxon *et al.* [30], by rearranging their Eq. (94e) and converting their notation to ours, we find

$$m = -\mathrm{Re}\left[\Psi_2 + \frac{1}{4}\dot{h}\bar{h}\right]. \tag{2.65}$$

The notation changes that are needed to convert from Moxon's work to ours are $\mathring{W}^{(2)} \to -2m$ and $\mathring{J}^{(1)} \to \bar{h}$, since Moxon takes $\mathring{J}^{(1)}$ to have spin-weight +2 rather than spin-weight −2, which is our convention.

2.B Bondi Angular Momentum Aspect

As was shown in Sec. 2.3.2.1, the ordinary contribution to the magnetic component of the memory is a function of the angular momentum aspect $\widehat{N}_A$. Thus, to compute the magnetic memory from numerical relativity waveforms, one needs to know the angular momentum aspect in terms of the strain and the Weyl scalar Ψ_1. We start by contracting the $O(r^{-3})$ part of Eq. (2.14) with q_A, from which we obtain

$$\mathcal{U}^{(3)} = -\frac{2}{3}N + \frac{1}{16}\eth(C_{AB}C^{AB}) + \frac{1}{2}q_A C^{AB} D^C C_{BC}. \tag{2.66}$$

Using $C_{AB}C^{AB} = 2h\bar{h}$ and $C^{AB}D^C C_{BC} = \mathrm{Re}\left[q^A h \bar{\eth}\bar{h}\right]$ [from Eq. (2.46b)], we can then rewrite Eq. (2.66) as

$$\mathcal{U}^{(3)} = -\frac{2}{3}N + \frac{1}{8}\eth(h\bar{h}) + \frac{1}{2}\bar{h}\eth h. \tag{2.67}$$

According to Bishop *et al.* [57] Eqs. (8) and (A2)

$$\partial_r \mathcal{U} = \frac{e^{2\beta}}{r^2}(KQ - \bar{h}\bar{Q}) \tag{2.68}$$

for

$$K \equiv \frac{1}{2} q^A \bar{q}^B \gamma_{AB} \quad \text{and} \quad Q \equiv q_A r^2 e^{-2\beta} \gamma^{AB} \partial_r \mathcal{U}_B. \tag{2.69}$$

Thus, by examining the $O(r^{-3})$ part of Eq. (2.68), we find

$$\begin{aligned} -3\mathcal{U}^{(3)} &= K^{(0)} Q^{(2)} - \bar{h}\bar{Q}^{(1)} + 2\beta_0 K^{(0)} Q^{(1)} \\ &= Q^{(2)} - \bar{h}\bar{Q}^{(1)}, \end{aligned} \tag{2.70}$$

seeing as $\beta_0 = 0$ by Flanagan and Nichols's Eq. (2.9b) [33]. Also, by explicit calculation and Flanagan and Nichols's Eq. (2.9a), since $q_A D_B C^{AB} = \bar{\eth}\bar{h}$, we can write $\bar{Q}^{(1)}$ as

$$\bar{Q}^{(1)} = -2\bar{U} = \eth h. \tag{2.71}$$

Furthermore, by Moxon *et al.'s* [30] Eq. (94c)

$$\Psi_1 = -\frac{3}{2}\eth\beta_1 + \frac{1}{8}\bar{h}\bar{Q}^{(1)} + \frac{1}{4}Q^{(2)}. \tag{2.72}$$

But, since Flanagan and Nichols's [33] Eq. (2.9c) implies

$$\beta_1 = -\frac{1}{32} C_{AB} C^{AB} = -\frac{1}{16} h\bar{h}, \tag{2.73}$$

we then have

$$Q^{(2)} = 4\Psi_1 - \frac{3}{8}\eth(h\bar{h}) - \frac{1}{2}\bar{h}\bar{Q}^{(1)}. \tag{2.74}$$

Combining Eq. (2.71) and Eq. (2.74), we obtain

$$\begin{aligned} -3\mathcal{U}^{(3)} &= 4\Psi_1 - \frac{3}{8}\eth(h\bar{h}) - \frac{3}{2}\bar{h}\bar{Q}^{(1)} \\ &= 4\Psi_1 - \frac{3}{8}\eth(h\bar{h}) - \frac{3}{2}\bar{h}\eth h \end{aligned} \tag{2.75}$$

Therefore,

$$N = 2\Psi_1. \tag{2.76}$$

Finally, since contracting Eq. (2.23) produces

$$\widehat{N} = N - u\eth m - \frac{1}{8}\eth(h\bar{h}) - \frac{1}{4}\bar{h}\eth h, \tag{2.77}$$

we can write the angular momentum aspect as

$$\widehat{N} = 2\Psi_1 - u\eth m - \frac{1}{8}\eth(h\bar{h}) - \frac{1}{4}\bar{h}\eth h. \tag{2.78}$$

As is shown in Secs. 2.3.2.2 and 2.3.2.3, we primarily care about real and imaginary components of this function, which are easily found from Eq. (2.78) to be

$$\begin{aligned}\mathrm{Re}(\bar{\eth}\widehat{N}) &= \mathrm{Re}\Big[2\bar{\eth}\Psi_1 - \frac{1}{4}\bar{\eth}(\bar{h}\eth h)\Big] \\ &\quad - D^2(um + \frac{1}{8}h\bar{h}), \qquad (2.79a)\\ \mathrm{Im}(\bar{\eth}\widehat{N}) &= \mathrm{Im}\Big[2\bar{\eth}\Psi_1 - \frac{1}{4}\bar{\eth}(\bar{h}\eth h)\Big]. \qquad (2.79b)\end{aligned}$$

2.C CM Memory

When calculating our expressions for the total memory, we briefly mentioned in Sec. 2.3.2.3 how the electric memory can be seen to contain terms relating to the CM memory. Currently, we are unaware of an explicit formula for the CM memory. For now, though, we present evidence for the CM memory effect in the waveforms produced by numerical relativity. As can be seen in Fig. 2.C, while there is no displacement memory present in the mode shown, the energy flux term indicates that when integrated with respect to retarded time this contribution will produce a memory effect, which is exactly the CM memory effect.

References

[1] Y. B. Zel'dovich and A. G. Polnarev, Sov. Astron. **18**, 17 (1974).

[2] V. B. Braginsky and K. S. Thorne, Nature **327**, 123 (1987).

[3] D. Christodoulou, Phys. Rev. Lett. **67**, 1486 (1991) 10.1103/PhysRevLett.67.1486.

[4] K. S. Thorne, Phys. Rev. D **45**, 520 (1992) 10.1103/PhysRevD.45.520.

[5] A. Strominger and A. Zhiboedov, (2014).

[6] S. Pasterski, A. Strominger, and A. Zhiboedov, Journal of High Energy Physics **2016**, 10.1007/jhep12(2016)053 (2016) 10.1007/jhep12(2016)053.

[7] D. A. Nichols, Physical Review D **98**, 10.1103/physrevd.98.064032 (2018) 10.1103/physrevd.98.064032.

[8] G. Compère, R. Oliveri, and A. Seraj, *The poincaré and bms flux-balance laws with application to binary systems*, 2019.

[9] H. Bondi, M. G. J. Van der Burg, and A. W. K. Metzner, Proceedings of the Royal Society of London. Series A. Mathematical and Physical Sciences **269**, 21 (1962) 10.1098/rspa.1962.0161.

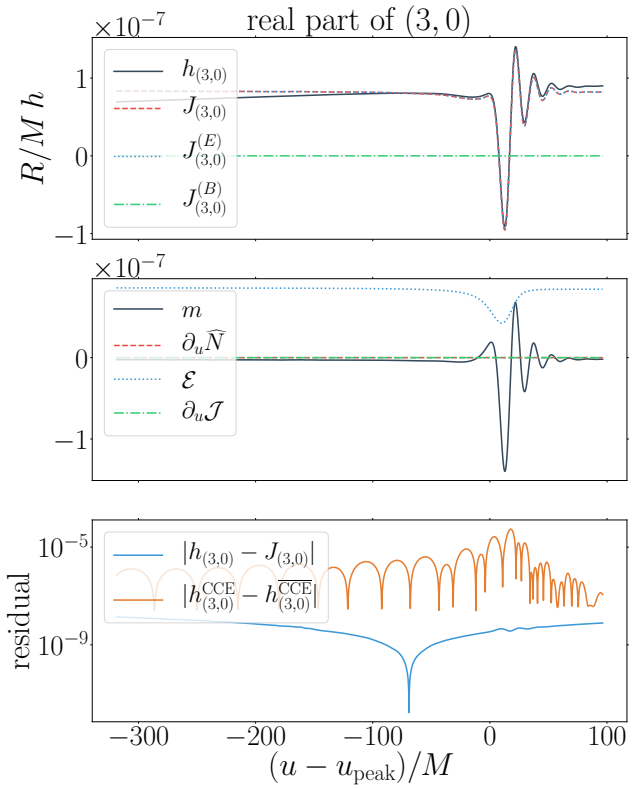

Figure 2.11: Comparison of the real part of the (3,0) mode of the strain extracted from simulation SXS:BBH:0305 to the strain computed from Eqs. (2.38) and (2.47). The top plot shows the extracted strain (black/solid), the strain computed from the BMS flux-balance laws (red/dashed), and its corresponding electric (blue/dotted) and magnetic (green/dashed/dotted) components from Eqs. (2.38) and (2.47). The middle plot shows the contributions that come from the mass aspect (black/solid), the angular momentum aspect (red/dashed), the energy flux (blue/dotted), and the angular momentum flux (green/dashed/dotted). We provide an estimate of the strain's corresponding numerical error in the bottom plot.

[10] R. K. : Sachs and H. Bondi, Proceedings of the Royal Society of London. Series A. Mathematical and Physical Sciences **270**, 103 (1962) 10.1098/rspa.1962.0206.

[11] G. Barnich and C. Troessaert, Physical Review Letters **105**, 10.1103/physrevlett.105.111103 (2010) 10.1103/physrevlett.105.111103.

[12] J. de Boer and S. N. Solodukhin, Nuclear Physics B **665**, 545 (2003) 10.1016/s0550-3213(03)00494-2.

[13] T. Banks, *A critique of pure string theory: heterodox opinions of diverse dimensions*, 2003.

[14] G. Barnich and C. Troessaert, *Supertranslations call for superrotations*, 2011.

[15] D. Kapec, V. Lysov, S. Pasterski, and A. Strominger, Journal of High Energy Physics **2014**, 10.1007/jhep08(2014)058 (2014) 10.1007/jhep08(2014)058.

[16] D. Kapec, P. Mitra, A.-M. Raclariu, and A. Strominger, Physical Review Letters **119**, 10.1103/physrevlett.119.121601 (2017) 10.1103/physrevlett.119.121601.

[17] T. He, D. Kapec, A. Raclariu, and A. Strominger, Journal of High Energy Physics **2017**, 10.1007/jhep08(2017)050 (2017) 10.1007/jhep08(2017)050.

[18] L. Bieri and D. Garfinkle, Physical Review D **89**, 10.1103/physrevd.89.084039 (2014) 10.1103/physrevd.89.084039.

[19] M. Favata, Physical Review D **80**, 10.1103/physrevd.80.024002 (2009) 10.1103/physrevd.80.024002.

[20] D. A. Nichols, Physical Review D **95**, 10.1103/physrevd.95.084048 (2017) 10.1103/physrevd.95.084048.

[21] P. D. Lasky, E. Thrane, Y. Levin, J. Blackman, and Y. Chen, Physical Review Letters **117**, 10.1103/physrevlett.117.061102 (2016) 10.1103/physrevlett.117.061102.

[22] C. Talbot, E. Thrane, P. D. Lasky, and F. Lin, Physical Review D **98**, 10.1103/physrevd.98.064031 (2018) 10.1103/physrevd.98.064031.

[23] O. M. Boersma, D. A. Nichols, and P. Schmidt, (2020).

[24] M. Hübner, C. Talbot, P. D. Lasky, and E. Thrane, Physical Review D **101**, 10.1103/physrevd.101.023011 (2020) 10.1103/physrevd.101.023011.

[25] D. Pollney and C. Reisswig, The Astrophysical Journal **732**, L13 (2011) 10.1088/2041-8205/732/1/l13.

[26] M. Favata, The Astrophysical Journal **696**, L159 (2009) 10.1088/0004-637x/696/2/l159.

[27] M. Favata, Classical and Quantum Gravity **27**, 084036 (2010) 10.1088/0264-9381/27/8/084036.

[28] M. Boyle, D. Hemberger, D. A. B. Iozzo, G. Lovelace, S. Ossokine, H. P. Pfeiffer, M. A. Scheel, L. C. Stein, C. J. Woodford, A. B. Zimmerman, and et al., Classical and Quantum Gravity **36**, 195006 (2019) 10.1088/1361-6382/ab34e2.

[29] *SpECTRE Code*, https://spectre-code.org.

[30] J. Moxon, M. A. Scheel, and S. A. Teukolsky, (2020).

[31] L. E. Kidder, Physical Review D **77**, 10.1103/physrevd.77.044016 (2008) 10.1103/physrevd.77.044016.

[32] L. Blanchet, G. Faye, B. R. Iyer, and S. Sinha, Classical and Quantum Gravity **25**, 165003 (2008) 10.1088/0264-9381/25/16/165003.

[33] É. É. Flanagan and D. A. Nichols, Physical Review D **95**, 10.1103/physrevd.95.044002 (2017) 10.1103/physrevd.95.044002.

[34] J. Winicour, Classical and Quantum Gravity **31**, 205003 (2014) 10.1088/0264-9381/31/20/205003.

[35] A. Ashtekar, T. D. Lorenzo, and N. Khera, *Compact binary coalescences: constraints on waveforms*, 2019.

[36] N. T. Bishop and C. Reisswig, General Relativity and Gravitation **46**, 10.1007/s10714-013-1643-5 (2013) 10.1007/s10714-013-1643-5.

[37] M. Boyle, D. Hemberger, and D. Iozzo, *Moble/gwframes: conda-forge release*, version 1.0, Aug. 2020, 10.5281/zenodo.3974963.

[38] M. Boyle, *Moble/postnewtonian: conda-forge release*, version v1.0, Sept. 2020, 10.5281/zenodo.4041962.

[39] https://github.com/moble/scri.

[40] M. Boyle, Physical Review D **87**, 104006 (2013) 10.1103/PhysRevD.87.104006.

[41] M. Boyle, Physical Review D **93**, 15 (2016) 10.1103/PhysRevD.93.084031.

[42] M. Boyle, L. E. Kidder, S. Ossokine, and H. P. Pfeiffer, arXiv (2014).

[43] M. Boyle, Phys. Rev. D **93**, 084031 (2016) 10.1103/PhysRevD.93.084031.

[44] M. Giesler, M. Isi, M. A. Scheel, and S. A. Teukolsky, Physical Review X **9**, 10.1103/physrevx.9.041060 (2019) 10.1103/physrevx.9.041060.

[45] A. Buonanno, G. B. Cook, and F. Pretorius, Phys. Rev. D **75**, 124018 (2007) 10.1103/PhysRevD.75.124018.

[46] V. Baibhav, E. Berti, V. Cardoso, and G. Khanna, Phys. Rev. D **97**, 044048 (2018) 10.1103/PhysRevD.97.044048.

[47] C. V. Vishveshwara, Phys. Rev. D **1**, 2870 (1970) 10.1103/PhysRevD.1.2870.

[48] W. H. Press, Astrophys. J. Lett. **170**, L105 (1971) 10.1086/180849.

[49] S. A. Teukolsky, Astophys. J. **185**, 635 (1973) 10.1086/152444.

[50] S. Chandrasekhar and S. Detweiler, Proceedings of the Royal Society of London. Series A, Mathematical and Physical Sciences **344**, 441 (1975).

[51] L. C. Stein, J. Open Source Softw. **4**, 1683 (2019) 10.21105/joss.01683.

[52] B. P. Abbott, R. Abbott, T. D. Abbott, M. R. Abernathy, F. Acernese, K. Ackley, C. Adams, T. Adams, P. Addesso, R. X. Adhikari, and et al., Physical Review Letters **116**, 10.1103/physrevlett.116.241102 (2016) 10.1103/physrevlett.116.241102.

[53] T. Regimbau, T. Dent, W. Del Pozzo, S. Giampanis, T. G. F. Li, C. Robinson, C. Van Den Broeck, D. Meacher, C. Rodriguez, B. S. Sathyaprakash, and K. Wójcik, Phys. Rev. D **86**, 122001 (2012) 10.1103/PhysRevD.86.122001.

[54] T. Robson, N. J. Cornish, and C. Liu, Classical and Quantum Gravity **36**, 105011 (2019) 10.1088/1361-6382/ab1101.

[55] K. Barkett, J. Moxon, M. A. Scheel, and B. Szilágyi, *Spectral cauchy-characteristic extraction of the gravitational wave news function*, 2019.

[56] N. T. Bishop and L. Rezzolla, Living Reviews in Relativity **19**, 10.1007/s41114-016-0001-9 (2016) 10.1007/s41114-016-0001-9.

[57] N. T. Bishop, R. Gómez, L. Lehner, M. Maharaj, and J. Winicour, Phys. Rev. D **56**, 6298 (1997) 10.1103/PhysRevD.56.6298.

Chapter 3

ADDING GRAVITATIONAL MEMORY TO WAVEFORM CATALOGS USING BMS BALANCE LAWS

K. Mitman et al., Phys. Rev. D **103**, 024031 (2021) 10.1103/PhysRevD.103.024031,

3.1 Abstract

Accurate models of gravitational waves from merging binary black holes are crucial for detectors to measure events and extract new science. One important feature that is currently missing from the Simulating eXtreme Spacetimes (SXS) Collaboration's catalog of waveforms for merging black holes, and other waveform catalogs, is the gravitational memory effect: a persistent, physical change to spacetime that is induced by the passage of transient radiation. We find, however, that by exploiting the Bondi-Metzner-Sachs (BMS) balance laws, which come from the extended BMS transformations, we can correct the strain waveforms in the SXS catalog to include the missing displacement memory. Our results show that these corrected waveforms satisfy the BMS balance laws to a much higher degree of accuracy. Furthermore, we find that these corrected strain waveforms coincide especially well with the waveforms obtained from Cauchy-characteristic extraction (CCE) that already exhibit memory effects. These corrected strain waveforms also evade the transient junk effects that are currently present in CCE waveforms. Last, we make our code for computing these contributions to the BMS balance laws and memory publicly available as a part of the python package `sxs`, thus enabling anyone to evaluate the expected memory effects and violation of the BMS balance laws.

3.2 Introduction

When Bondi, van der Burg, Metzner, and Sachs (BMS) tried to recover the Poincaré group of special relativity as the symmetry group of asymptotically flat spacetimes in general relativity, they instead found an unexpected infinite-dimensional group of transformations, known as the *BMS group* [1, 2]. Fundamentally, the BMS group extends the Poincaré group with an infinite number of transformations called *su-*

pertranslations.[1] More recent research [3–10] motivates the consideration of an extended BMS group that includes another set of transformations known as *super-Lorentz transformations*.[2] When these transformations are included, the group is then called the *extended* BMS group. Like rotations and boosts in special relativity, we refer to the magnetic parity piece of super-Lorentz transformations as *superrotations* and the electric parity piece as *superboosts*.

One of the extended BMS group's more useful features is that for each transformation there is a corresponding balance law. Just as the translation symmetries lead to the four-momentum and its balance laws at null infinity, the supertranslations and super-Lorentz transformations of the extended BMS group induce "super" balance laws. These super, or just BMS, balance laws can be extracted from the Einstein field equations by examining certain evolution equations [7, 11–13]. There is an infinite tower of balance laws: one for each point on the two-sphere or, equivalently, one for each spherical harmonic mode. Furthermore, the BMS flux part of these balance laws can be broken into two contributions, called "hard" and "soft," which are based on the order in which the gravitational wave strain appears: nonlinear for the hard contribution and linear for the curious soft contribution. An example of the relationship between BMS charges and BMS fluxes is the well-known mass loss equation [1]

$$\dot{m} = -\frac{1}{4}\dot{h}\dot{\bar{h}} + \frac{1}{4}\mathrm{Re}\left[\eth^2 \dot{h}\right], \tag{3.2}$$

where m is the Bondi mass aspect, h is the strain, and $\eth$ is the spin-weight operator (see Sec. 3.2.2 for more details). In Eq. (3.2), the left-hand side is the BMS charge, while the right-hand side is the BMS flux, with the "$\dot{h}\dot{\bar{h}}$" term being the hard contribution (notice that this term is just the time derivative of the energy flux) and the "$\eth^2\dot{h}$" term being the soft contribution.[3] When integrated with respect to time,

[1] Formally, the BMS group is simply a semidirect product of the Lorentz group with this infinite-dimensional Abelian group of spacetime supertranslations, which contains the usual translations as a normal subgroup. If one represents spacetime translations as the $\ell < 2$ spherical harmonics, then supertranslations can be viewed as the $\ell \geq 2$ spherical harmonics, i.e., when acted on by a supertranslation the Bondi time $u \equiv t - r$ changes as

$$u' = u - \alpha(\theta,\phi) \quad \text{for} \quad \alpha = \sum_{\ell\geq 2}\sum_{m\leq|\ell|} \alpha_{\ell m} Y_{\ell m}(\theta,\phi) \tag{3.1}$$

with $\alpha_{\ell,m} = (-1)^m \bar{\alpha}_{\ell,-m}$ to ensure that u' is real.

[2] Originally, these transformations were known as superrotations. They can be thought of as a Virasoro-like symmetry acting on the sphere at asymptotic infinity, i.e., the $|m| \geq 2$ elements of the Virasoro algebra, which is just an extension of the more common group of Möbius transformations.

[3] Originally [1], Eq. (3.2) was written after it had been integrated over the two-sphere so the "$\eth^2\dot{h}$" term could be ignored since its $\ell = 0, 1$ modes are zero.

Table 3.1: The three types of memory and their physical interpretations.

Memory type	BMS transformation	Physical interpretation
Displacement	Supertranslations	Change in the relative position of two freely falling, initially comoving observers. Appears in the strain.
Spin	Superrotations	Change in the relative time delay of two freely falling observers on initially counterorbiting trajectories. Appears in the retarded time integral of the strain.
Center-of-mass	Superboosts	Change in the relative time delay of two freely falling observers on initially antiparallel trajectories. Appears in the retarded time integral of the strain.

the soft contribution to the total BMS flux is then proportional to the *gravitational memory*, or just the *memory*, of the gravitational wave. Consequently, the BMS balance laws can be viewed as relating the memory to contributions coming from the BMS charges and the hard part of the flux of an arbitrary system.

The gravitational memory effect, on its own, has been studied for decades [14–22]. Only recently [23–26], however, have new memory effects started to be understood in relation to the elements of the extended BMS group. Because of this connection, memory has been categorized into three types based on which BMS transformations they correspond to. We outline these types in Table 3.2, along with their physical meanings. Apart from these characterizations, memory is also classified by its *ordinary* and *null* parts, with the ordinary part coming from the BMS charges and the null part coming from the hard part of the flux. Besides furthering the physical understanding of gravitational memory, however, the BMS balance laws can also offer practical uses to waveform modeling efforts. As was proposed in [27], and as we will show throughout this paper, the BMS balance laws can be used to both check the accuracy of waveforms and also improve them if they are missing certain flux contributions.

The framework provided by the extended BMS group is applicable only to asymptotic Bondi gauge waveforms. The waveforms that are extracted at finite radii in current numerical simulations do not fall into this category, however, since the simulation

coordinates are not necessarily in the Bondi gauge and there are subleading terms in the waveforms in addition to the asymptotic contribution [28]. Therefore, these finite-radius waveforms must be either extrapolated [29] or evolved [30–32] to asymptotic infinity with respect to Bondi coordinates.

Additionally, the extrapolated strain waveforms that are made publicly available in the SXS catalog [33, 34] and other waveform catalogs [35, 36] fail to capture the displacement memory for an unknown reason [20, 37]. But, by using an alternative waveform extraction technique called Cauchy-characteristic extraction (CCE) [30], the memory can be captured and the resulting waveforms appear to minimally violate the BMS balance laws [37]. Our goal in this paper is to use the balance laws to help improve the extrapolated strain waveforms; in particular, to make them exhibit the displacement memory effect so that they are more on a par with the CCE waveforms. Consequently, we not only need to know the total memory, but also how the memory evolves. That is, we must use the finite-time version of the balance laws as opposed to the global version, i.e., we must compare the BMS charges to the BMS fluxes as functions of time rather than the net changes in the two. This version of the BMS balance laws can be rewritten to give the gravitational wave strain h as a combination of two unique terms: an energy flux term $J_{\mathcal{E}}$ and a more oscillatory term J_{Ψ} that depends on the Weyl scalar Ψ_2.[4] With these new terms, we can then write the balance laws as

$$h = J_{\mathcal{E}} + J_{\Psi}. \tag{3.3}$$

The energy flux term, which is the primary contribution to the strain's total displacement memory [37, 38], was first computed in [38] and depends only on the news $\dot{h}$.[5] Because the current extrapolated strain waveforms in the SXS catalog fail to capture the displacement memory, we can therefore ask if these waveforms are reasonably modeled by just the J_{Ψ} term. If so, we can then add the $J_{\mathcal{E}}$ term to the extrapolated strain waveforms to see if the violation of the BMS balance laws and the mismatch between extrapolated and CCE waveforms are improved. Indeed, we find empirically that extrapolation gives the J_{Ψ} term to reasonable accuracy and adding the energy flux $J_{\mathcal{E}}$ term gives a more complete and improved waveform.

[4] While J_{Ψ} is certainly more oscillatory than $J_{\mathcal{E}}$, it is important to note that $J_{\mathcal{E}}$ does not always change monotonically and can exhibit oscillatory behavior as well for certain BBH systems, such as precessing systems.

[5] This term was also identified in [37] as being the null component of the electric parity piece of the displacement memory; see Table 3.2.

We find that when the expected memory $J_{\mathcal{E}}$ is added to the extrapolated strain waveforms, the extrapolated waveforms obey the BMS balance laws to roughly the same degree as those obtained by CCE. Furthermore, we observe that the mismatch between extrapolated and CCE waveforms near merger is considerably improved. We find that the next-leading cause for the violation of the BMS balance laws is due to the part of the waveform that is the primary contribution to the spin memory effect. For an unknown reason, there is already an incomplete[6] spin memory contribution to the extrapolated waveform, unlike the displacement memory contribution which is completely absent [37]. Unfortunately, this means that we have no justified way to correct the spin memory contribution without using the Weyl scalar Ψ_2, which has not yet been extracted for the simulations in the SXS catalog. Nonetheless, we find that the extrapolated waveform is indeed a good approximation to the J_{Ψ} term, although it does not wholly capture the spin memory. Therefore, whenever extrapolated waveforms are used for any kind of analysis, they should first be corrected by the $J_{\mathcal{E}}$ term to include memory and thus remain consistent with expectations from theory.

Apart from improving the extrapolated waveforms, we also observe that once the $J_{\mathcal{E}}$ correction is added, the Bondi frame of our extrapolated waveforms after ringdown is nearly the same as that of the waveforms obtained from CCE. This is important because gravitational wave astronomy expects the waveforms produced by numerical relativity to be close to, if not in, the super rest frame[7] to circumvent frame ambiguities. Without the displacement memory correction, however, the extrapolated waveforms in the SXS catalog would prompt one to think that the system was already fairly close to the super rest frame, which would be markedly incorrect. Consequently, the displacement memory correction not only serves as an important improvement to the extrapolated waveforms, but is also crucial for correctly comparing the Bondi frame of the multitude of waveforms in the SXS catalog to the super rest frame and ensuring that waveforms, when being compared to each other, are in the same Bondi frame.

We make our code for computing these contributions to the BMS balance laws and memory publicly available as a part of the python package `sxs` [39].

[6] We find that the spin memory present in the extrapolated strain is roughly 50% of what is seen in the CCE strain.

[7] See Sec. 3.4.3 for a more thorough explanation.

3.2.1 Overview

We organize our computations and results as follows. In Sec. 3.3 we outline the BMS balance laws that we will use to measure waveform accuracy, using results obtained in [27] and [37]. Following this, in Sec. 3.4.1 we illustrate the main sources of BMS balance law violations for the extrapolated waveforms in comparison to CCE and then explain which of these sources we can correct and why. Next, in Sec. 3.4.2 we present the changes to the extrapolated waveforms once displacement memory is included, explore other sources of the violation of the BMS balance laws, and then compare the corrected extrapolated waveforms to the waveforms that are obtained using CCE. Finally, in Sec. 3.4.3 we measure the Bondi frame of the corrected extrapolated waveforms and discuss prospects for mapping to the super rest frame.

3.2.2 Conventions

We set $c = G = 1$ and use the Newman-Penrose (NP) convention for the spin-weight operator $\eth$ [40] to coincide with the recent work of [30] and [37],

$$\eth_s Y_{\ell m} = +\sqrt{(\ell - s)(\ell + s + 1)}\, {}_{s+1}Y_{\ell m}, \tag{3.4}$$

$$\bar{\eth}_s Y_{\ell m} = -\sqrt{(\ell + s)(\ell - s + 1)}\, {}_{s-1}Y_{\ell m} \tag{3.5}$$

We denote the strain[8] by h and use the variable J to represent any contribution to the strain that comes from the BMS balance laws that we compute with our various numerical outputs. Further, we represent the strain in a spin-weight -2 spherical harmonic basis,

$$h(u, \theta, \phi) = \sum_{\ell,m} h_{\ell m}(u)\, {}_{-2}Y_{\ell m}(\theta, \phi), \tag{3.6}$$

where $u \equiv t - r$ is the Bondi time. For our calculations, we use the operators D^2 and $\mathfrak{D}$, which we construct as

$$D^2 = \bar{\eth}\eth, \tag{3.7a}$$

$$\mathfrak{D} = \frac{1}{8} D^2 \left(D^2 + 2 \right). \tag{3.7b}$$

Notice that D^2 is just the Laplacian on the two-sphere when it acts on spin-weight 0 functions. The actions of these operators on spin-weight 0 functions are

$$D^2 Y_{\ell m} = -\ell(\ell + 1) Y_{\ell m}, \tag{3.8a}$$

$$\mathfrak{D} Y_{\ell m} = \frac{1}{8}(\ell + 2)(\ell + 1)\ell(\ell - 1) Y_{\ell m}. \tag{3.8b}$$

[8] We explicitly define the strain as described in Appendix C of [34].

3.3 BMS Balance Laws and Memory

We now review some of the work on BMS balance laws and present equations that will prove useful to our analysis. As described in [27], the supermomentum balance law, which gives the electric parity part of the strain, can be written rather nicely as

$$\begin{aligned}\mathrm{Re}\left[\eth^2 h\right] = \\ \int_{-\infty}^{u} |\dot{h}|^2\, du - 4\mathrm{Re}\left[\Psi_2 + \frac{1}{4}\dot{h}\bar{h}\right] - 4M_{\mathrm{ADM}},\end{aligned} \tag{3.9}$$

for a system with ADM mass M_{ADM}, if one uses the "post-Newtonian Bondi frame" where $h \to 0$ as $u \to -\infty$. The magnetic parity part of the strain can be obtained from the relation between h and $\mathrm{Im}[\Psi_2]$:

$$\mathrm{Im}\left[\eth^2 h\right] = -4\mathrm{Im}\left[\Psi_2 + \frac{1}{4}\dot{h}\bar{h}\right]. \tag{3.10}$$

Consequently, by combining Eqs. (3.9) and (3.10) one has

$$\eth^2 h = \int_{-\infty}^{u} |\dot{h}|^2\, du - 4\left(\Psi_2 + \frac{1}{4}\dot{h}\bar{h}\right) - 4M_{\mathrm{ADM}}, \tag{3.11}$$

or equivalently

$$h = \frac{1}{2}\bar{\eth}^2\mathfrak{D}^{-1}\left[\frac{1}{4}\int_{-\infty}^{u} |\dot{h}|^2\, du - \left(\Psi_2 + \frac{1}{4}\dot{h}\bar{h}\right)\right],^{9} \tag{3.12}$$

where $\mathfrak{D}^{-1}$ is defined to map the $\ell \leq 1$ modes to zero. Equation (3.12) represents an infinite tower of balance laws: one for each point on the sphere or, alternatively, one for each spin-weight -2 spherical harmonic mode h_{lm}.

Numerically, however, we do not have access to the full past, i.e., $u \to -\infty$. Instead, we are restricted to some finite start time u_1. This truncation of the time integral in Eq. (3.12) will cause our computation of the right-hand side to differ from the limit $u_1 \to -\infty$ by an unknown angle-dependent constant. Additionally, there is another unknown angle-dependent discrepancy that arises because our numerical waveforms are not necessarily in the post-Newtonian Bondi frame, as required by Eq. (3.12). Consequently, when we compute the BMS strain J from the BMS balance laws as

$$J \equiv \frac{1}{2}\bar{\eth}^2\mathfrak{D}^{-1}\left[\frac{1}{4}\int_{u_1}^{u} |\dot{h}|^2\, du - \left(\Psi_2 + \frac{1}{4}\dot{h}\bar{h}\right)\right] + \alpha, \tag{3.13}$$

[9] The operator $\frac{1}{8}\bar{\eth}^2\mathfrak{D}^{-1}$ is equivalent to $\eth^{-2}$ on spin-weight 0 functions, but is in a form convenient for numerical evaluation.

we need to account for these angle-dependent shifts by including an unknown constant $\alpha \equiv \alpha(\theta, \phi)$. However, because we have access to both h, the asymptotic strain obtained from a numerical spacetime, and J, the strain computed from the BMS balance laws in Eq. (3.13), we may simply solve for α either by minimizing the L^2 norm of the difference between the two waveforms or by making the waveforms agree on the final time step of the simulation. We may then check the violation of the BMS balance laws in the numerical waveforms via

$$h - J = 0, \tag{3.14}$$

where, again, h is the strain output by numerical relativity and J is from Eq. (3.13), with α being the constant needed to make h and J agree on the simulation's final time step. We choose the final time step, rather than optimizing over all time steps, because this makes our comparison most accurate the farthest away from junk radiation. Equations (3.13) and (3.14) are then all that are needed to check the violation of the BMS balance laws.

As mentioned before, Eq. (3.3) can be used to break J into an energy flux term $J_{\mathcal{E}}$—the primary source of the displacement memory—and a more oscillatory term J_Ψ,

$$J_{\mathcal{E}} = \frac{1}{2}\bar{\eth}^2\mathfrak{D}^{-1}\left[\frac{1}{4}\int_{u_1}^{u} |\dot{h}|^2\, du\right] + \alpha, \tag{3.15a}$$

$$J_\Psi = \frac{1}{2}\bar{\eth}^2\mathfrak{D}^{-1}\left[-\left(\Psi_2 + \frac{1}{4}\dot{h}\bar{h}\right)\right]. \tag{3.15b}$$

The hypothesis we test below is that the SXS extrapolated strain waveforms contain only the primarily oscillatory piece J_Ψ, and one can simply compute and then add the energy flux piece $J_{\mathcal{E}}$ to obtain a waveform with the correct gravitational wave memory. If true, this procedure can then be performed for all of the numerical simulations in the public SXS catalog to substantially improve the extrapolated strain waveforms.

While Eqs. (3.13) and (3.14) are all that are needed to check the violation of the BMS balance laws, in [37] it was shown that J can be decomposed into four terms, which more directly relate to the various memory effects and prove useful when examining numerical waveforms. These terms are

$$J = J_m + J_{\mathcal{E}} + J_{\widehat{N}} + J_{\mathcal{J}}, \tag{3.16}$$

Table 3.2: The four contributions to J in terms of their parity, type of memory contribution, and interpretation in terms of more common quantities in general relativity.

Variable	Parity	Memory	Interpretation
J_m	Electric	Ordinary	Bondi mass aspect
$J_{\mathcal{E}}$	Electric	Null	Energy flux
$J_{\widehat{N}}$	Magnetic	Ordinary	Angular momentum aspect
$J_{\mathcal{J}}$	Magnetic	Null	Angular momentum flux

where

$$J_m = \frac{1}{2}\bar{\eth}^2\mathfrak{D}^{-1}m, \tag{3.17a}$$

$$J_{\mathcal{E}} = \frac{1}{2}\bar{\eth}^2\mathfrak{D}^{-1}\left[\frac{1}{4}\int_{u_1}^{u}|\dot{h}|^2\,du\right] + \alpha, \tag{3.17b}$$

$$J_{\widehat{N}} = \frac{1}{2}i\bar{\eth}^2\mathfrak{D}^{-1}D^{-2}\mathrm{Im}\left[\bar{\eth}\left(\partial_u\widehat{N}\right)\right], \tag{3.17c}$$

$$J_{\mathcal{J}} = \frac{1}{2}i\bar{\eth}^2\mathfrak{D}^{-1}D^{-2}\mathrm{Im}\left\{\frac{1}{8}\left[\eth\left(3h\bar{\eth}\dot{\bar{h}} - 3\dot{h}\bar{\eth}\bar{h} + \dot{\bar{h}}\bar{\eth}h - \bar{h}\bar{\eth}\dot{h}\right)\right]\right\}, \tag{3.17d}$$

and

$$m = -\mathrm{Re}\left[\Psi_2 + \frac{1}{4}\dot{h}\bar{h}\right], \tag{3.18a}$$

$$\widehat{N} = 2\Psi_1 - \frac{1}{4}\bar{h}\eth h - u\eth m - \frac{1}{8}\eth(h\bar{h}). \tag{3.18b}$$

The reason why we construct these contributions to J is because of their parity and type of memory contribution, which we list in Table 3.3. Note that one can eliminate the Ψ_1 term in Eq. (3.18b) by using one of the Bianchi identities for the Weyl scalars, which produces the relation

$$\dot{\Psi}_1 = -\frac{1}{2}\eth\Psi_2 + \frac{1}{4}\bar{h}\eth\dot{h}. \tag{3.19}$$

We now use these observables to examine whether the extrapolated strain waveforms actually capture all terms in Eq. (3.13) except $J_{\mathcal{E}}$. We do this by adding $J_{\mathcal{E}}$ and checking the violation of the BMS balance laws, Eq. (3.14), and comparing to CCE waveforms that already capture the gravitational memory effects.

3.4 Results

For the following results, we numerically evolved a set of 13 binary black hole (BBH) mergers with various mass ratios and spin configurations using the Spectral Einstein Code (SpEC) [41]. We list the parameters of these evolved BBH systems in Table 3.6. Each BBH simulation contains roughly 19 orbits prior to merger and is evolved until the gravitational waves from ringdown leave the domain. Unlike evolutions in the SXS catalog, the full set of Weyl scalars and the strain have been extracted from these runs and the asymptotic waveforms have been computed using both the extrapolation technique described in [29] and the CCE procedure described in [30, 31]. Extrapolation is performed using the python module `scri` [42–45] and CCE is performed using SpECTRE's CCE code [30–32]. For the CCE extractions, the four world tube radii are chosen to be equally spaced between $2\lambda\!\!\!^{-}_0$ and $21\lambda\!\!\!^{-}_0$, where $\lambda\!\!\!^{-}_0 = 1/\omega_0$ is the initial reduced gravitational wavelength as determined by the orbital frequency of the binary from the initial data. These 13 waveforms will be made publicly available in the SXS catalog [33].

As mentioned above, our asymptotic strain waveforms are computed using two methods: extrapolation and CCE. The first method uses Regge-Wheeler-Zerilli (RWZ) extraction to compute the strain on a series of concentric spheres of constant coordinate radius and then extrapolates these values to future null infinity using $1/r$ approximations [28, 29, 34, 46–48]. This is the strain that can be found in the SXS catalog. The other and more faithful extraction method, known as CCE, computes the strain by using the world tube data provided by a Cauchy evolution as the inner boundary data for a nonlinear evolution of the Einstein field equations on null hypersurfaces [30, 31]. CCE requires freely specifying the strain on the initial null hypersurface labeled $u = 0$. Like [37], we choose this field to match the value and the first radial derivative of h from the Cauchy data on the world tube, using the ansatz,

$$h(u = 0, r, \theta^A) = \frac{A(\theta^A)}{r} + \frac{B(\theta^A)}{r^3}, \tag{3.20}$$

where the two coefficients $A(\theta^A)$ and $B(\theta^A)$ are fixed by the Cauchy data on the world tube. Note that constructing a satisfactory initial null hypersurface for CCE is currently an open problem in numerical relativity. Consequences of this choice manifest as transient effects appearing at early times [37]. This hypersurface choice also determines the Bondi frame of the resulting asymptotic waveform.

As a result of these junklike transient effects in the CCE waveforms, we cannot expect

our extrapolated and CCE waveforms to be in the exact same Bondi frame. Two strain waveforms from the same physical system but in different Bondi frames have infinite degrees of freedom relating them. Therefore, it is only meaningful to compare waveforms if they are in the same Bondi frame. Fortunately, we can numerically apply a BMS transformation to our waveforms until they are in approximately the same Bondi frame [44]. Thus, for any comparisons between extrapolated and CCE waveforms we use an optimization to find the supertranslation that minimizes the L^2 norm[10] of the difference of the two strains. For this optimization, the $\ell \leq 2$ modes of the supertranslation are free parameters, while the $\ell > 2$ modes are set to zero since their inclusion tends to produce negligible changes.[11]

Last, we note that both our extrapolated and CCE waveforms have been post-processed so that they are approximately in the center-of-mass frame [49].

3.4.1 Issues with Extrapolated Waveforms

We first illustrate the extrapolated waveforms' inability to capture the energy flux term $J_{\mathcal{E}}$ in comparison to CCE and the strain from the BMS balance laws. As shown in the top panel of Fig. 3.4.1, the extrapolated strain waveform's $(2,0)$ mode is constant except for quasinormal mode oscillations near merger and ringdown. However, the strain that is computed from the BMS balance laws J not only contains these quasinormal mode oscillations, but also a contribution from the growth of the memory. Further, the bottom panel of Fig. 3.4.1 shows that the displacement memory contribution to J predominantly comes from the energy flux term $J_{\mathcal{E}}$. The dominance of $J_{\mathcal{E}}$ should not come as a surprise since it has been shown that the ordinary contributions to the displacement memory, J_m and $J_{\widehat{N}}$, should be negligible for BBH mergers [27, 50], and the contribution from $J_{\mathcal{J}}$ should be zero at late times since the news vanishes for Kerr spacetimes. What is perhaps surprising, though, is that the BMS balance law strain J that we compute from the extrapolated waveform is nearly identical to the CCE strain. We explore this comparison between extrapolated and CCE waveforms more thoroughly in Sec. 3.4.2.3. Note that for the plot in Fig. 3.4.1 and all of the following plots we take u_{peak} to be the time at which the L^2 norm of the extrapolated strain achieves its maximum value.

[10] Recall that the L^2 norm of a function $h(\Omega)$ is given by

$$||h(\Omega)|| \equiv \int |h(\Omega)|^2 d\Omega. \tag{3.21}$$

[11] This is because most of the transient effects that are present in CCE waveforms, which are the main causes of the misalignment, primarily manifest in the $\ell = 2$ modes.

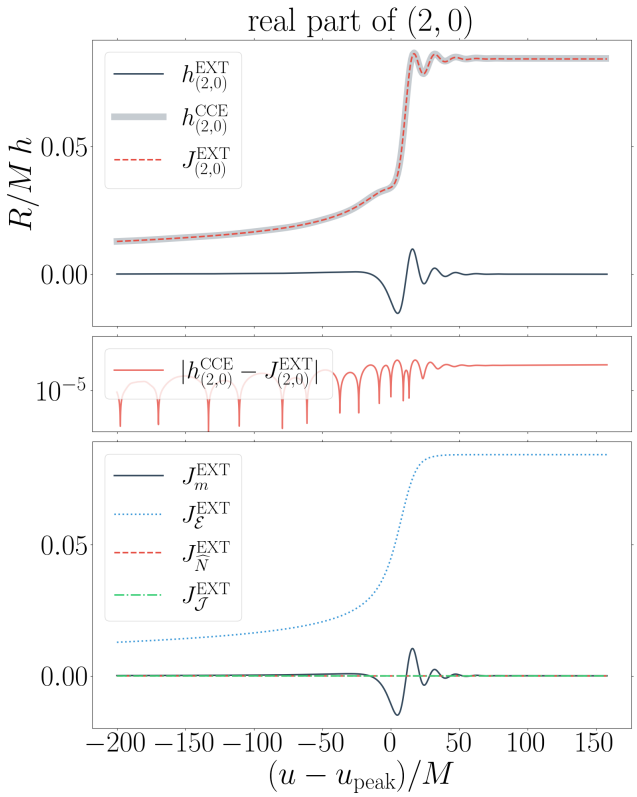

Figure 3.1: Comparison of the extrapolated strain $(2,0)$ mode ($h^{\rm EXT}$, black/solid) to the strain that is extracted using CCE ($h^{\rm CCE}$, gray/solid) and to what is expected according to the other modes of the extrapolated waveform using the various BMS balance laws ($J^{\rm EXT}$, red/dashed) computed by using the extrapolated waveform in Eq. (3.17). We take the news to be the retarded time derivative of the strain. In the middle panel, we plot the absolute error: $|h^{\rm CCE} - J^{\rm EXT}|$. In the bottom panel, we outline the individual contributions that come from the Bondi mass aspect (black/solid), the Bondi angular momentum aspect (red/dashed), the energy flux (blue/dotted), and the angular momentum flux (green/dashed/dotted).
BBH merger: `q1_nospin` (see Table 3.6).
CCE waveform: CCE-R0292 (with a supertranslation applied).

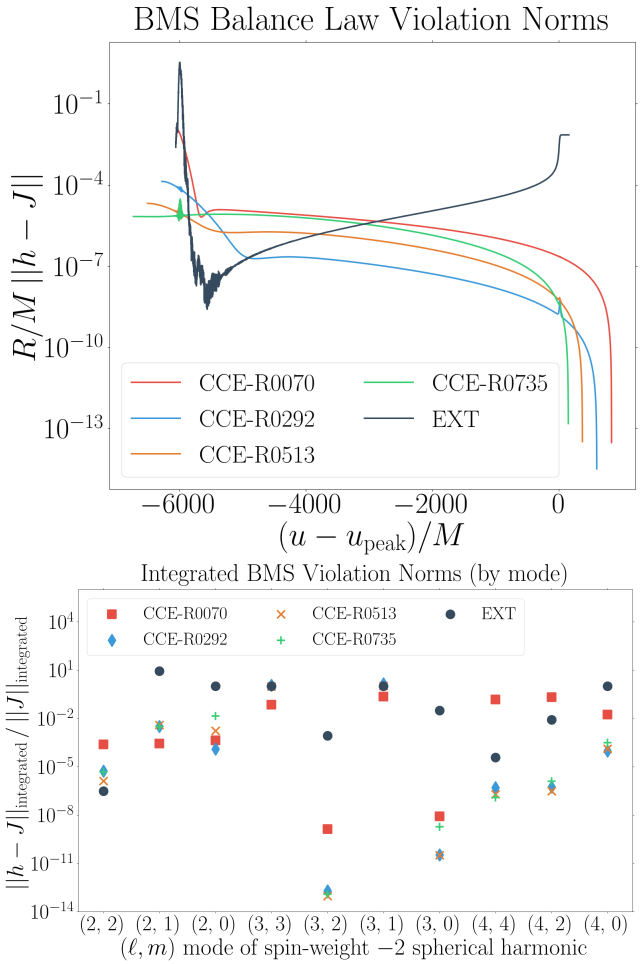

Figure 3.2: Violation of the BMS balance laws, Eq. (3.14), for extrapolated and CCE waveforms. In the top plot we show the norm of Eq. (3.14) over the two-sphere. Here J in Eq. (3.14) is computed by Eq. (3.13) and the Ψ_2 used in Eq. (3.13) for the extrapolated or CCE waveforms is extracted using the procedures described in [29] and [30, 31]. In the bottom plot we show the normalized time-integrated L^2 norm as a function of a few important spin-weight -2 spherical harmonic modes. Note that we integrate each of these modes by starting at one full orbit past the retarded time $u = 0\,M$ to suppress misleading effects that the Cauchy evolution junk radiation or the CCE transient effects may induce.
BBH merger: `q1_nospin` (see Table 3.6).

Because of the extrapolated waveforms' inability to capture the energy flux contribution, we expect their violation of the BMS balance laws, Eq. (3.14), to be much more significant than for waveforms extracted using CCE. In Fig. 3.4.1 we plot the violation of the BMS balance laws over the two-sphere (top plot) and as a function of certain modes (bottom plot) for the extrapolated waveforms and the CCE waveforms corresponding to the four available world tube extraction radii. The values that we plot in the bottom plot are the normalized time integrals of the BMS balance law violation from one full orbit past the retarded time $u = 0\,M$ onward. We exclude the first orbit to suppress misleading effects that the Cauchy evolution junk radiation or the CCE transient effects may induce [34, 37]. As can be seen in the top plot, the violation of the BMS balance laws by the extrapolated waveforms is roughly two orders of magnitude more than the worst-performing CCE waveform (R0070) and four orders of magnitude more than the best-performing CCE waveform (R0292). Moreover, in the bottom plot of Fig. 3.4.1, one can easily observe that sources of this violation are predominantly from the $m = 0$ primary memory modes, as is perhaps expected.

3.4.2 Correcting Extrapolated Waveforms

Having thoroughly described the problems with the extrapolated waveforms, we now discuss our method for "adding memory" to these waveforms. We then reevaluate their violation of the BMS balance laws and compare them to the CCE waveforms.

3.4.2.1 Adding Memory to Extrapolated Waveforms

As has been shown analytically in [27, 50] and also numerically in [37], the ordinary and magnetic contributions to the displacement memory should be negligible, if not vanish completely. In other words, the net change in the function J should be almost entirely sourced by $J_{\mathcal{E}}$, the energy flux contribution. In agreement with our hypothesis, Fig. 3.4.1 shows that the extrapolated waveform is indeed reasonably modeled by just the J_{Ψ} term, thereby implying that $J_{\mathcal{E}}$ provides the missing time evolution of the extrapolated strain. Consequently, since $J_{\mathcal{E}}$ is a function only of the news, we can recover the full time dependence of the displacement memory's growth.

Following the works of [37, 38], we now use Eq. (3.17b) to compute the time evolution of the displacement memory in the extrapolated strain. To avoid any memory effects that are induced by junk radiation, we do not time integrate the

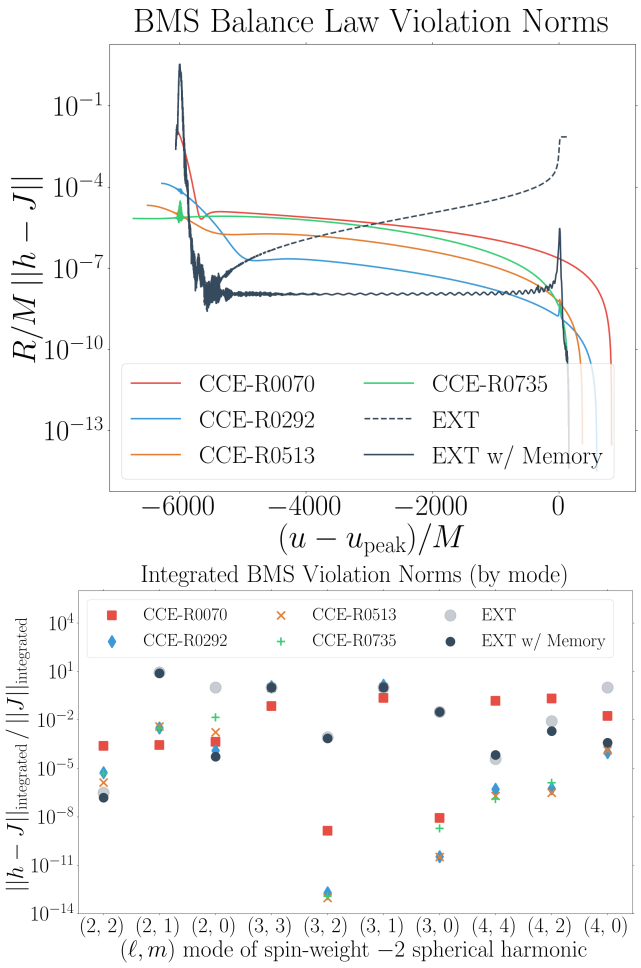

Figure 3.3: Identical to Fig. 3.4.1, but now with the violations for the memory-corrected extrapolated strain.
BBH merger: `q1_nospin` (see Table 3.6).

entire waveform. We instead take the lower limit u_1 to be half of one orbit past the retarded time $u = 0\,M$, which roughly matches up with the relaxation time, i.e., the time at which the junk radiation from the Cauchy evolution is considered to be negligible [34]. Unlike [38], after computing $J_{\mathcal{E}}$, we then add this contribution back to the strain to produce a more BMS-accurate waveform.

In Fig. 3.4.2.1 we show the violation of the BMS balance laws by the memory-corrected extrapolated strain over the two-sphere and as a function of certain modes. Again, the values that we plot in the bottom plot are the normalized time integrals of this violation from one full orbit past the retarded time $u = 0\,M$ onward. As expected, the overall violation of the BMS balance laws over the two-sphere improves by nearly four orders of magnitude, with the major improvements seen in the ℓ = even, $m = 0$

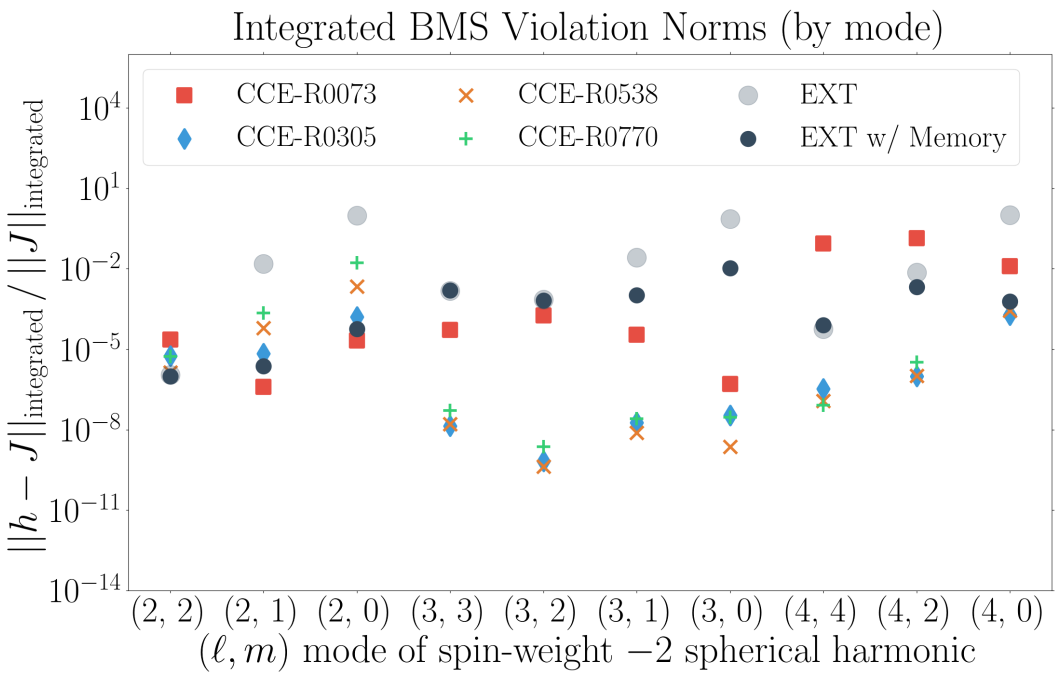

Figure 3.4: Identical to the bottom plot of Fig. 3.4.2.1, but now for an equal mass, precessing system.
BBH merger: `q1_precessing` (see Table 3.6).

memory modes, but also in unexpected modes, such as the $(2, 2)$ and $(4, 2)$ modes. For a precessing system, the improvement can be seen in many more modes, as shown in Fig. 3.4.2.1. We choose to show the results for the equal mass precessing system, rather than the $q = 4$ precessing system, because the memory is known to increase as the mass ratio approaches unity [37, 51]. We note that for evaluating the balance laws it is important to compute the BMS strain J from Eq. (3.13) rather than Eq. (3.17) since the Weyl scalar Ψ_1 tends to make extrapolated waveform computations of J noticeably worse, in terms of the balance law violation, because of spurious effects induced by junk radiation.

Figure 3.4.2.1 shows the time integral of the norm of the BMS balance law over the two-sphere for all the systems listed in Table 3.6, both before and after the memory corrections to the extrapolated strain waveforms. As can be seen, for every type of BBH merger that we present, the improvements to the extrapolated waveforms are quite considerable.

A few of the extrapolated waveforms in Fig. 3.4.2.1 seem to be better than the corresponding CCE waveforms. This is simply because our time-integration range

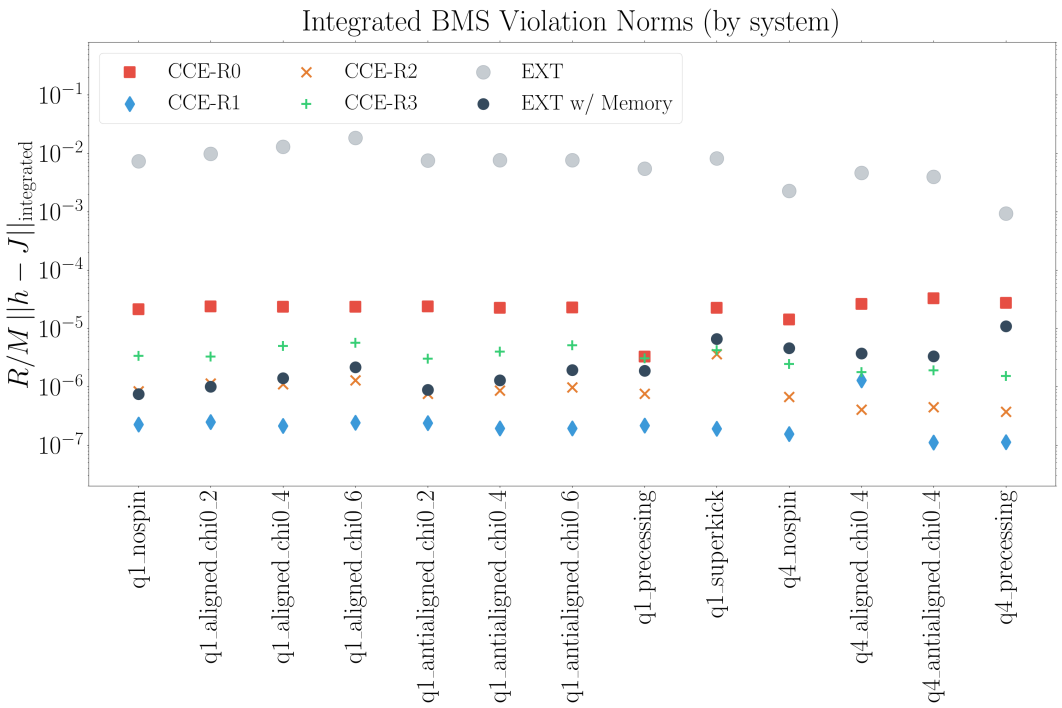

Figure 3.5: The time-integrated norm of the BMS balance law violation as a function of the BBH system. Integration is performed from one full orbit past the retarded time $u = 0\,M$ onward to avoid errors introduced by the Cauchy evolution junk radiation and most of the CCE transient effects. The labeling CCE-R[0,1,2,3] represents the four world tube radii (from smallest to largest). This plot demonstrates that the displacement memory can be effectively added to the extrapolated waveforms with the result satisfying the BMS balance laws to comparable accuracy as CCE. The parameters of these systems can be found in Table 3.6.

is chosen to ignore the Cauchy evolution's junk radiation completely, but not all of the longer-lasting transients caused by imperfect CCE initial null hypersurface data. If we instead choose u_1 to be later in the inspiral, then these CCE waveforms also outperform the corrected extrapolated waveforms. One can easily see this by comparing the violations for extrapolation and CCE around the time of merger in, for example, the top plot of Fig. 3.4.2.1.

3.4.2.2 Limitations of the Corrected Waveforms

As one may have noticed in the top plot of Fig. 3.4.2.1, while the overall violation of the BMS balance laws is improved by including the energy flux contribution, near merger the extrapolated waveforms' violation is much larger than that of the various CCE waveforms. The reason for this is that, while we have corrected the

extrapolated waveforms by adding just $J_{\mathcal{E}}$, we have done nothing regarding the magnetic terms $J_{\widehat{N}}$ and $J_{\mathcal{J}}$. These magnetic terms are, in part, the source of the spin memory effect when the strain is integrated with respect to retarded time [24, 26, 52]. The relevance of the magnetic component can be seen by noticing that the $(3,0)$, $(2,1)$, and $(3,2)$ modes—which are a few of the primary contributors to the spin memory—are the largest sources of the BMS balance law violation, even after the displacement memory correction is applied. (See, e.g., the bottom plot of Fig. 3.4.2.1.)

As has been shown previously [37], even though the extrapolated waveforms capture the spin memory effect—which we recall is a memory effect in the time integral of the strain—for some unknown reason the magnitude of the spin memory is roughly 50% of what it should be according to comparisons with the BMS balance laws and CCE waveforms. In Fig. 3.4.2.2, we compare the strain of the extrapolated waveform to the strain obtained from the BMS balance laws for the main spin memory mode: the imaginary part of the $(3,0)$ mode. As can readily be seen in the lower panel, the BMS strain is primarily sourced by the $J_{\widehat{N}}$ and $J_{\mathcal{J}}$ terms, with the contribution of $J_{\widehat{N}}$ representing the oscillatory part and the contribution of $J_{\mathcal{J}}$ representing the time derivative of the nonoscillatory spin memory. However, unlike the displacement memory mode, cf. Fig. 3.4.1, which is not present in the extrapolated waveforms, the top panel of Fig. 3.4.2.2 shows that there is a non-zero contribution to the time derivative of the spin memory. Consequently, without using the Weyl scalar Ψ_2, there is unfortunately no method to accurately correct the spin memory component of the extrapolated waveforms. While we could make this correction to our limited set of BBH simulations, we could not apply such a correction to the entire SXS catalog, since Ψ_2 has not been extracted for those simulations.

To provide a measurement of this subtle discrepancy, we compute the mismatch between the extrapolated strain with the memory correction and the BMS strain computed from the extrapolated waveform via

$$\mathcal{M}(u, h^{\mathrm{EXT}}_{\ell m}, J^{\mathrm{EXT}}_{\ell m}) \equiv 1 - \frac{\langle h^{\mathrm{EXT}}_{\ell m}, J^{\mathrm{EXT}}_{\ell m}\rangle}{\sqrt{\langle h^{\mathrm{EXT}}_{\ell m}, h^{\mathrm{EXT}}_{\ell m}\rangle \langle J^{\mathrm{EXT}}_{\ell m}, J^{\mathrm{EXT}}_{\ell m}\rangle}}, \tag{3.22}$$

where the inner product is given by

$$\langle h^{\mathrm{EXT}}_{\ell m}, J^{\mathrm{EXT}}_{\ell m}\rangle \equiv \int_{u_1}^{u} h^{\mathrm{EXT}}_{\ell m} \overline{J^{\mathrm{EXT}}_{\ell m}}\, du. \tag{3.23}$$

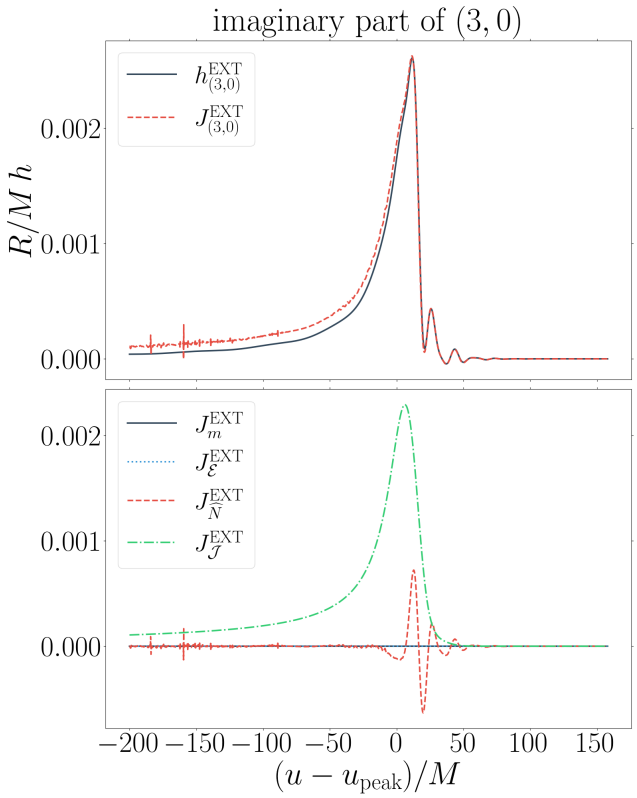

Figure 3.6: Comparison of the extrapolated strain $(3,0)$ mode ($h^{\rm EXT}$, black/solid) to the BMS strain that we compute using the terms in Eq. (3.17) ($J^{\rm EXT}$, red/dashed). In the bottom panel, we display the contributions that come from the Bondi mass aspect (black/solid), the Bondi angular momentum aspect (red/dashed), the energy flux (blue/dotted), and the angular momentum flux (green/dashed/dotted).
BBH merger: `q1_nospin` (see Table 3.6).

For an equal mass, non-spinning system the mismatches for the $(2,2)$, $(2,0)$, and $(3,0)$ modes are

$$\mathcal{M}(u_{\rm final}, h^{\rm EXT}_{(2,2)}, J^{\rm EXT}_{(2,2)}) = 6.84\times10^{-8}, \tag{3.24a}$$

$$\mathcal{M}(u_{\rm final}, h^{\rm EXT}_{(2,0)}, J^{\rm EXT}_{(2,0)}) = 2.43\times10^{-5}, \tag{3.24b}$$

$$\mathcal{M}(u_{\rm final}, h^{\rm EXT}_{(3,0)}, J^{\rm EXT}_{(3,0)}) = 1.36\times10^{-2}. \tag{3.24c}$$

Thus, we observe that the mismatch for the $(3,0)$ mode is considerably worse than the primary strain mode and the displacement memory mode. Nonetheless, despite the remaining problems with magnetic memory effects, it is clear that the physical accuracy of the extrapolated waveforms can be vastly improved by correcting the strain waveform via the addition of $J_{\mathcal{E}}$, as discussed above.

3.4.2.3 Comparisons with CCE

Finally, we compare our memory-corrected extrapolated waveforms to those of CCE. Figure 3.4.2.3 illustrates the mismatch between the memory-corrected extrapolated strain waveform and the CCE strain waveforms integrated over the two-sphere. Expressed differently, we plot

$$\mathcal{M}(u, h^{\mathrm{EXT}}, h^{\mathrm{CCE}}) \equiv 1 - \frac{\langle h^{\mathrm{EXT}}, h^{\mathrm{CCE}} \rangle}{\sqrt{\langle h^{\mathrm{EXT}}, h^{\mathrm{EXT}} \rangle \langle h^{\mathrm{CCE}}, h^{\mathrm{CCE}} \rangle}}, \tag{3.25}$$

where the inner product is given by

$$\langle h^{\mathrm{EXT}}, h^{\mathrm{CCE}} \rangle \equiv \int_{u_1}^{u} \int_{S^2} h^{\mathrm{EXT}} \overline{h^{\mathrm{CCE}}} \, d\Omega \, du. \tag{3.26}$$

Figure 3.4.2.3 shows the same mismatch but in the $(2,0)$ mode only, which is the primary displacement memory mode. For this figure, we compute the mismatch using Eq. (3.22), but with $J^{\mathrm{EXT}}_{\ell m}$ replaced by $h^{\mathrm{CCE}}_{\ell m}$ instead. Further, for the mode-by-mode comparison we use the CCE waveform corresponding to the second smallest extraction radius, since this waveform appears to be the most accurate in terms of the BMS balance laws. Recall that we also align the extrapolated and CCE waveforms by applying an $\ell \leq 2$ supertranslation to the CCE waveforms that minimizes the L^2 norm of the difference of the two strain waveforms. As can be seen in Fig. 3.4.2.3, the mismatch between the extrapolated and CCE waveforms is roughly the same for the unchanged and memory-corrected strains during the first 1000 M of the inspiral phase. But beyond this point, the mismatch between the waveforms is considerably better when using the memory-corrected extrapolated waveform. As expected, this improvement is primarily due to the smaller mismatch in the $\ell = \text{even}, m = 0$ modes, as shown for the $(2,0)$ mode in Fig. 3.4.2.3.

3.4.3 Measuring the Bondi Frame

Another important and useful aspect of the BMS group in numerical relativity is determining a BBH system's BMS frame.[12] The SXS catalog already provides waveforms that have a center-of-mass correction [34, 49]. Yet, just as space and time translation symmetries correspond to four-momentum, the symmetries of the supertranslations correspond to an infinite-dimensional group of conserved charges

[12] Generally the BMS frame refers to the asymptotic frame that is defined by all BMS freedoms, while the Bondi frame refers to the frame that is defined just by supertranslation freedoms.

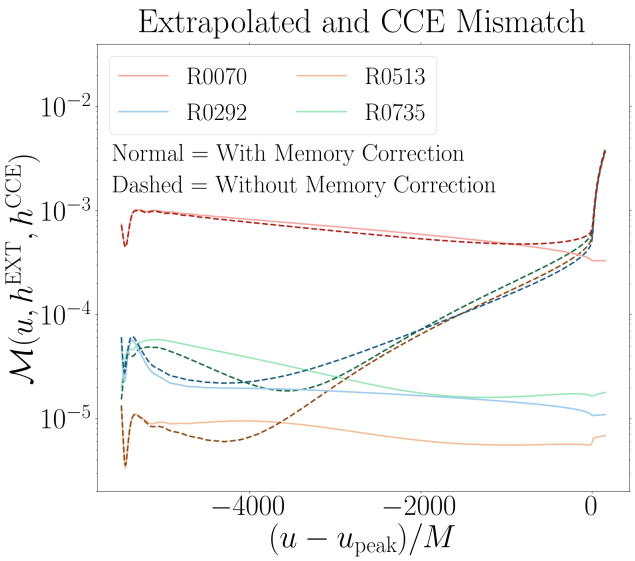

Figure 3.7: Mismatch between the extrapolated and CCE strains with (light/solid curves) and without (dark/dashed curves) the memory correction applied to the extrapolated strain. We compute the mismatch between the various waveforms according to Eq. (3.25). To improve the alignment between the extrapolated and CCE waveforms, we have applied an optimized $\ell \leq 2$ supertranslation to the CCE waveforms.
BBH merger: `q1_nospin` (see Table 3.6).

that are called the *supermomentum*. Further, analogous to how the four-momentum can be used to define a unique frame, such as the rest frame, up to an arbitrary spacetime translation, so can the supermomentum be used to define a unique Bondi frame up to some spacetime translation. This frame is known in the literature as the *nice section* or the *super rest frame*.

While there are many different constructions of the supermomentum [53–57], the one that corresponds to the Bondi frame of an asymptotic waveform is understood to be the Moreschi supermomentum [58],

$$\Psi^{\mathrm{M}}_{\ell m} \equiv -\frac{1}{\sqrt{4\pi}} \int_{S^2} Y_{\ell m} \left[\Psi_2 + \frac{1}{4} \dot{h} \bar{h} + \frac{1}{4} \eth^2 h \right] d\Omega, \tag{3.27}$$

where S^2 represents the two-sphere.

In Fig. 3.4.3, we plot the L^2 norm of the $\ell \geq 2$ modes of the Moreschi supermomentum for the various CCE waveforms and the extrapolated waveform, both with and without the memory correction, for the equal mass non-spinning system. We see from this plot that before the $J_{\mathcal{E}}$ contribution is added, i.e., the memory correction, the extrapolated waveform appears to be much closer to the super rest

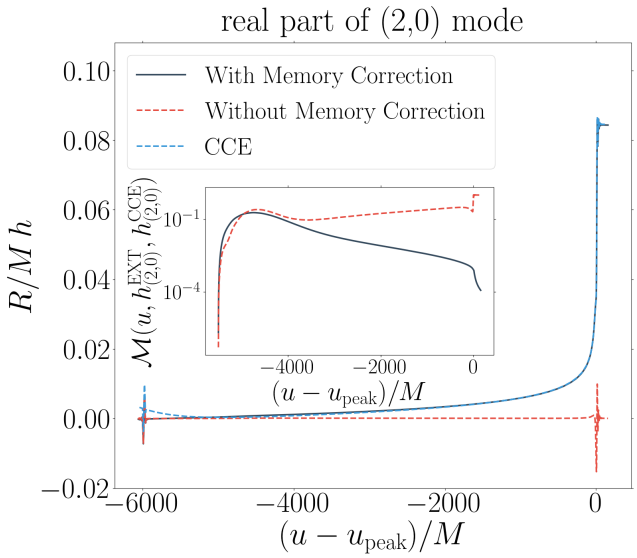

Figure 3.8: The strain $(2,0)$ mode for the CCE strain waveform (second smallest extraction radius) and the extrapolated strain waveform with and without the memory correction. In the inset panel, we plot the mismatch between the extrapolated and CCE strain waveforms for the same mode using Eq. (3.22). Further, to improve the alignment between the extrapolated and CCE waveforms, we have applied an $\ell \leq 2$ supertranslation to the CCE waveforms that minimizes the L^2 norm between the extrapolated and CCE waveforms. The negative slope in the CCE strain around $-6000\,M$ is an example of the junklike transient effects in CCE waveforms [37]. BBH merger: `q1_nospin` (see Table 3.6).

frame than the CCE waveforms. However, when the expected time evolution is included, the final Bondi frame of the extrapolated waveform is closer to the frames of the CCE waveforms from the three largest world tube radii. Consequently, we observe that correcting the extrapolated waveforms with displacement memory not only decreases the violation of the BMS balance laws and thus the accuracy of the waveforms, but also makes important changes to the Bondi frame. Were one to try to apply a "super rest correction," similar to that of a center-of-mass correction [49], it is critically important to use memory-corrected extrapolated strain waveforms, rather than the raw extrapolated strain waveforms in the SXS and other waveform catalogs.

3.5 Conclusion

Gravitational memory is a unique physical observable that occupies the low frequency range and will most likely be measured by a future gravitational wave detector, such as LIGO Voyager, the Einstein Telescope, or LISA. Consequently, it

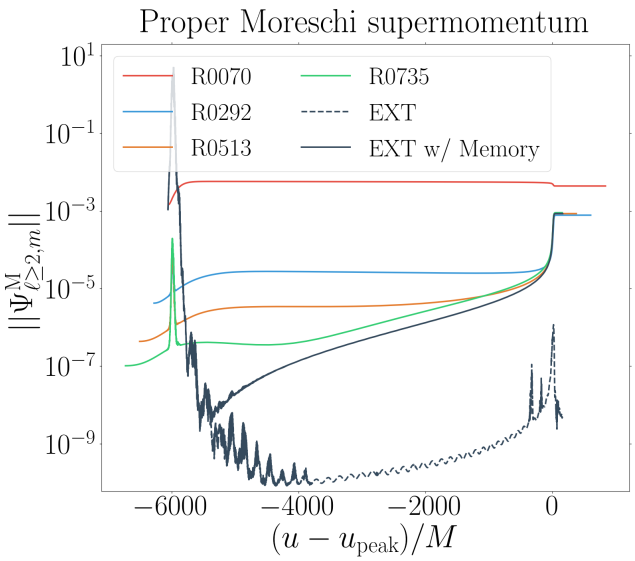

Figure 3.9: Norm of the proper Moreschi supermomentum, as defined by Eq. (3.27), for the extrapolated waveforms, both with and without memory corrections, and the CCE waveforms.
BBH merger: `q1_nospin` (see Table 3.6).

is imperative that the waveforms that are produced by numerical relativity include memory so that when such an effect is detected we can check for any discrepancies with general relativity. At present, however, while the waveforms produced by CCE exhibit memory, the many waveforms that are made publicly available in the SXS catalog [33, 34] and others [35, 36] do not. Throughout this paper, we have demonstrated that the SXS catalog's extrapolated waveforms can be corrected by adding the contribution to the displacement memory that is sourced by the system's energy flux.

We started by checking that the oscillatory J_Ψ contribution to the strain is indeed representative of the extrapolated strain waveform, as previously hypothesized. We then examined the BMS balance law violation both before and after applying our memory correction and found that adding the energy flux contribution improves the overall violation by roughly four orders of magnitude for 13 numerically evolved BBH systems that span a wide range of parameter space. After this, we noted that the main source of the remaining violation is from the time derivative of the spin memory contribution, which for an unknown reason is non-zero but is also not what is expected according to the BMS balance laws or by comparing to CCE waveforms. Finally, we showed that, besides satisfying the BMS balance laws, including the expected displacement memory also allows one to make a more

Name	q	$(\chi_A^{\hat{x}},$	$\chi_A^{\hat{y}},$	$\chi_A^{\hat{z}})$	$(\chi_B^{\hat{x}},$	$\chi_B^{\hat{y}},$	$\chi_B^{\hat{z}})$
q1_nospin	1.0	(0,	0,	0)	(0,	0,	0)
q1_aligned_chi0_2	1.0	(0,	0,	0.2)	(0,	0,	0.2)
q1_aligned_chi0_4	1.0	(0,	0,	0.4)	(0,	0,	0.4)
q1_aligned_chi0_6	1.0	(0,	0,	0.6)	(0,	0,	0.6)
q1_antialigned_chi0_2	1.0	(0,	0,	0.2)	(0,	0,	−0.2)
q1_antialigned_chi0_4	1.0	(0,	0,	0.4)	(0,	0,	−0.4)
q1_antialigned_chi0_6	1.0	(0,	0,	0.6)	(0,	0,	−0.6)
q1_precessing	1.0	(0.487,	0.125,	−0.327)	(−0.190,	0.051,	−0.227)
q1_superkick	1.0	(0.6,	0,	0)	(−0.6,	0,	0)
q4_nospin	4.0	(0,	0,	0)	(0,	0,	0)
q4_aligned_chi0_4	4.0	(0,	0,	0.4)	(0,	0,	0.4)
q4_antialigned_chi0_4	4.0	(0,	0,	0.4)	(0,	0,	−0.4)
q4_precessing	4.0	(0.487,	0.125,	−0.327)	(−0.190,	0.051,	−0.227)

Table 3.3: Parameters of the BBH mergers used in our results. The mass ratio is $q = M_A/M_B$, and the initial dimensionless spins of the two black holes are χ_A and χ_B.

correct measurement of the underlying system's BMS frame, which will prove vital for mapping waveforms to the super rest frame and making sure that waveforms computed by different methods are in the same frame.

3.6 Acknowledgments

We would like to thank Dennis Pollney for sharing data that was used in the early stages of this project. Computations were performed with the High Performance Computing Center and on the Wheeler cluster at Caltech, which is supported by the Sherman Fairchild Foundation and by Caltech. This work was supported in part by the Sherman Fairchild Foundation and by NSF Grants No. PHY-2011961, No. PHY-2011968, and No. OAC-1931266 at Caltech, NSF Grants No. PHY-1912081 and No. OAC- 1931280 at Cornell, and NSF Grant No. PHY-1806356, Grant No. UN2017-92945 from the Urania Stott Fund of the Pittsburgh Foundation, and the Eberly research funds of Penn State at Penn State.

References

[1] H. Bondi, M. G. J. Van der Burg, and A. W. K. Metzner, Proceedings of the Royal Society of London. Series A. Mathematical and Physical Sciences **269**, 21 (1962) 10.1098/rspa.1962.0161.

[2] R. K. : Sachs and H. Bondi, Proceedings of the Royal Society of London. Series A. Mathematical and Physical Sciences **270**, 103 (1962) 10.1098/rspa.1962.0206.

[3] J. de Boer and S. N. Solodukhin, Nuclear Physics B **665**, 545 (2003) 10.1016/s0550-3213(03)00494-2.

[4] T. Banks, *A critique of pure string theory: heterodox opinions of diverse dimensions*, 2003.

[5] G. Barnich and C. Troessaert, Physical Review Letters **105**, 10.1103/physrevlett.105.111103 (2010) 10.1103/physrevlett.105.111103.

[6] G. Barnich and C. Troessaert, PoS **CNCFG2010**, edited by K. N. Anagnostopoulos, D. Bahns, H. Grosse, N. Irges, and G. Zoupanos, 010 (2010) 10.22323/1.127.0010.

[7] G. Barnich and C. Troessaert, Journal of High Energy Physics **2011**, 10.1007/jhep12(2011)105 (2011) 10.1007/jhep12(2011)105.

[8] D. Kapec, V. Lysov, S. Pasterski, and A. Strominger, Journal of High Energy Physics **2014**, 10.1007/jhep08(2014)058 (2014) 10.1007/jhep08(2014)058.

[9] D. Kapec, P. Mitra, A.-M. Raclariu, and A. Strominger, Physical Review Letters **119**, 10.1103/physrevlett.119.121601 (2017) 10.1103/physrevlett.119.121601.

[10] T. He, D. Kapec, A. Raclariu, and A. Strominger, Journal of High Energy Physics **2017**, 10.1007/jhep08(2017)050 (2017) 10.1007/jhep08(2017)050.

[11] G. Barnich and P.-H. Lambert, Advances in Mathematical Physics **2012**, 1 (2012) 10.1155/2012/197385.

[12] É. É. Flanagan and D. A. Nichols, Physical Review D **95**, 10.1103/physrevd.95.044002 (2017) 10.1103/physrevd.95.044002.

[13] G. Compère, A. Fiorucci, and R. Ruzziconi, Journal of High Energy Physics **2018**, 10.1007/jhep11(2018)200 (2018) 10.1007/jhep11(2018)200.

[14] Y. B. Zel'dovich and A. G. Polnarev, Sov. Astron. **18**, 17 (1974).

[15] V. B. Braginsky and K. S. Thorne, Nature **327**, 123 (1987).

[16] D. Christodoulou, Phys. Rev. Lett. **67**, 1486 (1991) 10.1103/PhysRevLett.67.1486.

[17] K. S. Thorne, Phys. Rev. D **45**, 520 (1992) 10.1103/PhysRevD.45.520.

[18] M. Favata, Journal of Physics: Conference Series **154**, 012043 (2009) 10.1088/1742-6596/154/1/012043.

[19] M. Favata, The Astrophysical Journal **696**, L159 (2009) 10.1088/0004-637x/696/2/l159.

[20] M. Favata, Physical Review D **80**, 10.1103/physrevd.80.024002 (2009) 10.1103/physrevd.80.024002.

[21] M. Favata, Classical and Quantum Gravity **27**, 084036 (2010) 10.1088/0264-9381/27/8/084036.

[22] M. Favata, Phys. Rev. D **84**, 124013 (2011) 10.1103/PhysRevD.84.124013.

[23] A. Strominger and A. Zhiboedov, (2014).

[24] S. Pasterski, A. Strominger, and A. Zhiboedov, Journal of High Energy Physics **2016**, 10.1007/jhep12(2016)053 (2016) 10.1007/jhep12(2016)053.

[25] D. A. Nichols, Physical Review D **98**, 10.1103/physrevd.98.064032 (2018) 10.1103/physrevd.98.064032.

[26] G. Compère, R. Oliveri, and A. Seraj, Journal of High Energy Physics **2020**, 10.1007/jhep10(2020)116 (2020) 10.1007/jhep10(2020)116.

[27] A. Ashtekar, T. De Lorenzo, and N. Khera, Gen. Relativ. Gravit. (in press).

[28] M. Boyle and A. H. Mroué, Physical Review D **80**, 10.1103/physrevd.80.124045 (2009) 10.1103/physrevd.80.124045.

[29] D. A. B. Iozzo, M. Boyle, N. Deppe, J. Moxon, M. A. Scheel, L. E. Kidder, H. P. Pfeiffer, and S. A. Teukolsky, (2020).

[30] J. Moxon, M. A. Scheel, and S. A. Teukolsky, (2020).

[31] J. Moxon, N. Deppe, L. E. Kidder, G. Lovelace, K. Mitman, M. A. Scheel, S. Teukolsky, and W. Throwe, (In preparation).

[32] N. Deppe, W. Throwe, L. E. Kidder, N. L. Fischer, C. Armaza, G. S. Bonilla, F. Hébert, P. Kumar, G. Lovelace, J. Moxon, E. O'Shea, H. P. Pfeiffer, M. A. Scheel, S. A. Teukolsky, I. Anantpurkar, M. Boyle, F. Foucart, M. Giesler, D. A. B. Iozzo, I. Legred, D. Li, A. Macedo, D. Melchor, M. Morales, T. Ramirez, H. R. Rüter, J. Sanchez, S. Thomas, and T. Wlodarczyk, *SpECTRE*, version 2020.12.07, Dec. 2020, 10.5281/zenodo.4290405.

[33] *SXS Gravitational Waveform Database*, http://www.black-holes.org/waveforms.

[34] M. Boyle, D. Hemberger, D. A. B. Iozzo, G. Lovelace, S. Ossokine, H. P. Pfeiffer, M. A. Scheel, L. C. Stein, C. J. Woodford, A. B. Zimmerman, and et al., Classical and Quantum Gravity **36**, 195006 (2019) 10.1088/1361-6382/ab34e2.

[35] K. Jani, J. Healy, J. A. Clark, L. London, P. Laguna, and D. Shoemaker, Classical and Quantum Gravity **33**, 204001 (2016) 10.1088/0264-9381/33/20/204001.

[36] J. Healy, C. O. Lousto, Y. Zlochower, and M. Campanelli, Classical and Quantum Gravity **34**, 224001 (2017) 10.1088/1361-6382/aa91b1.

[37] K. Mitman, J. Moxon, M. A. Scheel, S. A. Teukolsky, M. Boyle, N. Deppe, L. E. Kidder, and W. Throwe, Phys. Rev. D **102**, 104007 (2020) 10.1103/PhysRevD.102.104007.

[38] C. Talbot, E. Thrane, P. D. Lasky, and F. Lin, Physical Review D **98**, 10.1103/physrevd.98.064031 (2018) 10.1103/physrevd.98.064031.

[39] M. Boyle, *Sxs-collaboration/sxs: release v2020.12.0*, version v2020.12.0, Dec. 2020, 10.5281/zenodo.4361521.

[40] E. Newman and R. Penrose, Journal of Mathematical Physics **3**, 566 (1962) 10.1063/1.1724257.

[41] https://www.black-holes.org/code/SpEC.html.

[42] M. Boyle, D. Iozzo, and L. C. Stein, *Moble/scri: v1.2*, version v1.2, Sept. 2020, 10.5281/zenodo.4041972.

[43] M. Boyle, Physical Review D **87**, 104006 (2013) 10.1103/PhysRevD.87.104006.

[44] M. Boyle, Phys. Rev. D **93**, 084031 (2016) 10.1103/PhysRevD.93.084031.

[45] M. Boyle, L. E. Kidder, S. Ossokine, and H. P. Pfeiffer, arXiv (2014).

[46] O. Sarbach and M. Tiglio, Physical Review D **64**, 084016 (2001) 10.1103/PhysRevD.64.084016.

[47] T. Regge and J. A. Wheeler, Physical Review **108**, 1063 (1957) 10.1103/PhysRev.108.1063.

[48] F. J. Zerilli, Physical Review Letters **24**, 737 (1970) 10.1103/PhysRevLett.24.737.

[49] C. J. Woodford, M. Boyle, and H. P. Pfeiffer, Phys. Rev. D **100**, 124010 (2019) 10.1103/PhysRevD.100.124010.

[50] A. Ashtekar, T. De Lorenzo, and N. Khera, Phys. Rev. D **101**, 044005 (2020) 10.1103/PhysRevD.101.044005.

[51] D. Pollney and C. Reisswig, The Astrophysical Journal **732**, L13 (2011) 10.1088/2041-8205/732/1/l13.

[52] D. A. Nichols, Physical Review D **95**, 10.1103/physrevd.95.084048 (2017) 10.1103/physrevd.95.084048.

[53] S. Dain and O. M. Moreschi, Classical and Quantum Gravity **17**, 3663 (2000) 10.1088/0264-9381/17/18/305.

[54] T. Dray and M. Streubel, Classical and Quantum Gravity **1**, 15 (1984) 10.1088/0264-9381/1/1/005.

[55] R. Geroch, "Asymptotic structure of space-time", in *Asymptotic structure of space-time*, edited by F. P. Esposito and L. Witten (Springer US, Boston, MA, 1977), pp. 1–105, 10.1007/978-1-4684-2343-3_1.

[56] R. Geroch and J. Winicour, Journal of Mathematical Physics **22**, 803 (1981) 10.1063/1.524987.

[57] A. Ashtekar and M. Streubel, Proceedings of the Royal Society of London. A. Mathematical and Physical Sciences **376**, 585 (1981).

[58] O. M. Moreschi, Classical and Quantum Gravity **21**, 5409 (2004) 10.1088/0264-9381/21/23/008.

Chapter 4

FIXING THE BMS FRAME OF NUMERICAL RELATIVITY WAVEFORMS

K. Mitman et al., Phys. Rev. D **104**, 024051 (2021) 10.1103/PhysRevD.104.024051,

4.1 Abstract

Understanding the Bondi-Metzner-Sachs (BMS) frame of the gravitational waves produced by numerical relativity is crucial for ensuring that analyses on such waveforms are performed properly. It is also important that models are built from waveforms in the same BMS frame. Up until now, however, the BMS frame of numerical waveforms has not been thoroughly examined, largely because the necessary tools have not existed. In this paper, we show how to analyze and map to a suitable BMS frame for numerical waveforms calculated with the Spectral Einstein Code (SpEC). However, the methods and tools that we present are general and can be applied to any numerical waveforms. We present an extensive study of 13 binary black hole systems that broadly span parameter space. From these simulations, we extract the strain and also the Weyl scalars using both SpECTRE's Cauchy-characteristic extraction module and also the standard extrapolation procedure with a displacement memory correction applied during postprocessing. First, we show that the current center-of-mass correction used to map these waveforms to the center-of-mass frame is not as effective as previously thought. Consequently, we also develop an improved correction that utilizes asymptotic Poincaré charges instead of a Newtonian center-of-mass trajectory. Next, we map our waveforms to the post-Newtonian (PN) BMS frame using a PN strain waveform. This helps us find the unique BMS transformation that minimizes the L^2 norm of the difference between the numerical and PN strain waveforms during the early inspiral phase. We find that once the waveforms are mapped to the PN BMS frame, they can be hybridized with a PN strain waveform much more effectively than if one used any of the previous alignment schemes, which only utilize the Poincaré transformations.

4.2 Introduction

As more and more astrophysical events are observed by gravitational wave detectors such as LIGO,[1] Virgo, and KAGRA,[2] accurate models of gravitational waves for these systems are indispensable for conducting precise parameter estimation as well as tests of general relativity. As of now, the most accurate models of gravitational waves are the waveforms from numerical relativity (NR) simulations, with the most prevalent being those that correspond to binary black hole (BBH) mergers [1–4].

Like any observable system in nature, however, the waveforms produced by numerical relativity simulations are functions of the frame that they are in. Currently, the Simulating eXtreme Spacetimes (SXS) Catalog [1]—the largest of the publicly available waveform catalogs—and the RIT Catalog [5] attempt to fix the Poincaré frame of their asymptotic waveforms by mapping them to the unique center-of-mass (CoM) frame through what they call a *center-of-mass correction* [1, 2, 5, 6].[3]

This correction—or this fixing of the Poincaré frame—uses the masses and the trajectories of the two black holes to construct the Newtonian center-of-mass trajectory

$$\vec{x}_{\rm CoM} \equiv \frac{m_a}{M}\vec{x}_a + \frac{m_b}{M}\vec{x}_b, \tag{4.1}$$

where m_a and m_b are the Christodoulou masses [7] of the primary and secondary black holes, $M \equiv m_a + m_b$ is the total initial mass of the BBH system, and $\vec{x}_a$ and $\vec{x}_b$ describe the motion of the black holes' centers, i.e., the simulation coordinate averages over each one of the black hole's apparent horizon. With this trajectory, the translation and boost that best map the system to the Newtonian center-of-mass frame can then be found by finding the transformation that minimizes the average square of the distance between the center-of-mass and the origin of the corrected frame [6].

While this method for fixing the Poincaré frame has proven useful, there are certain aspects of this correction that are concerning. For one, when more post-Newtonian (PN) terms are included in the Newtonian calculation of the center of mass in Eq. (4.1), the correction does not improve and, for higher mass-ratio or precessing systems, becomes noticeably worse [6]. Apart from this, it is also worrisome that

[1] The Laser Interferometer Gravitational-Wave Observatory.

[2] The Kamioka Gravitational Wave Detector.

[3] This fixing of the Poincaré frame was called a "correction" in the work of Ref. [6] because the BBH system's center-of-mass drift is an unexpected phenomenon in numerical relativity simulations. It appears to be related to an imperfect boundary condition on the gauge degrees of freedom at the outer boundary.

the frame of these waveforms is being fixed based on information from the bulk of spacetime, rather than information from the waveforms themselves, especially as it has been shown that the coordinate velocity of the black holes does not accurately correspond to the asymptotic velocity for complicated systems [8].

A better way to fix the Poincaré frame is to measure the Poincaré charges for asymptotic quantities and try to find the Poincaré transformation that changes these charges in a prescribed way. For example, to map a general relativistic system to the center-of-mass frame, one could compute the linear momentum charge and the boost charge from which the system's boost and translation away from the origin can be established. Or, as we will do in this work, one could instead compute just the center-of-mass charge and then determine which Poincaré transformation minimizes this charge.

Apart from the Poincaré frame, however, there is an additional freedom in general relativity arising from the extra symmetries of asymptotically flat spacetimes that extends the usual Poincaré group. This infinite group of symmetries, which was found by Bondi, van der Burg, Metzner, and Sachs [9, 10], is known as the *BMS group*.[4] Fundamentally, the BMS group is a semidirect product of the usual Lorentz group with an infinite-dimensional Abelian group of transformations called *supertranslations*, which contain the more familiar spacetime translations as a normal subgroup.

The most straightforward way to understand how a supertranslation affects coordinates is via the following. First define the Bondi time $u \equiv t - r$. Under an arbitrary spacetime translation $(\delta t, \delta\vec{x}) = (\delta t, \delta x, \delta y, \delta z)$, we can write the corresponding transformation of u as

$$u' = u - \sum_{\ell<2} \sum_{m\leq|\ell|} \alpha_{\ell m} Y_{\ell m}(\theta, \phi), \tag{4.2}$$

where

$$\alpha_{0,0} = \sqrt{4\pi}\delta t, \tag{4.3a}$$

$$\alpha_{1,\pm1} = -\sqrt{\frac{2\pi}{3}}(\mp\delta x + i\delta y), \tag{4.3b}$$

$$\alpha_{1,0} = -\sqrt{\frac{4\pi}{3}}\delta z. \tag{4.3c}$$

[4] There is also a proposed generalization of the BMS group, which promotes the Lorentz transformations to be the infinite group of local diffeomorphisms on S^2 [11, 12]. In this work, however, we will focus on just the BMS group and reserve an examination of the generalized BMS group for future study.

A proper supertranslation $\alpha(\theta, \phi)$, i.e., a supertranslation that is not one of the spacetime translations (see Eq. (4.2)), then acts on u as

$$u' = u - \alpha(\theta, \phi) \tag{4.4}$$

for

$$\alpha = \sum_{\ell \geq 2} \sum_{m \leq |\ell|} \alpha_{\ell m} Y_{\ell m}(\theta, \phi) \tag{4.5}$$

with $\alpha_{\ell,m} = (-1)^m \overline{\alpha}_{\ell,-m}$ to make sure that u' is real. Consequently, a supertranslation can be understood as a direction-dependent time translation on the boundary of asymptotically flat spacetimes, e.g., future null infinity. For example, if there exists a network of observers on a sphere surrounding a source, then ideally they could combine their received signals with some understanding of their clocks' synchronization. At future null infinity, such a synchronization becomes impossible and we could supply a separate time offset, i.e., a supertranslation, to each observer without changing the observable physics. An outline of how supertranslations transform the typical gravitational wave quantities, such as the strain h, the news $\dot{h}$, and the Weyl scalars Ψ_i, can be found in [13, 14].

There are really only two reasonable ways to fix this supertranslation freedom. The first, and simplest, is to find the supertranslation that minimizes the difference between a NR waveform and a PN waveform. The second, which is often the most common in the literature [15–17], can be understood as follows.

Like fixing the Poincaré frame by making use of the Poincaré charges, a fairly similar scheme can be executed to fix a BBH system's proper supertranslation freedom by utilizing the proper supertranslation charge. We refer to the frame that fixes this supertranslation freedom as the Bondi frame, while the frame that corresponds to fixing all of the freedom of our waveforms is called the BMS frame. Put differently, the BMS frame captures both the Poincaré and the proper supertranslation freedom, whereas the Bondi frame only involves the proper supertranslations. Just as the Bondi four-momentum is the charge that is related to spacetime translations, the *supermomentum*—an infinite extension of the usual Bondi four-momentum—is the charge that corresponds to supertranslations. Thus, the supertranslation freedom can also be uniquely fixed by finding the supertranslation that minimizes the proper supermomentum charge. The Bondi frame under this transformation is then related to the Poincaré frame that corresponds to the transformation that minimizes the

three-momentum, i.e., the rest frame. In this case, though, we call the Bondi frame with minimal[5] supermomentum the *nice section* [17] or the *super rest frame*.

In this work, we do exactly this. That is, we fix the Poincaré frame of our asymptotic waveforms by working with particular Poincaré charges to map the BBH systems to the center-of-mass frame. We then also fix the proper supertranslation freedom by finding the supertranslation that maps the waveforms to the Bondi frame that is ideal for current observations. Thus, we not only improve upon the work of [6] by using relativistic charges instead of Newtonian trajectories, but we also wholly fix the proper supertranslation freedom, thereby fixing the complete BMS frame of our numerical waveforms.

Most importantly, we find that the new and improved fixing of the Poincaré frame is a drastic improvement over the previous method that uses Newtonian trajectories. Based on our observations, we conclusively find that the previous center-of-mass correction appears to have only approximately worked for the equal mass nonspinning, aligned spins, and superkick systems, and fails for the nonequal mass, anti-aligned spins, or precessing systems. Further, even in the equal mass nonspinning systems where the previous correction was nearly the same as the charge-based one, this new method nonetheless shows obvious improvements, such as reducing the leakage of the strain $(2, 2)$ mode into other, subdominant strain modes. We show an example of this improvement in Fig. 4.5.1.3.

Apart from improving the fixing of the Poincaré frame, we also make a few important observations regarding the fixing of the supertranslation freedom. Even though it is often mentioned that the supertranslation freedom can be fixed by mapping to the super rest frame [15–17], we find that the most practical way to fix the supertranslations is by mapping our BBH systems to the PN Bondi frame. This is because LIGO expects numerical waveforms to agree with PN waveforms during the early inspiral phase of a BBH merger. Note, however, that for conducting any kind of analyses on quasinormal modes, the preferred BMS frame is actually the super rest frame, since this is the frame expected by the Teukolsky formalism.[6]

Previously, the BMS freedom of numerical waveforms has not been important because the SXS Collaboration's waveforms did not exhibit the displacement memory [18]. However, because waveforms with memory effects can now be easily

[5]The reason we say minimal rather than no supermomentum is because of a subtlety having to do with gravitational memory, which we discuss in the Appendix 4.A.

[6]This will be covered in a future work.

produced by numerical relativity [18] or can even have memory effects added to them via a correction [19], fixing this Bondi frame has become crucial, seeing as it is absolutely necessary for performing hybridizations between numerical and PN strain waveforms. We find that by mapping numerical waveforms to the PN BMS frame, we can significantly improve NR/PN strain hybridizations. Our main result regarding this is shown in Fig. 4.5.2.

Last, we also discover that by completely fixing the BMS frame of our waveforms, we can perform noticeably better convergence tests of numerical relativity waveforms, since waveforms from different resolutions can now be compared while in the same BMS frame.

4.2.1 Overview

We organize our computations and results as follows.

In Sec. 4.3 we introduce the four main Poincaré charges that are useful when examining asymptotic waveforms: the linear momentum, angular momentum, boost, and center-of-mass charges. Apart from this, we also discuss how the center-of-mass charge can be used to obtain the system's velocity and translation away from the origin. Following this, in Sec. 4.4 we discuss the two most natural Bondi frames and conclude that for practical purposes, the most useful frame to map to is the PN Bondi frame. Finally, in Secs. 4.5.1 and 4.5.2 we present our results for mapping to the center-of-mass frame as well as the PN BMS frame and thus illustrate how the BMS frame of numerical waveforms should be fixed for future analyses and, most importantly, future surrogate models [20–23].

4.2.2 Conventions

We set $c = G = 1$ and take $\eta_{\mu\nu}$ to be the $(-,+,+,+)$ Minkowski metric. When working with complex dyads, following the work of [24], we use

$$q_A = -\frac{1}{\sqrt{2}}(1, i\sin\theta) \text{ and } q^A = -\frac{1}{\sqrt{2}}(1, i\csc\theta), \tag{4.6}$$

and write the round metric on the two-sphere S^2 as q_{AB}. The complex dyad obeys the following properties

$$q_A q^A = 0, \quad q_A \bar{q}^A = 1, \quad q_{AB} = q_A \bar{q}_B + \bar{q}_A q_B. \tag{4.7}$$

Note that this convention differs from the related works of [18, 19, 25], which in contrast do not include the $1/\sqrt{2}$ normalization factor on the dyads in Eq. (4.6).

We choose this convention because it makes our expressions for the asymptotic charges in Eq. (4.15) more uniform. Nonetheless, for transparency we provide the conversion between our quantities and those of these previous works in Eq. (4.13). We build spin-weighted fields with the dyads as follows. For a tensor field $W_{A\cdots D}$, the function

$$W = W_{A\cdots BC\cdots D} q^A \cdots q^B \bar{q}^C \cdots \bar{q}^D \tag{4.8}$$

with m factors of q and n factors of $\bar{q}$ has a spin weight of $s = m - n$. When raising and lowering spin weights we use the Geroch-Held-Penrose differential spin-weight operators $\eth$ and $\bar{\eth}$ [26],

$$\eth W = (D_E W_{A\cdots BC\cdots D}) q^A \cdots q^B \bar{q}^C \cdots \bar{q}^D q^E, \tag{4.9a}$$

$$\bar{\eth} W = (D_E W_{A\cdots BC\cdots D}) q^A \cdots q^B \bar{q}^C \ldots \bar{q}^D \bar{q}^E. \tag{4.9b}$$

Here, D_A is the covariant derivative on the two-sphere. The $\eth$ and $\bar{\eth}$ operators in spherical coordinates are then

$$\eth W(\theta,\phi) = -\frac{1}{\sqrt{2}} (\sin\theta)^{+s} (\partial_\theta + i \csc\theta \partial_\phi) \left[(\sin\theta)^{-s} W(\theta,\phi) \right], \tag{4.10a}$$

$$\bar{\eth} W(\theta,\phi) = -\frac{1}{\sqrt{2}} (\sin\theta)^{-s} (\partial_\theta - i \csc\theta \partial_\phi) \left[(\sin\theta)^{+s} W(\theta,\phi) \right]. \tag{4.10b}$$

Thus, when acting on spin-weighted spherical harmonics, these operators produce

$$\eth ({}_sY_{\ell m}) = +\frac{1}{\sqrt{2}} \sqrt{(\ell - s)(\ell + s + 1)}\, {}_{s+1}Y_{\ell m}, \tag{4.11a}$$

$$\bar{\eth} ({}_sY_{\ell m}) = -\frac{1}{\sqrt{2}} \sqrt{(\ell + s)(\ell - s + 1)}\, {}_{s-1}Y_{\ell m}. \tag{4.11b}$$

We denote the gravitational wave strain[7] by h, which we represent in a spin-weight -2 spherical harmonic basis,

$$h(u,\theta,\phi) = \sum_{\ell,m} h_{\ell m}(u)\, {}_{-2}Y_{\ell m}(\theta,\phi), \tag{4.12}$$

[7] We explicitly define the strain as described in Appendix C of [2].

where, again, $u \equiv t - r$ is the Bondi time. We denote the Weyl scalars by Ψ_{0-4}. The conversion from the convention of [18, 19, 25] (denoted NR[8]) to ours (denoted MB[9]) is

$$h^{\mathrm{NR}} = 2\bar{\sigma}^{\mathrm{MB}} \quad \text{and} \quad \Psi_i^{\mathrm{NR}} = \frac{1}{2}(-\sqrt{2})^i \Psi_i^{\mathrm{MB}}. \tag{4.13}$$

Note that we will omit these superscripts and henceforth assume that everything is in the MB convention.

4.3 Fixing the $\ell < 2$ Transformations

As discussed in the Introduction, for the past few years the method for fixing the Poincaré frame of BBH systems in numerical relativity has relied on using the Newtonian center-of-mass trajectory, i.e., Eq. (4.1) [2, 5, 6]. While this has served as a successful first step, we can improve upon this by using certain Poincaré charges: specifically, the center-of-mass charge.

We first present the main asymptotic Poincaré charges. These charges are the linear momentum charge P_Ψ, the angular momentum charge J_Ψ, the boost charge K_Ψ, and the energy moment charge E_Ψ. Others have just called E_Ψ the center-of-mass charge, but this is misleading because E_Ψ really measures the center of mass scaled by the energy of the system. Thus, we instead refer to E_Ψ as the energy moment charge and reserve G_Ψ to represent the center-of-mass charge. These charges are computed by integrating the Bondi mass aspect m, the Lorentz aspect N, and the energy moment aspect E, which are derived in the NR convention in Appendixes A and B of [18]. In the MB convention these are

$$m \equiv -\mathrm{Re}\left[\Psi_2 + \sigma\dot{\bar{\sigma}}\right], \tag{4.14a}$$

$$N \equiv -\left(\Psi_1 + \sigma\eth\bar{\sigma} + u\eth m + \frac{1}{2}\eth\left(\sigma\bar{\sigma}\right)\right), \tag{4.14b}$$

$$E \equiv N + u\eth m = -\left(\Psi_1 + \sigma\eth\bar{\sigma} + \frac{1}{2}\eth\left(\sigma\bar{\sigma}\right)\right). \tag{4.14c}$$

[8] NR because this is the convention that corresponds to the outputs of the SXS simulations.

[9] MB because this corresponds to the Moreschi-Boyle convention used in the works [13, 24, 27] and the code `scri` [13, 28–30].

Consequently, the main Poincaré charges are

$$P_\Psi = \frac{1}{4\pi}\int_{S^2} \Psi\, m\, d\Omega, \tag{4.15a}$$

$$\begin{aligned} J_\Psi &\equiv \frac{1}{4\pi}\int_{S^2} \epsilon^{AB}\,(\partial_A\Psi)\,(\bar{q}_B N)\; d\Omega, \\ &= \frac{1}{4\pi}\int_{S^2} \mathrm{Re}\left[\left(\bar{\eth}\Psi\right)(-iN)\right]\; d\Omega, \end{aligned} \tag{4.15b}$$

$$\begin{aligned} K_\Psi &\equiv \frac{1}{4\pi}\int_{S^2} q^{AB}\,(\partial_A\Psi)\,(\bar{q}_B N)\; d\Omega, \\ &= \frac{1}{4\pi}\int_{S^2} \mathrm{Re}\left[\left(\bar{\eth}\Psi\right)N\right]\; d\Omega, \end{aligned} \tag{4.15c}$$

$$\begin{aligned} E_\Psi &\equiv \frac{1}{4\pi}\int_{S^2} q^{AB}\,(\partial_A\Psi)\,(\bar{q}_B\,(N+u\eth m))\; d\Omega, \\ &= \frac{1}{4\pi}\int_{S^2} \mathrm{Re}\left[\left(\bar{\eth}\Psi\right)(N+u\eth m)\right]\; d\Omega, \\ &= K_\Psi + uP_\Psi. \end{aligned} \tag{4.15d}$$

where ϵ^{AB} is the usual Levi-Civita tensor and Ψ is a real spin-weight 0 function on the two-sphere. This scalar Ψ is typically taken to be a unique combination of the $\ell \leq 1$ spherical harmonics so as to represent one of the four Cartesian coordinates t, x, y, z, i.e.,

$$\begin{aligned} t &= 1 \\ &= \sqrt{4\pi}Y_{(0,0)}, \end{aligned} \tag{4.16a}$$

$$\begin{aligned} x &= \sin\theta\cos\phi \\ &= \sqrt{\frac{4\pi}{3}}\left[\frac{1}{\sqrt{2}}\left(Y_{(1,-1)} - Y_{(1,+1)}\right)\right], \end{aligned} \tag{4.16b}$$

$$\begin{aligned} y &= \sin\theta\sin\phi \\ &= \sqrt{\frac{4\pi}{3}}\left[\frac{i}{\sqrt{2}}\left(Y_{(1,-1)} + Y_{(1,+1)}\right)\right], \end{aligned} \tag{4.16c}$$

$$\begin{aligned} z &= \cos\theta \\ &= \sqrt{\frac{4\pi}{3}}Y_{(1,0)}. \end{aligned} \tag{4.16d}$$

By utilizing some properties of the spherical harmonics, we can create a four-vector

from the projection of a charge along each Cartesian direction:

$$A^t = \frac{1}{\sqrt{4\pi}} A_{(0,0)}, \tag{4.17a}$$

$$A^x = \frac{1}{\sqrt{4\pi}} \frac{1}{\sqrt{6}} \mathrm{Re}\left[A_{(1,-1)} - A_{(1,+1)}\right], \tag{4.17b}$$

$$A^y = \frac{1}{\sqrt{4\pi}} \frac{1}{\sqrt{6}} \mathrm{Im}\left[A_{(1,-1)} + A_{(1,+1)}\right], \tag{4.17c}$$

$$A^z = \frac{1}{\sqrt{4\pi}} \frac{1}{\sqrt{3}} \mathrm{Re}\left[A_{(1,0)}\right], \tag{4.17d}$$

where $A_{(\ell,m)}$ is the (ℓ, m) mode of the aspect A when A is written in a spin-weight 0 or 1 spherical harmonic basis.[10] Note that all of these charges and aspects, which we have defined in Eq. (4.15), have been previously examined in earlier works such as [18, 31–34].

As mentioned in the introduction of this section, we are primarily interested in the center-of-mass charge G_Ψ, which is closely related to the energy moment charge E_Ψ in Eq. (4.15d). By definition, the center-of-mass charge is the energy moment divided by the energy of the system,

$$G_\Psi \equiv \frac{E_\Psi}{P^t} = \frac{E_\Psi}{\gamma M_B}, \tag{4.18}$$

where P^t is computed according to Eq. (4.17a) with $A = m$, γ is the Lorentz factor

$$\gamma = \sqrt{1 - \left|\vec{P}/P^t\right|^2}^{-1}, \tag{4.19}$$

and M_B is the Bondi mass [9]

$$M_B \equiv \sqrt{-\eta_{\mu\nu} P^\mu P^\nu}. \tag{4.20}$$

The charge G_Ψ measures the center of mass that evolves linearly as a function of momentum in the absence of gravitational radiation [34]. The reason why we are mainly interested in this Poincaré charge is because

$$\vec{G}|_{u=0} = \left(\vec{K}/\gamma M_B\right)|_{u=0}, \tag{4.21a}$$

$$\begin{aligned}
\dot{\vec{G}} &= \dot{u}\left[\left(\vec{K} + u\vec{P}\right)/(\gamma M_B)\right] \\
&= \vec{v} + u\dot{\vec{v}} - \frac{\vec{K}}{\gamma M_B}\left[\frac{\dot{M}_B}{M_B} - \gamma^2\left(\vec{v}\cdot\dot{\vec{v}}\right)\right] + \frac{\dot{\vec{K}}}{\gamma M_B} \\
&\approx \vec{v} + (\text{oscillations about } \vec{v}),
\end{aligned} \tag{4.21b}$$

[10] Note that $A = m$ is a spin-weight 0 function and $A = -iN$, N, and $N + u\eth m$ are spin-weight 1 functions.

since

$$\dot{M}_B \approx 0, \quad \dot{\vec{v}} \approx 0, \quad \text{and} \quad \dot{\vec{K}} \approx 0, \tag{4.22}$$

in the inspiral and ringdown phases of the BBH merger.[11] Therefore, the intercept of $\vec{G} \equiv (E^x, E^y, E^z)/P^t$ will be the center of mass of the system at $u = 0$ and the slope will be the three-velocity. This means that by fitting a degree one polynomial to this three-vector, we can obtain the amount a system is translated and boosted out of the center-of-mass frame and then apply the opposite Poincaré transformation to map our waveforms to the center-of-mass frame.[12] Note that these Poincaré charges in Eq. (4.15) can also be used to measure properties of the BBH system or the remnant black hole, as was illustrated in the recent and related work of [8].

4.4 Fixing the $\ell \geq 2$ Transformations

We now move on to a discussion about the proper supertranslation freedom.

4.4.1 Mapping to the super rest frame

While it is often mentioned that a system's Bondi frame should be fixed by minimizing the supermomentum [16],
current observatories expect their waveform models to resemble PN expansions. Therefore, even though fixing a system's Bondi frame using the supermomentum is a well-motivated option with unique benefits, we reserve a discussion of this for Appendix 4.A, since none of the results that we present involve this technique.

4.4.2 Mapping to the PN BMS frame

Besides using the supermomentum to map a system to its super rest frame, the supertranslation freedom of waveforms can also be fixed by mapping them to their corresponding PN Bondi frame. Unlike PN waveforms, the NR waveforms are finite in length and do not contain information from the BBH system's entire past history. As a result, when numerical strain waveforms that contain memory are created, either by using Cauchy-characteristic extraction (CCE) [18, 36] or by correcting extrapolated waveforms [19], their average during the inspiral phase will tend to be close to zero. By contrast, post-Newtonian waveforms typically have a memory contribution that is monotonically increasing with time and only approaches zero as

[11] We address issues with this assumption in Sec. 4.5.1.

[12] While we could also use the boost and linear momentum charges to obtain these transformations, computing both of these charges is more computationally expensive than if we just compute the center-of-mass charge, since there are fewer products of waveforms that need to be taken when finding $G\Psi$.

Name	q	$(\chi_A^{\hat{x}}$,	$\chi_A^{\hat{y}}$,	$\chi_A^{\hat{z}})$	$(\chi_B^{\hat{x}}$,	$\chi_B^{\hat{y}}$	$\chi_B^{\hat{z}})$
q1_nospin	1.0	(0,	0,	0)	(0,	0,	0)
q1_aligned_chi0_2	1.0	(0,	0,	0.2)	(0,	0,	0.2)
q1_aligned_chi0_4	1.0	(0,	0,	0.4)	(0,	0,	0.4)
q1_aligned_chi0_6	1.0	(0,	0,	0.6)	(0,	0,	0.6)
q1_antialigned_chi0_2	1.0	(0,	0,	0.2)	(0,	0,	−0.2)
q1_antialigned_chi0_4	1.0	(0,	0,	0.4)	(0,	0,	−0.4)
q1_antialigned_chi0_6	1.0	(0,	0,	0.6)	(0,	0,	−0.6)
q1_precessing	1.0	(0.487,	0.125,	−0.327)	(−0.190,	0.051,	−0.227)
q1_superkick	1.0	(0.6,	0,	0)	(−0.6,	0,	0)
q4_nospin	4.0	(0,	0,	0)	(0,	0,	0)
q4_aligned_chi0_4	4.0	(0,	0,	0.4)	(0,	0,	0.4)
q4_antialigned_chi0_4	4.0	(0,	0,	0.4)	(0,	0,	−0.4)
q4_precessing	4.0	(0.487,	0.125,	−0.327)	(−0.190,	0.051,	−0.227)

Table 4.1: Parameters of the BBH mergers used in our results. The mass ratio is $q = M_A/M_B$, and the initial dimensionless spins of the two black holes are χ_A and χ_B. These simulations have been made publicly available at [35].

$u \to -\infty$. Therefore, if hybridizations of the numerical waveforms are to be made with PN waveforms, a mapping to the PN Bondi frame is essential to ensure that the waveforms and their memory contributions can be properly aligned. While we examined the results of mapping our systems to the super rest frame, we find that, because of this hybridization concern, mapping to the PN Bondi frame is the more sensible procedure for fixing the Bondi frame. Consequently, in Sec. 4.5 we only present the results for mapping our various BBH systems to their corresponding PN BMS frame, as defined by a PN strain waveform, and reserve a study of the benefits of mapping to the super rest frame for future work.

4.5 Results

For the following results, we numerically evolved a set of 13 binary black hole mergers with various mass ratios and spin configurations using the Spectral Einstein Code (SpEC) [37]. We list the important parameters of these various BBH systems in Table 4.4.1. Each simulation contains roughly 19 orbits prior to merger and is evolved until the waves from ringdown leave the computational domain. Unlike the evolutions in the SXS catalog, the full set of Weyl scalars and the strain have been extracted from these runs and the waveforms have been computed using the

extrapolation technique described in [24] and the CCE procedure described in [25, 38]. Extrapolation is performed with the python module `scri` [13, 28–30] and CCE is run with SpECTRE's CCE module [25, 38, 39].

For the CCE extractions, the four world tubes that are available have radii that are equally spaced between $2\lambda\!\!\!^{-}_0$ and $21\lambda\!\!\!^{-}_0$, where $\lambda\!\!\!^{-}_0 = 1/\omega_0$ is the initial reduced gravitational wavelength as determined by the orbital frequency of the binary from the initial data. Based on the recent work of [19], however, we choose to use only the waveforms that correspond to the world tube with the second-smallest radius, since these waveforms have been shown to minimally violate the BMS balance laws. For clarity, we provide the world tube radius used for each system in Table 4.4.1. All of these 13 BBH systems' waveforms have been made publicly available at [35].

As mentioned above, the asymptotic strain waveforms are computed using two methods: extrapolation and CCE. The first method utilizes Regge-Wheeler-Zerilli (RWZ) extraction to compute the strain on a series of concentric spheres of constant coordinate radius and then proceeds to extrapolate these values to future null infinity $\mathcal{I}^+$ using $1/r$ approximations [2, 24, 40–43]. This is the strain that can be found in the SXS catalog. The other and more faithful extraction method, which is known as CCE, computes the strain by using the world tube data provided by a Cauchy evolution as the inner boundary data for a nonlinear evolution of the Einstein field equations on null hypersurfaces [25, 38]. CCE requires freely specifying the strain on the initial null hypersurface labeled $u = 0$. Like [18, 19], we choose this field to match the value and the first radial derivative of h from the Cauchy data on the world tube using the ansatz

$$h(u = 0, r, \theta^A) = \frac{A(\theta^A)}{r} + \frac{B(\theta^A)}{r^3}, \tag{4.23}$$

where the two coefficients $A(\theta^A)$ and $B(\theta^A)$ are fixed by the Cauchy data on the world tube. Unfortunately, constructing a satisfactory initial null hypersurface for CCE is currently an open issue in numerical relativity. Consequences of this choice manifest as transient effects arising at early times [18]. We address these in Sec. 4.5.1.1.

As for the extrapolated strain waveforms that we use, these have been postprocessed so that they exhibit the displacement memory effect and are thus more on par with the waveforms produced by CCE [19].

Last, when performing our analysis, we predominantly use the code `scri` [13, 28–30] to compute BMS charges and transform asymptotic waveform quantities.

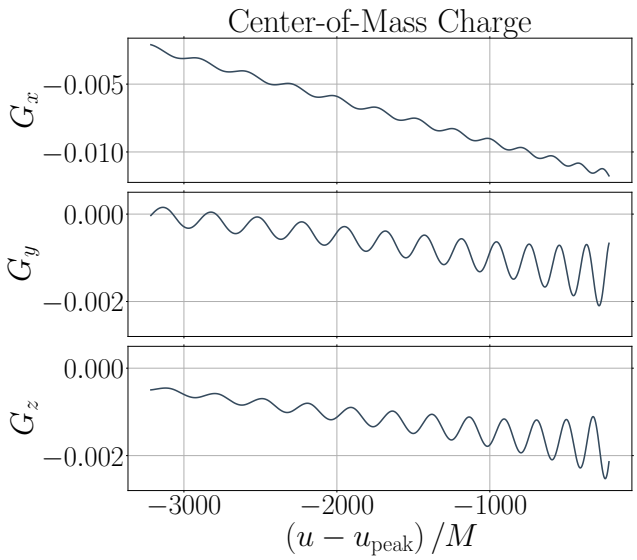

Figure 4.1: Example of what the center-of-mass charge looks like for a system with large center-of-mass velocity; in this case a $q = 4$, precessing system. The charges plotted are computed directly from Eq. (4.18), where $\vec{E}$ and P^t are obtained from Eq. (4.17) by using the energy moment aspect $E \equiv N + u\eth m$ and mass aspect m. We define the peak time to be the peak of the L^2 norm of the Geroch supermomentum [see Eq. (4.32b)], since this quantity is a supertranslation-invariant quantity [17, 44]. The waveform used is a CCE waveform.
BBH merger: `q4_precessing` (see Table 4.4.1).

4.5.1 $\ell < 2$ Results

As discussed in Sec. 4.3, a BBH system can be mapped to its center-of-mass frame by utilizing the center-of-mass charge $\vec{G}$. In Fig. 4.5.1, we show this charge for a $q = 4$, precessing BBH system (see Table 4.4.1). We compute the plotted charges from Eq. (4.18) by using a CCE waveform. As can be seen, in the $\hat{x}$, $\hat{y}$, and $\hat{z}$ directions the average of the center-of-mass charge is not constant with respect to the Bondi time. Further, if one imagines tracing these curves back in time then it can easily be observed that they begin with a nonzero value. Because of these results, we may assert that, with time, the BBH system is drifting through space away from a point that is not the origin. If the system under consideration were not drifting and were in the center-of-mass frame, then we would expect our charges to have both zero slope and zero intercept. Fortunately, because of the nature of this charge, to map to the center-of-mass frame one can simply boost and translate the system by the negative of the charge's slope and intercept. In the subsequent discussion, we first check to see if any of our of 13 binary systems, either before or after the Newtonian center-of-mass correction [6], are in the center-of-mass frame.

After this, we then proceed to apply our charge-based center-of-mass correction and evaluate the improvement it has on our waveforms.

4.5.1.1 A note on transient effects

Because numerical relativity simulations are evolved from imperfect initial data [2], the output waveforms contain unphysical effects referred to as *junk radiation*. In extrapolated waveforms, the junk radiation appears at early times and typically decays after an orbit or two. For CCE waveforms, however, the junk radiation tends to persist longer into the waveform [18]. As a result, because we examine extrapolated and CCE waveforms, we perform our analysis on the part of our waveforms that is three orbits past the start of the simulation, since the CCE-specific transient effects have decayed by then. We refer to this time throughout the results as u_1.

4.5.1.2 Determining the best method for fixing the Poincaré frame

We now compute the boosts and translations needed to map the 13 BBH systems to the center-of-mass frame. We first compute the charges according to Eq. (4.18). Next, we define an initial time u_1 to be three orbits past the start of the simulation and a final time that is three orbits before the peak time $u_{\rm peak}$. We define the peak time to be the peak of the L^2 norm of the Geroch supermomentum [see Eq. (4.32b)], since this quantity is a supertranslation-invariant quantity [17, 44]. We choose this final time to ensure that we are only working with the inspiral phase of the binary, rather than the merger phase. Note that one could fix the Poincaré frame using the remnant BH, i.e., mapping the kick velocity to zero, but this is not as instinctive as using the inspiral phase to fix the frame, even though it would matter for fitting quasinormal modes. Equipped with the charges and boundary times, we then linearly fit to the center-of-mass charge in the $\hat{x}$, $\hat{y}$, and $\hat{z}$ directions and take the needed boost to be the negative of the slope and the needed translation to be the negative of the vertical intercept at $u = 0$.

When we first applied this new Poincaré frame fixing, the improvements that we saw in the extreme systems, e.g., the $q = 4$ and fast-spinning systems, were remarkable. For the simpler systems, however, the improvements were not as large as we expected them to be. This is because these systems are already reasonably close to being in the center-of-mass frame. Thus the measured boosts and translations are more susceptible to errors that are introduced by oscillations in the charge and also by

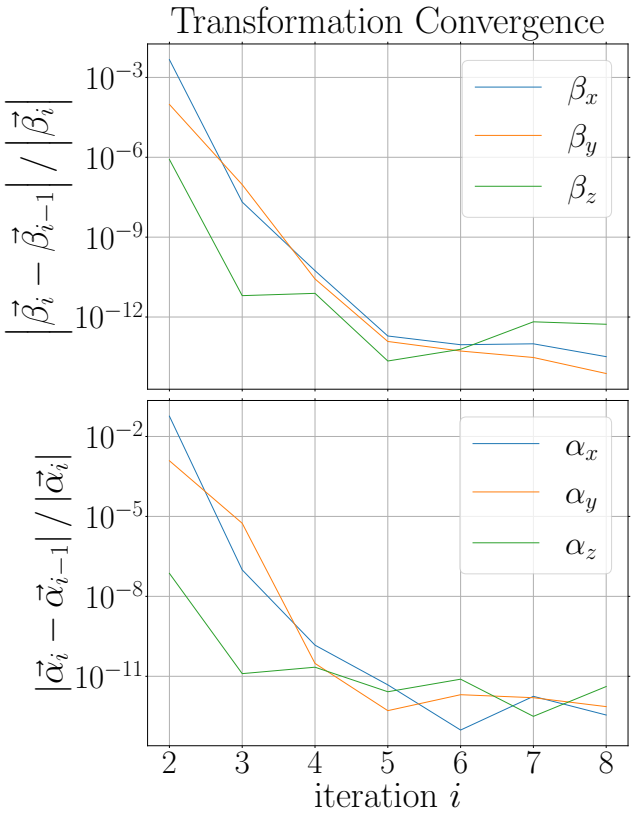

Figure 4.2: The convergence of the boost and translation vectors obtained by fitting to the center-of-mass charge. Here, β_i (α_i) represents the boost (translation) obtained after i iterations of fitting to the charge $\vec{G}$, transforming the untransformed waveform with the fit result, fitting to the new charge, and then composing that fit with the previous vector. For example, β_1 is obtained from fitting to the charge once, and β_2 is obtained from fitting to the charge transformed using β_1 and then composing that fit with β_1. Note that we show the result for `q1_aligned_chi0_6` because this simulation exhibits the slowest convergence out of the 13 systems that we examined. The waveform used is a CCE waveform.
BBH merger: `q1_aligned_chi0_6` (see Table 4.4.1).

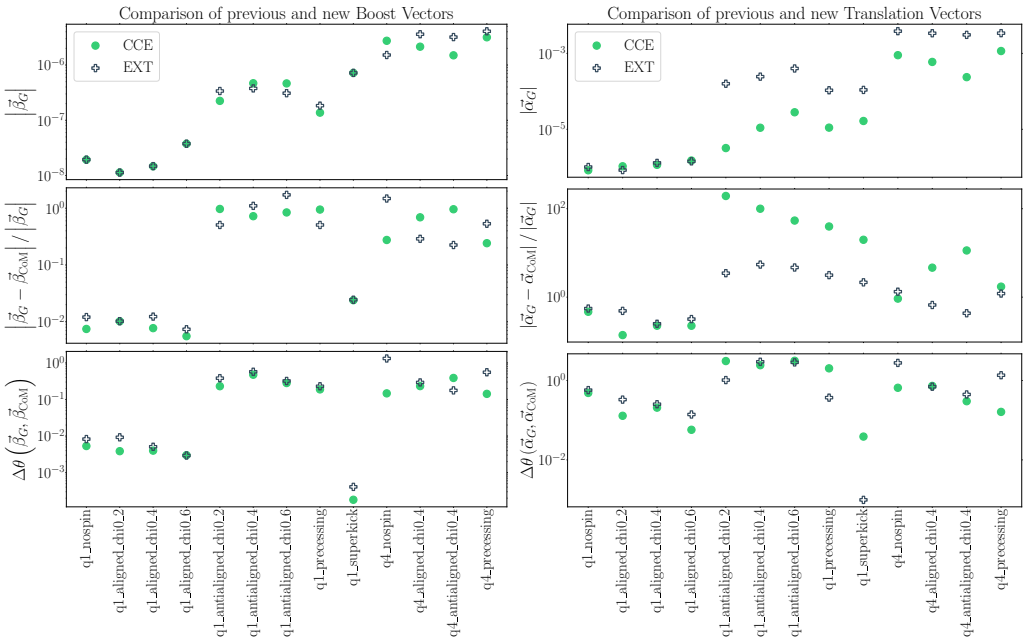

Figure 4.3: Examining the boost and translation vectors as measured by iteratively fitting to the center-of-mass charge $\vec{G}$, which is computed by using Eq. (4.17) to obtain the vector components of Eq. (4.18). In the top row we show the magnitude of these vectors, which we label $\vec{v}_G$ with $\vec{v} = \vec{\beta}$ for boosts (left) and $\vec{v} = \vec{\alpha}$ for translations (right). In the middle row we compute the relative error between these vectors and the vectors $\vec{v}_{\rm CoM}$, which are obtained by the previous center-of-mass correction that relies on the Newtonian trajectories of the black holes. In the bottom row we plot the angle between these vectors using Eq. (4.24).

the failure of the assumptions in Eq. (4.22) to hold because of non-Newtonian effects. Fortunately, because this method for mapping to the center-of-mass frame just involves the computation of charges, it can be iterated. That is, after the initial transformation is found, it can be applied, and then the center-of-mass charge can be computed again from the new asymptotic waveform. With this new charge, a new transformation can then be found, which may be composed with the previous transformation to obtain a more accurate mapping to the center-of-mass frame.

In Fig. 4.5.1.2 we plot the convergence of the boosts and translations for various iterations of this fitting procedure. We only show the results for `bbh_q1_aligned_chi0_6` because this system has the slowest convergence of the 13 binaries examined. In this figure, β_i (α_i) represents the boost (translation) obtained after i iterations of this charge fitting process. More specifically, this procedure is as follows:

I. Take $\vec{\beta}_0, \vec{\alpha}_0 = 0$.

II. If the iteration number i is not 0, transform the waveform with the Poincaré transformation $\vec{\beta}_i, \vec{\alpha}_i$.

III. Compute $\vec{G}$ from the transformed waveform.

IV. Obtain $\vec{\beta}$ and $\vec{\alpha}$ by fitting to $\vec{G}$ with a degree one polynomial ($\vec{\beta}$ = slope, $\vec{\alpha}$ = vertical intercept).

V. Compute $\vec{\beta}_{i+1} = \vec{\beta}_i + \vec{\beta}$ and $\vec{\alpha}_{i+1} = \vec{\alpha}_i + \vec{\alpha}$.

VI. Repeat.

As can be seen, even for this slowly converging system, the transformations converge rather quickly. Thus, based on this simulation, we choose a fixed number of five iterations for every one of our systems. With this many iterations, the improvements in the simpler systems then become as large as we would like to see.

4.5.1.3 Comparing the Newtonian trajectory and charge-based frame fixing methods

We now compare our iterative center-of-mass correction that uses the center-of-mass charge to the previous version that uses Newtonian trajectories. In Fig. 4.5.1.2 we show that of the 13 binaries examined, none of them are exactly in the center-of-mass frame after applying the correction that relies on Newtonian trajectories since all of the new Poincaré transformations are nonzero. More specifically, we plot two columns, one for the boosts on the left and one for the translations on the right. In the top row, we plot the magnitude of these vectors as obtained from fitting to the center-of-mass charge, which is a proxy for how much the system fails to be in the center-of-mass frame. In the middle row, we plot the relative difference between this charge-based vector $\vec{v}_{\rm G}$, and the vector obtained from the Newtonian center-of-mass correction $\vec{v}_{\rm CoM}$. This serves as a proxy for how much the system fails to be in the center-of-mass frame, even after the Newtonian correction. Finally, in the bottom row, we plot the angle between these two vectors. That is,

$$\Delta\theta(\vec{v}_{\rm G}, \vec{v}_{\rm CoM}) \equiv \arccos\left(\frac{\vec{v}_{\rm G}}{|\vec{v}_{\rm G}|} \cdot \frac{\vec{v}_{\rm CoM}}{|\vec{v}_{\rm CoM}|}\right). \tag{4.24}$$

As can be seen in the top row, the equal mass nonspinning and aligned systems are reasonably close to being in the center-of-mass frame, while the other systems, especially the $q = 4$ systems, are not. According to the other rows, though, because

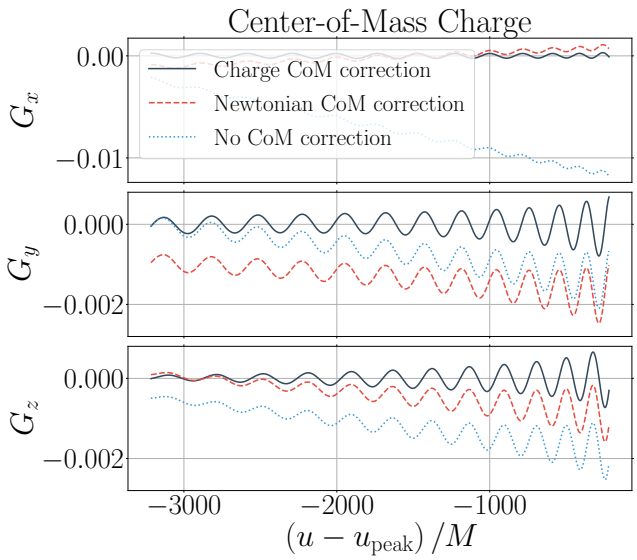

Figure 4.4: Comparing the center-of-mass charge from waveforms transformed using the Newtonian center-of-mass correction (red/dashed curves) to the charge obtained from those transformed using the charge-based method (black/solid curves). As a reference, we also plot the charge obtained from the untransformed waveforms (blue/dotted curves). The charges plotted are computed directly from Eq. (4.18), where $\vec{E}$ and P^t are obtained from Eq. (4.17) by using the energy moment aspect $E \equiv N + u\eth m$ and mass aspect m. The waveform used is a CCE waveform.
BBH merger: `q4_precessing` (see Table 4.4.1).

the differences between the vectors are so large, we realize that the Newtonian method for mapping to the center-of-mass frame is not nearly as successful as previously thought. Consequently, it is now evident that this Newtonian method for mapping a BBH system to its center-of-mass frame does not achieve its objective and the method based on the center-of-mass charge, which we explore in more detail now, is necessary.

4.5.1.4 Examining improvements to waveforms

At this point, we examine how the strain waveforms change under the center-of-mass charge-based mapping to the center-of-mass frame. First, though, in Fig. 4.5.1.3 we show how the center-of-mass charge changes under the Newtonian center-of-mass correction versus the new charge-based method. What this plot shows is that while the Newtonian center-of-mass correction only corrects the $\hat{x}$ component of the center-of-mass charges for the `q4_precessing` system, the new method produces

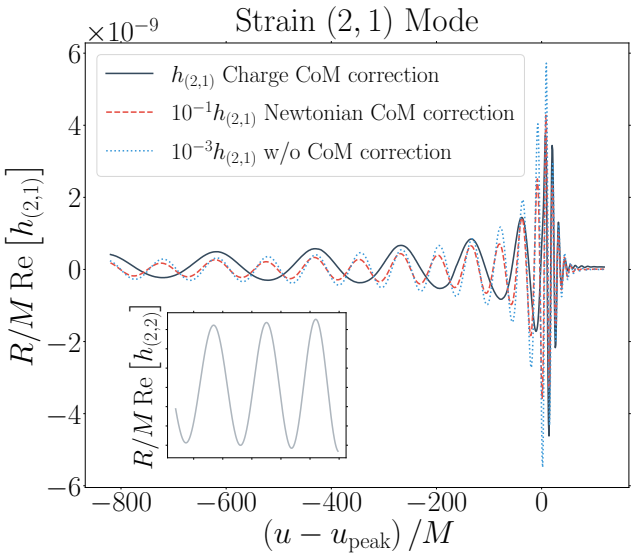

Figure 4.5: The strain $(2,1)$ mode of the original waveform (blue/dotted curve, scaled by 10^{-3}) compared to that of the Newtonian (red/dashed curve, scaled by 10^{-1}) and the charge-based (black/solid curve) center-of-mass corrections. In the inset plot we provide the strain $(2,2)$ mode of the original waveform to illustrate that unless the charge-based correction is used, the $(2,1)$ mode exhibits the same frequency as the $(2,2)$ mode. Note that the time axis of the inset plot matches up with the main plot's. The waveform used is a CCE waveform.
BBH merger: `q1_nospin` (see Table 4.4.1).

an average value of exactly zero for every vector component.

In Fig. 4.5.1.3 we show the most important consequence of improving the fixing of the Poincaré frame by using asymptotic Poincaré charges. For this example, we show the strain $(2,1)$ mode of `q1_nospin` as it is, after the Newtonian center-of-mass transformation, and after our new center-of-mass transformation. We show this mode because it exhibits the largest mismatch (see Eq. (4.25)) when comparing strains that have been transformed using both the previous and the new center-of-mass corrections. Based on PN theory, during the system's inspiral phase we expect the frequency of this mode to be half the strain $(2,2)$ mode's frequency.[13] However, as can be seen by comparing the original and transformed waveforms, after correctly mapping to the center-of-mass frame the frequency of the strain $(2,1)$ mode is roughly half of what it was before. This is because, previously, the system was

[13] Really we expect this mode to be exactly zero because of the symmetry of the system; however, because the two spins and the eccentricity of the black holes in the `bbh_q1_nospin` simulation are not precisely zero, owing to numerical error, there is an unexpected nonzero contribution to this mode.

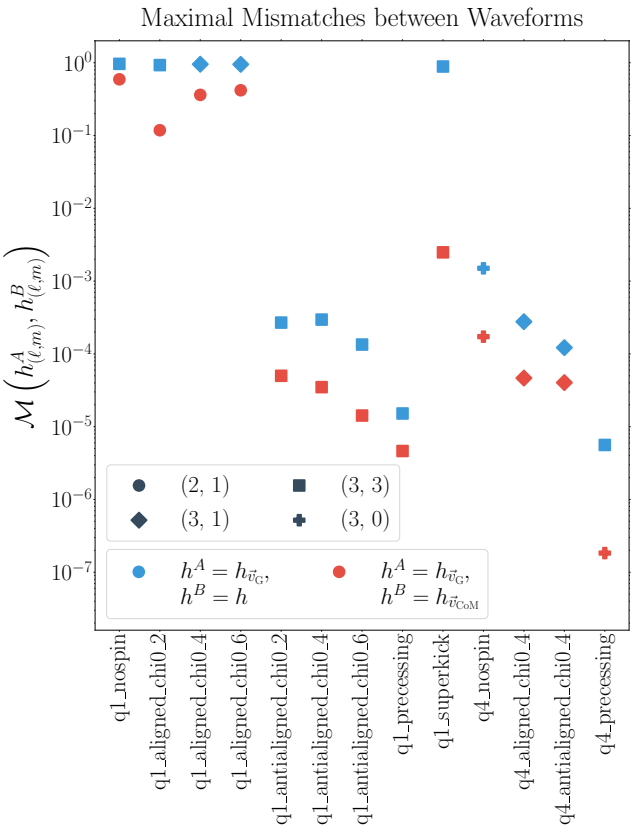

Figure 4.6: The modes that produce the largest mismatches between the charge-based center-of-mass corrected strains and both the original strains (blue) and the strains corrected using the Newtonian center-of-mass correction (red). The mismatch in each mode is computed by using Eq. (4.25). As shown in the plot's legend, the shape of each point represents the mode while the color represents the strains used in the mismatch. Note that the mismatches for the $q = 1$ nonspinning and aligned-spin systems are so large because these systems have a rotation by π symmetry, and thus when the charge-based center-of-mass correction is used the $m =$ odd modes become much closer to their expected value of zero. The waveforms used in these computations are CCE waveforms.

not truly in the center-of-mass frame so the strain $(2,2)$ mode was leaking into the $(2,1)$ mode. Note that in Fig. 4.5.1.3 we have scaled the original waveform and the waveform transformed with the Newtonian center-of-mass correction by factors of 10^{-3} and 10^{-1} to make them more comparable to the waveform transformed with the charge-based center-of-mass correction.

Last, to show the impact this charge-based method has more broadly, we provide Fig. 4.5.1.3. This figure shows the mismatch between the newly transformed waveforms and both the original waveforms and the waveforms that have been transformed using the previous Newtonian correction. In this plot, we compute the mismatch between a mode of two strain waveforms via

$$\mathcal{M}(h^A_{(\ell,m)}, h^B_{(\ell,m)}) \equiv 1 - \frac{\langle h^A_{(\ell,m)}, h^B_{(\ell,m)}\rangle}{\sqrt{\langle h^A_{(\ell,m)}, h^A_{(\ell,m)}\rangle \langle h^B_{(\ell,m)}, h^B_{(\ell,m)}\rangle}}, \tag{4.25}$$

in which the inner product is given by

$$\langle h^A_{(\ell,m)}, h^B_{(\ell,m)}\rangle \equiv \int_{u_1}^{+\infty} h^A_{(\ell,m)} \overline{h^B_{(\ell,m)}} du, \tag{4.26}$$

where $u = +\infty$ is the final time of the simulation.

4.5.2 $\ell \geq 2$ Results

With the $\ell < 2$ modes of our waveforms properly fixed using the new center-of-mass correction, we now explore how to fix the $\ell \geq 2$ modes, i.e., choosing a Bondi frame. As discussed in Sec. 4.4, there are really only two options: mapping the systems to their super rest frame or their PN Bondi frame. As described earlier, we prefer to map to the PN BMS frame since this tends to best improve the hybridization between two NR and PN strain waveforms.

To map our various systems to their PN BMS frame, we begin by creating a 3PN-order strain waveform from the orbital frequency of the two black holes using the code `GWFrames` [28, 29]. To generate this PN waveform, we obtain the orbital frequency of the system from the horizon information and evolve it backward in time using the PN evolution equations. We then simultaneously find the Poincaré transformation and the $2 \leq \ell \leq 4$ supertranslation that minimize the L^2 norm of the difference between the strain and the PN waveform. The norm is computed over the time interval starting at u_1 and continuing for four orbits. To perform this minimization, we use SciPy's minimize function corresponding to the sequential least squares programming algorithm (SLSQP) [45] and define the following function:

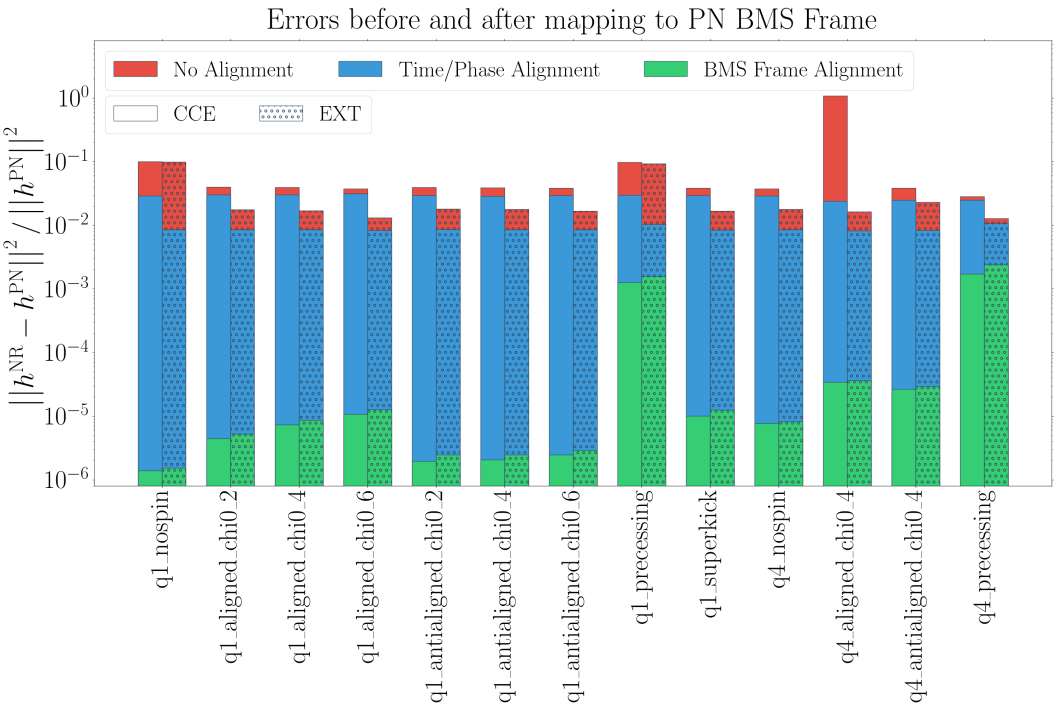

Figure 4.7: Comparing the BMS alignment results between NR and PN strain waveforms. In red, we show the initial misalignment. In blue, we show the misalignment if the usual alignment procedure is used, i.e., finding the time translation and frame rotation that best aligns a NR strain waveform that has undergone the previous center-of-mass correction to a PN strain waveform. Finally, in green, we show the misalignment after the new BMS frame alignment procedure has been used, that is, finding the BMS transformation (up to $\ell = 4$) that minimizes the average L^2 norm of the difference of the NR and PN strain waveforms. Note that the measure of this misalignment, $||f(u,\theta,\phi)||^2$, is defined to be $||f(u,\theta,\phi)||^2 = \int_{u_1}^{u_1+\text{four orbits}} \int_{S^2} f\bar{f}\, d\Omega\, du$.

I. Take, as inputs, a NR strain, a PN strain, and also a center-of-mass transformation.

II. Consider the ordered list of transformations

   1. $\ell = 2$ supertranslation,
   2. time translation,
   3. frame rotation,
   4. $\ell = 3$ supertranslation,
   5. $\ell = 4$ supertranslation.

III. Begin with iteration $n = 1$.

IV. For iteration n, include all transformations from the above list up to transformation n as free parameters. Use the findings from iteration $n-1$ as initial guesses for the $n-1$ transformations.

V. Use SciPy's SLSQP minimize function to find the collection of n transformations that, when composed with the center-of-mass transformation (see below), best map the NR strain to the frame of the PN strain, i.e., the transformations that minimize the L^2 norm of the difference of the two waveforms, integrated over the time interval from u_1 to four orbits past u_1.

VI. Repeat until $n = 5$.

We find that it is important to start this procedure with the $\ell = 2$ supertranslation, because this tends to be the largest source of error. Beyond this, however, the order of the transformations is fairly inconsequential and chosen as such to minimize run time. Note though that it is also important to allow the previous transformations to be free parameters in the next iteration because each new transformation tends to influence the previous ones.

With this function, we then run the iterative procedure:

I. Find the center-of-mass transformation that maps the NR strain waveform to the center-of-mass frame using the charge-based center-of-mass correction.

II. Provide this transformation and the NR and PN strain waveforms to the minimizing function.

III. Apply the optimized BMS transformation to the raw NR strain[14] and find the center-of-mass transformation needed to map this new waveform to the center-of-mass frame.

IV. Compose this new transformation with the original center-of-mass transformation and then repeat steps II. - IV. with the previous BMS transformation as an initial guess until a desired precision is obtained.

We find that by running this procedure 4 times we can obtain rather impressive alignments between the input NR and PN strain waveforms for most of our systems.

[14] We apply the BMS transformation to the raw waveform to ensure that we are not transforming the same object more than once, which would introduce numerical error.

We choose to run this method, rather than optimizing over all BMS transformations, because this method not only produces the best alignment but it also tends to keep the system much closer to its center-of-mass frame.

In Fig. 4.5.2, we show the results of mapping the various CCE and extrapolated waveforms from our 13 systems to their corresponding PN BMS frame. In red, we show the initial misalignment. In blue, we show the misalignment if the usual alignment procedure is performed, i.e., finding the time translation and frame rotation that best aligns a PN strain waveform to a NR strain waveform that has undergone the previous center-of-mass correction. Finally, in green, we show the misalignment after using the new BMS frame alignment procedure. As is clearly illustrated, by capitalizing on the full BMS freedom of NR waveforms one can perform substantially better alignment between NR and PN strain waveforms. Apart from this, though, one can also observe the failure of the PN waveform to accurately model the BBH system, e.g., as the total spin or the mass ratio of the system increases, or if the system is precessing, the success of the BMS alignment between the NR and PN strains tends to worsen. This is expected, however, since the PN waveform is only of 3PN order. Regardless, this shows that not only can the Bondi frame, and really the whole BMS frame, be fixed by utilizing a PN strain waveform, but doing so is critically important for aligning, and thus hybridizing, NR and PN waveforms.

With our NR waveforms now optimally mapped to the PN BMS frame, we perform strain hybridizations between NR and PN to illustrate the operations this alignment procedure allows for. To create these hybridizations, we use the smoothing function

$$f(x) = \begin{cases} 0 & x \leq 0, \\ \left(1 + \exp\left[\frac{1}{x-1} + \frac{1}{x}\right]\right)^{-1} & 0 < x < 1, \\ 1 & x \geq 1. \end{cases} \tag{4.27}$$

so that before the hybridization interval, which is the same as the alignment interval, the hybrid is equal to the PN waveform and after it is equal to the NR waveform. Put differently, we build the hybrid waveform h^{hybrid} via

$$h^{\text{hybrid}} = h^{\text{PN}} + f\left(\frac{u - u_1}{u_2 - u_1}\right)\left(h^{\text{NR}} - h^{\text{PN}}\right), \tag{4.28}$$

where u_2 is the time that is four orbits past u_1.

In Fig. 4.5.2, we show three plots, one for each of the strain $(2,2)$, $(2,1)$, and $(2,0)$ modes. In each plot, we compare the hybrid waveform to the NR and PN

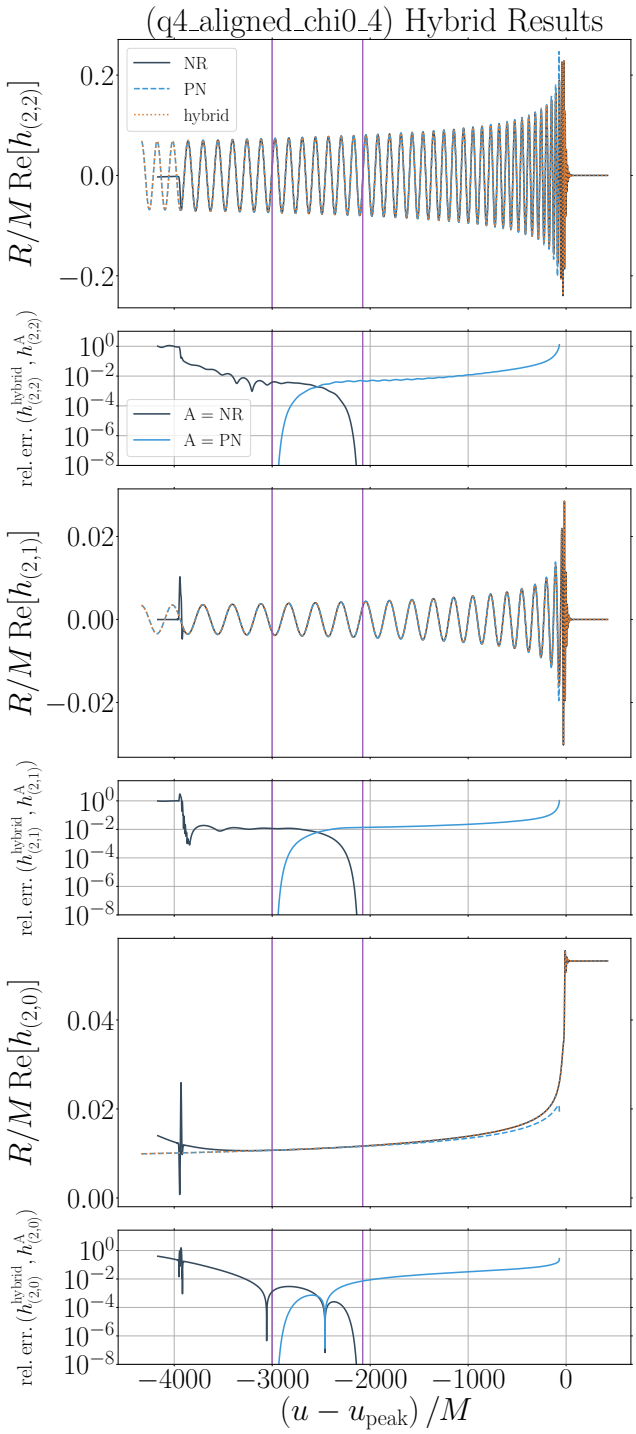

Figure 4.8: The NR and PN strain hybrid. We present three plots, one for each of the $(2,2)$, $(2,1)$, and $(2,0)$ modes. In each plot, in the top panel we show the NR waveform (black/solid curve), the PN waveform (blue/dashed curve), and also the hybrid waveform (orange/dotted curve), while in the bottom panel we plot the relative error between the hybrid waveform and both the NR waveform (black curve) and the PN waveform (blue curve). In each panel, we also show the hybridization interval in purple. The NR waveform in each of these plots is a CCE waveform. BBH merger: `q4_aligned_chi0_4` (see Table 4.4.1).

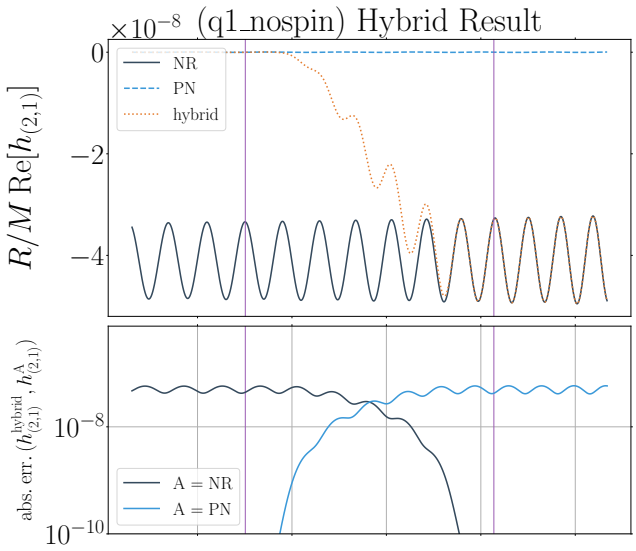

Figure 4.9: Illustrating a caveat about NR and PN hybridizations, as shown through the strain $(2, 1)$ mode. In the top panel we plot the NR waveform (black/solid curve), the PN waveform (blue/dashed curve), and also the hybrid waveform (orange/dotted curve), while in the bottom panel we plot the absolute error between the hybrid waveform and both the NR waveform (black curve) and the PN waveform (blue curve). In each panel, we also show the hybridization interval in purple. See the text for more details. The NR waveform in this plot is a CCE waveform.
BBH merger: `q1_nospin` (see Table 4.4.1).

strains for simulation `q4_aligned_chi0_4`. In each top panel, we show the strain modes, while in each bottom panel, we show the relative error between the hybrid and the NR and PN strain waveforms. As is expected from our alignment results in Fig. 4.5.2, there is fairly impressive agreement in every mode. Furthermore, the plot of the strain $(2, 0)$ mode shows that the initial value of the hybrid now agrees with PN, i.e., it exhibits the memory that we expect to be there due to the emission of radiation throughout the entire past history of the binary's inspiral. Apart from these important positive results, though, there is one minor caveat regarding this hybridization procedure that is worth mentioning to avoid confusion.

Recall that when mapping a NR strain waveform to its corresponding PN BMS frame, we apply certain $2 \leq \ell \leq 4$ supertranslations. Because supertranslations also affect the Bondi time u, however, when we supertranslate the strain we not only have to act on it with the supertranslation, but we also have to interpolate the waveform on to a new series of Bondi times. So, when applying a supertranslation with only one nonzero mode, not only will that mode of the strain change, but so will every other mode because of the time interpolation. The reason why this is

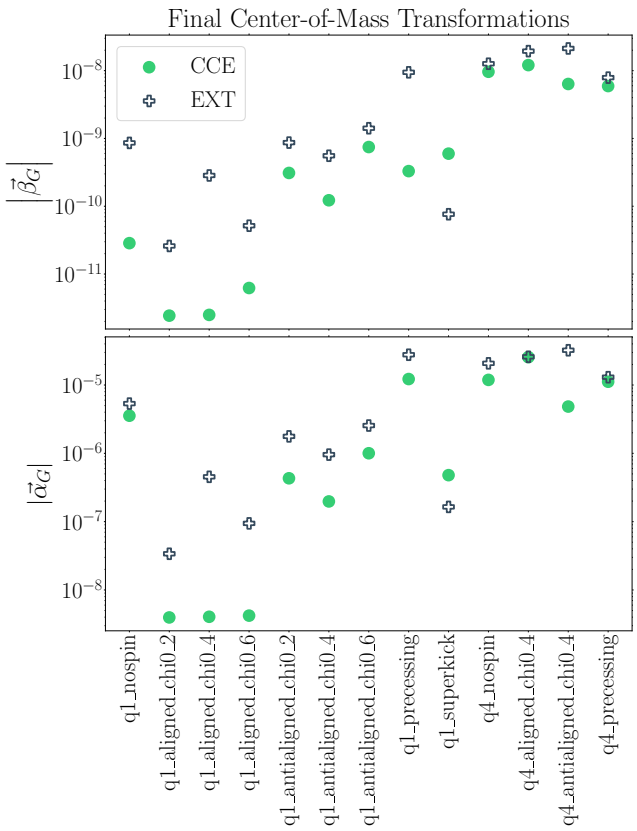

Figure 4.10: The magnitudes of the boosts and translations needed to map the NR strains in the PN BMS frame to their center-of-mass frame. The reason these are not exactly zero is because a few of the BMS transformations that are not involved in the center-of-mass correction do not commute with the center-of-mass transformation, causing the system to be pushed slightly away from the center-of-mass frame to obtain better alignment with the PN strain waveform. Nonetheless, these transformations are fairly negligible, especially when compared to those in the top plots of Fig. 4.5.1.2.

important is illustrated in Fig. 4.5.2.

In Fig. 4.5.2, we show the $(2, 1)$ mode of the strain hybrid for simulation `q1_nospin`. Based purely on symmetry, we would normally expect this mode to be zero, but because of numerical error, the spins and eccentricity of this system are not exactly zero. We therefore observe nonzero values in this mode of the NR waveform, even though they are negligible. Thus, the $(2, 1)$ mode of the hybrid looks a bit strange because of this difference between NR and PN.

Apart from this, however, one may also notice that the zero average value of the PN strain is not matched by the nonzero average of the NR strain. This oddity results from the supertranslation's broader influence on the whole of the strain waveform

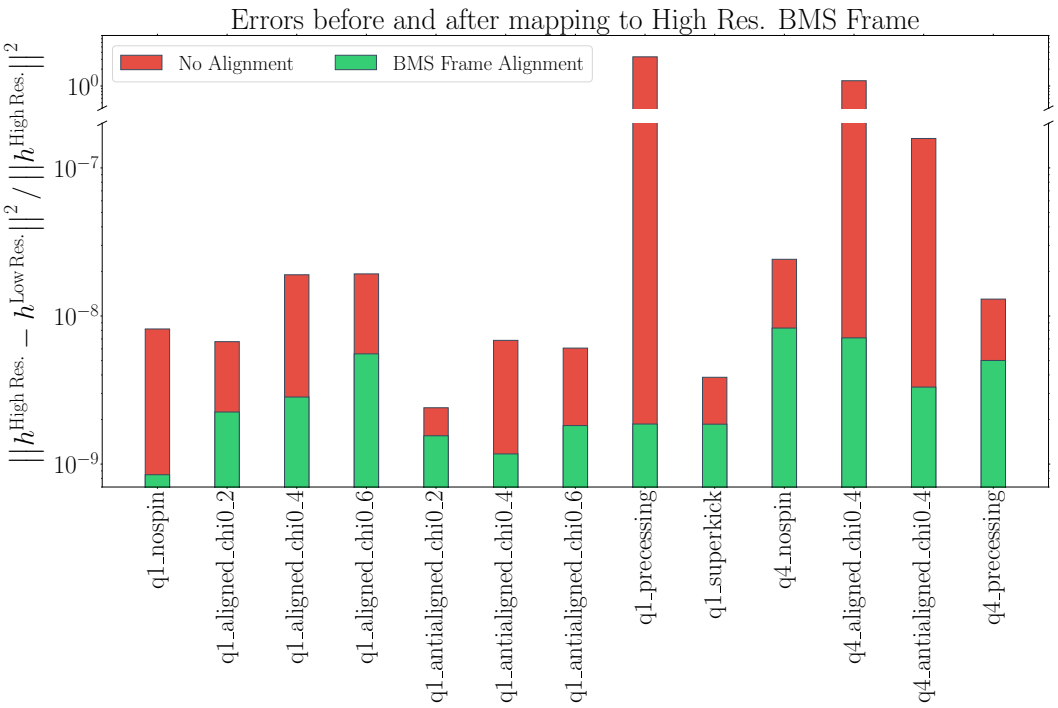

Figure 4.11: Comparing the BMS alignment results between a high resolution and a lower resolution numerical relativity waveform. In red, we show the initial misalignment, while in green, we show the misalignment after using the new BMS frame alignment: that is, finding the BMS transformation (up to $\ell = 4$) that minimizes the average L^2 norm of the difference of the two waveforms. Note that the measure of this misalignment, $||f(u,\theta,\phi)||^2$, is defined to be $||f(u,\theta,\phi)||^2 = \int_{u_1}^{u_1+\text{four orbits}} \int_{S^2} f\bar{f}\, d\Omega du$.

because of the needed time interpolation, as mentioned earlier. In other words, supertranslating the $(2,1)$ mode away from an average of zero improves the error in other modes more than it worsens the error in the $(2,1)$ mode. Consequently, while this kind of behavior in the hybridized waveform is certainly undesirable, it is a natural consequence of the PN waveform not being a perfect theoretical model for the numerical BBH system. Furthermore, we note that this behavior only occurs in modes whose amplitude is rather negligible, i.e., 10^{-6} or less.

It is also fairly important to note that, because the center-of-mass transformation does not commute with the other BMS transformations, this procedure of mapping to the PN BMS frame does not exactly map our systems to the center-of-mass frame, even though they are very close. We illustrate this in Fig. 4.5.2, which shows the remaining boosts and translations needed to map the waveform in the

PN BMS frame to its center-of-mass frame. As is shown, the necessary boosts and translations are nearly zero, especially when compared to the transformations in the top plots of Fig. 4.5.1.2. Therefore, we consider this mapping to the PN BMS frame to be remarkably successful, especially since the improvements in Fig. 4.5.2 are so notable.

Finally, we show our last result regarding the benefit of utilizing the whole BMS freedom of numerical waveforms. When examining physical quantities that are output by numerical relativity, it is important to run convergence tests to ensure that conclusions can be made with respect to numerical error. In Fig. 4.5.2 we show how convergence tests can be improved by mapping waveforms that are from simulations of different numerical resolutions to the same BMS frame before they are compared with one another. To do this, we perform the same iterative process as described earlier, but we now optimize over every BMS transformation, rather than everything but the center-of-mass transformation. In red, we show the initial misalignment, while in green we show the misalignment after the BMS frame alignment procedure. As is shown, the improvements are relatively minor, but could still prove to be important for numerical simulations run with newer codes, such as SpECTRE [39], which will be more accurate than the SXS Collaboration's current code SpEC.

4.6 Conclusion

Like any physical system, understanding the frame that a binary black hole merger is in relative to a family of observers is essential. Understanding this frame will help us ensure that any analyses on waveform models are performed properly and no misleading assertions are made. For gravitational-wave physics, fixing the frame is not as simple as fixing the Poincaré frame, since the symmetries of asymptotically flat spacetimes are characterized by an infinite extension of the Poincaré group: the BMS group.

Currently, gravitational-wave physicists who analyze models of gravitational waves expect those models to be in the center-of-mass frame and the PN Bondi frame, since this is the BMS frame that analytic models are in. However, the waveforms that are currently produced by numerical relativity—the supplier of the most accurate models of gravitational waves—typically are not in such a frame because of an unexpected center-of-mass drift in numerical simulations and a lack of initial data that contains information about the entire past history of the binary black hole's

inspiral. Consequently, they are instead in some other BMS frame. But with a proper understanding of the BMS group, one can postprocess these waveforms and map them to the desired BMS frame after the BBH simulation is complete. As of now, such a postprocessing technique is used for the Poincaré frame by using the Newtonian center of mass [6], but there is no such postprocessing for the Bondi frame.

In this paper, by utilizing asymptotic Poincaré charges, i.e., the center-of-mass charge (see Eq. (4.18)), we show that this method that relies on Newtonian trajectories for mapping to the center of mass Frame is not as successful as previously thought. As a result, we develop an improved procedure for fixing the Poincaré frame, which shows large benefits in terms of exhibiting the expected behavior in the asymptotic Poincaré charges and also in minimizing certain modes of the strain waveform that are expected to be zero because of axisymmetry.

We also found that we can meaningfully fix the whole BMS frame of our numerical waveforms by mapping them to their corresponding PN BMS frame using a 3PN-order strain waveform. With this BMS frame fixing procedure, we observe that we can produce much more favorable hybridizations between NR and PN strain waveforms than if one were to use an alignment scheme that only utilized the Poincaré transformations. Last, we also find that such a BMS frame alignment will prove important for future numerical relativity codes that will be able to run simulations at higher resolutions and will need to properly test the convergence of their waveforms.

With this new method of fully fixing the BMS frame of asymptotic waveforms, many important improvements to gravitational wave modeling can be made. For example, by correctly mapping to the center-of-mass Poincaré frame and PN BMS frame, we can produce much better PN and NR hybridizations. Furthermore, because we can now ensure that waveforms are in the same BMS frame, surrogate models built from such waveforms should be more accurate since they are no longer trying to link waveforms in radically different BMS frames. It would be very interesting to see how parameter estimation using a NR surrogate changes depending on whether the waveforms used to build the surrogate have been mapped to a consistent BMS frame, such as the PN BMS frame.

4.7 Acknowledgments

Computations were performed with the High Performance Computing Center and the Wheeler cluster at Caltech. This work was supported in part by the Sherman Fairchild Foundation and by NSF Grants No. PHY-2011961, No. PHY-2011968, and No. OAC-1931266 at Caltech, NSF Grants No. PHY-1912081 and No. OAC-1931280 at Cornell, and NSF Grant No. PHY-1806356, Grant No. UN2017-92945 from the Urania Stott Fund of the Pittsburgh Foundation, and the Eberly research funds of Penn State at Penn State.

4.A Fixing the supertranslation freedom with the Moreschi supermomentum

As mentioned earlier, an alternative method for fixing the Bondi frame of NR waveforms, apart from mapping to the PN BMS frame, is to map to the super rest frame. Therefore, since this technique could prove rather useful in future analyses—such as quasinormal mode fitting— we now briefly illustrate how to perform this procedure. According to Moreschi [15, 16], a reasonable choice for the supermomentum is

$$\Psi^{\rm M}(u,\theta,\phi) \equiv \sum_{\ell\geq 0}\sum_{m\leq|\ell|} \Psi^{\rm M}_{\ell m}(u) Y_{\ell m}(\theta,\phi), \tag{4.29}$$

where

$$\Psi^{\rm M}_{\ell m}(u) \equiv -\frac{1}{\sqrt{4\pi}}\int_{S^2} Y_{\ell m}\Psi^{\rm M}(u)\, d\Omega, \tag{4.30}$$

and

$$\Psi^{\rm M}(u) \equiv \Psi_2 + \sigma\dot{\bar{\sigma}} + \eth^2\bar{\sigma}. \tag{4.31}$$

While this is the supermomentum that correctly defines the Bondi frame, it is important to note that there are many other supermomenta that have been proposed in the literature, e.g., the Bondi-Sachs (BS), Geroch (G), and Geroch-Winicour (GW) supermomenta [17, 31, 46, 47]

$$\Psi^{\rm BS}(u) \equiv \Psi_2 + \sigma\dot{\bar{\sigma}}, \tag{4.32a}$$

$$\Psi^{\rm G}(u) \equiv \Psi_2 + \sigma\dot{\bar{\sigma}} + \left(\eth^2\bar{\sigma} - \bar{\eth}^2\sigma\right), \tag{4.32b}$$

$$\Psi^{\rm GW}(u) \equiv \Psi_2 + \sigma\dot{\bar{\sigma}} - \bar{\eth}^2\sigma. \tag{4.32c}$$

While all of these agree on their $\ell < 2$ modes,[15] the Moreschi supermomentum is the supermomentum that can most easily be used to map to the super rest frame for reasons discussed in [15–17, 48].

[15] The $\ell < 2$ modes of the supermomenta in Eq. (4.32) all correspond to the usual Bondi four-momentum.

It is important to note, however, that

$$\begin{aligned}\Delta\Psi^{\mathrm{M}} &\equiv \int_{u_1}^{u_2} \dot{\Psi}^{\mathrm{M}}(u)\, du \\ &= \int_{u_1}^{u_2} \left[\left(\dot{\Psi}_2 + \left[\sigma\ddot{\bar{\sigma}} + \eth^2\dot{\bar{\sigma}}\right]\right) + |\dot{\sigma}|^2\right] du \\ &= \int_{u_1}^{u_2} |\dot{\sigma}|^2\, du \end{aligned} \tag{4.33}$$

since

$$\dot{\Psi}_2 = -\left[\sigma\ddot{\bar{\sigma}} + \eth^2\dot{\bar{\sigma}}\right] \tag{4.34}$$

by the Bianchi identities. Consequently, since Eq. (4.33) is proportional to the radiated energy, this means that the Moreschi supermomentum can never be made zero so long as there is energy radiated in gravitational waves.[16]

With Ψ^{M}, a similar procedure as the one presented in Sec. 4.5.2 for mapping to the PN BMS frame can then be performed. But, instead of minimizing the L^2 norm of the difference of NR and PN strain waveforms, one would simply find the proper supertranslation that minimizes the L^2 norm of Ψ^{M} at a certain time or over some finite time interval, such as the ringdown phase.

References

[1] *SXS Gravitational Waveform Database*, http://www.black-holes.org/waveforms.

[2] M. Boyle et al., Class. Quant. Grav. **36**, 195006 (2019) 10.1088/1361-6382/ab34e2.

[3] K. Jani, J. Healy, J. A. Clark, L. London, P. Laguna, and D. Shoemaker, Class. Quant. Grav. **33**, 204001 (2016) 10.1088/0264-9381/33/20/204001.

[4] J. Healy, C. O. Lousto, Y. Zlochower, and M. Campanelli, Class. Quant. Grav. **34**, 224001 (2017) 10.1088/1361-6382/aa91b1.

[5] J. Healy and C. O. Lousto, Phys. Rev. D **102**, 104018 (2020) 10.1103/PhysRevD.102.104018.

[6] C. J. Woodford, M. Boyle, and H. P. Pfeiffer, Phys. Rev. D **100**, 124010 (2019) 10.1103/PhysRevD.100.124010.

[7] D. Christodoulou, Phys. Rev. Lett. **25**, 1596 (1970) 10.1103/PhysRevLett.25.1596.

[16] This also corresponds to the electric part of the null memory [18].

[8] D. A. B. Iozzo, N. Khera, L. C. Stein, K. Mitman, M. Boyle, N. Deppe, F. Hébert, L. E. Kidder, J. Moxon, H. P. Pfeiffer, M. A. Scheel, W. Throwe, and S. A. Teukolsky, In Production (2021).

[9] H. Bondi, M. G. J. van der Burg, and A. W. K. Metzner, Proc. Roy. Soc. Lond. A **269**, 21 (1962) 10.1098/rspa.1962.0161.

[10] R. K. Sachs, Proc. Roy. Soc. Lond. A **270**, 103 (1962) 10.1098/rspa.1962.0206.

[11] M. Campiglia and A. Laddha, Phys. Rev. D **90**, 124028 (2014) 10.1103/PhysRevD.90.124028.

[12] M. Campiglia and A. Laddha, JHEP **04**, 076 (2015) 10.1007/JHEP04(2015)076.

[13] M. Boyle, Phys. Rev. D **93**, 084031 (2016) 10.1103/PhysRevD.93.084031.

[14] L. A. Gómez López and G. D. Quiroga, Rev. Mex. Fis. **63**, 275 (2017).

[15] O. M. Moreschi, Class. Quant. Grav. **5**, 423 (1988) 10.1088/0264-9381/5/3/004.

[16] O. M. Moreschi and S. Dain, J. Math. Phys. **39**, 6631 (1998) 10.1063/1.532646.

[17] S. Dain and O. M. Moreschi, Class. Quant. Grav. **17**, 3663 (2000) 10.1088/0264-9381/17/18/305.

[18] K. Mitman, J. Moxon, M. A. Scheel, S. A. Teukolsky, M. Boyle, N. Deppe, L. E. Kidder, and W. Throwe, Phys. Rev. D **102**, 104007 (2020) 10.1103/PhysRevD.102.104007.

[19] K. Mitman et al., Phys. Rev. D **103**, 024031 (2021) 10.1103/PhysRevD.103.024031.

[20] J. Blackman, S. E. Field, M. A. Scheel, C. R. Galley, D. A. Hemberger, P. Schmidt, and R. Smith, Phys. Rev. D **95**, 104023 (2017) 10.1103/PhysRevD.95.104023.

[21] J. Blackman, S. E. Field, M. A. Scheel, C. R. Galley, C. D. Ott, M. Boyle, L. E. Kidder, H. P. Pfeiffer, and B. Szilágyi, Phys. Rev. D **96**, 024058 (2017) 10.1103/PhysRevD.96.024058.

[22] V. Varma, S. E. Field, M. A. Scheel, J. Blackman, L. E. Kidder, and H. P. Pfeiffer, Phys. Rev. D **99**, 064045 (2019) 10.1103/PhysRevD.99.064045.

[23] D. Williams, I. S. Heng, J. Gair, J. A. Clark, and B. Khamesra, Phys. Rev. D **101**, 063011 (2020) 10.1103/PhysRevD.101.063011.

[24] D. A. B. Iozzo, M. Boyle, N. Deppe, J. Moxon, M. A. Scheel, L. E. Kidder, H. P. Pfeiffer, and S. A. Teukolsky, Phys. Rev. D **103**, 024039 (2021) 10.1103/PhysRevD.103.024039.

[25] J. Moxon, M. A. Scheel, and S. A. Teukolsky, Phys. Rev. D **102**, 044052 (2020) 10.1103/PhysRevD.102.044052.

[26] R. Geroch, A. Held, and R. Penrose, J. Math. Phys. **14**, 874 (1973).

[27] O. M. Moreschi, Class. Quantum Gravity **3**, 503 (1986).

[28] M. Boyle, D. Iozzo, and L. C. Stein, *Moble/scri: v1.2*, version v1.2, Sept. 2020, 10.5281/zenodo.4041972.

[29] M. Boyle, Phys. Rev. D **87**, 104006 (2013) 10.1103/PhysRevD.87.104006.

[30] M. Boyle, L. E. Kidder, S. Ossokine, and H. P. Pfeiffer, (2014).

[31] T. Dray and M. Streubel, Class. Quant. Grav. **1**, 15 (1984) 10.1088/0264-9381/1/1/005.

[32] T. Dray, Class. Quant. Grav. **2**, L7 (1985) 10.1088/0264-9381/2/1/002.

[33] É. É. Flanagan and D. A. Nichols, Phys. Rev. D **95**, 044002 (2017) 10.1103/PhysRevD.95.044002.

[34] G. Compère, R. Oliveri, and A. Seraj, JHEP **10**, 116 (2020) 10.1007/JHEP10(2020)116.

[35] https://data.black-holes.org/waveforms/extcce_catalog.html.

[36] D. Pollney and C. Reisswig, Astrophys. J. Lett. **732**, L13 (2011) 10.1088/2041-8205/732/1/L13.

[37] https://www.black-holes.org/code/SpEC.html.

[38] J. Moxon, N. Deppe, L. E. Kidder, G. Lovelace, K. Mitman, M. A. Scheel, S. Teukolsky, and W. Throwe, (In preparation).

[39] N. Deppe, W. Throwe, L. E. Kidder, N. L. Fischer, C. Armaza, G. S. Bonilla, F. Hébert, P. Kumar, G. Lovelace, J. Moxon, E. O'Shea, H. P. Pfeiffer, M. A. Scheel, S. A. Teukolsky, I. Anantpurkar, M. Boyle, F. Foucart, M. Giesler, D. A. B. Iozzo, I. Legred, D. Li, A. Macedo, D. Melchor, M. Morales, T. Ramirez, H. R. Rüter, J. Sanchez, S. Thomas, and T. Wlodarczyk, *SpECTRE*, version 2020.12.07, Dec. 2020, 10.5281/zenodo.4290405.

[40] O. Sarbach and M. Tiglio, Phys. Rev. D **64**, 084016 (2001) 10.1103/PhysRevD.64.084016.

[41] T. Regge and J. A. Wheeler, Phys. Rev. **108**, 1063 (1957) 10.1103/PhysRev.108.1063.

[42] F. J. Zerilli, Phys. Rev. Lett. **24**, 737 (1970) 10.1103/PhysRevLett.24.737.

[43] M. Boyle and A. H. Mroue, Phys. Rev. D **80**, 124045 (2009) 10.1103/PhysRevD.80.124045.

[44] A. Ashtekar and M. Streubel, Proceedings of the Royal Society of London. Series A, Mathematical and Physical Sciences **376**, 585 (1981).

[45] P. Virtanen et al., Nature Meth. **17**, 261 (2020) 10.1038/s41592-019-0686-2.

[46] R. Geroch, "Asymptotic structure of space-time", in *Asymptotic structure of space-time*, edited by F. P. Esposito and L. Witten (Springer US, Boston, MA, 1977), pp. 1–105, 10.1007/978-1-4684-2343-3_1.

[47] R. P. Geroch and J. Winicour, J. Math. Phys. **22**, 803 (1981) 10.1063/1.524987.

[48] E. Gallo and O. M. Moreschi, Phys. Rev. D **89**, 084009 (2014) 10.1103/PhysRevD.89.084009.

Chapter 5

FIXING THE BMS FRAME OF NUMERICAL RELATIVITY WAVEFORMS WITH BMS CHARGES

K. Mitman et al., Phys. Rev. D **106**, 084029 (2022) 10.1103/PhysRevD.106.084029,

5.1 Abstract

The Bondi-van der Burg-Metzner-Sachs (BMS) group, which uniquely describes the symmetries of asymptotic infinity and therefore of the gravitational waves that propagate there, has become increasingly important for accurate modeling of waveforms. In particular, waveform models, such as post-Newtonian (PN) expressions, numerical relativity (NR), and black hole perturbation theory, produce results that are in different BMS frames. Consequently, to build a model for the waveforms produced during the merging of compact objects, which ideally would be a hybridization of PN, NR, and black hole perturbation theory, one needs a fast and robust method for fixing the BMS freedoms. In this work, we present the first means of fixing the entire BMS freedom of NR waveforms to match the frame of either PN waveforms or black hole perturbation theory. We achieve this by finding the BMS transformations that change certain charges in a prescribed way—e.g., finding the center-of-mass transformation that maps the center-of-mass charge to a mean of zero. We find that this new method is 20 times faster, and more correct when mapping to the superrest frame, than previous methods that relied on optimization algorithms. Furthermore, in the course of developing this charge-based frame fixing method, we compute the PN expression for the Moreschi supermomentum to 3PN order without spins and 2PN order with spins. This Moreschi supermomentum is effectively equivalent to the energy flux or the null memory contribution at future null infinity $\mathscr{I}^+$. From this PN calculation, we also compute oscillatory ($m \neq 0$ modes) and spin-dependent memory terms that have not been identified previously or have been missing from strain expressions in the post-Newtonian literature.

5.2 Introduction

In the coming years, as gravitational wave detectors such as LIGO, Virgo, and KAGRA commence their next observing run, the catalog of astrophysical binary

events is predicted to considerably increase [1–3]. With so many more gravitational-wave events, tests of Einstein's theory of general relativity can then become even more robust and informative [4, 5]. From an analysis point of view, however, regardless of how much the gravitational-wave transient catalog increases in size over time, our ability to examine these events will always be limited by the accuracy of our waveform models, since they serve as the basis against which we can compare our observations.

Currently, and likely for the foreseeable future, the most accurate models for the gravitational waves emitted by the most commonly observed astrophysical binary system, binary black holes (BBHs), are the waveforms produced by numerical relativity (NR). Numerical waveforms uniquely maintain their precision throughout the whole evolution of the binary system. By contrast, other waveform models can only be considered correct during certain phases of the binary merger—e.g., post-Newtonian (PN) theory during inspiral or black hole perturbation theory during ringdown. However, numerical simulations are finite in time and thus can never produce the full waveform emitted by a binary event. Therefore, the best waveform model that we can hope to build is a hybridization of these models: a waveform that is PN from far into the past until we approach the merger regime, numerical throughout the merger phase, and then black hole perturbation theory during the final stages of ringdown. But, to construct such a waveform requires knowledge of how these models are related to each other. More specifically, to perform such a hybridization one needs to be able to ensure that these waveform models are in the same *frame*.

Like any observable in nature, the gravitational waves that we detect are emitted by a system that is in a certain frame relative to us. Often, this frame is best interpreted by using the symmetries of the system to understand the transformation between the system and the detector. For the gravitational radiation that we observe, which for practical purposes can be interpreted as existing at asymptotic infinity, the symmetry group is not the usual Poincaré group, but an extension: the *BMS group* [6, 7].

The BMS group is the symmetry group of asymptotically flat, Lorentzian spacetimes at null infinity $\mathscr{I}$ [6, 7]. It can be viewed as a combination of the Lorentz group with an infinite dimensional group of transformations called *supertranslations* [6, 7].[1] While surprising at first, these supertranslations have a natural origin. Con-

[1] Formally, the BMS group is understood to be a semidirect product of the Lorentz group with the infinite-dimensional Abelian group of supertranslations containing the spacetime translations as

sider, for example, a network of observers positioned on a sphere of finite radius encompassing a source. With some effort, these observers could combine their received signals with some understanding of their clocks' synchronization. But, if we move these observers to asymptotic infinity, then such a synchronization becomes impossible because of the infinite separation of the observers. More specifically, they will no longer be in causal contact. Thus, we can freely time translate—i.e., supertranslate—each observer without changing the observable physics. Put differently, supertranslations are time translations applied to each point on the two-sphere at asymptotic infinity. That is, they are simply direction-dependent time translations. Consequently, supertranslations change the retarded or Bondi time $u \equiv t - r$ via

$$\begin{aligned} u'(u,\theta,\phi) &= u - \alpha(\theta,\phi) \\ &= u - \sum_{\ell=0}^{\infty} \sum_{|m|\leq\ell} \alpha_{(\ell,m)} Y_{(\ell,m)}(\theta,\phi). \end{aligned} \tag{5.1}$$

In Eq. (5.1), $\alpha(\theta,\phi)$ is the supertranslation parameter, with $\alpha_{\ell,m} = (-1)^m \overline{\alpha}_{\ell,-m}$ to make sure that the transformed Bondi time u' is real. Using spherical harmonics to express supertranslations in components is useful because we see that the usual spacetime translations are nothing more than the $\ell \leq 1$ supertranslations, while supertranslations with $\ell \geq 2$ are the new, proper supertranslations [8, 9].

When we compare waveform models, we need to make sure that the Poincaré freedoms are equivalently fixed, e.g., to ensure that both models represent a binary in the center-of-mass frame. However, because of these new symmetries that arise at asymptotic infinity through the $\ell \geq 2$ supertranslations, we must also require that the supertranslation freedom of each model is fixed in an equivalent manner. In the work of [9] this task of fixing the BMS frame of a numerical waveform to match that of a PN system was pursued for the first time. Reference [9] did this by minimizing the error between a NR strain waveform and a PN strain waveform, iterating through various BMS transformations to find the best transformations to apply to the NR system. Because the BMS group is infinite dimensional, to restrict the parameter space, Ref. [9] restricted the transformations to only include supertranslations up to $\ell \leq 4$, producing a 22-dimensional parameter space (10 Poincaré + 12 supertranslations).[2] Because of this, the optimization algorithm

a normal subgroup.

[2] Actually, their parameter space was only 16-dimensional because they fixed the center-of-mass transformation using the system's center-of-mass charge. However, the following argument that we make is nonetheless valid because of the large number of parameters that were involved in the minimization.

required a large amount of CPU time: nearly 12 hours per system.[3] Furthermore, because of this need to restrict the number of transformations that can be applied for the sake of the optimization algorithm, it is clear that this method of fixing the BMS frame will not be sufficient when we want to include higher order modes in our models, which will be important for future detectors.

In this work, we present a more sophisticated means of fixing the BMS frame, which relies solely on BMS charges and thus removes the need for optimization algorithms.[4] This idea is motivated by the success that the authors of [9] had when fixing the center-of-mass frame with the center-of-mass charge.[5] In this work, the charges used to fix the Poincaré frame are the center-of-mass charge and rotation charge, while the charge used to constrain the supertranslation freedom is a charge known as the Moreschi supermomentum, which is an extension of the usual Bondi four-momentum [10]. With these charges we then map the NR waveforms to two unique frames: the PN BMS frame, i.e., the frame that PN waveforms are in, and the superrest frame at timelike infinity i^+, i.e., the frame that quasi-normal modes (QNMs) are computed in. To map to the PN BMS frame, we find that we need to compute the PN Moreschi supermomentum to 3PN order with spins and 2PN order without spins. Upon doing so, we discover oscillatory memory terms and spin-dependent memory terms that have not been identified or have been missing from the PN strain in the literature. We find that by fixing the frame of the numerical waveforms using this charge-based method, rather than the optimization used in [9], we can not only obtain the same, if not better, errors between waveform models, but also do so in roughly 30 minutes compared to the previous run time of 12 hours.

5.2.1 Overview

We organize our computations and results as follows. In Sec. 5.3 we describe how the BMS transformations transform the asymptotic variables. We also present the three BMS charges that we will be using in our analyses: the center-of-mass charge, the rotation charge, and the Moreschi supermomentum. Following this, in Sec. 5.4, we calculate the PN Moreschi supermomentum and present the new PN memory terms that have been missing from earlier calculations of the PN strain. Finally, in

[3] Moreover, because the BMS transformations were found using an optimizer rather than a physically motivated scheme, the waveforms produced tended to be in an error-minimizing but physically incorrect BMS frame. See, for example, Fig. 9 of [9].

[4] Note that here we use the term 'charge' in a more relaxed way, i.e., not in the sense of a symmetry algebra acting on a system.

[5] See, for example, Figs. 4 and 5 of [9].

Sec. 5.5 we show our numerical results. In Sec. 5.5.1 we outline our method for fixing the BMS frame with BMS charges. In Sec. 5.5.2 we compare this new charge-based method's ability to map the NR system to either the PN BMS frame or the remnant black hole's superrest frame to that of the previous method. In Sec. 5.5.3 we then highlight how waveforms produced via Cauchy-characteristic extraction are much more applicable and correct than the previously used extrapolated waveforms, once their BMS frame has been fixed with this new charge-based method. Lastly, in Appendices 5.A and 5.B we present the complete results of our PN calculations for the Moreschi supermomentum and the memory terms missing from the PN strain.

5.2.2 Conventions

We set $c = G = 1$ and take $\eta_{\mu\nu}$ to be the $(-,+,+,+)$ Minkowski metric. When working with complex dyads, following the work of [9, 11], we use

$$q_A = -\frac{1}{\sqrt{2}}(1, i\sin\theta) \text{ and } q^A = -\frac{1}{\sqrt{2}}(1, i\csc\theta), \tag{5.2}$$

and write the round metric on the two-sphere S^2 as q_{AB}. The complex dyad obeys the following properties

$$q_A q^A = 0, \quad q_A \bar{q}^A = 1, \quad q_{AB} = q_A \bar{q}_B + \bar{q}_A q_B. \tag{5.3}$$

Note that this convention differs from the related works of [12–14], which in contrast do not include the $1/\sqrt{2}$ normalization factor on the dyads in Eq. (5.2). We choose this convention because it makes our expressions for the asymptotic charges in Eq. (5.17) more uniform. Nonetheless, for transparency we provide the conversion between our quantities and those of these previous works in Eq. (5.9).

We build spin-weighted fields with the dyads as follows. For a tensor field $W_{A\cdots D}$, the function

$$W = W_{A\cdots BC\cdots D} q^A \cdots q^B \bar{q}^C \cdots \bar{q}^D \tag{5.4}$$

with m factors of q and n factors of $\bar{q}$ has a spin-weight of $s = m - n$. When raising and lowering spin-weights we use the Geroch-Held-Penrose differential spin-weight operators $\eth$ and $\bar{\eth}$ [15],

$$\eth W = (D_E W_{A\cdots BC\cdots D}) q^A \cdots q^B \bar{q}^C \cdots \bar{q}^D q^E, \tag{5.5a}$$

$$\bar{\eth} W = (D_E W_{A\cdots BC\cdots D}) q^A \cdots q^B \bar{q}^C \ldots \bar{q}^D \bar{q}^E. \tag{5.5b}$$

Here, D_A is the covariant derivative on the two-sphere. The $\eth$ and $\bar{\eth}$ operators in spherical coordinates are then

$$\eth W(\theta,\phi) = -\frac{1}{\sqrt{2}}(\sin\theta)^{+s}(\partial_\theta + i\csc\theta\partial_\phi) \left[(\sin\theta)^{-s} W(\theta,\phi)\right], \tag{5.6a}$$

$$\bar{\eth} W(\theta,\phi) = -\frac{1}{\sqrt{2}}(\sin\theta)^{-s}(\partial_\theta - i\csc\theta\partial_\phi) \left[(\sin\theta)^{+s} W(\theta,\phi)\right]. \tag{5.6b}$$

Thus, when acting on spin-weighted spherical harmonics, these operators produce

$$\eth({}_sY_{(\ell,m)}) = +\frac{1}{\sqrt{2}}\sqrt{(\ell-s)(\ell+s+1)}\,{}_{s+1}Y_{(\ell,m)}, \tag{5.7a}$$

$$\bar{\eth}({}_sY_{(\ell,m)}) = -\frac{1}{\sqrt{2}}\sqrt{(\ell+s)(\ell-s+1)}\,{}_{s-1}Y_{(\ell,m)}. \tag{5.7b}$$

We denote the gravitational wave strain[6] by h, which we represent in a spin-weight -2 spherical harmonic basis,

$$h(u,\theta,\phi) = \sum_{\ell,m} h_{(\ell,m)}(u)\,{}_{-2}Y_{(\ell,m)}(\theta,\phi), \tag{5.8}$$

where, again, $u \equiv t - r$ is the Bondi time. We denote the Weyl scalars by Ψ_{0-4}. The conversion from the convention of [12, 14] (`NR`[7]) to ours (`MB`[8]) is

$$h^{\mathtt{NR}} = 2\bar{\sigma}^{\mathtt{MB}} \quad \text{and} \quad \Psi_i^{\mathtt{NR}} = \frac{1}{2}(-\sqrt{2})^i \Psi_i^{\mathtt{MB}}. \tag{5.9}$$

Note that we will omit these superscripts and henceforth assume that everything is in the `MB` convention.

5.3 BMS transformations and charges

As discussed in the introduction, the symmetry group of asymptotic infinity is not the usual Poincaré group, but the BMS group, in which the spacetime translations are extended through an infinite-dimensional group of transformations called supertranslations [6, 7]. Therefore, to understand the frame of asymptotic radiation, we must understand how the asymptotic variables transform under an arbitrary BMS

[6] We explicitly define the strain as described in Appendix C of [16].

[7] `NR` because this is the convention that corresponds to the outputs of the SXS simulations.

[8] `MB` because this corresponds to the Moreschi-Boyle convention used in the works [8–11, 17, 18] and the code `scri` [8, 19–21].

transformation. Every BMS transformation can be uniquely decomposed as a pure supertranslation followed by a Lorentz transformation. In terms of retarded time u and a complex stereographic coordinate ζ on the two-sphere,

$$(u, \zeta) \equiv \left(t - r, e^{i\phi} \cot(\theta/2)\right) \tag{5.10}$$

a BMS transformation acts on the coordinates as [8, 17]

$$(u, \zeta) \to (u', \zeta') = \left(k\,(u - \alpha)\,, \frac{a\zeta + b}{c\zeta + d}\right), \tag{5.11}$$

where the conformal factor is

$$k(\zeta, \bar{\zeta}) \equiv \frac{1 + \zeta\overline{\zeta}}{(a\zeta + b)\left(\overline{a}\overline{\zeta} + \overline{b}\right) + (c\zeta + d)\left(\overline{c}\overline{\zeta} + \overline{d}\right)}, \tag{5.12}$$

(a, b, c, d) are complex coefficients satisfying $ad - bc = 1$, and the parameter $\alpha(\zeta, \bar{\zeta})$ is a real-valued and smooth function on the celestial two-sphere. The parameters (a, b, c, d) encode Lorentz transformations—both boost and rotations—whereas the function $\alpha(\zeta, \bar{\zeta})$ describes supertranslations, and thus also translations. By examining how the associated tetrad transforms under a BMS transformation [8, 22], one then finds that the shear and the Weyl scalars transform as

$$\sigma' = \frac{e^{2i\lambda}}{k}\left[\sigma - \eth^2\alpha\right], \tag{5.13a}$$

$$\Psi'_A = \frac{e^{(2-A)i\lambda}}{k^3}\sum_{a=A}^{4}\binom{4-A}{a-A}\left(-\frac{\eth u'}{k}\right)^{a-A}\Psi_a, \tag{5.13b}$$

where $A \in \{0, 1, 2, 3, 4\}$ and λ is the spin phase [8, 22]:

$$\exp(i\lambda) = \left[\frac{\partial\overline{\zeta'}}{\partial\overline{\zeta}}\left(\frac{\partial\zeta'}{\partial\zeta}\right)^{-1}\right]^{1/2} = \frac{c\zeta + d}{\overline{c}\overline{\zeta} + \overline{d}}. \tag{5.14}$$

For a Lorentz transformation parameterized by (a, b, c, d) and a supertranslation parameterized by α, Eqs. (5.11) and (5.13) are the primary ingredients for understanding how the asymptotic variables, namely the shear as well as the Weyl scalars, transform under a BMS transformation. All that remains is a method for finding the necessary frame-fixing BMS transformation, which we outline in Secs. 5.3.1 for the Poincaré transformations and 5.3.2 for the proper supertranslations.

5.3.1 Poincaré charges

In this section, following the work of [9], we outline the Poincaré charges that will be used to completely fix the Poincaré transformation freedom of the asymptotic shear and Weyl scalars. As was shown in [6, 9, 23–30], by examining the expansion of the Bondi-Sachs metric near future null infinity, one can identify certain functions that yield the Poincaré charges when integrated over the celestial two-sphere. They are the Bondi mass aspect m, the Lorentz aspect N, and the energy moment aspect E, which in the `MB` convention are

$$m(u,\theta,\phi) \equiv -\mathrm{Re}\left[\Psi_2 + \sigma\dot{\bar{\sigma}}\right], \tag{5.15a}$$

$$N(u,\theta,\phi) \equiv -\left(\Psi_1 + \sigma\eth\bar{\sigma} + u\eth m + \frac{1}{2}\eth\left(\sigma\bar{\sigma}\right)\right), \tag{5.15b}$$

$$\begin{aligned} E(u,\theta,\phi) &\equiv N + u\eth m \\ &= -\left(\Psi_1 + \sigma\eth\bar{\sigma} + \frac{1}{2}\eth\left(\sigma\bar{\sigma}\right)\right). \end{aligned} \tag{5.15c}$$

Thus, by defining a collection of spin-0 scalar functions, $\mathbf{n}(\theta,\phi)$, whose components are unique combinations of the $\ell \leq 1$ spherical harmonics so as to represent one of the four Cartesian coordinates t, x, y, or z, i.e.,

$$\begin{aligned} n^t &= 1 \\ &= \sqrt{4\pi}Y_{(0,0)}, \end{aligned} \tag{5.16a}$$

$$\begin{aligned} n^x &= \sin\theta\cos\phi, \\ &= \sqrt{\frac{4\pi}{3}}\left[\frac{1}{\sqrt{2}}\left(Y_{(1,-1)} - Y_{(1,+1)}\right)\right], \end{aligned} \tag{5.16b}$$

$$\begin{aligned} n^y &= \sin\theta\sin\phi \\ &= \sqrt{\frac{4\pi}{3}}\left[\frac{i}{\sqrt{2}}\left(Y_{(1,-1)} + Y_{(1,+1)}\right)\right], \end{aligned} \tag{5.16c}$$

$$\begin{aligned} n^z &= \cos\theta \\ &= \sqrt{\frac{4\pi}{3}}Y_{(1,0)}, \end{aligned} \tag{5.16d}$$

we can then compute each Cartesian component of the translation, rotation, boost, and center-of-mass charges. For $a \in \{t, x, y, z\}$, these four Poincaré charges are

$$P^a(u) = \frac{1}{4\pi} \int_{S^2} n^a m \, d\Omega, \tag{5.17a}$$

$$J^a(u) = \frac{1}{4\pi} \int_{S^2} \mathrm{Re}\left[\left(\bar{\eth} n^a\right)(-iN)\right] \, d\Omega, \tag{5.17b}$$

$$K^a(u) = \frac{1}{4\pi} \int_{S^2} \mathrm{Re}\left[\left(\bar{\eth} n^a\right) N\right] \, d\Omega, \tag{5.17c}$$

$$\begin{aligned} G^a(u) &= \left(K^a + uP^a\right)/P^t \\ &= \frac{1}{4\pi} \int_{S^2} \mathrm{Re}\left[\left(\bar{\eth} n^a\right)(N + u\eth m)\right] \, d\Omega/P^t. \end{aligned} \tag{5.17d}$$

Then, by making use of the orthogonality property of spherical harmonics, we find that the four vector of a Poincaré charge Π is simply

$$\Pi^t = \frac{1}{\sqrt{4\pi}} \Pi_{(0,0)}, \tag{5.18a}$$

$$\Pi^x = \frac{1}{\sqrt{4\pi}} \frac{1}{\sqrt{6}} \mathrm{Re}\left[\Pi_{(1,-1)} - \Pi_{(1,+1)}\right], \tag{5.18b}$$

$$\Pi^y = \frac{1}{\sqrt{4\pi}} \frac{1}{\sqrt{6}} \mathrm{Im}\left[\Pi_{(1,-1)} + \Pi_{(1,+1)}\right], \tag{5.18c}$$

$$\Pi^z = \frac{1}{\sqrt{4\pi}} \frac{1}{\sqrt{3}} \mathrm{Re}\left[\Pi_{(1,0)}\right], \tag{5.18d}$$

where $\Pi_{(\ell,m)}$ is the (ℓ, m) mode of the charge Π in the basis of spin-s spherical harmonics ($s = 0$ for m, and $s = 1$ for $-iN, N$, and $N + u\eth m$). These charges in Eqs. (5.17) have simple interpretations by analogy to kinematics in Minkowski space. P^a is the total linear momentum, J^a is the total angular momentum—orbital plus spin, K^a is proportional to the center-of-mass at time $u = 0$, and G^a is the center-of-mass at time u. For more on these charges in the PN formulation, see [31] for an analysis using conservative point particle theory, [32] for an analysis when radiation is involved, and [33] for a connection to the Poincaré and BMS flux-balance laws.

While the Poincaré charges in Eq. (5.17) are the most natural to work with for fixing frames, since we will be comparing the frame of numerical waveforms to that of PN waveforms, we need either PN or BH perturbation theory expressions for these charges. Notice, however, that Eqs. (5.17) contain the Weyl scalars Ψ_1 and Ψ_2. Thus we need the PN expressions for these Weyl scalars, which have not been computed thus far in the PN literature.[9] Fortunately, PN waveforms are inherently constructed

[9] This would be a valuable calculation to carry out in the future.

in the center-of-mass frame. The center-of-mass charge G^a, given in Eq. (5.17d), can be taken to have an average of zero, i.e., an intercept and a slope of zero when fitted to with a linear function in time, though it is oscillatory at high enough PN order. For mapping to the superrest frame, we can also map the center-of-mass charge to have an average of zero, seeing as we want our remnant black hole to asymptote to a stationary Kerr black hole.

The rotation charge, Eq. (5.17b), however, tends to be some nontrivial function of time. Therefore, for fixing the rotation freedom to match that of PN waveforms, we require an alternative rotation charge that is independent of the Ψ_1 and Ψ_2 Weyl scalars. In the work of [20] such a rotation charge was built by finding the angular velocity which keeps the radiative fields as constant as possible in the corotating frame. Following the notation of [20, 34], this vector, with "$\cdot$" the usual dot product, is

$$\vec{\omega}(u) = -\langle \vec{L}\vec{L}\rangle^{-1} \cdot \langle \vec{L}\partial_t\rangle, \tag{5.19}$$

where we use the u-dependent vector and matrix

$$\langle \vec{L}\partial_t\rangle^a \equiv \sum_{\ell,m,m'} \mathrm{Im}\left[\bar{f}_{(\ell,m')}\langle \ell, m'|L^a|\ell, m\rangle \dot{f}_{(\ell,m)}\right], \tag{5.20a}$$

$$\langle \vec{L}\vec{L}\rangle^{ab} \equiv \sum_{\ell,m,m'} \bar{f}_{(\ell,m')}\langle \ell, m'|L^{(a}L^{b)}|\ell, m\rangle f_{(\ell,m)}, \tag{5.20b}$$

and $f(u,\theta,\phi)$ is some function that corresponds to the asymptotic radiation, e.g., the shear σ or the news $\dot{\sigma}$. This data is represented in the basis $|\ell, m\rangle$ of spin-weighted spherical harmonics, with time-dependent mode weights $f_{(\ell,m)}$, i.e. $|f\rangle = \sum_{\ell,m} f_{(\ell,m)}|\ell, m\rangle$. The operator $\vec{L}$ is the infinitesimal generator of rotations, whose related charge is the total angular momentum charge J^a provided in Eq. (5.17b). Therefore, when fixing the frame of the waveforms to match that of the PN system, i.e., to match the frames at spacelike infinity, we will use the vector in Eq. (5.19).

For fixing the rotation at timelike infinity—the case of a system consisting of a single black hole—we also choose to use a rotation charge that is not the charge seen in Eq. (5.17b). This is because at timelike infinity, provided that we are in the center-of-mass frame of the remnant black hole, we do not expect there to be any orbital angular momentum contributions, but instead only spin angular momentum contributions. Thus, for fixing the rotation freedom it is more useful to work with the asymptotic dimensionless spin vector [11]:

$$\vec{\chi}(u) = \frac{\gamma}{M_{\mathrm{B}}^2}\left(\vec{J} + \vec{v}\times\vec{K}\right) - \frac{\gamma-1}{M_{\mathrm{B}}^2}\left(\hat{v}\cdot\vec{J}\right)\hat{v}, \tag{5.21}$$

where

$$\gamma(u) \equiv \sqrt{1 - |\vec{v}|^2}^{-1} \tag{5.22}$$

is the Lorentz factor,

$$M_{\rm B}(u) \equiv \sqrt{-\eta_{\mu\nu} P^\mu P^\nu} \tag{5.23}$$

is the Bondi mass,

$$\vec{v}(u) \equiv \vec{P}/P^t \tag{5.24}$$

is the velocity vector, and the vectors $\vec{J}$ and $\vec{K}$ are the angular momentum and boost Poincaré charges, i.e., Eqs. (5.17b) and (5.17c), evaluated at the vector $\vec{n} = (\vec{x}, \vec{y}, \vec{z})$. With this charge, we can then fix the rotation freedom by solving for the rotation that maps this charge to be parallel to the positive z-axis: the standard convention for studying QNMs. This fully fixes the rotation freedom of our system, up to a $U(1)$ transformation that can be thought of as a constant phase change. For mapping to the PN BMS frame, this remaining $U(1)$ freedom is fixed while running a time and phase alignment that minimizes the residual between the NR and PN strain waveforms. For mapping to the superrest frame at timelike infinity, no phase fixing is performed as it is not necessary for analyzing QNMs.

5.3.2 $\ell \geq 2$ supertranslation charge

For fixing the supertranslation freedom of a system, because the supertranslations are just extensions of the usual spacetime translations, it is reasonable to ask if there is a clear extension of the Bondi four-momentum [6]

$$P^a(u) = \frac{1}{4\pi} \int_{S^2} n^a \mathrm{Re}\left[\Psi_2 + \sigma \dot{\bar{\sigma}}\right] \, d\Omega. \tag{5.25}$$

As was pointed out by Dray and Streubel [35], and also independently realized later by Wald and Zoupas [36], the possible choices for a *supermomentum* can be written as

$$\Psi_{p,q}(u, \theta, \phi) = \Psi_2 + \sigma \dot{\bar{\sigma}} + p\left(\eth^2 \bar{\sigma}\right) - q\left(\bar{\eth}^2 \sigma\right), \tag{5.26}$$

where p and q are arbitrary real numbers. From this supermomentum expression, one can show that if $p = q$ then there is no supermomentum flux in Minkowski space and if $p + q = 1$ then the supermomentum is real [35, 36]. This leads to a natural

choice of supermomentum being the Geroch (G) supermomentum with $p = q = \frac{1}{2}$, i.e.,

$$\Psi_{\rm G}(u,\theta,\phi) \equiv \Psi_2 + \sigma\dot{\bar{\sigma}} + \frac{1}{2}\left(\eth^2\bar{\sigma} - \bar{\eth}^2\sigma\right). \tag{5.27}$$

It turns out, though, that in regimes that are nonradiative (i.e., $\dot{\sigma} = 0$), the Geroch supermomentum is not changed by a supertranslation since

$$\begin{aligned}\Psi'_{\rm G} &= \frac{1}{k^3}\left(\Psi_{\rm G} - \frac{1}{2}\left[2\eth\alpha\eth\dot{\bar{\sigma}} + \left(\eth^2\alpha\right)\dot{\bar{\sigma}} + (\eth\alpha)^2\ddot{\bar{\sigma}} + \text{c.c.}\right]\right)\\ &\to \frac{1}{k^3}\Psi_{\rm G} \quad (\text{for } \dot{\sigma}\to 0)\,.\end{aligned} \tag{5.28}$$

Therefore, while the Geroch supermomentum may be an ideal choice for a physical supermomentum, for fixing the supertranslation freedom of our system it will instead be useful to construct a supertranslation charge that does transform under supertranslations. But what are the features of the system that we would like to control using these supertranslation transformations?

When we examine how supertranslations transform asymptotic radiation, Eq. (5.13a) shows that the shear is changed by a term constant in time and proportional to the supertranslation parameter $\alpha(\theta,\phi)$. Consequently, because supertranslations affect the value of the shear even in nonradiative regimes, we can interpret them as also being related to the gravitational memory effect—i.e., the physical observable that corresponds to the permanent net change in the metric due to the passage of transient gravitational radiation [37–39].[10]

Gravitational memory can best be understood through the supermomentum balance law [43], which says that the real part of the shear can be written as

$$\begin{aligned}\text{Re}\left[\bar{\eth}^2\sigma\right] &= m + \int_{-\infty}^{u}|\dot{\sigma}|^2 du + \left(\text{Re}\left[\bar{\eth}^2\sigma\right] - m\right)|^{-\infty}\\ &= m + \mathcal{E} - M_{\rm ADM},\end{aligned} \tag{5.29}$$

where

$$\mathcal{E}(u,\theta,\phi) \equiv \int_{-\infty}^{u}|\dot{\sigma}|^2 du \tag{5.30}$$

is proportional to the energy radiated up to time u into the direction (θ,ϕ), and $M_{\rm ADM}$ is the Arnowitt-Deser-Misner (ADM) mass [44]. If one evaluates this equation

[10] Supertranslations and the memory effect both correspond to changes in the value of the strain: supertranslations are merely gauge transformations, while the memory effect can be understood as corresponding to holonomy [40–42].

between early times and late times (i.e., $\pm\infty$), then the net change in the shear (the memory) has two unique contributions: one from the net change in the mass aspect (the *ordinary*[11] memory) and one from the net change in the system's energy flux (the *null*[12] memory). Note that the ADM mass does not contribute to the memory because it is a constant on the two-sphere and therefore has no $\ell \geq 2$ components. Typically, ordinary memory occurs in systems that have unbound masses, such as hyperbolic black holes, while null memory occurs in systems that have bound masses, such as binary black holes. Furthermore, if one examines how this equation changes under a BMS transformation, one finds

$$\begin{aligned} m' &= \frac{1}{k^3}\left(m + \frac{1}{2}\left[2\eth\alpha\eth\dot{\bar{\sigma}} + \left(\eth^2\alpha\right)\dot{\bar{\sigma}} + (\eth\alpha)^2\ddot{\bar{\sigma}} + \text{c.c.}\right]\right) \\ &\to \frac{1}{k^3}m \quad \text{(when nonradiative)}\,, \end{aligned} \tag{5.31a}$$

$$\mathcal{E}' = \frac{1}{k^3}\left(\mathcal{E} - \eth^2\bar{\eth}^2\alpha\right) \quad \text{(always)}\,. \tag{5.31b}$$

So, when written in terms of its charge (m) and flux ($\mathcal{E}$) contributions, the only part of the shear that transforms under a supertranslation in nonradiative regimes of $\mathscr{I}^+$ is the energy flux contribution. This suggests that the charge that would be the ideal charge for measuring what supertranslation we should apply to our system would be something equivalent to the energy flux. Fortunately, such a charge, the Moreschi supermomentum, has already been examined by Dain and Moreschi [10, 17, 18, 22]:

$$\Psi_{\text{M}}(u,\theta,\phi) \equiv \Psi_2 + \sigma\dot{\bar{\sigma}} + \eth^2\bar{\sigma}. \tag{5.32}$$

This is simply Eq. (5.26) with coefficients $p = 1$ and $q = 0$. By rewriting the first term in Eq. (5.32) as a time integral, making use of the Bianchi identity

$$\dot{\Psi}_2 = -\sigma\ddot{\bar{\sigma}} + \eth^2\bar{\sigma}, \tag{5.33}$$

and integrating by parts we find

$$\begin{aligned} \Psi_{\text{M}} &= \left(\int_{-\infty}^{u} \dot{\Psi}_2\, du - M_{\text{ADM}}\right) + \sigma\dot{\bar{\sigma}} + \eth^2\bar{\sigma} \\ &= \left(\int_{-\infty}^{u} \left(-\sigma\ddot{\bar{\sigma}} + \eth^2\bar{\sigma}\right) du - M_{\text{ADM}}\right) + \sigma\dot{\bar{\sigma}} + \eth^2\bar{\sigma} \\ &= \int_{-\infty}^{u} |\dot{\sigma}|^2 du - M_{\text{ADM}} \\ &= \mathcal{E} - M_{\text{ADM}}. \end{aligned} \tag{5.34}$$

[11] Also called linear memory [37].
[12] Also called nonlinear or Christodoulou memory [38, 39]

Because of this, the Moreschi supermomentum can also be thought of as the memory part of the mass moment.[13] Furthermore, by using Eq. (5.31b) with Eq. (5.34), one finds that the Moreschi supermomentum transforms as

$$\Psi'_{\rm M} = \frac{1}{k^3}\left(\Psi_{\rm M} - \eth^2\bar{\eth}^2\alpha\right). \tag{5.35}$$

Equations (5.29) and (5.35) then imply that we can rewrite the transformation of the shear under a supertranslation in a nonradiative regime of $\mathscr{I}^+$ as

$$\begin{aligned}\mathrm{Re}\left[\bar{\eth}^2\sigma\right]' &= m' + \Psi'_{\rm M}\\ &= m + \left(\Psi_{\rm M} - \eth^2\bar{\eth}^2\alpha\right).\end{aligned} \tag{5.36}$$

This shows that by fixing the supertranslation freedom with the Moreschi supermomentum one also immediately has an understanding of how the shear will transform. Consider applying the supertranslation that maps the $\ell \geq 1$, i.e., the nontemporal, components of $\Psi_{\rm M}$ to zero in a nonradiative regime of $\mathscr{I}^+$. For bound systems, which asymptote to regimes of $\mathscr{I}^+$ that are nonradiative and stationary,[14] such a transformation also maps the shear to zero in the nonradiative regime of $\mathscr{I}^+$ because in this regime $\mathrm{Re}\left[\bar{\eth}^2\sigma\right] = \Psi_{\rm M}$. Consequently, for systems like BBHs, by performing such a mapping at $u \to -\infty$ or at $u \to +\infty$, one can wholly fix the supertranslation freedom of the system so that it agrees with PN waveforms or QNM models. Moreschi calls a frame in which the $\ell \geq 1$ components of $\Psi_{\rm M}$ are zero a *nice section* of $\mathscr{I}^+$; we, like [9, 46], will instead call it the *superrest* frame. Furthermore, since $\Psi_{\rm M}$ in the superrest frame at $u \to \pm\infty$ is equal to Bondi mass $M_{\rm B}$, the supertranslation α that maps to the superrest frame at a single time can be computed with relative ease via the implicit equation

$$\eth^2\bar{\eth}^2\alpha = \Psi_{\rm M}(u = \alpha, \theta, \phi) + k_{\rm rest}(\alpha, \theta, \phi)^3 M_{\rm B}(\alpha). \tag{5.37}$$

This equation for α is obtained by taking $\Psi'_{\rm M} = M_{\rm B}$ in Eq. (5.35) and rearranging terms. Note that here the conformal factor on the right, $k_{\rm rest}$, is a special case of the conformal factor given in Eq. (5.12): namely the one coming from a boost to the instantaneous rest frame at some fixed time, computed via

$$k_{\rm rest}(u, \theta, \phi) \equiv \frac{1}{\gamma\,(1 - \vec{v}\cdot\vec{r})} = \frac{M_B}{P_a n^a}. \tag{5.38}$$

[13] See, for example, Eq. (2.26) of [45].

[14] For bound systems, there exist frames at $u \to \pm\infty$ where the $\ell \geq 2$ components of the Bondi mass aspect m are exactly zero. While these frames at $u \to \pm\infty$ exist, they need not be the same.

Apart from this, Dain and Moreschi also proved that, provided a certain condition on the energy flux, which is always obeyed by nonradiative regimes of $\mathscr{I}^+$, this equation always has a regular solution [18]. Therefore, for the frames that we are mapping to, such a supertranslation will always exist. Furthermore, Dain and Moreschi also showed that Eq. (5.37) can be solved iteratively. That is, if one wishes to find the supertranslation that maps the system to the superrest frame at time u_0, they can take Eq. (5.37) and evaluate the right-hand side at time $u = u_0$, solve for α, evaluate the right-hand side at time $u = \alpha$, solve for a new α, etc., until α converges to a solution. We will make use of this fact in Sec. 5.5.

What remains unclear at this point, however, is whether the Moreschi supermomentum is also the right charge to use for fixing the frame of systems with unbound masses. For these unbound systems, the $\ell \geq 2$ components of m can have a nonzero net change between $u \to \pm\infty$, which means that mapping the $\ell \geq 1$ components of $\Psi_{\rm M}$ to zero need not map the system to a shear-free section of $\mathscr{I}^+$. Despite this, it may be that shear-free sections are not necessarily that meaningful and really what one should strive for when fixing the supertranslation freedom is ensuring that the shear has only hard contributions [24], i.e., no contribution from the energy flux. In this work, however, because we focus on bound systems, like BBHs and perturbed BHs, it will suffice to only consider the Moreschi supermomentum as the charge for fixing the supertranslation freedom of our systems.

5.4 PN supermomentum

With the Moreschi supermomentum now identified as the supertranslation charge that can map BBH systems (or other bound systems) to shear-free sections of $\mathscr{I}^+$, there are two obvious BMS frames that one can map to: the superrest frame at either $u \to -\infty$ or $u \to +\infty$. The first choice can be understood as mapping the system to the same frame as PN waveforms, i.e., shear-free in the infinite past. The second is naturally understood as mapping to the superrest frame of the remnant BH, i.e., making the metric equivalent to the Kerr metric rather than a supertranslated Kerr metric [47]. Waveforms produced by numerical relativity, however, are finite in time and thus do not contain information about $u \to -\infty$ or $u \to +\infty$. Thus, for fixing the frame of these waveforms we need to know what we should be mapping the numerical Moreschi supermomentum to with the Bondi times that we have access to. For mapping to the superrest frame of the remnant BH ($u \to +\infty$), this is simple because the radiation decays fast enough that mapping at or near the end of the simulation is a reasonable approximation to $u \to +\infty$. For mapping to the

same frame as PN waveforms, however, we cannot rely on approximations because the radiation during the inspiral of a BBH merger cannot be considered negligible. We instead need to know the Moreschi supermomentum predicted by PN theory. This will allow us to map the numerical supermomentum to equal that of the PN system, which serves as a proxy for mapping our NR system to the superrest frame at spacelike infinity. Accordingly, we now perform a PN calculation of the Moreschi supermomentum.

5.4.1 PN Moreschi supermomentum

The main ingredients for this PN calculation are the PN expressions for the strain both with and without the BH spins [21, 45, 48, 49],[15] the orbital energy [48, 50, 51], and the luminosity [48, 50, 51]. Using Eq. (5.9) to replace the shear by the strain in Eq. (5.34) and then moving the ADM mass to the other side of the equation yields

$$\Psi_{\rm M} + M_{\rm ADM} = \int_{-\infty}^{u} |\dot{\sigma}|^2 du = \frac{1}{4}\int_{-\infty}^{u} |\dot{h}|^2 du, \tag{5.39}$$

Therefore, provided a spherical harmonic decomposition of the PN strain, any spherical harmonic mode of the supermomentum can be computed by integrating the product of various spin-weighted spherical harmonics over the two-sphere as well as integrating the products of various modes of the strain with respect to time:

$$\begin{aligned}\Psi_{\rm M}^{(\ell,m)} = \frac{1}{4} \sum_{\ell_1,|m_1|\leq\ell_1} \sum_{\ell_2,|m_2|\leq\ell_2} \\ \left[\int_{S^2} \overline{{}_0Y_{\ell,m}}\, \overline{{}_{-2}Y_{\ell_1,m_1}}\, {}_{-2}Y_{\ell_2,m_2} d\Omega\right] \\ \left[\int \overline{\dot{h}^{(\ell_1,m_1)}}\, \dot{h}^{(\ell_2,m_2)} du\right].\end{aligned} \tag{5.40}$$

The first of these integrals can be easily computed from the spin-weighted spherical harmonics' relationship to the Wigner D-matrices combined with the known integral of a product of three D matrices [52], which produces

$$\begin{aligned}\int_{S^2} {}_{s_1}Y_{\ell_1 m_1}\, {}_{s_2}Y_{\ell_2 m_2}\, {}_{s_3}Y_{\ell_3 m_3} d\Omega = \sqrt{\frac{(2\ell_1+1)(2\ell_2+1)(2\ell_3+1)}{4\pi}} \\ \begin{pmatrix} \ell_1 & \ell_2 & \ell_3 \\ m_1 & m_2 & m_3 \end{pmatrix} \begin{pmatrix} \ell_1 & \ell_2 & \ell_3 \\ -s_1 & -s_2 & -s_3 \end{pmatrix}.\end{aligned} \tag{5.41}$$

[15] Note that there was a mistake made in [21] when calculating the spin-spin terms at 2PN order. We have corrected this mistake prior to using the PN strain in our calculations that follow.

For this part of the calculation, we also need the identity

$$\overline{{}_sY_{\ell,m}} = (-1)^{s+m}\,{}_{-s}Y_{\ell,-m}. \tag{5.42}$$

Next consider the integral with respect to time in the final part of Eq. (5.40). Because any mode of the strain can be written as

$$h^{(\ell,m)} = \frac{2M\nu x}{R}\sqrt{\frac{16\pi}{5}}\mathcal{H}^{(\ell,m)}e^{-im\psi}, \tag{5.43}$$

where $M \equiv m_1 + m_2$, $\nu \equiv m_1 m_2/M^2$, $x \equiv (M\omega)^{2/3}$ is the usual PN parameter, ψ is the auxiliary phase variable (see Eq. (321) of [48]), and $\mathcal{H}^{(\ell,m)}$ is a polynomial in x, we can perform a change of coordinates from u to x to obtain a series of integrals of the form

$$\int_{x_0}^{x} \dot{x}\,(d\psi/dx)^a\,x^b e^{-iA\psi(x)}dx, \tag{5.44}$$

where $a \in \{0,1,2\}$, $b \in \mathbb{N}$, $A \in \mathbb{Z}$, and x_0 corresponds to an arbitrary initial frequency ω_0. To evaluate these various integrals over x, consider first integrating the following expression by parts to obtain

$$\begin{aligned}
&\int_{x_0}^{x} f(x)e^{\varphi(x)}dx = \\
&\left[\left(\frac{d\varphi}{dx}\right)^{-1} f e^{\varphi}\right]_{x_0}^{x} \\
&-\int_{x_0}^{x}\left[\left(\frac{d\varphi}{dx}\right)^{-1}\frac{df}{dx} - \left(\frac{d\varphi}{dx}\right)^{-2}\frac{d^2\varphi}{dx^2}f\right]e^{\varphi}dx.
\end{aligned} \tag{5.45}$$

Because $\varphi \propto \psi \sim x^{-5/2}$, the PN order of the integrand on the right-hand side ends up being 2.5PN higher than the original integrand. Thus we can evaluate these integrals by integrating by parts until the unevaluated integrals have been pushed to a PN order above what we consider. Alternatively, one can evaluate such integrals with either the stationary phase approximation or the method of steepest descent [53], but the result should be the same. By carrying out this integration procedure, we then find that we can compute the PN Moreschi supermomentum to relative 3PN order when spins are not included and relative 2PN order when spins are included, with the limiting factor being the available PN order of the strain that we input into Eq. (5.39). We write the modes of the Moreschi supermomentum as

$$\Psi_{\mathrm{M}}^{(\ell,m)} = \frac{2M\nu x}{R^2}\sqrt{\frac{\pi}{4}}\mathcal{P}^{(\ell,m)}e^{-im\psi} - M\delta_{\ell,0}\delta_{m,0} \tag{5.46}$$

where $\mathcal{P}^{(\ell,m)}$ is a polynomial in x. The term in M that arises when $(\ell, m) = (0, 0)$ is because of the presence of the ADM mass in Eq. (5.34). While we write our results in full in Appendices 5.A and 5.B, we provide a few of the most interesting modes below. These results have been obtained using `Mathematica`.[16]

$$\mathcal{P}^{(0,0)} = 1 + x\left(-\frac{3}{4} - \frac{\nu}{12}\right) + x^2\left(-\frac{27}{8} + \frac{19\nu}{8} - \frac{\nu^2}{24}\right) + x^3\left(-\frac{675}{64} + \left(\frac{34445}{576} - \frac{205\pi^2}{96}\right)\nu - \frac{155\nu^2}{96} - \frac{35\nu^3}{5184}\right), \tag{5.47a}$$

$$\mathcal{P}^{(0,0)}_{\text{spin}} = x^{3/2}\left(\frac{14S_\ell}{3M^2} + \frac{2\delta\Sigma_\ell}{M^2}\right) + x^2\Bigg(-\frac{16\vec{S}\cdot\vec{S} + 3\vec{\Sigma}\cdot\vec{\Sigma} + 32S_\ell^2 + 9\Sigma_\ell^2}{12M^4} - \frac{4\delta\left(\vec{S}\cdot\vec{\Sigma} + 2S_\ell\Sigma_\ell\right)}{3M^4} + \frac{4\left(\vec{\Sigma}\cdot\vec{\Sigma} + 2\Sigma_\ell^2\right)\nu}{3M^4}\Bigg), \tag{5.47b}$$

$$\mathcal{P}^{(1,1)} = \frac{43}{70}\sqrt{\frac{3}{2}}\left\{x^3\left(\frac{1856\delta\nu}{129}\right)\right\}, \tag{5.47c}$$

$$\mathcal{P}^{(1,1)}_{\text{spin}} = 0, \tag{5.47d}$$

$$\mathcal{P}^{(2,0)} = \frac{2}{7}\sqrt{5}\Bigg\{1 + x\left(-\frac{4075}{4032} + \frac{67\nu}{48}\right) + x^2\left(-\frac{151877213}{67060224} - \frac{123815\nu}{44352} + \frac{205\nu^2}{352}\right) + \pi x^{5/2}\left(-\frac{253}{336} + \frac{253\nu}{84}\right) + x^3\Bigg(-\frac{4397711103307}{532580106240} + \left(\frac{700464542023}{13948526592} - \frac{205\pi^2}{96}\right)\nu + \frac{69527951\nu^2}{166053888} + \frac{1321981\nu^3}{5930496}\Bigg)\Bigg\}, \tag{5.47e}$$

$$\mathcal{P}^{(2,0)}_{\text{spin}} = \frac{2}{7}\sqrt{5}\Bigg\{x^{3/2}\left(\frac{16S_\ell}{3M^2} + \frac{419\delta\Sigma_\ell}{160M^2}\right) + x^2\Bigg(-\frac{128\vec{S}\cdot\vec{S} + 24\vec{\Sigma}\cdot\vec{\Sigma} + 256S_\ell^2 + 75\Sigma_\ell^2}{96M^4} - \frac{4\delta\left(\vec{S}\cdot\vec{\Sigma} + 2S_\ell\Sigma_\ell\right)}{3M^4} + \frac{4\left(\vec{\Sigma}\cdot\vec{\Sigma} + 2\Sigma_\ell^2\right)\nu}{3M^4}\Bigg)\Bigg\}, \tag{5.47f}$$

[16] The authors are willing to share the `Mathematica` notebook used for this calculation upon reasonable request.

Name	q	$(\chi_A^{\hat{x}},$	$\chi_A^{\hat{y}},$	$\chi_A^{\hat{z}})$	$(\chi_B^{\hat{x}},$	$\chi_B^{\hat{y}},$	$\chi_B^{\hat{z}})$
q1_nospin	1.0	(0,	0,	0)	(0,	0,	0)
q1_aligned_chi0_2	1.0	(0,	0,	0.2)	(0,	0,	0.2)
q1_aligned_chi0_4	1.0	(0,	0,	0.4)	(0,	0,	0.4)
q1_aligned_chi0_6	1.0	(0,	0,	0.6)	(0,	0,	0.6)
q1_antialigned_chi0_2	1.0	(0,	0,	0.2)	(0,	0,	−0.2)
q1_antialigned_chi0_4	1.0	(0,	0,	0.4)	(0,	0,	−0.4)
q1_antialigned_chi0_6	1.0	(0,	0,	0.6)	(0,	0,	−0.6)
q1_precessing	1.0	(0.487,	0.125,	−0.327)	(−0.190,	0.051,	−0.227)
q1_superkick	1.0	(0.6,	0,	0)	(−0.6,	0,	0)
q4_nospin	4.0	(0,	0,	0)	(0,	0,	0)
q4_aligned_chi0_4	4.0	(0,	0,	0.4)	(0,	0,	0.4)
q4_antialigned_chi0_4	4.0	(0,	0,	0.4)	(0,	0,	−0.4)
q4_precessing	4.0	(0.487,	0.125,	−0.327)	(−0.190,	0.051,	−0.227)
SXS:BBH:0305x	1.221	(0,	0,	0.330)	(0,	0,	−0.440)

Table 5.1: Parameters of the BBH mergers used in our results. The mass ratio is $q = M_A/M_B$ and the initial dimensionless spins of the two black holes are χ_A and χ_B. These simulations have been made publicly available at [54, 55].

$$\mathcal{P}^{(3,1)} = \frac{223}{120\sqrt{21}}\left\{x^3\left(\frac{3872\delta\nu}{223}\right)\right\}, \tag{5.47g}$$

$$\mathcal{P}^{(3,1)}_{\text{spin}} = 0. \tag{5.47h}$$

For the terms in these expressions that include spins, with M_1 and M_2 and $\vec{S}_1$ and $\vec{S}_2$ the masses and spins of the two black holes,

$$\vec{S} \equiv \vec{S}_1 + \vec{S}_2 \tag{5.48}$$

is the total spin vector,

$$\vec{\Sigma} \equiv M\left(\frac{\vec{S}_2}{M_2} - \frac{\vec{S}_1}{M_1}\right) \tag{5.49}$$

can be viewed as an effective antisymmetric spin vector, $\delta \equiv (M_1 - M_2)/M$, $\hat{n}$ is the unit vector pointing from black hole 2 to black hole 1, $\hat{\lambda}$ is the unit vector in the direction of $d\hat{n}/du$, and $\hat{\ell} = \hat{n} \times \hat{\lambda}$. We include these modes here for the following reasons. The $(0,0)$ mode is proportional to the energy radiated to future null infinity, and matches the orbital energy results of [48, 50, 51, 56] to 3PN order

without spins and also to 2PN order with spins. The $(1,1)$ mode corresponds to the radiated momentum and therefore highlights that at 3PN order without spins the center-of-mass is not stationary but oscillates about the origin. When spins are not included, the expression for the $(2,0)$ mode, which is the main memory mode, recovers the previous PN memory result of [45].[17] But, when spins are included, we observe new memory terms that are proportional to spin. This is a new result in PN theory, even though this behavior has been known in the numerical community [12, 57]. Last, the $(3,1)$ mode highlights a new identification in post-Newtonian theory, namely the existence of oscillatory memory modes, which arise at 3PN order and have been known to exist but have not been computed in a memory context, even though the 3PN strain without spins is complete [45, 58].

5.5 Numerical analysis

With the charges needed for fixing the BMS frame summarized in Sec. 5.3, we now present numerical results of mapping BBH waveforms to either the PN BMS frame or the superrest frame of the remnant black hole at i^+. We numerically evolved a set of 14 binary black hole mergers with varying mass ratios and spin configurations using the spectral Einstein code (SpEC) [59]. We list the important parameters of these various BBH systems in Table 5.4.1. Each simulation contains roughly 19 orbits prior to merger and is evolved until the waves from ringdown leave the computational domain. Unlike the evolutions in the SXS catalog [55], the full set of Weyl scalars has been extracted from these runs. The waveforms have been computed using both the extrapolation technique described in [60] and the Cauchy-characteristic extraction (CCE) procedure outlined in [14, 61]. Extrapolation is performed with the python module `scri` [8, 19–21] and CCE is run with SpECTRE's CCE module [14, 61, 62].

For the CCE extractions, the four world tubes that are available have radii that are equally spaced between $2\lambda\!\!\!^{-}_0$ and $21\lambda\!\!\!^{-}_0$, where $\lambda\!\!\!^{-}_0 \equiv 1/\omega_0$ is the initial reduced gravitational wavelength as determined by the orbital frequency of the binary from the initial data. Based on the recent work of [13], however, we choose to use only the waveforms that correspond to the world tube with the second-smallest radius, since these waveforms have been shown to minimally violate the Bianchi identities. For clarity, we provide the world tube radius used for each system in Table 5.4.1.

[17] Actually our result is only proportional to the earlier result of [45]. The two differ by a factor of $\frac{1}{2}\sqrt{6}$, which comes from the factor of $\frac{1}{2}$ needed to change the shear to the strain and the factor of $\sqrt{6}$ that arises when applying the $\eth^2$ operator to an $\ell = 2$ spin-weight -2 spherical harmonic mode.

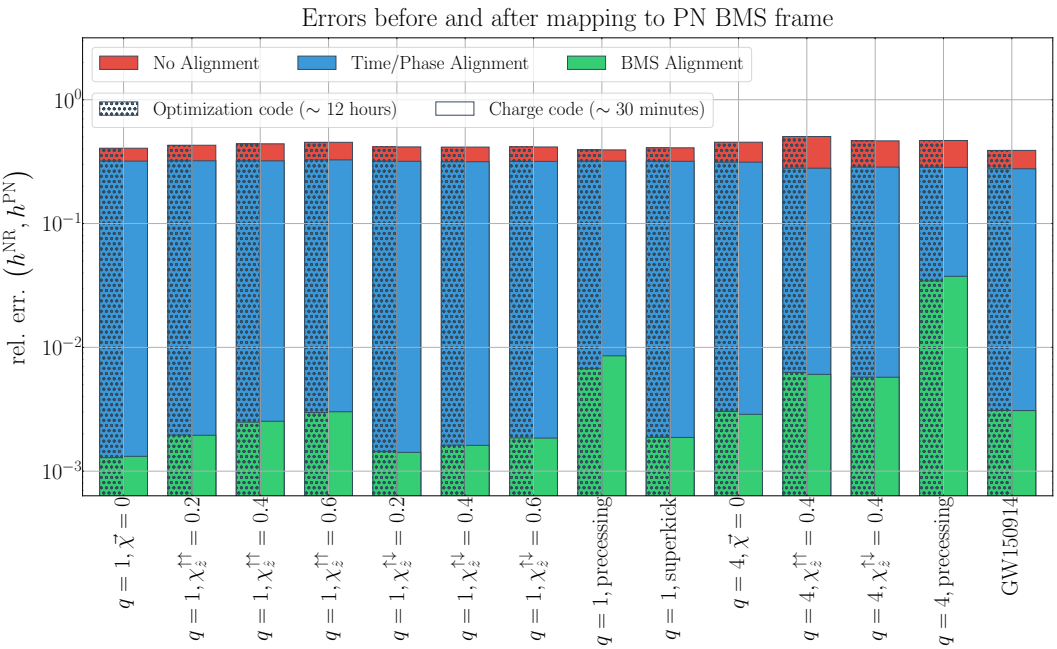

Figure 5.1: Comparison of the new charge-based frame fixing method (plain bars) to the previous method, which determined the BMS transformations by minimizing the L^2 norm of the absolute difference of the NR and PN strains (patterned bars) when mapping to the PN BMS frame. The top of each bar is the relative error between the NR and PN strain waveforms over a three-orbit window that begins $1200M$ past the initial time of the simulation. The red bars correspond to the error when no frame fixing is performed; the blue bars correspond to the error when the time and phase freedom is fixed; the green bars correspond to the error when the whole BMS frame is fixed. These simulations correspond to those found in Table 5.4.1.

All of these 14 BBH systems' waveforms have been made publicly available at [54, 55].

As mentioned above, the asymptotic strain waveforms are created using two methods: extrapolation and CCE. The first method utilizes Regge-Wheeler-Zerilli (RWZ) extraction to compute the strain waveform on a series of concentric spheres of constant coordinate radius and then extrapolates these values to future null infinity $\mathscr{I}^+$ by fitting a power series in $1/r$ [16, 60, 63–66]. This is the strain found in the SXS catalog. The CCE method, which is more faithful, instead uses world tube data from a Cauchy evolution as the inner boundary data for a nonlinear evolution of the Einstein field equations on null hypersurfaces extending to $\mathscr{I}^+$ [14, 61]. CCE requires freely specifying the strain on the initial null hypersurface of the simulation. As in [9, 12, 13, 46], we choose this field to match the value and the first radial

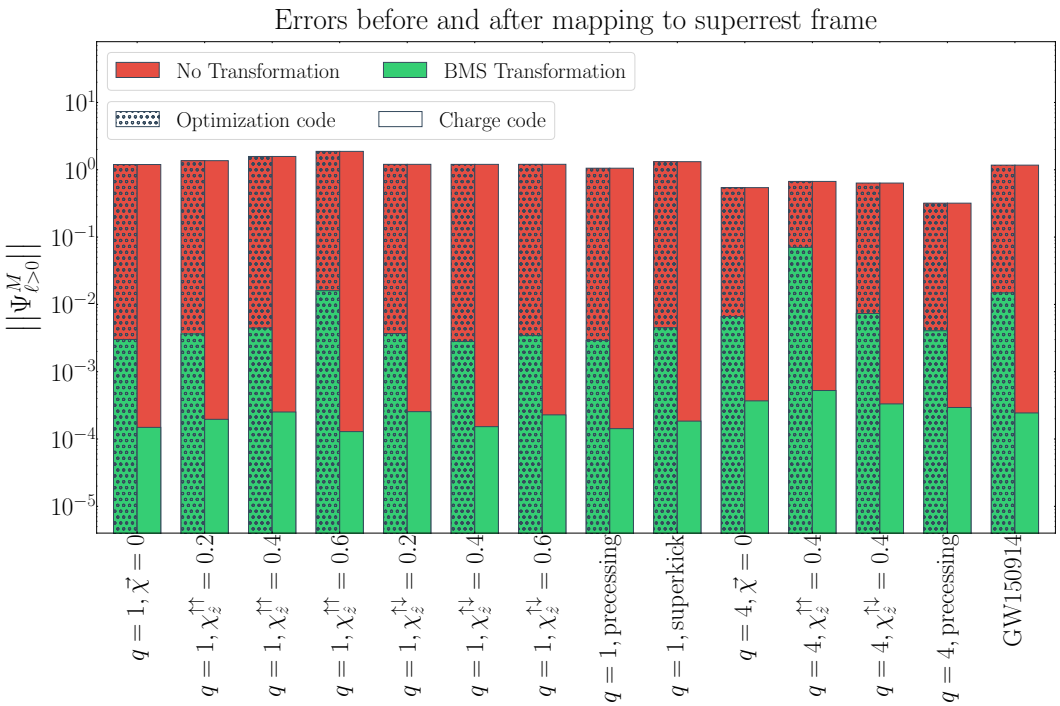

Figure 5.2: Comparison of the new charge-based frame fixing method (plain bars) to the previous method, which determined the BMS transformations by minimizing the L^2 norm of the $\ell > 0$ components of the Moreschi supermomentum (patterned bars) when mapping to the superrest frame. The top of each bar is the norm of the $\ell > 0$ components of the Moreschi supermomentum computed using Eq. (5.32). The red bars correspond to the norm when no frame fixing is performed, while the green bars correspond to the norm when the BMS frame is fixed. These simulations correspond to those found in Table 5.4.1.

derivative of h from the Cauchy data on the world tube using the ansatz

$$h(u=0, r, \theta^A) = \frac{A(\theta^A)}{r} + \frac{B(\theta^A)}{r^3}, \tag{5.50}$$

where the two coefficients $A(\theta^A)$ and $B(\theta^A)$ are fixed by the Cauchy data on the world tube.

Lastly, when we compute BMS charges and transform our asymptotic variables to either the PN BMS frame or the superrest frame, we use the code `scri` [8, 19–21], specifically the function `map_to_superrest_frame`.

5.5.1 Fixing the BMS frame

For fixing the Poincaré freedom of our systems, Sec. 5.3.1 pointed out that the ideal charge for fixing the translation and boost transformations is the center-of-mass

charge, Eq. (5.17d), and the ideal charge for fixing the rotation would typically be the usual angular momentum charge. However, because we want to map numerical waveforms to the PN BMS frame, for which the Ψ_1 and Ψ_2 Weyl scalars are unknown, for this mapping it is more convenient to use the charge that corresponds to the rotations on future null infinity, Eq. (5.19). Meanwhile, for mapping to superrest frame we use the spin vector, Eq. (5.21), because when we are in the center-of-mass frame of the remnant black hole there is no orbital angular momentum, so we need only care about the spin contribution. Apart from these Poincaré freedoms, Sec. 5.3.2 illustrated that for the supertranslation freedom the Moreschi supermomentum can be used to map NR waveforms for comparison to either PN waveforms or QNM models. Thus, the entire BMS freedom of the system can be fixed via these charges: the center-of-mass charge, the rotation charge, and the Moreschi supermomentum.

For our NR systems, however, we find that obtaining BMS transformations from these charges must be done iteratively to ensure the convergence of the process.[18] Consequently, we fix the BMS frame as follows:

I. Find the space translation and boost that minimize the center-of-mass charge G^a over a large window; i.e., compute the center-of-mass charge and fit it with a linear function in time. The boost is the slope and the space translation is the intercept.

II. Find the proper supertranslation that maps the $\ell \geq 2$ components of $\Psi_{\rm M}$ to the values obtained by PN (PN BMS frame) or to M_B (superrest frame); i.e., compute the supertranslation using Eq. (5.35) where $\Psi'_{\rm M}$ is either $\Psi^{\rm PN}_{\rm M}$ or $M_{\rm B}$. More practically, for fixing the frame using data at time $u = u_0$, we solve Eq. (5.35) for $\eth^2\bar{\eth}^2\alpha$ by taking $\alpha = u_0$ on the right-hand side, compute an approximate α by inverting $\eth^2\bar{\eth}^2$, and then iterate this procedure by taking α on the right-hand side to be the α obtained from the prior iteration until α converges.

III. Apply the supertranslation (the space translation and the proper supertranslation) to the original asymptotic quantities.

IV. Compute the rotation that maps the rotation charge (either the charge in Eq. (5.19) for the PN BMS frame or in Eq. (5.21) for the superrest frame)

[18] It may be that this need to find these transformations iteratively is true in the analytical case as well, but this is beyond the scope of this paper.

to the values computed using a PN waveform (PN BMS frame) or to be parallel to the $+\hat{z}$-axis (superrest frame). We do this calculation using Davenport's solution to Wahba's problem to find the quaternion that best aligns the two charge vectors (see Sec. 5.3 of [67]).

V. Apply both the supertranslation and rotation to the original asymptotic quantities.

VI. Repeat step I to obtain a new space translation and boost transformation for the transformed quantities.

VII. Apply the center-of-mass transformation to the transformed asymptotic quantities.

VIII. If mapping to the PN BMS frame, perform a time/phase alignment using a 2D minimization of the error between the NR and PN strain waveforms.

When finding these BMS transformations from the BMS charges, we find them iteratively. Put differently, we solve for the transformation, transform the charge, solve for the transformation again, etc., until the transformation we are computing converges. This typically happens within five iterations, which matches the results of [9] for the center-of-mass transformations. Note that the reason why we apply a space translation and boost after solving for the supertranslation and rotation and transforming the asymptotic quantities is because we find that doing so is necessary to obtain the behavior that we expect from the center-of-mass transformation. Empirically we found that to minimize the new center-of-mass-charge, we must apply a space translation and boost after solving for the supertranslation and rotation, and transforming the asymptotic quantities.

As for the values of the transformations output by this charge-based frame fixing method, we find the following. The center-of-mass transformation is consistent with the work of [9]. The rotation quaternion tends to be close to the unit quaternion, except when working with systems that are precessing, in which case it is hard to predict. The modes of the supertranslation tend to be nearly zero when $m \neq 0$ and fairly nontrivial when $m = 0$. But this is simply because the $m = 0$ memory modes dominate in PN theory, so we must correspondingly apply a supertranslation with larger $m = 0$ coefficients.

Figure 5.3: Comparison of the relative error between a CCE waveform and a PN waveform (green) to the relative error between an extrapolated waveform and a PN waveform (red). The relative error is computed over a three-orbit window that begins at $1200M$ past the initial time of the simulation. For the CCE waveforms, we show two errors: one where the error is computed when the time and phase freedom is fixed (faint) and one where the error is computed when the BMS freedom is fixed (full). With the extrapolated waveforms, we only fix the time and phase freedom. The top panel shows the relative error when only the $(2,2)$, $(2,1)$, $(3,3)$, $(3,2)$, $(3,1)$, $(4,4)$, $(4,3)$, $(4,2)$, and $(5,5)$ modes are included, while the bottom panel shows the error when every mode up to $\ell = 8$ is included. These simulations correspond to those found in Table 5.4.1.

All of the code used to perform these computations and frame transformations has been incorporated into the open-source code `scri` [8, 19–21], which has been validated by unit tests and prior works [8, 9, 19–21].

5.5.2 Comparison of charge to optimizer method

Here we compare the charge-based scheme for fixing the BMS frame to the previous method, which relied on optimization algorithms. First, in Fig. 5.5 we show the relative error between the NR and PN strain waveforms once the NR system is mapped to the PN BMS frame. For reference, we show the relative error between these waveforms when no frame fixing is performed, or when only a time and phase fixing is performed by minimizing the absolute error between the NR and

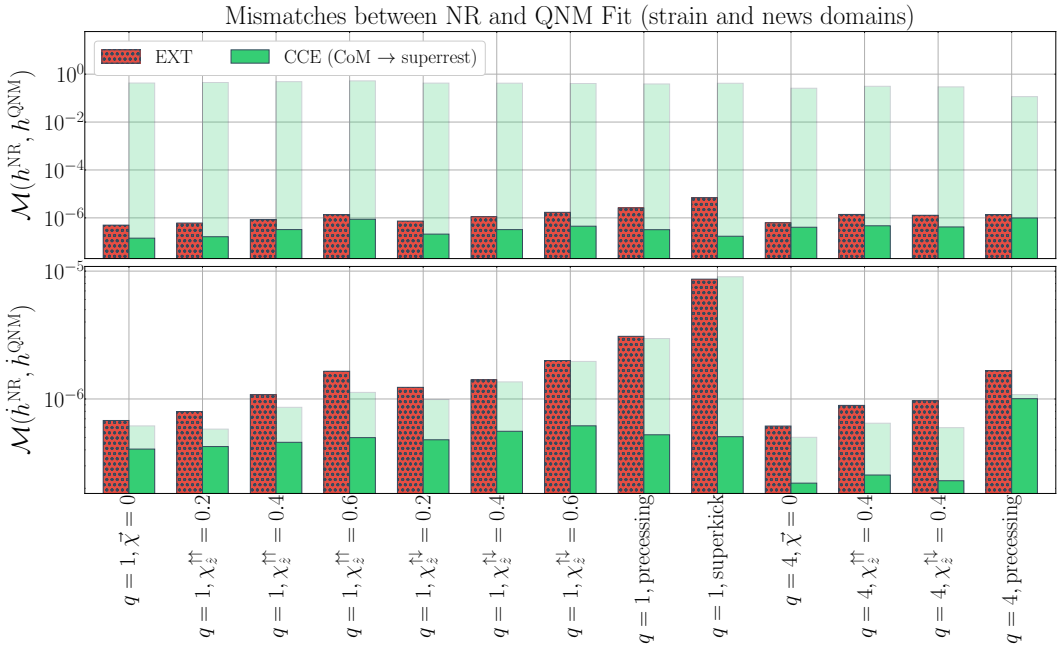

Figure 5.4: Comparison of the mismatch (the top of each bar) between a CCE waveform and the best-fit QNM model built from 100 modes chosen using the algorithm presented in [46] (green), to the mismatch obtained when using an extrapolated waveform instead of the CCE waveform (red). The mismatch is computed from the peak of the L^2 norm of the news onward to be consistent with [46]. The mass and spin of the remnant black hole are obtained from the Bondi rest mass and the spin charge, Eq. (5.21). For the CCE waveforms, we show two mismatches: one where the mismatch is computed using a CCE waveform in the center-of-mass frame of the remnant black hole (faint) and one where the CCE waveform is in the superrest frame of the remnant black hole (full). For the extrapolated waveforms, we only change each mode by a constant so that the waveform decays to zero at the end of the simulation. The top panel shows the mismatch between the strain waveforms, while the bottom panel shows the mismatch between the news waveforms. These simulations correspond to those found in Table 5.4.1.

PN waveforms.[19] Both methods compute the relative error between these two waveforms over a three-orbit window during the early inspiral phase and over the whole two-sphere for every spin-weighted spherical harmonic mode up to $\ell_{\rm max} = 8$. Explicitly,

$$\text{rel. err.}\left(h^{\rm NR}, h^{\rm PN}\right) = ||h^{\rm NR} - h^{\rm PN}||/||h^{\rm PN}||, \tag{5.51}$$

where

$$||h|| \equiv \sqrt{\int_{S^2}\left(\int_{u_1}^{u_2} |h(\ell_{\rm min} \leq \ell \leq \ell_{\rm max})|^2\, du\right) d\Omega}. \tag{5.52}$$

Here u_1 is the time that is $1200M$ past the beginning of the NR simulation, u_2 the time three-orbits beyond u_1, $\ell_{\rm min} = 2$, and $\ell_{\rm max} = 8$. As can be seen by comparing the plain green bars (charge-based method) to the patterned green bars (optimization algorithm) throughout Fig. 5.5, the charge-based frame fixing method produces an error that is nearly identical to the previous method for every BBH system, but with a typical run time of 30 minutes instead of 12 hours: a speedup of $\sim 24\times$.

In Fig. 5.5.1 we show the norm of the $\ell > 0$ components of $\Psi_{\rm M}$ during the final $100M$ of the numerical simulation, which is roughly $200M$ past the peak of the L^2 norm of the strain. We calculate this peak time by finding the time at which the square of Eq. (5.52), without the time integration, reaches its maximum value. As can be seen by comparing the plain green bars (charge-based method) to the patterned green bars (optimization algorithm), the new method produces errors that are roughly two orders of magnitude better than the optimization algorithm used in [9, 46]. Thus, it is evident that fixing the BMS frame to be the superrest frame of the remnant black hole is remarkably improved when using the new, charge-based frame fixing method. This improvement is primarily due to our ability to obtain more physically motivated supertranslations from the Moreschi supermomentum via Eq. (5.37), rather than an optimization algorithm that need not produce physical results.

5.5.3 Comparison of NR to PN and QNMs

Thus far, we have shown why fixing the BMS frame of NR systems is important for comparing NR waveforms to PN waveforms or for modeling the ringdown phase of NR waveforms with QNMs. We now show why CCE waveforms and BMS

[19] The main reason why the time and phase fixing produces such poor results is because the waveforms being compared contain memory effects, which require a supertranslation to be aligned.

frame fixing will help usher in the next generation of NR waveforms. We do so by comparing both CCE and extrapolated waveforms to PN waveforms in Fig. 5.5.2 and QNMs in Fig. 5.5.2.

In Fig. 5.5.2, like Fig. 5.5, we show the relative error between a NR and a PN strain waveform over a three-orbit window. In the top panel, we compute the relative error between these waveforms using the $(2,2)$, $(2,1)$, $(3,3)$, $(3,2)$, $(3,1)$, $(4,4)$, $(4,3)$, $(4,2)$, and $(5,5)$ modes. These are typically the most important modes without the $m = 0$ modes. This collection of modes also matches those used in the `NRHybSur3dq8` surrogate [68]. In the bottom panel, we instead compute the relative error using every mode up to $\ell = 8$. The error obtained when using CCE waveforms is shown in green, while the error when using extrapolated waveforms is shown in red. Furthermore, for the CCE waveforms we show two errors: one where we perform a time/phase alignment (faint) and one where we perform a BMS frame alignment (full). For the extrapolated waveforms, however, the error is computed only with a time/phase alignment, since this is what has been used before Ref. [9].[20] As can be seen throughout the top panel, where the $m = 0$ modes have been excluded, provided that we have fixed the BMS frame of the CCE waveforms, then these waveforms are on a par with the extrapolated waveforms.[21] However, if we include the $m = 0$ modes as in the bottom panel, then we find that the CCE waveforms are easily able to outperform the extrapolated waveforms for every type of system considered. This is because CCE waveforms, unlike extrapolated waveforms, contain memory effects that are also present in the PN treatment.

For working in the superrest frame, in Fig. 5.5.2, we show the mismatch between a NR waveform and a QNM model constructed from 100 QNM modes that are chosen using the ranking system presented in [46].[22] In the top panel we show the mismatch between the strain waveforms, while in the bottom panel we show the mismatch between the news waveforms, where the news waveform is just the time derivative of the strain waveform. The mismatch when using CCE waveforms is shown in green, while the mismatch when using extrapolated waveforms is shown

[20] We should also note that this charge-based method for fixing the BMS frame cannot be performed on the vast majority of the publicly available extrapolated waveforms in the SXS Catalog [55], since their Weyl scalars have not been extracted.

[21] The reason why the faint bars produce such poor errors is because the CCE waveforms are output in an arbitrary BMS frame and thus require a supertranslation to obtain sensible results.

[22] While there is an ongoing debate within the QNM community concerning the possible overfitting of QNMs to NR waveforms, because we are only comparing fits to different waveforms rather than the fits themselves this is not important to our results.

in red. We compute the mismatch via

$$\mathcal{M}\left(h^A, h^B\right) \equiv 1 - \mathrm{Re}\left[\frac{\langle h^A, h^B\rangle}{\sqrt{\langle h^A, h^A\rangle\langle h^B, h^B\rangle}}\right], \tag{5.53}$$

where

$$\langle h^A, h^B\rangle \equiv \int_{S^2}\int_{u_0}^{\infty} h^A\overline{h^B}\, du\, d\Omega. \tag{5.54}$$

Again, for CCE we show two mismatches: one where the CCE system is in the center-of-mass frame of the remnant black hole (faint) and one in the superrest frame of the remnant black hole (full). As can be seen in the top panel, mapping to the superrest frame is essential for modeling CCE waveforms with QNMs. This is because, unlike extrapolated waveforms, CCE waveforms contain memory effects so the CCE waveform will not decay to zero at timelike infinity, while the QNMs will. As a result, to model these NR waveforms with QNMs, fixing the supertranslation freedom is vitally important so that the waveforms do decay to zero. However, this is not the only impact that fixing the BMS frame has on NR waveforms. In the bottom panel, which shows the mismatch between the news waveforms, there continues to be an improvement by mapping to the superrest frame, even though there is no memory in these news waveforms. This is because when applying a supertranslation, there is also important mode mixing from expressing the first term of (5.13a) in terms of the untransformed time, i.e.,

$$\sigma(u') = \sum_{n=0}^{\infty}\frac{1}{n!}\left[(k(u-\alpha)-u)\,\frac{\partial}{\partial u}\right]^n \sigma(u). \tag{5.55}$$

For more on this, see Fig. 7 of [46] and the related text. Lastly, we should also note that by comparing Fig. 5.5.2 to Fig. 10 of [46], one can see that the mismatches obtained are practically identical, which means that the results of [46] should not be impacted by this new scheme for mapping to the superrest frame using BMS charges.

5.6 Discussion

We have presented a new procedure for fixing the entire BMS frame of the data produced by NR simulations. The method relies on the use of BMS charges rather than optimization algorithms, like those used in [9, 46]. This charge-based frame fixing method fixes the system's frame using the center-of-mass charge (Eq. (5.17d)) and the rotation charge (Eq. (5.19)) for the Poincaré freedoms, and the Moreschi

supermomentum Ψ_M (Eq. (5.32)) for the supertranslation freedom. If the time and phase freedoms need to be fixed, e.g., for comparing NR systems to PN, then a 2D minimization of the error between NR and PN strain waveforms is performed. This code has been made publicly available in the python module `scri` [8, 19–21].

The BMS transformations are obtained by finding the transformation that changes the corresponding charge in a prescribed way. For example, to map to the system's center-of-mass frame we find the transformation that maps the center-of-mass charge to have an average of zero. Accordingly, the transformations can be found much faster than if they were computed with a minimization scheme. For the BBH systems and frames we considered, we found that this new charge-based method converges in roughly 30 minutes, rather than the 12 or more hours that are needed by the previous optimization algorithm.

In particular, using the charge-based frame fixing, we mapped 14 binary systems to the PN BMS frame, i.e., the frame that PN waveforms are in. Apart from this, we mapped these systems to the superrest frame, i.e., the frame in which the metric of the remnant black hole matches the Kerr metric at timelike infinity. For mapping to the PN BMS frame, we fixed the Poincaré frame by mapping the center-of-mass charge to an average of zero and the rotation charge to match the rotation charge of the PN waveform. For the supertranslation freedom, however, we found that it was necessary to calculate the PN Moreschi supermomentum so that we could find the supertranslation via Eq. (5.35), which maps the numerical Moreschi supermomentum to the PN supermomentum during the early inspiral phase.

In Sec. 5.4 we performed this calculation by using the relation that writes Ψ_M in terms of the energy flux (see, e.g., Eq. (5.34)). This calculation provides Ψ_M to 3PN order without spins and 2PN order with spins. Moreover, this calculation also leads to oscillatory and spin-dependent memory terms that either have not been identified or have been missing from the existing PN strain expressions. These strain terms, as well as the complete expression for the PN Moreschi supermomentum, can be found in Appendices 5.A and 5.B.

In Sec. 5.5.1 we then described our procedure for fixing the BMS frame. In Sec. 5.5.2 we used our new code to map to the PN BMS frame (see Fig. 5.5) or to minimize the Moreschi supermomentum during ringdown, that is, map to the superrest frame (see Fig. 5.5.1). In each case, we compared with the previous code that relied on minimizers. Overall, we found that these two procedures tend to yield the same errors when mapping to the PN BMS frame, while the new charge-based procedure

yields better errors when mapping to the superrest frame.

Finally, in Sec. 5.5.3 we considered CCE waveforms whose BMS frame has been fixed with this new method to be either the PN BMS frame or the superrest frame of the remnant black hole. We showed that such waveforms can notably outperform extrapolated waveforms, which are the current waveforms in the SXS catalog. This suggests that CCE waveforms and BMS frame fixing will be vital in the future for performing more correct numerical relativity simulations and conducting better waveform modeling.

5.7 Acknowledgments

L.C.S. thanks Laura Bernard for insightful discussions, and the Benasque science center and organizers of the conference "New frontiers in strong gravity" for enabling these conversations. We thank Laura Bernard, Luc Blanchet, Guillaume Faye, and Tanguy Marchand for sharing a `Mathematica` notebook that included the PN expressions from Appendix B of [69]. Computations for this work were performed with the Wheeler cluster at Caltech. This work was supported in part by the Sherman Fairchild Foundation and by NSF Grants No. PHY-2011961, No. PHY-2011968, and No. OAC-1931266 at Caltech, as well as NSF Grants No. PHY-1912081 and No. OAC-1931280 at Cornell. The work of L.C.S. was partially supported by NSF CAREER Award PHY-2047382.

5.A PN Moreschi Supermomentum

The complete results from our PN calculation of the modes of the Moreschi supermomentum are as follows:

$$\begin{aligned}\mathcal{P}^{(0,0)} &= 1 + x\left(-\frac{3}{4} - \frac{\nu}{12}\right) + x^2\left(-\frac{27}{8} + \frac{19\nu}{8} - \frac{\nu^2}{24}\right) \\ &\quad + x^3\left(-\frac{675}{64} + \left(\frac{34445}{576} - \frac{205\pi^2}{96}\right)\nu - \frac{155\nu^2}{96} - \frac{35\nu^3}{5184}\right), \qquad (5.56a)\\ \mathcal{P}^{(0,0)}_{\text{spin}} &= x^{3/2}\left(\frac{14S_\ell}{3M^2} + \frac{2\delta\Sigma_\ell}{M^2}\right) \\ &\quad + x^2\Bigg(-\frac{16\vec{S}\cdot\vec{S} + 3\vec{\Sigma}\cdot\vec{\Sigma} + 32S_\ell^2 + 9\Sigma_\ell^2}{12M^4} \\ &\quad - \frac{4\delta\left(\vec{S}\cdot\vec{\Sigma} + 2S_\ell\Sigma_\ell\right)}{3M^4} + \frac{4\left(\vec{\Sigma}\cdot\vec{\Sigma} + 2\Sigma_\ell^2\right)\nu}{3M^4}\Bigg), \qquad (5.56b)\end{aligned}$$

$$\mathcal{P}^{(1,1)} = \frac{43}{70}\sqrt{\frac{3}{2}}\left\{x^3\left(\frac{1856\delta\nu}{129}\right)\right\}, \tag{5.56c}$$

$$\mathcal{P}^{(1,1)}_{\rm spin} = 0, \tag{5.56d}$$

$$\mathcal{P}^{(2,1)} = 0, \tag{5.56e}$$

$$\begin{aligned}\mathcal{P}^{(2,1)}_{\rm spin} = \frac{61}{14\sqrt{30}}\Bigg\{x^{3/2}\left(-\frac{(S_n - iS_\lambda)}{M^2} - \frac{375\delta\,(\Sigma_n - i\Sigma_\lambda)}{488M^2}\right)\\ + x^2\Bigg(\frac{10\,(3S_l\,(S_n - iS_\lambda) + \Sigma_l\,(\Sigma_n - i\Sigma_\lambda))}{61M^4}\\ + \frac{15\delta\,((S_n - iS_\lambda)\,\Sigma_l + S_l\,(\Sigma_n - i\Sigma_\lambda))}{61M^4}\\ - \frac{30\nu\Sigma_l\,(\Sigma_n - i\Sigma_\lambda)}{61M^4}\Bigg)\Bigg\},\end{aligned} \tag{5.56f}$$

$$\begin{aligned}\mathcal{P}^{(2,0)} = \frac{2}{7}\sqrt{5}\Bigg\{1 + x\left(-\frac{4075}{4032} + \frac{67\nu}{48}\right)\\ + x^2\left(-\frac{151877213}{67060224} - \frac{123815\nu}{44352} + \frac{205\nu^2}{352}\right) + \pi x^{5/2}\left(-\frac{253}{336} + \frac{253\nu}{84}\right)\\ + x^3\Bigg(-\frac{4397711103307}{532580106240} + \left(\frac{700464542023}{13948526592} - \frac{205\pi^2}{96}\right)\nu\\ + \frac{69527951\nu^2}{166053888} + \frac{1321981\nu^3}{5930496}\Bigg)\Bigg\},\end{aligned} \tag{5.56g}$$

$$\begin{aligned}\mathcal{P}^{(2,0)}_{\rm spin} = \frac{2}{7}\sqrt{5}\Bigg\{x^{3/2}\left(\frac{16S_\ell}{3M^2} + \frac{419\delta\Sigma_\ell}{160M^2}\right)\\ + x^2\Bigg(-\frac{128\vec{S}\cdot\vec{S} + 24\vec{\Sigma}\cdot\vec{\Sigma} + 256S_\ell^2 + 75\Sigma_\ell^2}{96M^4}\\ - \frac{4\delta\left(\vec{S}\cdot\vec{\Sigma} + 2S_\ell\Sigma_\ell\right)}{3M^4} + \frac{4\left(\vec{\Sigma}\cdot\vec{\Sigma} + 2\Sigma_\ell^2\right)\nu}{3M^4}\Bigg)\Bigg\},\end{aligned} \tag{5.56h}$$

$$\mathcal{P}^{(3,3)} = -\frac{44x^3\delta\nu}{27\sqrt{35}}, \tag{5.56i}$$

$$\mathcal{P}^{(3,3)}_{\rm spin} = 0, \tag{5.56j}$$

$$\mathcal{P}^{(3,1)} = \frac{223}{120\sqrt{21}}\left\{x^3\left(\frac{3872\delta\nu}{223}\right)\right\}, \tag{5.56k}$$

$$\mathcal{P}^{(3,1)}_{\rm spin} = 0, \tag{5.56l}$$

$$\mathcal{P}^{(4,4)} = -\frac{4}{3} i \sqrt{\frac{2}{35}} x^{5/2} \nu, \tag{5.56m}$$

$$\mathcal{P}^{(4,4)}_{\text{spin}} = 0, \tag{5.56n}$$

$$\mathcal{P}^{(4,1)} = 0, \tag{5.56o}$$

$$\begin{aligned}\mathcal{P}^{(4,1)}_{\text{spin}} = \frac{13}{56\sqrt{5}} \Bigg\{ & x^{3/2} \left(-\frac{(S_n - i S_\lambda)}{M^2} - \frac{34\delta \left(\Sigma_n - i \Sigma_\lambda\right)}{39 M^2} \right) \\ & + x^2 \Bigg(\frac{10 \left(3 S_l \left(S_n - i S_\lambda\right) + \Sigma_l \left(\Sigma_n - i \Sigma_\lambda\right)\right)}{117 M^4} \\ & + \frac{5\delta \left(\left(S_n - i S_\lambda\right) \Sigma_l + S_l \left(\Sigma_n - i \Sigma_\lambda\right)\right)}{39 M^4} \\ & - \frac{10 \nu \Sigma_l \left(\Sigma_n - i \Sigma_\lambda\right)}{39 M^4} \Bigg) \Bigg\}, \end{aligned} \tag{5.56p}$$

$$\begin{aligned}\mathcal{P}^{(4,0)} = \frac{1}{42} \Bigg\{ & 1 + x \left(-\frac{180101}{29568} + \frac{27227 \nu}{1056} \right) \\ & + x^2 \left(\frac{2201411267}{158505984} - \frac{34829479 \nu}{432432} + \frac{844951 \nu^2}{27456} \right) \\ & + x^{5/2} \left(-\frac{13565\pi}{1232} + \frac{13565 \pi \nu}{308} \right) \\ & + x^3 \Bigg(\frac{15240463356751}{781117489152} + \left(-\frac{1029744557245}{27897053184} - \frac{205\pi^2}{96} \right) \nu \\ & - \frac{4174614175 \nu^2}{36900864} + \frac{221405645 \nu^3}{11860992} \Bigg) \Bigg\}, \end{aligned} \tag{5.56q}$$

$$\begin{aligned}\mathcal{P}^{(4,0)}_{\text{spin}} = \frac{1}{42} \Bigg\{ & x^{3/2} \left(\frac{10 S_\ell}{M^2} + \frac{57 \delta \Sigma_\ell}{8 M^2} \right) \\ & + x^2 \Bigg(-\frac{64 \vec{S} \cdot \vec{S} + 12 \vec{\Sigma} \cdot \vec{\Sigma} + 128 S_\ell^2 + 41 \Sigma_\ell^2}{48 M^4} \\ & - \frac{4\delta \left(\vec{S} \cdot \vec{\Sigma} + 2 S_\ell \Sigma_\ell \right)}{3 M^4} + \frac{4 \left(\vec{\Sigma} \cdot \vec{\Sigma} + 2 \Sigma_\ell^2 \right) \nu}{3 M^4} \Bigg) \Bigg\}, \end{aligned} \tag{5.56r}$$

$$\mathcal{P}^{(5,5)} = -\frac{36 x^3 \delta \nu}{5\sqrt{77}}, \tag{5.56s}$$

$$\mathcal{P}^{(5,5)}_{\text{spin}} = 0, \tag{5.56t}$$

$$\mathcal{P}^{(5,3)} = \frac{4 x^3 \delta \nu}{27\sqrt{385}}, \tag{5.56u}$$

$$\mathcal{P}^{(5,3)}_{\rm spin} = 0, \tag{5.56v}$$

$$\mathcal{P}^{(5,1)} = \frac{2}{21}\sqrt{\frac{2}{165}}\left\{x^3\,(26\delta\nu)\right\}, \tag{5.56w}$$

$$\mathcal{P}^{(5,1)}_{\rm spin} = 0, \tag{5.56x}$$

$$\begin{aligned}\mathcal{P}^{(6,0)} = -\frac{4195}{177408\sqrt{13}}x\Bigg\{1 - \frac{3612\nu}{839} + x\left(-\frac{45661561}{6342840} + \frac{101414\nu}{2517} - \frac{48118\nu^2}{839}\right)\\ + x^{3/2}\left(\frac{1248\pi}{839} - \frac{4992\pi\nu}{839}\right)\\ + x^2\Bigg(\frac{3012132889099}{144921208320} - \frac{27653500031\nu}{191694720}\\ + \frac{1317967427\nu^2}{4107744} - \frac{24793657\nu^3}{342312}\Bigg)\Bigg\},\end{aligned} \tag{5.56y}$$

$$\mathcal{P}^{(6,0)}_{\rm spin} = 0, \tag{5.56z}$$

$$\begin{aligned}\mathcal{P}^{(8,0)} = \frac{75601}{8895744\sqrt{17}}x^2\Bigg\{1 - \frac{452070\nu}{75601} + \frac{733320\nu^2}{75601}\\ + x\Bigg(-\frac{265361599}{33869248} + \frac{18177898147\nu}{321757856}\\ - \frac{722521125\nu^2}{5745676} + \frac{261283995\nu^3}{2872838}\Bigg)\Bigg\},\end{aligned} \tag{5.56aa}$$

$$\mathcal{P}^{(8,0)}_{\rm spin} = 0. \tag{5.56bb}$$

5.B PN Strain New Memory Terms

The post-Minkowski expansion of gravitational waves in radiative coordinates yields the strain in terms of the radiative mass and current moments, $\mathrm{U}^{(\ell,m)}$ and $\mathrm{V}^{(\ell,m)}$ (see [48], but here following the conventions of [45]),

$$h^{(\ell,m)} = \frac{G}{\sqrt{2}Rc^{\ell+2}}\left(\mathrm{U}^{(\ell,m)} - \frac{i}{c}\mathrm{V}^{(\ell,m)}\right), \tag{5.57}$$

and when expressing the radiative moments in terms of the six types of source moments, $\mathrm{U}^{(\ell,m)}$ is then even further decomposed in terms that are called instantaneous, memory, tail, tail-of-tail, . . . pieces:

$$\mathrm{U}^{(\ell,m)} = \mathrm{U}^{(\ell,m)}_{\rm inst} + \mathrm{U}^{(\ell,m)}_{\rm tail} + \mathrm{U}^{(\ell,m)}_{\rm tail\text{-}tail} + \mathrm{U}^{(\ell,m)}_{\rm mem} + \ldots \tag{5.58}$$

Therefore, we simply define

$$h^{(\ell,m)}_{\rm mem} = \frac{G}{\sqrt{2}Rc^{\ell+2}} \mathrm{U}^{(\ell,m)}_{\rm mem}. \tag{5.59}$$

Then the memory arises as (Eq. (2.26) of [45], from Eq. (2.43c) of [70], and changing from STF tensors to spherical harmonics)

$$h^{(\ell,m)}_{\rm mem} = \frac{16\pi G}{Rc^4}\sqrt{\frac{(\ell-2)!}{(\ell+2)!}}\times \int_{-\infty}^{u} du' \int d\Omega \frac{dE^{\rm GW}}{du d\Omega}\overline{Y}^{(\ell,m)}, \tag{5.60}$$

where

$$\frac{dE^{\rm GW}}{du d\Omega} = \frac{R^2}{16\pi G}|\dot{h}|^2. \tag{5.61}$$

Consequently, we find

$$h^{(\ell,m)}_{\rm mem} = \frac{4}{Rc^4}\sqrt{\frac{(\ell-2)!}{(\ell+2)!}}\Psi^{(\ell,m)}_{\rm M}, \tag{5.62}$$

or, in terms of the $\mathcal{P}^{(\ell,m)}$ decomposition of Eq. (5.46),

$$h^{(\ell,m)}_{\rm mem} = \frac{2M\nu x}{R}\sqrt{\frac{(\ell-2)!}{(\ell+2)!}}\sqrt{4\pi}\mathcal{P}^{(\ell,m)}e^{-im\psi}. \tag{5.63}$$

Another way to derive this expression is by writing Eq. (5.29) with the strain, ignoring the contribution coming from the Bondi mass aspect, and then moving the factor of $\eth^2$ to the right-hand side.

Using Eq. (5.63) and the $\mathcal{P}^{(\ell,m)}$ expressions in Eq. (5.56) gives new oscillatory and spin-dependent memory terms which have not been identified or have been missing from the PN literature.

Finally we should point out the following interpretation of our BMS frame fixing procedure, by studying Eq. (5.62). Our procedure fixed the BMS frame by matching $\Psi_{\rm M}$, mode by mode, to $\Psi^{\rm PN}_{\rm M}$. Then, because of the simple mode-wise proportionality $h^{(\ell,m)}_{\rm mem} \propto \Psi^{(\ell,m)}_{\rm M}$, it turns out that our frame-fixing is equivalent to matching $h_{\rm mem}$ (except that, being a spin-weight -2 field, $h_{\rm mem}$ is missing the $\ell = 0, 1$ information from $\Psi_{\rm M}$).

References

[1] R. Abbott et al. (LIGO Scientific, Virgo), Phys. Rev. X **11**, 021053 (2021) 10.1103/PhysRevX.11.021053.

[2] R. Abbott et al. (LIGO Scientific, VIRGO, KAGRA), (2021).

[3] B. P. Abbott et al. (KAGRA, LIGO Scientific, Virgo, VIRGO), Living Rev. Rel. **21**, 3 (2018) 10.1007/s41114-020-00026-9.

[4] E. Berti, K. Yagi, and N. Yunes, Gen. Rel. Grav. **50**, 46 (2018) 10.1007/s10714-018-2362-8.

[5] E. Berti, K. Yagi, H. Yang, and N. Yunes, Gen. Rel. Grav. **50**, 49 (2018) 10.1007/s10714-018-2372-6.

[6] H. Bondi, M. G. J. Van der Burg, and A. W. K. Metzner, Proceedings of the Royal Society of London. Series A. Mathematical and Physical Sciences **269**, 21 (1962) 10.1098/rspa.1962.0161.

[7] R. K. Sachs and H. Bondi, Proceedings of the Royal Society of London. Series A. Mathematical and Physical Sciences **270**, 103 (1962) 10.1098/rspa.1962.0206.

[8] M. Boyle, Phys. Rev. D **93**, 084031 (2016) 10.1103/PhysRevD.93.084031.

[9] K. Mitman et al., Phys. Rev. D **104**, 024051 (2021) 10.1103/PhysRevD.104.024051.

[10] O. M. Moreschi, Class. Quant. Grav. **5**, 423 (1988) 10.1088/0264-9381/5/3/004.

[11] D. A. B. Iozzo et al., Phys. Rev. D **103**, 124029 (2021) 10.1103/PhysRevD.103.124029.

[12] K. Mitman, J. Moxon, M. A. Scheel, S. A. Teukolsky, M. Boyle, N. Deppe, L. E. Kidder, and W. Throwe, Phys. Rev. D **102**, 104007 (2020) 10.1103/PhysRevD.102.104007.

[13] K. Mitman et al., Phys. Rev. D **103**, 024031 (2021) 10.1103/PhysRevD.103.024031.

[14] J. Moxon, M. A. Scheel, S. A. Teukolsky, N. Deppe, N. Fischer, F. Hébert, L. E. Kidder, and W. Throwe, (2021).

[15] R. P. Geroch, A. Held, and R. Penrose, J. Math. Phys. **14**, 874 (1973) 10.1063/1.1666410.

[16] M. Boyle et al., Class. Quant. Grav. **36**, 195006 (2019) 10.1088/1361-6382/ab34e2.

[17] O. M. Moreschi and S. Dain, J. Math. Phys. **39**, 6631 (1998) 10.1063/1.532646.

[18] S. Dain and O. M. Moreschi, Class. Quant. Grav. **17**, 3663 (2000) 10.1088/0264-9381/17/18/305.

[19] M. Boyle, D. Iozzo, L. Stein, A. Khairnar, H. Rüter, M. Scheel, V. Varma, and K. Mitman, *Moble/scri: v2022.8.0*, version 2022.8.0, Aug. 2022, 10.5281/zenodo.6975014.

[20] M. Boyle, Phys. Rev. D **87**, 104006 (2013) 10.1103/PhysRevD.87.104006.

[21] M. Boyle, L. E. Kidder, S. Ossokine, and H. P. Pfeiffer, (2014).

[22] O. M. Moreschi, Classical and Quantum Gravity **3**, 503 (1986).

[23] G. Barnich and C. Troessaert, Phys. Rev. Lett. **105**, 111103 (2010) 10.1103/PhysRevLett.105.111103.

[24] A. Strominger, JHEP **07**, 152 (2014) 10.1007/JHEP07(2014)152.

[25] T. He, V. Lysov, P. Mitra, and A. Strominger, JHEP **05**, 151 (2015) 10.1007/JHEP05(2015)151.

[26] D. Kapec, V. Lysov, S. Pasterski, and A. Strominger, JHEP **08**, 058 (2014) 10.1007/JHEP08(2014)058.

[27] S. Pasterski, A. Strominger, and A. Zhiboedov, JHEP **12**, 053 (2016) 10.1007/JHEP12(2016)053.

[28] G. Barnich and C. Troessaert, JHEP **05**, 062 (2010) 10.1007/JHEP05(2010)062.

[29] A. Strominger and A. Zhiboedov, JHEP **01**, 086 (2016) 10.1007/JHEP01(2016)086.

[30] É. É. Flanagan and D. A. Nichols, Phys. Rev. D **95**, 044002 (2017) 10.1103/PhysRevD.95.044002.

[31] V. C. de Andrade, L. Blanchet, and G. Faye, Class. Quant. Grav. **18**, 753 (2001) 10.1088/0264-9381/18/5/301.

[32] L. Blanchet and G. Faye, Class. Quant. Grav. **36**, 085003 (2019) 10.1088/1361-6382/ab0d4f.

[33] G. Compère, R. Oliveri, and A. Seraj, JHEP **10**, 116 (2020) 10.1007/JHEP10(2020)116.

[34] R. O'Shaughnessy, B. Vaishnav, J. Healy, Z. Meeks, and D. Shoemaker, Phys. Rev. D **84**, 124002 (2011) 10.1103/PhysRevD.84.124002.

[35] T. Dray and M. Streubel, Class. Quant. Grav. **1**, 15 (1984) 10.1088/0264-9381/1/1/005.

[36] R. M. Wald and A. Zoupas, Phys. Rev. D **61**, 084027 (2000) 10.1103/PhysRevD.61.084027.

[37] Y. B. Zel'dovich and A. G. Polnarev, Sov. Astron. **18**, 17 (1974).

[38] D. Christodoulou, Phys. Rev. Lett. **67**, 1486 (1991) 10.1103/PhysRevLett.67.1486.

[39] K. S. Thorne, Phys. Rev. D **45**, 520 (1992) 10.1103/PhysRevD.45.520.

[40] É. É. Flanagan and D. A. Nichols, Phys. Rev. D **92**, [Erratum: Phys.Rev.D 93, 049905 (2016)], 084057 (2015) 10.1103/PhysRevD.92.084057.

[41] A. M. Grant and D. A. Nichols, Phys. Rev. D **105**, 024056 (2022) 10.1103/PhysRevD.105.024056.

[42] A. Seraj and T. Neogi, (2022).

[43] A. Ashtekar, T. De Lorenzo, and N. Khera, Gen. Rel. Grav. **52**, 107 (2020) 10.1007/s10714-020-02764-1.

[44] R. Arnowitt, S. Deser, and C. W. Misner, Phys. Rev. **116**, 1322 (1959) 10.1103/PhysRev.116.1322.

[45] M. Favata, Phys. Rev. D **80**, 024002 (2009) 10.1103/PhysRevD.80.024002.

[46] L. Magaña Zertuche, K. Mitman, N. Khera, L. C. Stein, M. Boyle, N. Deppe, F. Hébert, D. A. B. Iozzo, L. E. Kidder, J. Moxon, H. P. Pfeiffer, M. A. Scheel, S. A. Teukolsky, W. Throwe, and N. Vu, Phys. Rev. D **105**, 104015 (2022) 10.1103/PhysRevD.105.104015.

[47] G. Compère and J. Long, Class. Quant. Grav. **33**, 195001 (2016) 10.1088/0264-9381/33/19/195001.

[48] L. Blanchet, Living Rev. Rel. **17**, 2 (2014) 10.12942/lrr-2014-2.

[49] A. Buonanno, G. Faye, and T. Hinderer, Phys. Rev. D **87**, 044009 (2013) 10.1103/PhysRevD.87.044009.

[50] A. Bohé, G. Faye, S. Marsat, and E. K. Porter, Class. Quant. Grav. **32**, 195010 (2015) 10.1088/0264-9381/32/19/195010.

[51] S. Marsat, Class. Quant. Grav. **32**, 085008 (2015) 10.1088/0264-9381/32/8/085008.

[52] W. B. Campbell and T. Morgan, Physica **53**, 264 (1971) 10.1016/0031-8914(71)90074-7.

[53] C. Bender, S. Orszag, and S. Orszag, *Advanced mathematical methods for scientists and engineers i: asymptotic methods and perturbation theory*, Advanced Mathematical Methods for Scientists and Engineers (Springer, 1999).

[54] *SXS Ext-CCE Waveform Database*, https://data.black-holes.org/waveforms/extcce_catalog.html.

[55] *SXS Gravitational Waveform Database*, http://www.black-holes.org/waveforms.

[56] S. Isoyama and H. Nakano, Class. Quant. Grav. **35**, 024001 (2018) 10.1088/1361-6382/aa96c5.

[57] D. Pollney and C. Reisswig, Astrophys. J. Lett. **732**, L13 (2011) 10.1088/2041-8205/732/1/L13.

[58] L. Blanchet, T. Damour, G. Esposito-Farese, and B. R. Iyer, Phys. Rev. Lett. **93**, 091101 (2004) 10.1103/PhysRevLett.93.091101.

[59] https://www.black-holes.org/code/SpEC.html.

[60] D. A. B. Iozzo, M. Boyle, N. Deppe, J. Moxon, M. A. Scheel, L. E. Kidder, H. P. Pfeiffer, and S. A. Teukolsky, Phys. Rev. D **103**, 024039 (2021) 10.1103/PhysRevD.103.024039.

[61] J. Moxon, M. A. Scheel, and S. A. Teukolsky, Phys. Rev. D **102**, 044052 (2020) 10.1103/PhysRevD.102.044052.

[62] N. Deppe, W. Throwe, L. E. Kidder, N. L. Fischer, C. Armaza, G. S. Bonilla, F. Hébert, P. Kumar, G. Lovelace, J. Moxon, E. O'Shea, H. P. Pfeiffer, M. A. Scheel, S. A. Teukolsky, I. Anantpurkar, M. Boyle, F. Foucart, M. Giesler, D. A. B. Iozzo, I. Legred, D. Li, A. Macedo, D. Melchor, M. Morales, T. Ramirez, H. R. Rüter, J. Sanchez, S. Thomas, and T. Wlodarczyk, *SpECTRE*, version 2020.12.07, Dec. 2020, 10.5281/zenodo.4290405.

[63] O. Sarbach and M. Tiglio, Phys. Rev. D **64**, 084016 (2001) 10.1103/PhysRevD.64.084016.

[64] T. Regge and J. A. Wheeler, Phys. Rev. **108**, 1063 (1957) 10.1103/PhysRev.108.1063.

[65] F. J. Zerilli, Phys. Rev. Lett. **24**, 737 (1970) 10.1103/PhysRevLett.24.737.

[66] M. Boyle and A. H. Mroue, Phys. Rev. D **80**, 124045 (2009) 10.1103/PhysRevD.80.124045.

[67] F. L. Markley and J. L. Crassidis, *Fundamentals of spacecraft attitude determination and control* (Springer New York, 2014), 10.1007/978-1-4939-0802-8.

[68] V. Varma, S. E. Field, M. A. Scheel, J. Blackman, L. E. Kidder, and H. P. Pfeiffer, Phys. Rev. D **99**, 064045 (2019) 10.1103/PhysRevD.99.064045.

[69] L. Bernard, L. Blanchet, G. Faye, and T. Marchand, Phys. Rev. D **97**, 044037 (2018) 10.1103/PhysRevD.97.044037.

[70] L. Blanchet and T. Damour, Phys. Rev. D **46**, 4304 (1992) 10.1103/PhysRevD.46.4304.

Chapter 6

NUMERICAL RELATIVITY SURROGATE MODEL WITH MEMORY EFFECTS AND POST-NEWTONIAN HYBRIDIZATION

J. Yoo et al., Phys. Rev. D **108**, 064027 (2023) 10.1103/PhysRevD.108.064027,

6.1 Abstract

Numerical relativity simulations provide the most precise templates for the gravitational waves produced by binary black hole mergers. However, many of these simulations use an incomplete waveform extraction technique—extrapolation—that fails to capture important physics, such as gravitational memory effects. Cauchy-characteristic evolution (CCE), by contrast, is a much more physically accurate extraction procedure that fully evolves Einstein's equations to future null infinity and accurately captures the expected physics. In this work, we present a new surrogate model, `NRHybSur3dq8_CCE`, built from CCE waveforms that have been mapped to the post-Newtonian (PN) BMS frame and then hybridized with PN and effective one-body (EOB) waveforms. This model is trained on 102 waveforms with mass ratios $q \leq 8$ and aligned spins χ_{1z}, $\chi_{2z} \in [-0.8, 0.8]$. The model spans the entire LIGO-Virgo-KAGRA (LVK) frequency band (with $f_{\rm low} = 20$Hz) for total masses $M \gtrsim 2.25 M_\odot$ and includes the $\ell \leq 4$ and $(\ell, m) = (5, 5)$ spin-weight -2 spherical harmonic modes, but not the $(3, 1)$, $(4, 2)$ or $(4, 1)$ modes. We find that `NRHybSur3dq8_CCE` can accurately reproduce the training waveforms with mismatches $\lesssim 2 \times 10^{-4}$ for total masses $2.25 M_\odot \leq M \leq 300 M_\odot$ and can, for a modest degree of extrapolation, capably model outside of its training region. Most importantly, unlike previous waveform models, the new surrogate model successfully captures memory effects.

6.2 Introduction

To date, there have been a total of 90 joint detections of gravitational wave (GW) signals by the LIGO[1] [1] and Virgo [2] collaborations. But, with increased sensitivity in future observation runs and the inclusion of KAGRA[2] [3] as well as other proposed

[1] The Laser Interferometer Gravitational-Wave Observatory.
[2] The Kamioka Gravitational Wave Detector.

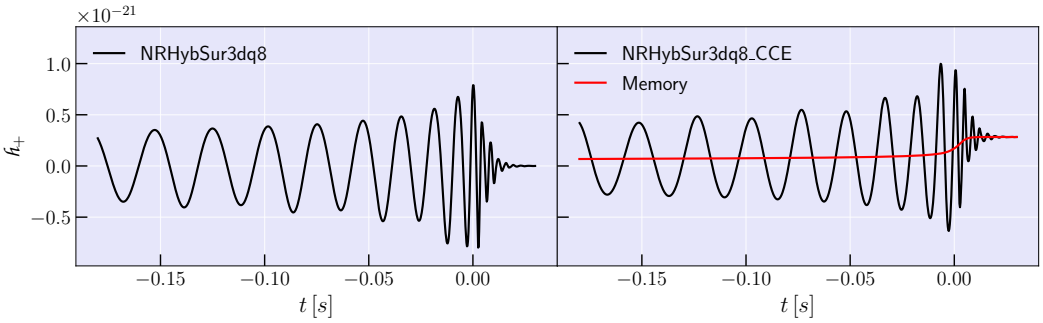

Figure 6.1: Plus polarization of the strain for a GW150914-like event computed using the previous surrogate `NRHybSur3dq8` (left) and the new surrogate `NRHybSur3dq8_CCE` (right). The exact parameters that are used to calculate these two waveforms are $m_1 = 36M_\odot$, $m_2 = 29M_\odot$, $\chi_{1z} = 0.32$, $\chi_{2z} = -0.44$, $D_L = 410$Mpc, $\iota = \pi/2$, and $\varphi = 0$. Because we wish to highlight the main difference between these surrogates, we used an inclination angle of $\iota = \pi/2$, i.e., the "edge on" orientation, for which the memory (red) (computed using Eq. (17b) of Ref. [9]) is maximized. Note that the memory roughly scales as $\sin^2(\iota)$.

future detectors, such as the Einstein Telescope [4], the Cosmic Explorer [5], and the space-based LISA[3] [6], the number of gravitational wave observations is expected to increase dramatically [7, 8]. To fully take advantage of the ever-expanding catalog of gravitational wave signals from compact binaries, it is crucial that we have high-fidelity waveform templates to compare the observed signals to. This is because accurate waveform templates are necessary for reliably extracting astrophysical source properties that provide important information about the binaries' formation channels and also for performing unique tests of general relativity.

Numerical relativity (NR) is the only *ab initio* method for solving Einstein's equations for the coalescence of two compact objects and has played a fundamental role in both GW theory and GW astronomy [10–13]. Even so, despite continued efforts by the NR community to make simulations more computationally efficient, they are still prohibitively expensive for key multi-query applications, such as parameter estimation. Because of this bottleneck, numerous waveform models have been developed [14–19] that can be evaluated much faster than evolving an entire NR simulation. By construction, these semi-analytical models rely on physically-motivated or phenomenological assumptions to reduce the complexity of parameter space. They then calibrate the remaining free parameters by comparing to the waveforms

[3]The Laser Interferometer Space Antenna.

produced by NR simulations. While these waveform models tend to be fast enough for performing GW data analyses, they are not nearly as accurate or reliable as NR waveforms.

NR surrogate models are a more recent addition to the collection of compact binary waveform models [20–26]. Unlike semi-analytic models, NR surrogates instead take a data-driven approach: training the waveform model directly on the waveforms output by simulations without the need to make any assumptions about the physics. Consequently, these surrogates recover NR waveforms much more faithfully than other semi-analytical models. However, because of this unique data-driven approach to waveform modeling, NR surrogate models can only be constructed for the regions of parameter space in which NR simulations exist.[4]

Both NR surrogates and other semi-analytical models have played a crucial role in studying previous detections of gravitational waves [29–36]. Up until now, however, every waveform model has always either been trained or calibrated by working with 'extrapolated' waveforms. Because NR simulations of binaries are necessarily run in a finite volume, one needs a method of 'extracting' the asymptotic waveform from the finite-volume data that is produced by the simulation. This is because the gravitational radiation that we observe on Earth can be well-approximated by the radiative solutions to Einstein's equations at future null infinity. In NR, an 'extrapolated' waveform refers to the asymptotic waveform from an extraction procedure called extrapolation.[5] However, a major limitation of these extrapolated waveforms, which are the waveforms currently included in the SXS [13, 38] and other catalogs [40, 41], is that they do not accurately capture phenomena known as memory effects [42–45].

Gravitational memory effects correspond to persistent phenomena that two observers can measure after the passage of gravitational radiation [42–45]. In particular, to measure memory effects, observers must measure the change in spacetime induced by the passage of radiation between two times: one before and one after the radiation. While there are several types of memory effects [46, 47], the two most prominent, and therefore detectable, effects are the displacement [42–45] and the spin [48] memories. The displacement memory is what two initially comoving observers will measure, while the spin memory is what two observers with initial relative velocities

[4] Surrogate models have also been constructed for semi-analytical EOB models [27, 28].

[5] Extrapolation uses Regge-Wheeler-Zerilli extraction to compute the strain waveform on a series of concentric spheres of constant coordinate radius and then extrapolates these values to future null infinity by fitting a power series in $1/r$ [37–39].

will measure, in conjunction with the usual displacement that they experience due to their nonzero relative velocities [47].

Apart from this classification of memory by the changes experienced by observers, there is also a classification in the way in which memory is sourced: ordinary and null.[6] Ordinary memory refers to the memory that is sourced by changes in the $\ell \geq 2$ mass multipole moment of "ordinary" unbound masses, while null memory refers to the memory that is sourced by a change in the energy radiated per unit solid angle due to the radiation of "null" gravitons. Consequently, null memory can be thought of as a form of the ordinary memory in which the unbound masses are individual gravitons. Generally, ordinary memory will be most prominent in unbound scattering processes, such as hyperbolic black hole encounters [50–55]. In contrast, null memory will be most prominent in bound scattering processes, such as binary black hole mergers. Because of this, in this work we will primarily be interested in the null memory.

While memory effects are an undetected phenomenon, various works have investigated their detectability using a forecast of future binary merger observations [56–58] and their observational consequences [59–61]. Furthermore, apart from their allure as a means to test Einstein's theory of relativity, memory effects have also attracted significant attention in the theory community because of their inherent connection to asymptotic symmetries and soft theorems [46, 48, 62–66]. Accordingly, it is crucial that templates for gravitational waves contain memory.

While extrapolated NR waveforms ultimately fail to correctly capture memory effects,[7,8] there is a much more robust type of asymptotic waveform extraction, called Cauchy-characteristic evolution (CCE), which fully evolves Einstein's equations to future null infinity and correctly resolves the various memory effects [68–71].

In this work, we build a hybridized NR surrogate model, `NRHybSur3dq8_CCE`, which is trained on CCE waveforms that have been created using the CCE module of the code `SpECTRE` [69, 70, 72]. Furthermore, to build our hybrid waveforms, using the

[6] Originally this classification was linear and nonlinear [42–44], but this terminology changed in recent years to more accurately reflect the physics sourcing this phenomenon [49].

[7] The reason why memory effects are not correctly resolved in extrapolated waveforms is because memory effects tend to have a much longer spatial dependence than the oscillatory components of the waveform. Consequently, when expressing the waveform as a series of $1/r$ terms, the convergence of the memory's contribution to the waveform is very slow and hard to capture [37–39].

[8] While some of the missing memory in extrapolated waveforms can be computed through post-processing [9, 67], there are certain types of memory effects that cannot be corrected, e.g., spin memory, which makes extrapolated waveforms impractical for formal analyses of memory.

technique outlined in [73], we first map our NR waveforms to the post-Newtonian (PN) BMS frame [73, 74] before we hybridize them with effective one-body (EOB) phase-corrected PN waveforms. By doing so, we find that `NRHybSur3dq8_CCE` performs on par with a related extrapolated version of this surrogate, `NRHybSur3dq8`, and in certain scenarios even outperforms `NRHybSur3dq8`, all while containing previously unresolved physical effects. As an illustration of our waveform model, we provide Fig. 6.1, which shows the correct waveform for a GW150914-like binary black hole merger event.

Throughout this paper, we adopt the common notations used by previous works. The mass ratio is denoted as $q = m_1/m_2$, where m_1 (m_2) denotes the mass of heavier (lighter) black hole, while the aligned spin of the heavier (lighter) black hole (in the direction of the binary's orbital angular momentum) is denoted as χ_{1z} (χ_{2z}). We use D_L to denote the luminosity distance, ι to denote the inclination angle between the orbital angular momentum and the line-of-sight to the detector, and φ to denote the azimuthal angle. Furthermore, when outputting our waveform templates, we represent the two polarizations of the gravitational wave—the plus and cross polarizations—as a single complex waveform, $h = h_+ - ih_\times$, which we then further decompose into a sum of spin-weight -2 spherical harmonic modes denoted as $h_{\ell m}$:

$$h(t, \iota, \varphi) = \sum_{\ell=2}^{\infty} \sum_{m=-\ell}^{\ell} h_{\ell m}(t)\, {}_{-2}Y_{\ell m}(\iota, \varphi). \tag{6.1}$$

Here ${}_{-2}Y_{\ell m}$ are the spin-weight -2 spherical harmonics. In Eq. (6.1), the quadrupole modes ($\ell = |m| = 2$) typically dominate the sum; however, the other modes are also important for estimating binary source properties [75–79]. Therefore, our new model `NRHybSur3dq8_CCE` includes $\ell \leq 4$ and $(5, 5)$ spin-weighted spherical harmonic modes, but not the $(3, 1)$, $(4, 2)$ and $(4, 1)$ modes. The reason for excluding these three modes is explained in Appendix 6.A. Like its predecessor, the new model `NRHybSur3dq8_CCE` is an aligned-spin model, restricted to binary black holes (BBHs) whose spins are aligned with the system's orbital angular momentum. Thus, due to orbital-plane symmetry, we do not have to model the $m < 0$ modes separately as they can be obtained from $m > 0$ through the well-known relation $h_{\ell\,(-m)} = (-1)^\ell h^*_{\ell m}$, where $h^*_{\ell m}$ represents the complex conjugate of $h_{\ell m}$.

The rest of the paper is organized as follows. In Sec. 6.3, we describe the entire construction of `NRHybSur3dq8_CCE`. In Sec. 6.4, we then evaluate the errors involved in building this model. In particular, we check the error due to hybridization,

the error of the surrogate itself, the success of the surrogate in extrapolating to values outside its training range, and the difference between `NRHybSur3dq8` and `NRHybSur3dq8_CCE`. Finally, in Sec. 6.5, we conclude with a few closing remarks. `NRHybSur3dq8_CCE`, our new surrogate model, has been made publicly available through the python package `gwsurrogate` [80].

6.3 Methods

In this section, we outline the steps that are required for building the new surrogate model `NRHybSur3dq8_CCE`. More specifically, in the subsequent text, we discuss the parameter space that our training waveforms will cover, Bondi-van der Burg-Metzner-Sachs (BMS) frame fixing, hybridization, and, finally, the routine for constructing the surrogate model `NRHybSur3dq8_CCE`.

6.3.1 Training set generation

To build the new surrogate model `NRHybSur3dq8_CCE`, we need a set of training waveforms in addition to their corresponding binary parameters. One cannot know, a priori, the optimal distribution of binary parameters for training the surrogate model. Fortunately, a previous surrogate model, `NRHybSur3dq8`, already explored the parameter space that we are interested in: mass ratio $q \in [1, 8]$ and $|\chi_{1z}|$, $|\chi_{2z}| \leq 0.8$, where χ_{1z} (χ_{2z}) is the spin of the heavier (lighter) black hole in the direction of the orbital angular momentum [23]. Hence, we use the same set of existing NR simulations (SXS:BBH:1419–1509, but not SXS:BBH:1468 or SXS:BBH:1488) that was used for training `NRHybSur3dq8`. For an equal mass simulation with unequal spins, we can exchange the two BHs to obtain an extra training data point. This is performed by applying a rotation (along the z-axis, defined as the axis of the orbital angular momentum of the BBH) by π to the waveform of $(q, \chi_{1z}, \chi_{2z}) = (1, \chi, \tilde{\chi})$ to obtain an extra waveform corresponding to $(q, \chi_{1z}, \chi_{2z}) = (1, \tilde{\chi}, \chi)$ for $\chi \neq \tilde{\chi}$. From the above 89 NR simulations, there are 13 of these cases, leading to 102 distinct training data.[9] In Fig. 6.2, we show the three-dimensional distribution $(q, \chi_{1z}, \chi_{2z})$ of our training parameters.

For each NR simulation used in our model, we extract the asymptotic waveform at future null infinity $\mathscr{I}^+$ using the `SpECTRE` code's implementation of CCE [69, 70, 72]. We run CCE on each of the four finite-radius worldtubes that the Cauchy

[9] Note that two NR simulations (SXS:BBH:1468 and 1488) are missing the world tube data that is necessary to produce the CCE waveforms of interest. This is why in this work we have 102 training data rather than the 104 training data used in [23].

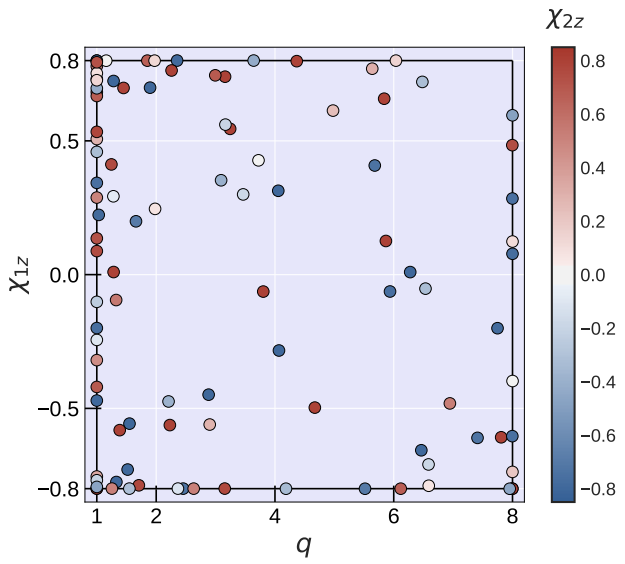

Figure 6.2: Training set parameters used in the construction of the new surrogate model `NRHybSur3dq8_CCE`. There are a total of 102 training data points used for `NRHybSur3dq8_CCE`, which exactly match those of `NRHybSur3dq8` minus two points, for which the initial world tube data for CCE was not available. The boundary of the training region is represented with the black rectangle: $1 \leq q \leq 8$ and $-0.8 \leq \chi_{1z}, \chi_{2z} \leq 0.8$.

evolution outputs. While in principle the CCEs that use these various worldtubes should yield valid and identical waveforms, we find that because of how the initial data for CCE is constructed there tends to be one worldtube that yields a more physically correct asymptotic waveform. We determine the best worldtube and waveform by examining which waveform's time derivative has the lowest L^2 norm after the ringdown phase. We find that this test is consistent with the previous method of checking which waveform and Weyl scalars minimally violate the five Bianchi identities [9, 71, 73, 74], but tends to yield waveforms with less junk radiation in the inspiral phase. As for the resolution of the CCE, we simply use the highest setting possible which yields errors in the CCE that are well below the errors from the Cauchy evolution. The waveforms that we use are interpolated to a uniform time step of $0.1M$, which is a dense enough time array to capture the important features of the waveform, including those that emerge near and during the merger phase.

Like extrapolated waveforms, CCE waveforms contain 'initial data transients' due to the imperfect initial data on the first null hypersurface of the characteristic evolution. These unphysical features, however, tend to persist much longer than those observed in the extrapolated waveforms. Fortunately, we find that by truncating the earlier

parts of the CCE waveforms, we can avoid this issue when constructing our training set in every mode except the $(3,1)$ and $(4,2)$ modes. Therefore, we exclude these modes in our new model. For more details about these modes and why we choose to exclude them, see Appendix 6.A.

6.3.2 BMS frame fixing

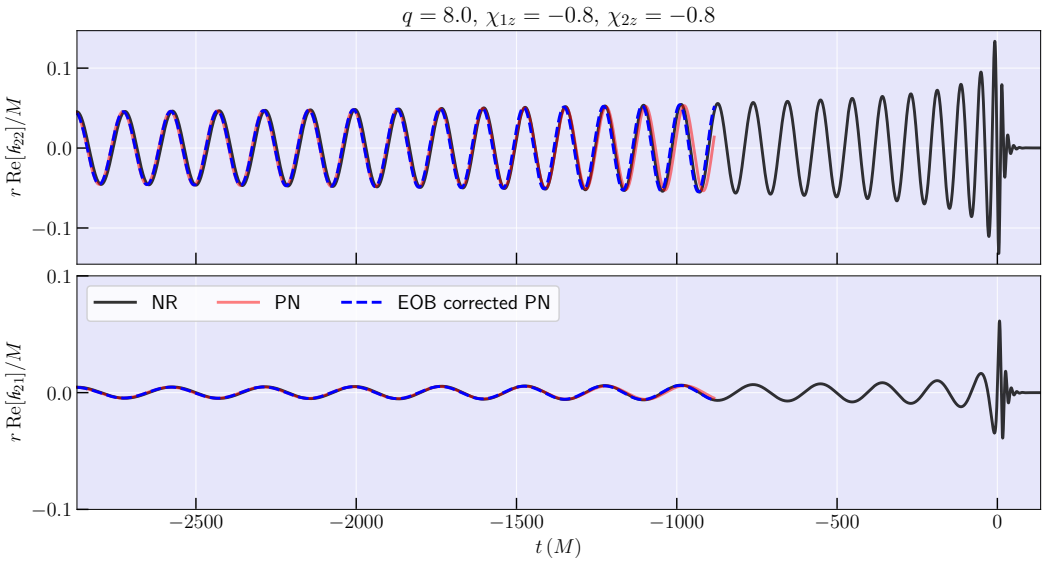

Figure 6.3: NR (black), PN (red), and EOB-corrected PN (blue) waveforms for an example simulation with binary parameters $q = 8.0$, $\chi_{1z} = -0.8$, and $\chi_{2z} = -0.8$. The real part of both the $(2,2)$ and $(2,1)$ modes are shown in the top and bottom panels. Notice that the EOB-corrected PN waveform is more faithful to the NR waveform than the PN waveform.

When building surrogate models, it is important to ensure that the training waveforms are in the same frame. Otherwise, undesired gauge artifacts can complicate or even interfere with the various fitting and interpolation steps that are used when building the surrogate model. The earlier surrogate model, `NRHybSur3dq8`, for example, implemented a center-of-mass corrected version of the extrapolated waveforms, in which the waveforms were mapped to a "Newtonian" center-of-mass frame of the binary using the coordinate trajectories of the black hole apparent horizons from the simulation [13].

However, the true gauge degree of freedom possessed by the gravitational waves at future null infinity is not the usual Poincaré group, but the BMS group, which includes an infinite-dimensional group of transformations that are called supertrans-

lations [81, 82] in addition to the usual Poincaré transformations. As a result, before using NR waveforms for any analysis, one should first fix these BMS freedoms.[10] In Refs. [73, 74] this task of fixing the BMS frame was performed by computing the various BMS charges that correspond to the symmetries of the BMS group and then finding the transformations that change those charges in a desired way. For example, to fix the translation and boost symmetries Refs. [73, 74] found a transformation that mapped the center-of-mass charge to have a mean of zero. More specifically, they found the transformation which minimized the time integral of the L^2 norm of this charge over a three-orbit window. Similarly, for fixing the system's supertranslation freedom, the same works also found what supertranslation to apply to the waveforms by examining a charge known as the Moreschi supermomentum—an extension of the usual Bondi four-momentum. By finding the supertranslation that mapped the Moreschi supermomentum to the value expected from PN theory, it was found that NR waveforms could be made to much better agree with PN waveforms once they were mapped to the same BMS frame of PN. This frame is called the PN BMS frame.

Because the surrogate model that we are building is for hybrid waveforms in which PN waveforms are stitched to the NR waveforms, the natural BMS frame to work with is, similarly, the PN BMS frame. Therefore, to fix the BMS frame of our waveforms we use the frame fixing procedure described in Ref. [73] and the python module `scri` [83–86]. That is, we fix the translation and boost freedoms by mapping the center-of-mass charge to have a mean of zero, we fix the rotation freedom by mapping the angular velocity vector to be aligned with that of a PN waveform, and we fix the supertranslation freedom by mapping the NR Moreschi supermomentum to agree with the PN Moreschi supermomentum [73]. We perform this frame fixing using a three-orbit window that starts $\sim 2500 - 3500M$ before the peak of the L^2 norm of the NR strain. This choice of BMS frame implies that the $\ell \geq 1$ components of the Moreschi supermomentum of our BBH vanish at $t \to -\infty$. This is equivalent to matching the PN memory terms with the NR system's memory over the hybridization window. This choice also implies that `NRHybSur3dq8_CCE`'s strains vanish at $t \to -\infty$.

[10] Note though that while fixing the BMS frame is important for modeling purposes, e.g., constructing or comparing waveform models, when examining waveforms at a point on the two-sphere, the only frame freedom that is relevant is the Poincaré freedom. This is because when looking at a point on the sky, supertranslations become degenerate with time translations.

6.3.3 Hybridization

Because of computational limits, NR simulations of BBHs typically only cover the last 20 orbits of inspiral. Thus, they are not nearly long enough to span the full LVK detection band for stellar mass binaries. More precisely, the initial frequency of (2,2) mode of these waveforms falls within the LVK band, taken to begin at $f_{\rm low} = 20$Hz, for total masses $M = m_1 + m_2 \gtrsim 60M_\odot$. To address this limitation and extend the validity of our model to lower values of total mass, we hybridize the CCE waveforms that are obtained from NR with the early inspiral parts of EOB phase-corrected PN waveforms. We create pure PN waveforms using the python package `GWFrames` [87]. For the PN orbital phase we include non-spinning terms up to 4 PN order [88–92] and spinning terms up to 2.5 PN order [93–95]. For the PN amplitude we include non-memory terms to 3.5 PN order [96–98], non-spinning memory terms to 3 PN order, and spinning memory terms up to 2 PN order [73, 99]. We use the TaylorT4 [100] approximant to compute the PN phase, but we replace this with an EOB-derived phase for the following reasons.

As noted in the previous work with `NRHybSur3dq8` [23], the accuracy of the inspiral parts from PN waveforms can be improved by replacing the PN phase with the phase that is derived from an EOB model, which undergoes an NR calibration. This improvement is typically larger for high mass-ratio systems, where the PN deviation from NR tends to be more significant, as is shown in Fig. 6.3. For the phase correction[11] to the PN waveforms used in this new surrogate model, we use the EOB model `SEOBNRv4_opt` [101, 102].[12]

Currently, the waveforms produced by CCE contain 'initial data transients' or 'junk radiation' because of imperfect initial data that forces us to discard early parts of the waveforms [71]. We find that the transients present in the CCE waveforms typically last noticeably longer than the junk radiation of the extrapolated waveforms [70]. Because of this, we instead use a hybridization window that is closer to the merger: roughly $2500 - 3500M$ before the peak of the L^2 norm of the strain. The later window further necessitates our use of the EOB-corrected phase for the inspiral part fo the PN waveforms.

Once the NR waveforms are mapped to the same frame as the EOB-corrected PN

[11] The phase correction procedure is identical to that described in Sec. IV B of Ref. [23].

[12] While `SEOBNRv4_opt` is trained on extrapolated waveforms rather than CCE waveforms, we do not expect this feature to noticeably impact the surrogate because the phase evolution of these different waveforms should still be comparable. Still, it would be interesting to see how our surrogate model construction changes when using EOB waveforms that have been calibrated with CCE waveforms.

waveforms via the procedures described in 6.3.2,[13] we then hybridize NR and PN together, for each spin-weighted spherical harmonic mode, $h_{\ell m}$, as:

$$h^{\rm hyb}_{\ell m} = h^{\rm PN}_{\ell m} + f\left(\frac{t-t_1}{t_2-t_1}\right)\left(h^{\rm NR}_{\ell m} - h^{\rm PN}_{\ell m}\right), \tag{6.2}$$

using the following transition function

$$f(x) = \begin{cases} 0 & x \leq 0, \\ \left(1+\exp\left[\frac{1}{x-1}+\frac{1}{x}\right]\right)^{-1} & 0 < x < 1, \\ 1 & x \geq 1. \end{cases} \tag{6.3}$$

Our choice of transition function matches that used in Ref. [74]. In the previous surrogate, `NRHybSur3dq8`, instead of hybridizing the complex waveforms directly, the waveforms were decomposed into amplitude and frequency before these components were hybridized independently. This was done to avoid undesirable artifacts that their transition function introduced, which are shown in Fig. 4 of Ref. [23]. Because CCE waveforms contain memory, which acts as a time-dependent offset in the waveforms, the decomposition into amplitude and frequency is not as useful as it is for the extrapolated waveforms which do not contain memory. Therefore, we choose to not use the previous hybridization method and instead directly stitch the NR and PN waveforms together. We do observe some minor glitches in the orbital frequency of a few of our hybrid waveforms in the hybridization window. However, these effects are largely negligible when compared to the other modeling errors for `NRHybSur3dq8_CCE`.

6.3.4 Post-processing the training data

In this section, we now describe how we construct the surrogate model from the hybrid waveforms of Sec. 6.3.3.

6.3.4.1 Down-sampling and common time array

First, we apply a time shift to each training waveform such that the peak of the L^2 norm

$$A_{\rm tot}(t) = \sqrt{\sum_{\ell,m} |h_{\ell m}(t)|^2} \tag{6.4}$$

[13] Even though we are using EOB-corrected PN waveforms as the target waveform in the BMS frame fixing procedure, because the EOB correction tends to zero as $t \to -\infty$, the frame that we map our NR waveforms to is still consistent with the PN BMS frame. The EOB-correction simply helps ensure that our mapping to the PN BMS frame is as accurate as possible.

is aligned at $t = 0$. The peak time of this curve is determined from a quadratic fit using 5 time samples that are adjacent to the discrete maximum of $A_{\rm tot}$. When we compute the sum in Eq. (6.4), we use every mode of the hybrid waveform, including the $m < 0$ modes.

To begin with, the length of each hybrid waveform is determined by ensuring that the initial orbital frequency is $\omega_{\rm orb} = 2 \times 10^{-4}\,{\rm rad}/M$, where $\omega_{\rm orb}$ is approximated from ϕ_{22}, the phase of the (2,2) mode, using

$$\omega_{\rm orb} = \frac{1}{2}\frac{d\phi_{22}}{dt} \tag{6.5}$$

This frequency choice, however, results in waveforms with different lengths for different mass ratios and spins. The surrogate-building procedure, however, requires that every training waveform share a common time array. Therefore, to remedy this issue we truncate the training waveforms such that they begin with time $t = -5.8 \times 10^8 M$, which is the first time of the shortest waveform in the surrogate's training set. After truncation, the training set's largest starting orbital frequency is $\omega_{\rm orb} = 2.8 \times 10^{-4}\,{\rm rad}/M$. Consequently, this frequency is the low-frequency limit of validity for the surrogate model.

For the LVK observatories, if we assume that 20Hz is the lowest GW frequency that can be measured, then the $(2, 2)$ mode of the surrogate model can be considered valid for total masses $M \geq 0.9 M_\odot$. The highest spin-weighted spherical harmonic mode included in `NRHybSur3dq8_CCE` is the $(5, 5)$ mode for which the corresponding frequency is a factor of $5/2$ more than that of the $(2, 2)$ mode. Thus, the entire surrogate is valid for total masses $M \geq 2.25 M_\odot$.

Because the hybrid waveforms are millions of M long, it is not practical to sample the entire waveform with a small uniform time step like $0.1M$, as is typically used for NR-only surrogates [24]. Fortunately, the early inspiral, low-frequency portion of the waveform does not require as dense a sampling as the later high-frequency portion. Therefore, we instead down-sample the time arrays of the truncated waveforms such that there are only 5 points per orbit for the shortest hybrid waveform of the training set. However, for $t \geq -1000M$, we switch to uniformly spaced time samples with a time step of $0.1M$ to ensure that we have sufficiently dense sampling for the late inspiral and merger-ringdown phases where the frequency reaches its peak. We retain times up to $135M$ after the peak to ensure that we fully capture the numerically resolvable parts of the ringdown phase.

Given the common down-sampled time array, we then use cubic splines to interpolate all of the waveforms in the training set onto the common time array. However, we first transform the waveforms to the co-orbital frame, which we construct via

$$\text{co-orbital frame: } \begin{cases} h^C_{\ell m} = h_{\ell m} e^{im\phi_{\rm orb}} \\ h_{22} = A_{22} e^{i\phi_{22}} \\ \phi_{\rm orb} = \phi_{22}/2 \end{cases} \tag{6.6}$$

where $h_{\ell m}$ is the inertial frame waveform, $\phi_{\rm orb}$ is the orbital phase, and A_{22} and ϕ_{22} are the amplitude and phase of the $(2,2)$ mode. The co-orbital frame is roughly co-rotating with the binary and is obtained by applying a time-dependent rotation about the $\hat{z}$-axis by an amount measured by the instantaneous orbital phase. As the waveforms are slowly varying functions of time in the co-orbital frame, by transforming to this frame we can increase the interpolation accuracy. For the $(2,2)$ mode, we sample the amplitude A_{22} and phase ϕ_{22}, while for all other modes we use the real and imaginary parts of $h^C_{\ell m}$.

6.3.4.2 Phase alignment

After interpolating to a common time array, we align the phases of the waveforms by rotating the waveforms about the $\hat{z}$-axis such that the orbital phase $\phi_{\rm orb}$ is zero at time $t = -1000M$. This ensures that each waveform corresponds to a binary with its heavier black hole on the $\hat{x}$-axis at that time. Note that this frame is constructed using information from the waveform at future null infinity, and as a result these BH positions need not correspond to the gauge-dependent BH positions in the NR simulations.

6.3.4.3 Data decomposition

As mentioned earlier, it is easier to build a model for slowly varying functions of time. Because of this, we decompose the inertial frame strain $h_{\ell m}$, which is oscillatory, into simpler waveform data pieces and build a separate surrogate model for each of these data pieces. For the $(2,2)$ mode, we decompose this mode into the amplitude A_{22} and the phase ϕ_{22}, while for the other $m \neq 0$ waveform modes, we model the real and imaginary parts of the co-orbital frame strain, h^C_{lm}, using Eq. (6.6). For the $m = 0$ modes of non-precessing systems, $h^C_{\ell m}$ is purely real (imaginary) for even (odd) ℓ. Because of this, we only model the non-trivial part for the $m = 0$ modes.

Because our hybrid waveforms are rather long—extending over roughly 3×10^4 orbits—ϕ_{22} roughly spans 10^5 radians. Accurately modeling the phase evolution of such long hybrid waveforms poses a challenge. We find that we can resolve this issue, however, by subtracting the leading-order Taylor T3 PN phase [103], $\phi_{22}^{\rm T3}$, and simply modeling the phase residual, $\phi_{22}^{\rm res} = \phi_{22} - \phi_{22}^{\rm T3}$, as was performed in Ref. [23]. The leading-order prediction from the TaylorT3 PN approximant [103] is

$$\phi_{22}^{\rm T3} = \phi_{\rm ref}^{\rm T3} - \frac{2}{\eta\theta^5} \tag{6.7}$$

with

$$\theta = [\eta(t_{\rm ref} - t)/(5M)]^{-1/8}, \tag{6.8}$$

where $\phi_{\rm ref}^{\rm T3}$ is an arbitrary integration constant, $t_{\rm ref}$ is an arbitrary time offset, and $\eta = q/(1+q)^2$ is the symmetric mass ratio. Because, by definition, θ diverges at $t = t_{\rm ref}$, to avoid such divergences we set $t_{\rm ref} = 1000M$, which is sufficiently long after the end of the waveform. We also choose $\phi_{\rm ref}^{\rm T3}$ such that $\phi_{22}^{\rm T3} = 0$ at $t = -1000M$, i.e., the time at which we align the phase, as outlined in Sec. 6.3.4.2.

6.3.5 Surrogate building

Given the decomposed waveform data pieces, we build a surrogate model for each individual data piece using the same procedure as that of Sec. V. C of Ref. [23], with a few minor modifications, which we summarize below.

For each waveform data piece, we begin by constructing a linear basis in parameter space, so that we can reduce the training data set to a smaller representative data set. The basis functions that we use are chosen in the following iterative manner [104–107], called the 'greedy algorithm':

1. Pick out the training data with the largest L^2 norm and add it to the basis set as the first basis function;

2. Compute the projection error between each of the training data and the basis set;

3. Determine which of the training data has the highest projection error and add this to the basis set;

4. Repeat steps 2–3 until a pre-determined number of basis functions for each data piece is obtained.

For step 4, we determine the number of basis functions used for each of the data pieces through trial and error. That is, we increase the number of basis functions until the inclusion of new basis functions introduces noise into the model or gives diminishing returns in terms of minimizing the projection errors. The number of basis functions that is used for each data piece is shown in Table 6.3.5.

data piece	number of basis functions
A_{22}, ϕ_{22}	15
Re h^C_{21}, Im h^C_{21}	12
Re h^C_{20}	12
Im h^C_{30}	12
Re h^C_{43}, Im h^C_{43}	12
Re h^C_{55}, Im h^C_{55}	8
others	10

Table 6.1: Number of basis functions for each data piece.

Next, we build empirical time interpolants [105, 108–111] with the same number of empirical nodes as the number of basis functions that are used to model the data piece. Following the methodology of Ref. [23] we also require that the start of the waveform always be included as one of the empirical nodes. This provides an 'anchor point' that ensures that the waveform data pieces start with the correct value. In Ref. [23], no empirical nodes were picked at times past $t > 50M$ to ensure that little to no numerical noise was being modeled, particularly for the phase data piece. We follow the same convention for the phase data pieces; however, for the other data pieces we allow time nodes past $t > 50M$ to ensure that the surrogate correctly models the memory throughout the entirety of the ringdown phase.

Finally, for each empirical time node, we construct a parametric fit for the waveform data piece, following the Gaussian process regression (GPR) fitting method described in the supplementary material of Ref. [112], using the python package `scikit-learn` [113]. For the fit itself, we use the parameterization used in Ref. [23]. That is, we use the parameters $\log(q)$, $\hat{\chi}$, and χ_a, where $\hat{\chi}$ is the leading order spin parameter [114–117] for the GW phase in the PN expression

$$\hat{\chi} = \frac{\chi_{\rm eff} - 38\eta(\chi_{1z} + \chi_{2z})/113}{1 - 76\eta/113}, \tag{6.9}$$

with

$$\chi_{\rm eff} = \frac{q\chi_{1z} + \chi_{2z}}{1+q}, \tag{6.10}$$

and χ_a is the anti-symmetric spin defined as

$$\chi_a = \frac{1}{2}(\chi_{1z} - \chi_{2z}). \tag{6.11}$$

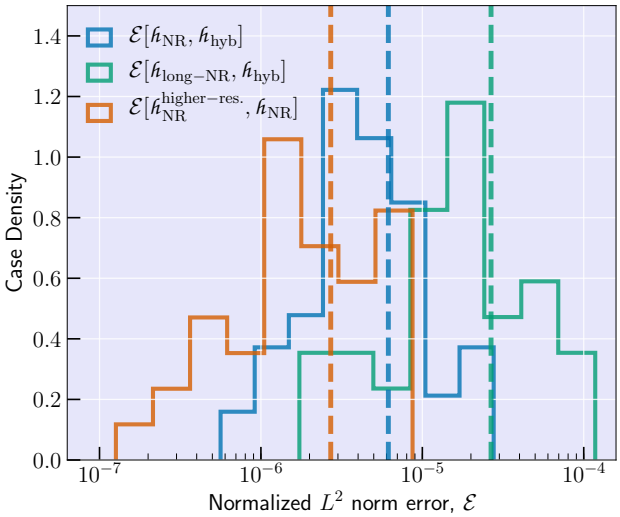

Figure 6.4: Two unique estimates of the hybridization error. $\mathcal{E}\left[h_{\rm NR}, h_{\rm hyb}\right]$, using Eq. (6.12), computes the error between the hybrid and the NR waveforms in the hybridization window. Meanwhile, $\mathcal{E}\left[h_{\rm long-NR}, h_{\rm hyb}\right]$ computes the error between the hybrid and the long NR waveforms from an initial time of $t_1 = -6000M$ to the end of hybridization window. We also include $\mathcal{E}\left[h_{\rm NR}^{\rm higher-res}, h_{\rm NR}\right]$ as a resolution error between the two highest resolution NR waveforms, computed within the hybridization window. $\mathcal{E}\left[h_{\rm NR}, h_{\rm hyb}\right]$ was computed for every one of the 102 training waveforms, while $\mathcal{E}\left[h_{\rm long-NR}, h_{\rm hyb}\right]$ and $\mathcal{E}\left[h_{\rm NR}^{\rm higher-res}, h_{\rm NR}\right]$ were computed for the 37 waveforms for which longer and higher resolution simulations were available. The dashed lines represent the median values.

6.4 Error Quantification

With the methodology behind the construction of our surrogate model outlined in Sec. 6.3, we now examine the quality of `NRHybSur3dq8_CCE` by conducting a variety of model consistency checks and waveform comparisons. This process involves examining both the error in the hybridization and the error in the surrogate model itself as well as the ability of the surrogate to model waveforms outside of its training parameter space.

6.4.1 Hybridization errors

Before building the surrogate model, we first have to map the NR waveforms to be in the same frame as the EOB-corrected PN waveforms. As described in Sec. 6.3.2,

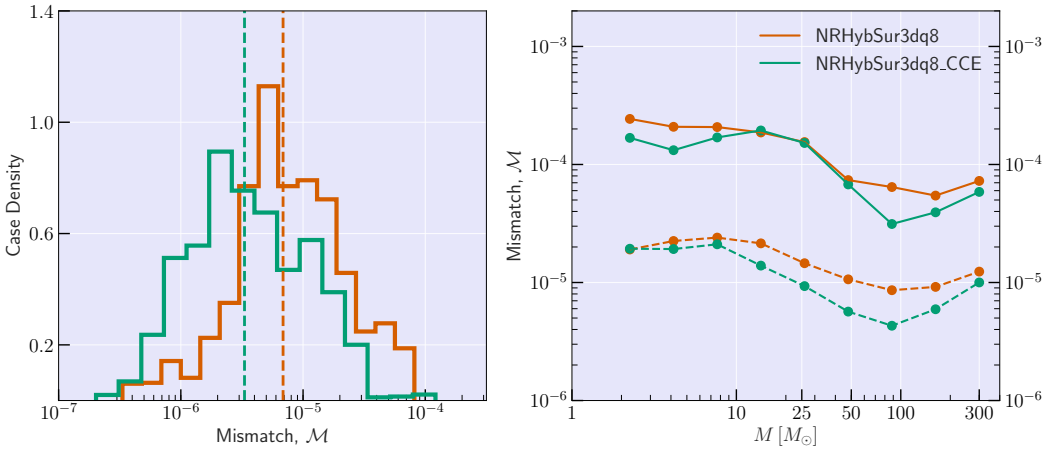

Figure 6.5: Frequency-domain mismatches for the `NRHybSur3dq8` and `NRHybSur3dq8_CCE` surrogates when compared to their respective training hybridized waveforms (extrapolated and CCE, respectively). The results for `NRHybSur3dq8` are taken from Fig. 6 of Ref. [23] and are plotted for comparison with `NRHybSur3dq8_CCE`. For both of these surrogate models, we compute leave-five-out errors at several points in the sky of the source frame using all available modes in each model: $\ell \leq 4$ and $(5,5)$, but excluding $(3,1)$, $(4,2)$, and $(4,1)$ for `NRHybSur3dq8_CCE` and $(4,1)$ and $(4,0)$ for `NRHybSur3dq8`. ***Left***: Mismatches computed using a flat noise curve for only the late inspiral part (NR part) of the hybrid waveforms. The dashed vertical line represents the median mismatch value. ***Right***: Mismatches computed using the Advanced-LIGO noise curve as a function of the system's total mass. The solid (dashed) line represents 95$^{\text{th}}$ percentile (median) mismatch values.

this fixes the BMS freedom of the NR waveforms by mapping the waveforms to the PN BMS frame using the procedure outlined in Ref. [73]. Following this, we then stitch the two waveforms to create a hybrid waveform that we use as our training waveform. One of the important checks for the quality of our final training waveform is to understand the errors that result from performing this hybridization procedure between NR and PN waveforms. There are two natural ways to conduct this check.

First, we can simply compare the hybrid waveform to the NR waveform in the hybridization window. This check will determine the combined discrepancy that results from the discrepancy between the PN and NR waveforms and from using the smooth transition function in Eq. (6.3). Next, to examine the error introduced from using PN for the early inspiral parts of our hybrid waveform, we can compare the hybrid to a simulation that has identical binary parameters, but a larger initial BH separation. Fortunately, of the simulations that we include in our surrogate's

training data set, 37 of them have these longer extensions that we can use for a comparison with the hybrid waveforms.

To quantify the error for these comparisons, we use the following function:

$$\mathcal{E}\left[h^{(1)}, h^{(2)}\right] \equiv \frac{1}{2}\frac{\sum_{\ell,m}\int_{t_1}^{t_2}|h^{(1)}_{\ell m}(t) - h^{(2)}_{\ell m}(t)|^2 dt}{\sum_{\ell,m}\int_{t_1}^{t_2}|h^{(1)}_{\ell m}(t)|^2 dt}. \tag{6.12}$$

For the first comparison, we compute the error within the hybridization window, where t_1 is roughly $3000M$ before merger and t_2 is the time at which the system has undergone 3 orbits since t_1. For the latter comparison, we first map the long NR waveforms to the BMS frame of the training NR waveforms and then compute the error between these waveforms from $t_1 = -6000M$ to the end of the hybridization widow. The results of these comparisons are shown in Fig. 6.4. We observe that our two estimates for the hybridization error are low, but tend to be higher than the estimate of the NR resolution error. Note, though, that the NR resolution errors, which were computed for a smaller subset of NR simulations for which the higher resolution data was available, come from simulations that are for more comparable mass binaries. Because the difficulty of NR simulations increases with mass ratio, we therefore expect that the NR resolution error that we computed is a minor underestimate of the true error. Regardless, Fig. 6.4 suggests that our training waveforms are primarily limited by the accuracy of the PN waveforms, rather than the NR resolution error.

6.4.2 Model errors

We now evaluate the accuracy of the surrogate model `NRHybSur3dq8_CCE` by comparing the waveforms that it produces to the hybridized PN/NR waveforms that were used to train it. We quantify this model accuracy by computing the frequency-domain mismatch $\mathcal{M}$ between two waveforms h_1 and h_2 via

$$\mathcal{M} = 1 - \frac{\langle h_1, h_2\rangle}{\sqrt{\langle h_1, h_1\rangle \langle h_2, h_2\rangle}} \tag{6.13}$$

with

$$\langle h_1, h_2\rangle = 4\mathrm{Re}\left[\int_{f_{\min}}^{f_{\max}} \frac{\tilde{h}_1(f)\tilde{h}_2^*(f)}{S_n(f)}\, df\right], \tag{6.14}$$

where $\tilde{h}(f)$ denotes the Fourier transform of the strain $h(t)$, * the complex conjugate, and $S_n(f)$ the one-sided power spectral density of, say, a GW detector. The

mismatches are optimized over shifts in time, polarization angle, and the initial orbital phase following the procedure described in Appendix D of Ref. [21]. For each pair of waveforms, we compute mismatches at a total of 37 sky points that are uniformly distributed over the two-sphere.

Before performing the Fourier transform, we taper both ends of the time domain waveform.[14] The tapering at the start of the waveform is done over 1.5 cycles of the $(2, 2)$ mode. Because the waveforms that we are examining include memory effects, tapering them in the ringdown region can produce a significant level of windowing effects[15] in the Fourier spectrum. Therefore, before computing mismatches we first pad the end of the waveforms with their final values for $1000M$ and then taper them over this padded region. We find that a padding length of $1000M$ is enough to significantly reduce windowing effects from tapering and that the mismatch result is not very sensitive to this choice of padding length.

Because we use all available hybrid waveforms for the training of the model `NRHybSur3dq8_CCE`, if we compute the mismatch of our model against hybrid waveforms we would obtain a training error, rather than an estimate of the true modeling error. Thus, we instead estimate the out-of-sample error by performing leave-five-out analyses for the `NRHybSur3dq8` and `NRHybSur3dq8_CCE` models. We construct exactly 20 trial surrogates, leaving out 5 or 6 waveforms from the training set for each surrogate. By calculating the mismatch between each surrogate and the left-out waveforms, we are then able to assess the performance of each surrogate against waveforms that were not used in the training process.

The left panel of Fig. 6.5 shows the mismatches for `NRHybSur3dq8_CCE` that are computed using a flat (white) noise curve ($S_n = 1$) over the late inspiral part (NR part) of the hybrid waveforms, truncating the waveforms to start at $t = -3500M$ for `NRHybSur3dq8` and at $t = -2500M$ for `NRHybSur3dq8_CCE`.[16]

The right panel of Fig. 6.5 show results that are more relevant to GW observations: namely, the mismatches computed with the Advanced-LIGO design sensitivity Zero-

[14] A value mismatch at both ends of the waveform tends to result in the presence of Gibbs phenomenon in the Fourier spectrum. To avoid this, we taper the waveform to zero at both ends using a Planck window [118].

[15] A new scheme for pre-processing that potentially reduces this windowing effect is proposed in Ref. [119].

[16] The discrepancy is due to the later hybridization window that was used for `NRHybSur3dq8_CCE` as explained in Sec. 6.3.3. We define $f_{\rm min}$ to be the frequency of the $(2, 2)$ mode at the end of the initial tapering window, and $f_{\rm max} = 5 f_{22}^{\rm peak}$, where $f_{22}^{\rm peak}$ is the frequency of the $(2, 2)$ mode at its peak. The choice of $f_{\rm max}$ ensures that we capture the peak frequency of every mode.

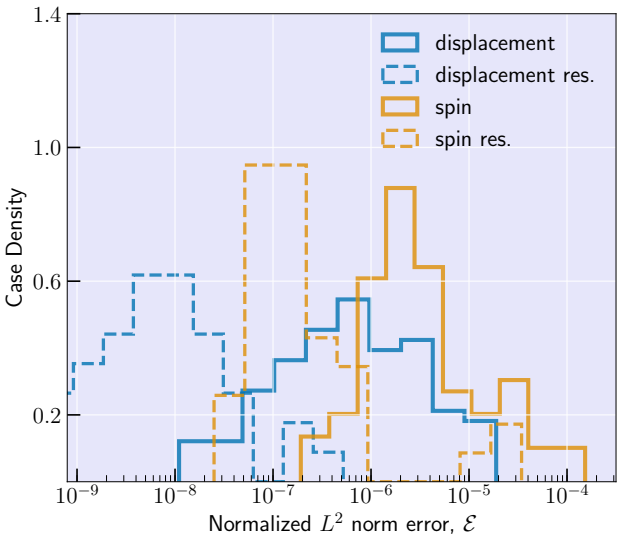

Figure 6.6: Errors for the displacement (blue) and spin (orange) memory effects computed by comparing the training waveforms to `NRHybSur3dq8_CCE`'s output using Eq. (6.12). For this result, we show the leave-five-out cross-validation errors (solid line). As a reference, we also include the errors computed between the two highest resolution waveforms (dashed line).

Detuned-High-Power noise curve [120] with $f_{\rm min} = 20$Hz and $f_{\rm max} = 2000$Hz for various total masses. We also include the mismatch result for `NRHybSur3dq8` from Ref. [23] for comparison. On the horizontal axis, different total masses correspond to different portions of the waveform falling within the $[20\text{Hz}, 2000\text{Hz}]$ window. This roughly implies that the low end of the total mass axis is a proxy for the fidelity of the early inspiral part of the waveforms, while the high end is a proxy for the late inspiral parts. We show the mismatch for various total masses: from the lower limit of the range of validity of the surrogate, i.e., $M \gtrsim 2.25 M_\odot$, up to $M = 300 M_\odot$. For each total mass point that we plot, we show both the median and the $95^{\rm th}$ percentile mismatches.

For the surrogate modeling errors, we obtain values that are comparable to—and often better than—those of `NRHybSur3dq8`, despite the additional modeling challenges resulting from the new contributions due to the presence of memory. The $95^{\rm th}$ percentile mismatches fall below $\sim 3 \times 10^{-4}$ for the entire mass range.

Last, we test how well the surrogate models both the displacement and spin memory contributions. To do this, we compute the displacement and spin null memories, i.e., Eqs. (17b) and (17d) from Ref. [9] which only depend on the strain, using both the training waveforms and the surrogate evaluation, and then calculate the normalized

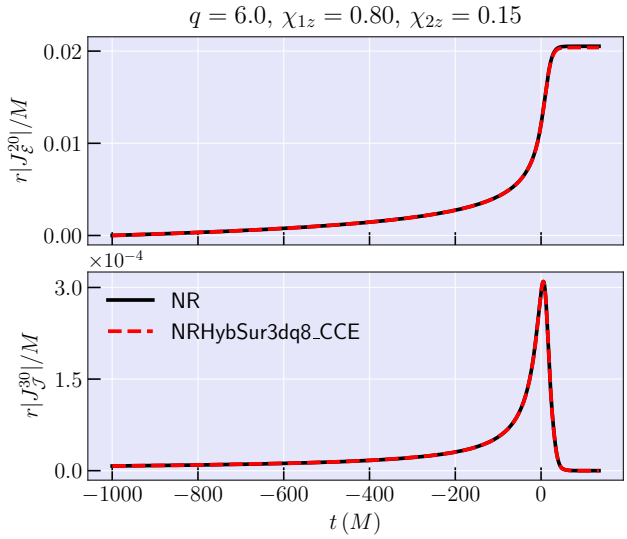

Figure 6.7: Amplitudes of the most dominant modes of the displacement and spin memory effects when computed from the NR waveform and the surrogate evaluation for the case with the largest errors in Fig. 6.6. The top and bottom panels show the $(2,0)$ mode of the displacement null memory and the $(3,0)$ mode of the spin null memory.

L^2 norm error between the two using Eq. (6.12) over the $t \in [-1000M, 135M]$ window. The choice of the window's starting time is arbitrary but early enough to capture most of the memory. For this check, we again perform leave-five-out analyses to estimate `NRHybSur3dq8_CCE`'s modeling error. As a reference for these errors, we also show the numerical resolution error from the same set of 37 simulations used for Fig. 6.4. As shown in Fig. 6.6, the modeling error for the two memory effects is at a reasonable level, albeit higher than our estimate of the resolution error. As shown in Fig. 6.7, even for the case that corresponds to the largest error value in Fig. 6.6, the memory effects computed from the surrogate evaluation closely agree with those computed from NR waveforms.

We suspect that the spin memory accuracy is typically worse than that of the displacement memory because the spin memory is smaller than the displacement memory and is thus harder to resolve. The discrepancy between the modeling error and the resolution error suggests that there is room for future improvements in modeling the memory contribution. Building future surrogate models using CCE waveforms from higher resolution and longer NR simulations might help improve this modeling error; however, a new data decomposition scheme or even a new modeling strategy could be necessary to obtain an improved modeling of memory

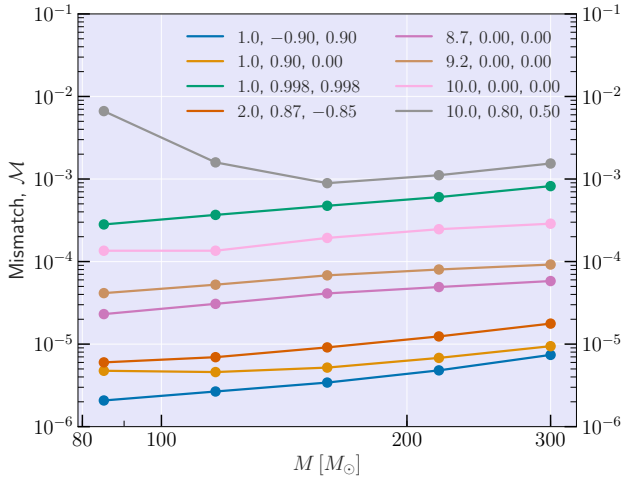

Figure 6.8: Noise-weighted frequency-domain mismatches between `NRHybSur3dq8_CCE` and NR simulations that are outside the model's training region. The numbers in the legend correspond to the NR simulation's mass ratio q, primary spin χ_{1z}, and secondary spin χ_{2z}. The mismatches that are shown are computed at several points in the sky of the source frame using the Advanced-LIGO noise curve. Each of the solid lines represents the 95$^{\text{th}}$ percentile mismatch values.

effects.

6.4.3 Extrapolating outside training region

The errors that we have examined thus far have been restricted to the training region of the parameter space: $q \leq 8$, $\chi_{1z}, \chi_{2z} \in [-0.8, 0.8]$. It is possible, however, to evaluate the surrogate outside the training region, e.g., for larger mass ratio, q, or even higher primary or secondary spin magnitudes: $|\chi_{1z}|$, $|\chi_{2z}|$. Consequently, to understand the extrapolation capability of the model, we compute errors of the model against a few existing simulations (SXS:BBH:0185, 0189, 0199, 1124 2085, 2105, 2132, and 2515) [13, 20, 38, 121] that have relatively high mass ratios or spin magnitudes.

As shown in Fig. 6.8, the mismatch results, while worse than those shown in Fig. 6.5, are nonetheless reasonable. The highest three mismatch results correspond to the three most extreme parameter simulations: mass ratio $q = 10$ or spin magnitude $|\chi_{1z}|, |\chi_{2z}| = 0.998$, for which we do not expect the `NRHybSur3dq8_CCE` to perform well. Apart from these, we find that the surrogate performs well for a modest degree of extrapolation, with many of the mismatches falling below values near $\sim 10^{-4}$.

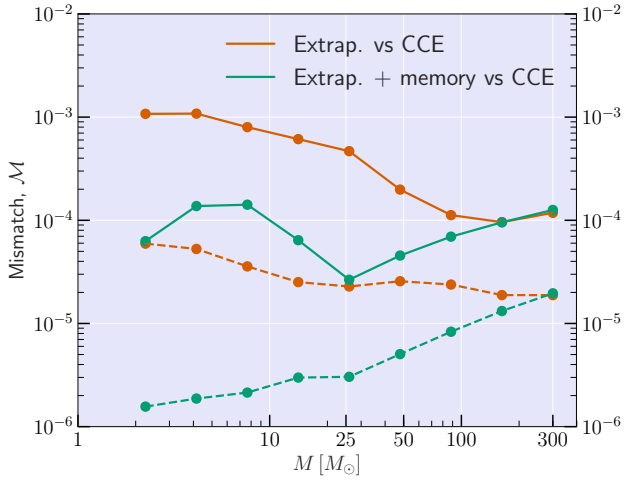

Figure 6.9: Noise-weighted frequency-domain mismatches between extrapolated and CCE hybrid waveforms in red. These are the hybrid waveforms that were used to train `NRHybSur3dq8` and `NRHybSur3dq8_CCE`. Apart from this, we also include the mismatches between the memory-corrected extrapolated and CCE waveforms in green. The mismatches that are shown are computed at several points in the sky of the source frame using the Advanced-LIGO noise curve. The solid (dashed) line represents the 95$^{\text{th}}$ percentile (median) mismatch values.

6.4.4 Systematic bias in waveforms that omit memory or add it through post-processing

Finally, in Fig. 6.9, we show the mismatch between the training waveforms used for `NRHybSur3dq8_CCE` and those that were used for `NRHybSur3dq8`. The primary purpose of this analysis is to obtain a rough estimate of the level of systematic bias that one could expect from analyzing a GW signal that contains memory using a waveform that does not. Apart from this, we also show the mismatch between an extrapolated waveform, once we have added the expected memory contribution to it using Eq. (17b) of Ref. [9], and a CCE waveform from the same simulation. This highlights that, while there is a noticeable difference between CCE waveforms and extrapolated waveforms, these discrepancies are largely reduced by adding memory to the extrapolated waveform. Because of this result, we suspect that memory-detection studies that have used this memory-correction technique, like Refs. [56–58, 122, 123], would likely obtain similar estimates had they used our new surrogate model `NRHybSur3dq8_CCE`. Note though that `NRHybSur3dq8_CCE` will be better for performing analyses of the spin memory, seeing as the contribution of spin memory to extrapolated waveforms cannot be as easily corrected [9]. Regardless, it would still be interesting to see if the conclusions made by these studies on memory, or

even parameter estimation results, change when using NRHybSur3dq8_CCE instead of NRHybSur3dq8.

6.5 Conclusion

In this work, we present a new surrogate model, NRHybSur3dq8_CCE, the first GW model to contain both the oscillatory and memory components of the strain. Consequently, NRHybSur3dq8_CCE is the first model to fully capture the expected GW physics of binary black hole mergers. The model is trained on 102 NR/PN hybrid waveforms from aligned-spin binary BH systems with mass ratios $q \leq 8$ and aligned spins $|\chi_{1z}|, |\chi_{2z}| \leq 0.8$. These hybrid waveforms are constructed by first mapping CCE waveforms to the PN BMS frame before hybridizing them with PN waveforms whose phase has been corrected using EOB waveforms. Performing this frame fixing helps eliminate unwanted gauge artifacts that could potentially interfere with modeling. The model includes $\ell \leq 4$ and $(5,5)$ spin-weighted spherical harmonic modes, but not the $(3,1)$, $(4,2)$, or $(4,1)$ modes, and spans the entire LVK band (with $f_{\rm low} = 20$Hz) for total masses $M \geq 2.25 M_\odot$. By conducting a series of leave-five-out cross-validation analyses, we find that NRHybSur3dq8_CCE can accurately reproduce the hybrid waveforms that were used to train it with mismatches below $\sim 3 \times 10^{-4}$ for total masses in the range $2.25 M_\odot \leq M \leq 300 M_\odot$. These accuracies are on par with—and often better than—the previous aligned-spin NR surrogate model, NRHybSur3dq8, despite the modeling challenges that result from the inclusion of new modes and memory effects. Apart from this, we also importantly find that NRHybSur3dq8_CCE can successfully capture the null memory contributions with mismatches below $\sim 2 \times 10^{-4}$. Last, NRHybSur3dq8_CCE is also found to reproduce waveforms outside of its trained region of parameter space for a moderate degree of extrapolation; however, we advise caution when extrapolating the model. This new model is made publicly available through the python package `gwsurrogate` [80].

With the expected advances in detector sensitivity for both current and future gravitational wave observatories, waveform templates with memory effects will prove to be crucial for analyzing future compact binary detections. The new surrogate model NRHybSur3dq8_CCE serves as the first step in an important endeavor to produce a complete set of waveform templates that contain these undetected effects and thus correctly capture the expected gravitational wave physics of binary black hole mergers.

6.6 Acknowledgments

This work was supported in part by the Sherman Fairchild Foundation and by NSF Grants PHY-2011961, PHY-2011968, and OAC-2209655 at Caltech, and NSF Grants PHY-2207342 and OAC-2209655 at Cornell. `SpECTRE` uses `Charm++/Converse` [124], which was developed by the Parallel Programming Laboratory in the Department of Computer Science at the University of Illinois at Urbana-Champaign. V.V. acknowledges support from the European Union's Horizon 2020 research and innovation program under the Marie Skłodowska-Curie grant agreement No. 896869. L.C.S. was partially supported by NSF CAREER Award PHY-2047382. S.E.F acknowledges partial support from NSF Grant PHY-2110496 and by UMass Dartmouth's Marine and Undersea Technology (MUST) Research Program funded by the Office of Naval Research (ONR) under Grant No. N00014-23-1–2141. This material is based upon work supported by NSF's LIGO Laboratory which is a major facility fully funded by the NSF. This project made use of `Python` libraries including `SciPy` [125] and `NumPy` [126], and the figures were produced using `matplotlib` [127] and `seaborn` [128].

6.A Challenges in modeling certain modes

6.A.1 Impact of long-lived transient junk

The waveforms produced by CCE contain initial data transients that typically persist much longer than those of the Cauchy evolution. Because of this effect, as was outlined in Sec. 6.3.3, we choose to remove the early parts of our NR waveforms when constructing our surrogate's training waveforms. Nevertheless, even after we perform this truncation, some of the waveforms that we use for the surrogate still exhibit unphysical effects that we do not see when using extrapolated waveforms, or CCE waveforms from higher resolution or longer Cauchy evolutions.

We find that initial data transients are most pronounced in the $(3, 1)$ and $(4, 2)$ modes, and are often identified by unphysical amplitude oscillations, as shown in Fig. 6.10. As is the case with all models, the surrogate model `NRHybSur3dq8_CCE` is only as good as the data that it is trained on. In fact, we find that having even only a few training waveforms with these issues can result in noisy and unphysical features being modeled by the surrogate.

We find that these unphysical oscillations in certain modes are significantly reduced for waveforms extracted from both higher resolution and longer Cauchy evolutions. Unfortunately, such simulations only exist for one third of our training data set.

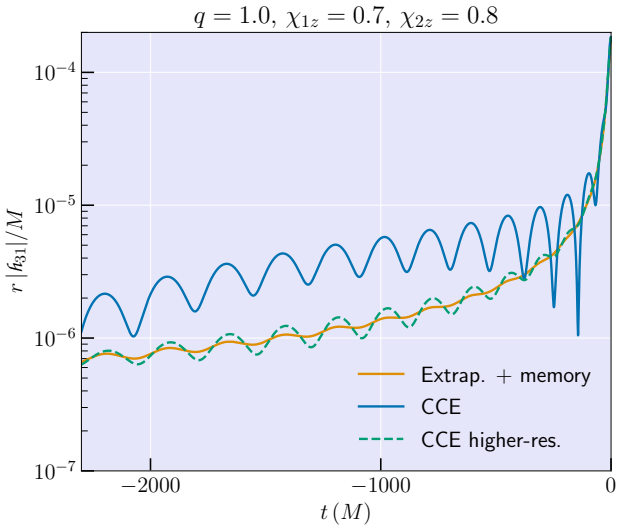

Figure 6.10: An example of the unphysical oscillations that are seen in the amplitude of the $(3, 1)$ mode for one of the CCE training waveforms (blue). As a reference, we also show the extrapolated waveform (orange) for the same simulation and the higher-resolution CCE waveform (green).

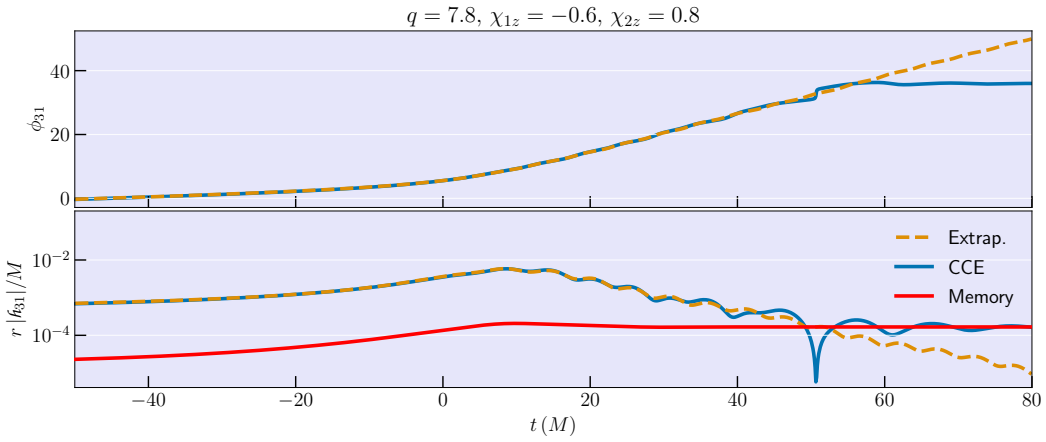

Figure 6.11: Phase and amplitude of the $(3, 1)$ mode for a CCE (blue) and an extrapolated (orange) waveform. We also include the memory contribution (red) to highlight the fact that the CCE waveform does not decay to zero as $t \to \infty$.

Therefore, we instead choose to not model the $(3, 1)$ and $(4, 2)$ modes in our new surrogate `NRHybSur3dq8_CCE`. We also omit the $(4, 1)$ mode because it is subdominant to the $(4, 2)$ mode and, as a result, does not significantly impact the overall waveform accuracy provided that the $(4, 2)$ is already excluded. For future surrogate models that are built using CCE waveforms, it is important that we have

higher resolution and longer NR simulations to avoid these issues until the problem of constructing initial data for CCE is resolved.

6.A.2 Impact of a simulation-dependent BMS frame

As stressed in Sec. 6.3.2, it is crucial to ensure that the training waveforms are in the same BMS frame to avoid undesired frame artifacts that tend to complicate the waveform modeling. Because the surrogate model that we are building is for hybrid waveforms, we work with waveforms that are in the PN BMS frame. However, while this ensures that the waveforms are in the same frame during the inspiral phase,[17] this is not necessarily true for the ringdown phase [129]. This is because, for example, the remnant black holes can have different kick velocities or supertranslation fields because of complicated effects that arise during the merger phase. Consequently, there are unresolved frame artifacts during the ringdown phase that can impact the modeling of the strain waveforms.

These additional challenges of modeling the strain in the ringdown using the current PN BMS framework are most pronounced for the $(3,1)$ and $(4,2)$ modes where the strain is oscillatory and does not decay to zero due to the impact of memory. Because these modes do not decay to zero as $t \to \infty$, we find that the decomposition of the strain into co-orbital frame data does not work well as the phase of these two modes is ill-defined. We highlight this phase issue in Fig. 6.11, which shows the amplitude and the phase of the $(3,1)$ mode for both a CCE waveform and an extrapolated waveform. One potential remedy to this problem is to instead work in a co-BMS frame, in which there is little-to-no time evolution of the BMS charges, i.e., a non-inertial frame similar to the co-rotating frame that simplifies the waveform data. However, such a project is non-trivial and we therefore postpone it for future work.

References

[1] J. Aasi et al. (LIGO Scientific), Class. Quant. Grav. **32**, 074001 (2015) 10.1088/0264-9381/32/7/074001.

[2] F. Acernese et al. (Virgo), Class. Quant. Grav. **32**, 024001 (2015) 10.1088/0264-9381/32/2/024001.

[3] T. Akutsu et al. (KAGRA), PTEP **2021**, 05A101 (2021) 10.1093/ptep/ptaa125.

[17] Formally, this only ensures that the waveforms are in the same BMS frame at $t \to -\infty$.

[4] M. Punturo et al., Class. Quant. Grav. **27**, 194002 (2010) 10.1088/0264-9381/27/19/194002.

[5] D. Reitze et al., Bull. Am. Astron. Soc. **51**, 035 (2019).

[6] P. Amaro-Seoane et al. (LISA), (2017).

[7] B. P. Abbott et al. (KAGRA, LIGO Scientific, VIRGO), Living Rev. Rel. **21**, 3 (2018) 10.1007/s41114-018-0012-9, 10.1007/lrr-2016-1.

[8] B. P. Abbott et al. (LIGO Scientific), Class. Quant. Grav. **34**, 044001 (2017) 10.1088/1361-6382/aa51f4.

[9] K. Mitman et al., Phys. Rev. D **103**, 024031 (2021) 10.1103/PhysRevD.103.024031.

[10] F. Pretorius, Phys. Rev. Lett. **95**, 121101 (2005) 10.1103/PhysRevLett.95.121101.

[11] M. Campanelli, C. O. Lousto, P. Marronetti, and Y. Zlochower, Phys. Rev. Lett. **96**, 111101 (2006) 10.1103/PhysRevLett.96.111101.

[12] J. G. Baker, J. Centrella, D.-I. Choi, M. Koppitz, and J. van Meter, Phys. Rev. Lett. **96**, 111102 (2006) 10.1103/PhysRevLett.96.111102.

[13] SXS Collaboration, *The SXS collaboration catalog of gravitational waveforms*, http://www.black-holes.org/waveforms.

[14] S. Ossokine et al., Phys. Rev. D **102**, 044055 (2020) 10.1103/PhysRevD.102.044055.

[15] S. Khan, F. Ohme, K. Chatziioannou, and M. Hannam, Phys. Rev. D **101**, 024056 (2020) 10.1103/PhysRevD.101.024056.

[16] G. Pratten et al., Phys. Rev. D **103**, 104056 (2021) 10.1103/PhysRevD.103.104056.

[17] H. Estellés, M. Colleoni, C. García-Quirós, S. Husa, D. Keitel, M. Mateu-Lucena, M. d. L. Planas, and A. Ramos-Buades, (2021).

[18] A. Nagar, G. Riemenschneider, G. Pratten, P. Rettegno, and F. Messina, Phys. Rev. D **102**, 024077 (2020) 10.1103/PhysRevD.102.024077.

[19] S. Akcay, R. Gamba, and S. Bernuzzi, Phys. Rev. D **103**, 024014 (2021) 10.1103/PhysRevD.103.024014.

[20] J. Blackman, S. E. Field, C. R. Galley, B. Szilágyi, M. A. Scheel, M. Tiglio, and D. A. Hemberger, Phys. Rev. Lett. **115**, 121102 (2015) 10.1103/PhysRevLett.115.121102.

[21] J. Blackman, S. E. Field, M. A. Scheel, C. R. Galley, D. A. Hemberger, P. Schmidt, and R. Smith, Phys. Rev. **D95**, 104023 (2017) 10.1103/PhysRevD.95.104023.

[22] J. Blackman, S. E. Field, M. A. Scheel, C. R. Galley, C. D. Ott, M. Boyle, L. E. Kidder, H. P. Pfeiffer, and B. Szilágyi, Phys. Rev. **D96**, 024058 (2017) 10.1103/PhysRevD.96.024058.

[23] V. Varma, S. E. Field, M. A. Scheel, J. Blackman, L. E. Kidder, and H. P. Pfeiffer, Phys. Rev. **D99**, 064045 (2019) 10.1103/PhysRevD.99.064045.

[24] V. Varma, S. E. Field, M. A. Scheel, J. Blackman, D. Gerosa, L. C. Stein, L. E. Kidder, and H. P. Pfeiffer, Phys. Rev. Research. **1**, 033015 (2019) 10.1103/PhysRevResearch.1.033015.

[25] T. Islam, V. Varma, J. Lodman, S. E. Field, G. Khanna, M. A. Scheel, H. P. Pfeiffer, D. Gerosa, and L. E. Kidder, Phys. Rev. D **103**, 064022 (2021) 10.1103/PhysRevD.103.064022.

[26] J. Yoo, V. Varma, M. Giesler, M. A. Scheel, C.-J. Haster, H. P. Pfeiffer, L. E. Kidder, and M. Boyle, Phys. Rev. D **106**, 044001 (2022) 10.1103/PhysRevD.106.044001.

[27] M. Pürrer, Class. Quant. Grav. **31**, 195010 (2014) 10.1088/0264-9381/31/19/195010.

[28] B. Gadre, M. Pürrer, S. E. Field, S. Ossokine, and V. Varma, (2022).

[29] R. Abbott et al. (LIGO Scientific, Virgo), Phys. Rev. D **103**, 122002 (2021) 10.1103/PhysRevD.103.122002.

[30] R. Abbott et al. (LIGO Scientific, VIRGO), (2021).

[31] R. Abbott et al. (LIGO Scientific, VIRGO, KAGRA), (2021).

[32] R. Abbott et al. (LIGO Scientific, Virgo), Phys. Rev. Lett. **125**, 101102 (2020) 10.1103/PhysRevLett.125.101102.

[33] V. Varma, M. Isi, S. Biscoveanu, W. M. Farr, and S. Vitale, Phys. Rev. D **105**, 024045 (2022) 10.1103/PhysRevD.105.024045.

[34] V. Varma, S. Biscoveanu, M. Isi, W. M. Farr, and S. Vitale, Phys. Rev. Lett. **128**, 031101 (2022) 10.1103/PhysRevLett.128.031101.

[35] V. Varma, S. Biscoveanu, T. Islam, F. H. Shaik, C.-J. Haster, M. Isi, W. M. Farr, S. E. Field, and S. Vitale, Phys. Rev. Lett. **128**, 191102 (2022) 10.1103/PhysRevLett.128.191102.

[36] V. Varma, M. Isi, and S. Biscoveanu, Phys. Rev. Lett. **124**, 101104 (2020) 10.1103/PhysRevLett.124.101104.

[37] M. Boyle and A. H. Mroue, Phys. Rev. **D80**, 124045 (2009) 10.1103/PhysRevD.80.124045.

[38] M. Boyle et al., Class. Quant. Grav. **36**, 195006 (2019) 10.1088/1361-6382/ab34e2.

[39] N. T. Bishop and L. Rezzolla, Living Rev. Rel. **19**, 2 (2016) 10.1007/s41114-016-0001-9.

[40] K. Jani, J. Healy, J. A. Clark, L. London, P. Laguna, and D. Shoemaker, Class. Quant. Grav. **33**, 204001 (2016) 10.1088/0264-9381/33/20/204001.

[41] J. Healy, C. O. Lousto, Y. Zlochower, and M. Campanelli, Class. Quant. Grav. **34**, 224001 (2017) 10.1088/1361-6382/aa91b1.

[42] Y. B. Zel'dovich and A. G. Polnarev, Sov. Astron. **18**, 17 (1974).

[43] V. B. Braginsky and K. S. Thorne, Nature **327**, 123 (1987) 10.1038/327123a0.

[44] K. S. Thorne, Phys. Rev. D **45**, 520 (1992) 10.1103/PhysRevD.45.520.

[45] D. Christodoulou, Phys. Rev. Lett. **67**, 1486 (1991) 10.1103/PhysRevLett.67.1486.

[46] G. Compère, Phys. Rev. Lett. **123**, 021101 (2019) 10.1103/PhysRevLett.123.021101.

[47] A. M. Grant and D. A. Nichols, Phys. Rev. D **105**, 024056 (2022) 10.1103/PhysRevD.105.024056.

[48] S. Pasterski, A. Strominger, and A. Zhiboedov, JHEP **12**, 053 (2016) 10.1007/JHEP12(2016)053.

[49] L. Bieri and D. Garfinkle, Phys. Rev. D **89**, 084039 (2014) 10.1103/PhysRevD.89.084039.

[50] M. Turner, The Astrophysical Journal **216**, 610 (1977) 10.1086/155501.

[51] T. Damour, F. Guercilena, I. Hinder, S. Hopper, A. Nagar, and L. Rezzolla, Phys. Rev. D **89**, 081503 (2014) 10.1103/PhysRevD.89.081503.

[52] G. Cho, A. Gopakumar, M. Haney, and H. M. Lee, Phys. Rev. D **98**, 024039 (2018) 10.1103/PhysRevD.98.024039.

[53] A. Nagar, P. Rettegno, R. Gamba, and S. Bernuzzi, Phys. Rev. D **103**, 064013 (2021) 10.1103/PhysRevD.103.064013.

[54] T. Damour and P. Rettegno, Phys. Rev. D **107**, 064051 (2023) 10.1103/PhysRevD.107.064051.

[55] P. Rettegno, G. Pratten, L. Thomas, P. Schmidt, and T. Damour, (2023).

[56] M. Hübner, C. Talbot, P. D. Lasky, and E. Thrane, Phys. Rev. D **101**, 023011 (2020) 10.1103/PhysRevD.101.023011.

[57] O. M. Boersma, D. A. Nichols, and P. Schmidt, Phys. Rev. D **101**, 083026 (2020) 10.1103/PhysRevD.101.083026.

[58] A. M. Grant and D. A. Nichols, Phys. Rev. D **107**, 064056 (2023) 10.1103/PhysRevD.107.064056.

[59] M. Ebersold and S. Tiwari, Phys. Rev. D **101**, 104041 (2020) 10.1103/PhysRevD.101.104041.

[60] S. Tiwari, M. Ebersold, and E. Z. Hamilton, Phys. Rev. D **104**, 123024 (2021) 10.1103/PhysRevD.104.123024.

[61] D. Lopez, S. Tiwari, and M. Ebersold, (2023).

[62] A. Strominger and A. Zhiboedov, JHEP **01**, 086 (2016) 10.1007/JHEP01(2016)086.

[63] T. He, V. Lysov, P. Mitra, and A. Strominger, JHEP **05**, 151 (2015) 10.1007/JHEP05(2015)151.

[64] S. Weinberg, Phys. Rev. **140**, B516 (1965) 10.1103/PhysRev.140.B516.

[65] S. Haco, S. W. Hawking, M. J. Perry, and A. Strominger, JHEP **12**, 098 (2018) 10.1007/JHEP12(2018)098.

[66] S. W. Hawking, M. J. Perry, and A. Strominger, Phys. Rev. Lett. **116**, 231301 (2016) 10.1103/PhysRevLett.116.231301.

[67] C. Talbot, E. Thrane, P. D. Lasky, and F. Lin, Phys. Rev. D **98**, 064031 (2018) 10.1103/PhysRevD.98.064031.

[68] N. T. Bishop, R. Gomez, L. Lehner, and J. Winicour, Phys. Rev. **D54**, 6153 (1996) 10.1103/PhysRevD.54.6153.

[69] J. Moxon, M. A. Scheel, and S. A. Teukolsky, Phys. Rev. D **102**, 044052 (2020) 10.1103/PhysRevD.102.044052.

[70] J. Moxon, M. A. Scheel, S. A. Teukolsky, N. Deppe, N. Fischer, F. Hébert, L. E. Kidder, and W. Throwe, (2021).

[71] K. Mitman, J. Moxon, M. A. Scheel, S. A. Teukolsky, M. Boyle, N. Deppe, L. E. Kidder, and W. Throwe, Phys. Rev. D **102**, 104007 (2020) 10.1103/PhysRevD.102.104007.

[72] N. Deppe, W. Throwe, L. E. Kidder, N. L. Vu, F. Hébert, J. Moxon, C. Armaza, G. S. Bonilla, Y. Kim, P. Kumar, G. Lovelace, A. Macedo, K. C. Nelli, E. O'Shea, H. P. Pfeiffer, M. A. Scheel, S. A. Teukolsky, N. A. Wittek, et al., *SpECTRE v2023.02.09*, 10.5281/zenodo.7626579, version 2023.02.09, Feb. 2023, 10.5281/zenodo.7626579.

[73] K. Mitman et al., Phys. Rev. D **106**, 084029 (2022) 10.1103/PhysRevD.106.084029.

[74] K. Mitman et al., Phys. Rev. D **104**, 024051 (2021) 10.1103/PhysRevD.104.024051.

[75] V. Varma and P. Ajith, Phys. Rev. **D96**, 124024 (2017) 10.1103/PhysRevD.96.124024.

[76] V. Varma, P. Ajith, S. Husa, J. C. Bustillo, M. Hannam, and M. Pürrer, Phys. Rev. **D90**, 124004 (2014) 10.1103/PhysRevD.90.124004.

[77] C. Capano, Y. Pan, and A. Buonanno, Phys. Rev. **D89**, 102003 (2014) 10.1103/PhysRevD.89.102003.

[78] F. H. Shaik, J. Lange, S. E. Field, R. O'Shaughnessy, V. Varma, L. E. Kidder, H. P. Pfeiffer, and D. Wysocki, Phys. Rev. D **101**, 124054 (2020) 10.1103/PhysRevD.101.124054.

[79] T. Islam, S. E. Field, C.-J. Haster, and R. Smith, Phys. Rev. D **104**, 084068 (2021) 10.1103/PhysRevD.104.084068.

[80] J. Blackman, S. Field, C. Galley, and V. Varma, *Gwsurrogate*, https://pypi.python.org/pypi/gwsurrogate/.

[81] H. Bondi, M. G. J. van der Burg, and A. W. K. Metzner, Proc. Roy. Soc. Lond. **A269**, 21 (1962) 10.1098/rspa.1962.0161.

[82] R. K. Sachs, Proc. Roy. Soc. Lond. A **270**, 103 (1962) 10.1098/rspa.1962.0206.

[83] M. Boyle, D. Iozzo, and L. C. Stein, *Moble/scri: v1.2*, https://github.com/moble/scri, version v1.2, Sept. 2020, 10.5281/zenodo.4041972.

[84] M. Boyle, Phys. Rev. **D87**, 104006 (2013) 10.1103/PhysRevD.87.104006.

[85] M. Boyle, L. E. Kidder, S. Ossokine, and H. P. Pfeiffer, (2014).

[86] M. Boyle, Phys. Rev. **D93**, 084031 (2016) 10.1103/PhysRevD.93.084031.

[87] M. Boyle, D. Hemberger, and D. Iozzo, *Moble/gwframes*, https://github.com/moble/GWFrames, version 1.0, Aug. 2020, 10.5281/zenodo.3974963.

[88] L. Blanchet, T. Damour, G. Esposito-Farese, and B. R. Iyer, Phys. Rev. Lett. **93**, 091101 (2004) 10.1103/PhysRevLett.93.091101.

[89] L. Blanchet, Living Rev. Rel. **17**, 2 (2014) 10.12942/lrr-2014-2.

[90] P. Jaranowski and G. Schäfer, Phys. Rev. D **87**, 081503 (2013) 10.1103/PhysRevD.87.081503.

[91] D. Bini and T. Damour, Phys. Rev. D **87**, 121501 (2013) 10.1103/PhysRevD.87.121501.

[92] D. Bini and T. Damour, Phys. Rev. D **89**, 064063 (2014) 10.1103/PhysRevD.89.064063.

[93] L. E. Kidder, Phys. Rev. D **52**, 821 (1995) 10.1103/PhysRevD.52.821.

[94] C. M. Will and A. G. Wiseman, Phys. Rev. D **54**, 4813 (1996) 10.1103/PhysRevD.54.4813.

[95] A. Bohe, S. Marsat, G. Faye, and L. Blanchet, Class. Quant. Grav. **30**, 075017 (2013) 10.1088/0264-9381/30/7/075017.

[96] L. Blanchet, G. Faye, B. R. Iyer, and S. Sinha, Class. Quant. Grav. **25**, [Erratum: Class.Quant.Grav. 29, 239501 (2012)], 165003 (2008) 10.1088/0264-9381/25/16/165003.

[97] G. Faye, S. Marsat, L. Blanchet, and B. R. Iyer, Class. Quant. Grav. **29**, 175004 (2012) 10.1088/0264-9381/29/17/175004.

[98] G. Faye, L. Blanchet, and B. R. Iyer, Class. Quant. Grav. **32**, 045016 (2015) 10.1088/0264-9381/32/4/045016.

[99] M. Favata, Phys. Rev. D **80**, 024002 (2009) 10.1103/PhysRevD.80.024002.

[100] M. Boyle, D. A. Brown, L. E. Kidder, A. H. Mroue, H. P. Pfeiffer, M. A. Scheel, G. B. Cook, and S. A. Teukolsky, Phys. Rev. **D76**, 124038 (2007) 10.1103/PhysRevD.76.124038.

[101] A. Bohé et al., Phys. Rev. **D95**, 044028 (2017) 10.1103/PhysRevD.95.044028.

[102] C. Devine, Z. B. Etienne, and S. T. McWilliams, Class. Quant. Grav. **33**, 125025 (2016) 10.1088/0264-9381/33/12/125025.

[103] T. Damour, B. R. Iyer, and B. S. Sathyaprakash, Phys. Rev. D **63**, [Erratum: Phys.Rev.D 72, 029902 (2005)], 044023 (2001) 10.1103/PhysRevD.63.044023.

[104] S. E. Field, C. R. Galley, F. Herrmann, J. S. Hesthaven, E. Ochsner, and M. Tiglio, Phys. Rev. Lett. **106**, 221102 (2011) 10.1103/PhysRevLett.106.221102.

[105] S. E. Field, C. R. Galley, J. S. Hesthaven, J. Kaye, and M. Tiglio, Phys. Rev. X **4**, 031006, 031006 (2014) 10.1103/PhysRevX.4.031006.

[106] P. Binev, A. Cohen, W. Dahmen, R. DeVore, G. Petrova, and P. Wojtaszczyk, SIAM journal on mathematical analysis **43**, 1457 (2011).

[107] R. DeVore, G. Petrova, and P. Wojtaszczyk, Constructive Approximation **37**, 455 (2013).

[108] S. Chaturantabut and D. C. Sorensen, SIAM Journal on Scientific Computing **32**, 2737 (2010).

[109] Y. Maday, N. C. Nguyen, A. T. Patera, and S. H. Pau, Communications on Pure and Applied Analysis **8**, 383 (2009) 10.3934/cpaa.2009.8.383.

[110] Hesthaven, Jan S., Stamm, Benjamin, and Zhang, Shun, ESAIM: M2AN **48**, 259 (2014) 10.1051/m2an/2013100.

[111] H. Antil, S. E. Field, F. Herrmann, R. H. Nochetto, and M. Tiglio, Journal of Scientific Computing **57**, 604 (2013).

[112] V. Varma, D. Gerosa, L. C. Stein, F. Hébert, and H. Zhang, Phys. Rev. Lett. **122**, 011101 (2019) 10.1103/PhysRevLett.122.011101.

[113] F. Pedregosa, G. Varoquaux, A. Gramfort, V. Michel, B. Thirion, O. Grisel, M. Blondel, P. Prettenhofer, R. Weiss, V. Dubourg, J. VanderPlas, A. Passos, D. Cournapeau, M. Brucher, M. Perrot, and E. Duchesnay, CoRR **abs/1201.0490** (2012).

[114] S. Khan, S. Husa, M. Hannam, F. Ohme, M. Pürrer, X. Jiménez Forteza, and A. Bohé, Phys. Rev. **D93**, 044007 (2016) 10.1103/PhysRevD.93.044007.

[115] P. Ajith, **84**, 084037 (2011) 10.1103/PhysRevD.84.084037.

[116] C. Cutler and E. E. Flanagan, Phys. Rev. D **49**, 2658 (1994) 10.1103/PhysRevD.49.2658.

[117] E. Poisson and C. M. Will, Phys. Rev. **D52**, 848 (1995) 10.1103/PhysRevD.52.848.

[118] D. J. A. McKechan, C. Robinson, and B. S. Sathyaprakash, Class. Quant. Grav. **27**, 084020 (2010) 10.1088/0264-9381/27/8/084020.

[119] Y. Chen, M. Boyle, and S. A. Teukolsky, "Improved frequency spectra of gravitational waves with memory in a binary-black-hole simulation", to be published.

[120] LIGO Scientific Collaboration, *Updated advanced ligo sensitivity design curve*, tech. rep., https://dcc.ligo.org/LIGO-T1800044/public (2018).

[121] T. Chu, H. Fong, P. Kumar, H. P. Pfeiffer, M. Boyle, D. A. Hemberger, L. E. Kidder, M. A. Scheel, and B. Szilagyi, Class. Quant. Grav. **33**, 165001 (2016) 10.1088/0264-9381/33/16/165001.

[122] T. Islam, S. E. Field, G. Khanna, and N. Warburton, arXiv preprint arXiv:2109.00754 (2021).

[123] S. Gasparotto, R. Vicente, D. Blas, A. C. Jenkins, and E. Barausse, (2023).

[124] L. Kale, B. Acun, S. Bak, A. Becker, M. Bhandarkar, N. Bhat, A. Bhatele, E. Bohm, C. Bordage, R. Brunner, R. Buch, S. Chakravorty, K. Chandrasekar, J. Choi, M. Denardo, J. DeSouza, M. Diener, H. Dokania, I. Dooley, W. Fenton, J. Galvez, F. Gioachin, A. Gupta, G. Gupta, M. Gupta, A. Gursoy, V. Harsh, F. Hu, C. Huang, N. Jagathesan, N. Jain, P. Jetley, P. Jindal, R. Kanakagiri, G. Koenig, S. Krishnan, S. Kumar, D. Kunzman, M. Lang, A. Langer, O. Lawlor, C. W. Lee, J. Lifflander, K. Mahesh, C. Mendes, H. Menon, C. Mei, E. Meneses, E. Mikida, P. Miller, R. Mokos, V. Narayanan, X. Ni, K. Nomura, S. Paranjpye, P. Ramachandran, B. Ramkumar, E. Ramos, M. Robson, N. Saboo, V. Saletore, O. Sarood, K. Senthil, N. Shah, W. Shu, A. B. Sinha, Y. Sun, Z. Sura, E. Totoni, K. Varadarajan, R. Venkataraman, J. Wang, L. Wesolowski, S. White, T. Wilmarth, J. Wright, J. Yelon, and

G. Zheng, *Uiuc-ppl/charm: charm++ version 6.10.2*, version v6.10.2, Aug. 2020, 10.5281/zenodo.3972617.

[125] P. Virtanen, R. Gommers, T. E. Oliphant, M. Haberland, T. Reddy, D. Cournapeau, E. Burovski, P. Peterson, W. Weckesser, J. Bright, S. J. van der Walt, M. Brett, J. Wilson, K. J. Millman, N. Mayorov, A. R. J. Nelson, E. Jones, R. Kern, E. Larson, C. J. Carey, İ. Polat, Y. Feng, E. W. Moore, J. VanderPlas, D. Laxalde, J. Perktold, R. Cimrman, I. Henriksen, E. A. Quintero, C. R. Harris, A. M. Archibald, A. H. Ribeiro, F. Pedregosa, P. van Mulbregt, and SciPy 1.0 Contributors, Nature Methods **17**, 261 (2020) 10.1038/s41592-019-0686-2.

[126] C. R. Harris, K. J. Millman, S. J. van der Walt, R. Gommers, P. Virtanen, D. Cournapeau, E. Wieser, J. Taylor, S. Berg, N. J. Smith, R. Kern, M. Picus, S. Hoyer, M. H. van Kerkwijk, M. Brett, A. Haldane, J. F. del Río, M. Wiebe, P. Peterson, P. Gérard-Marchant, K. Sheppard, T. Reddy, W. Weckesser, H. Abbasi, C. Gohlke, and T. E. Oliphant, Nature **585**, 357 (2020) 10.1038/s41586-020-2649-2.

[127] J. D. Hunter, Computing in Science & Engineering **9**, 90 (2007) 10.1109/MCSE.2007.55.

[128] M. L. Waskom, Journal of Open Source Software **6**, 3021 (2021) 10.21105/joss.03021.

[129] L. Magaña Zertuche et al., Phys. Rev. D **105**, 104015 (2022) 10.1103/PhysRevD.105.104015.

Chapter 7

NONLINEARITIES IN BLACK HOLE RINGDOWNS

K. Mitman et al., Phys. Rev. Lett. **130**, 081402 (2023) 10.1103/PhysRevLett.130.081402,

7.1 Abstract

The gravitational wave strain emitted by a perturbed black hole (BH) ringing down is typically modeled analytically using first-order BH perturbation theory. In this Letter we show that second-order effects are necessary for modeling ringdowns from BH merger simulations. Focusing on the strain's $(\ell, m) = (4, 4)$ angular harmonic, we show the presence of a quadratic effect across a range of binary BH mass ratios that agrees with theoretical expectations. We find that the quadratic $(4, 4)$ mode's amplitude exhibits quadratic scaling with the fundamental $(2, 2)$ mode—its parent mode. The nonlinear mode's amplitude is comparable to or even larger than that of the linear $(4, 4)$ mode. Therefore, correctly modeling the ringdown of higher harmonics—improving mode mismatches by up to 2 orders of magnitude—requires the inclusion of nonlinear effects.

7.2 Introduction

Nonlinearity is responsible for the rich phenomenology of general relativity (GR). While many exact nonlinear solutions are known [1, 2], LIGO-Virgo-KAGRA observables—gravitational waves (GWs) from merging binary black holes (BHs)—must be predicted by numerical relativity (NR). Analytic perturbation theory has an important role far from the merger: at early times, post-Newtonian (PN) theory, and at late times (ringdown), black hole perturbation theory [3–5], provided that the remnant asymptotes to a perturbed Kerr BH [6, 7]. PN theory has been pushed to high perturbative order [8], but the standard paradigm for modeling ringdown is only linear theory (see [9] for a review). It may then come as a surprise if linear theory can be used to model ringdown even at the peak of the strain [10–15], the most nonlinear phase of a BH merger.

The "magic" nature of the Kerr geometry [16] leads to a decoupled, separable wave equation for first-order perturbations (the Teukolsky equation [5]), schematically

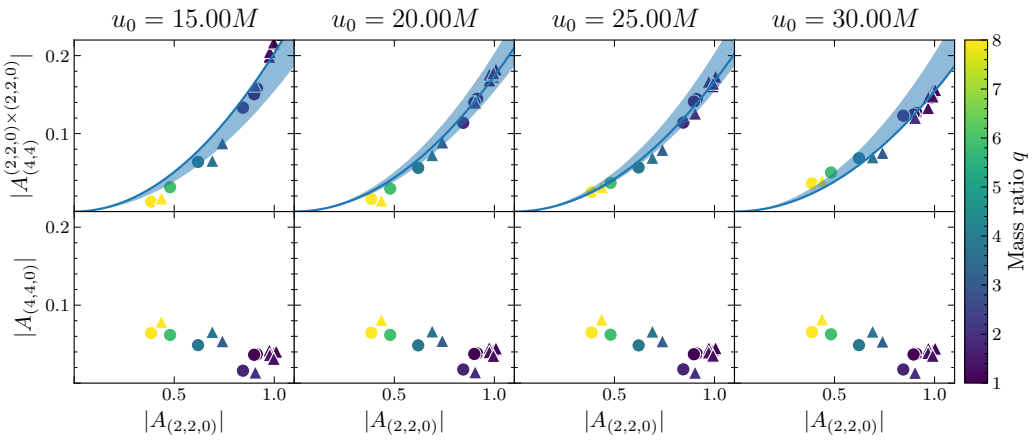

Figure 7.1: Relationship between the peak amplitudes of the linear $(2,2,0)$ and the quadratic $(2,2,0)\times(2,2,0)$ QNMs (top) as well as the linear $(4,4,0)$ QNM (bottom), at different model start times u_0. Colors show different mass ratios q, and circles and triangles denote systems with remnant dimensionless spin $\chi_f \approx 0.5$ and $\chi_f \approx 0.7$, respectively. Each blue curve is a pure quadratic fit with start time u_0, and the shaded region brackets every one of the individual fits.

written as

$$\mathcal{T}\psi = \mathcal{S}, \tag{7.1}$$

where $\mathcal{S}$ is a source term that vanishes for linear perturbations in vacuum, ψ is related to the first-order correction to the curvature scalar ψ_4, and the linear differential Teukolsky operator $\mathcal{T}$ depends on the dimensionless spin parameter $\chi \equiv |S|/M^2$ through the combination $a = |S|/M$, where S is the BH spin angular momentum and M is the BH mass (throughout we use geometric units $G = c = 1$). The causal Green's function $\mathcal{G} \sim \mathcal{T}^{-1}$ has an infinite, but discrete set of complex frequency poles $\omega_{(\ell,m,n)}$.[1] This makes GWs during ringdown well described by a superposition of exponentially damped sinusoids, called quasinormal modes (QNMs). The real and imaginary parts of $\omega_{(\ell,m,n)}$ determine the QNM oscillation frequency and decay timescale, respectively. These modes are labeled by two angular harmonic numbers (ℓ, m) and an overtone number n. The combination $M\omega_{(\ell,m,n)}$ is entirely determined by χ.

[1] For this study we focus only on prograde modes (in the sense described in [17]), and therefore omit the additional prograde/retrograde label $\pm$. The Green's function also has branch cuts, which lead to power-law tails [18], which we ignore here.

To date, the linear QNM spectrum has been used to analyze current GW detections [15, 19–21], forecast the future detectability of ringdown [22–24], and perform tests of gravity in the strong field regime [25, 26].

Since the sensitivity of GW detectors will increase in the coming years [27–30], there is the potential to observe nonlinear ringdown effects in high signal-to-noise ratio (SNR) events. A few previous works have shown that second-order perturbation effects can be identified in some NR simulations of binary BH mergers [31, 32]. In this Letter we show that quadratic QNMs—the damped sinusoids coming from second-order perturbation theory in GR—are a ubiquitous effect present in simulations across various binary mass ratios and remnant BH spins. In particular, for the angular harmonic $(\ell, m) = (4, 4)$, we find that the quadratic QNM amplitude exhibits the expected quadratic scaling relative to its parent—the fundamental $(2, 2)$ mode. The quadratic amplitude also has a value that is comparable to that of the linear $(4, 4)$ QNMs for every simulation considered, thus highlighting the need to include nonlinear effects in ringdown models of higher harmonics.

7.3 Quadratic QNMs

Second-order perturbation theory has been studied for both Schwarzschild and Kerr BHs [33–43]. This involves the same Teukolsky operator as in Eq. (7.1) acting on the second-order curvature correction, and a complicated source $\mathcal{S}$ that depends quadratically on the linear perturbations [41, 42, 44]. The second-order solution results from a rather involved integral of this source against the Green's function $\mathcal{G}$ [38, 43]. We only need to know that it is quadratic in the linear perturbation and that, after enough time, it is well approximated by the quadratic QNMs.

The frequency spectrum of quadratic QNMs is distinct from the linear QNM spectrum. For each pair of linear QNM frequencies $\omega_{(\ell_1,m_1,n_1)}$ and $\omega_{(\ell_2,m_2,n_2)}$ (in either the left or right half complex plane), there will be a corresponding quadratic QNM frequency

$$\omega \equiv \omega_{(\ell_1,m_1,n_1)} + \omega_{(\ell_2,m_2,n_2)}. \tag{7.2}$$

As the linear $(2, \pm 2, 0)$ modes are most important, it is promising to investigate the quadratic QNMs they generate, which primarily appear in the $(\ell, m) = (4, \pm 4)$ modes [36, 37, 43]. The quadratic QNM coming from the $(2, 2)$ mode would have frequency $\omega_{(2,2,0)\times(2,2,0)} \equiv 2\omega_{(2,2,0)}$ and would decay faster than the linear fundamental mode $(4, 4, 0)$, but slower than the first linear overtone $(4, 4, 1)$, regardless

of the BH spin.[2]

The NR strain at future null infinity contains all of the angular information of the GW and is decomposed as

$$h^{\rm NR}(u,\theta,\phi) \equiv \sum_{\ell=2}^{\infty}\sum_{|m|\leq\ell} h^{\rm NR}_{(\ell,m)}(u)\,{}_{-2}Y_{(\ell,m)}(\theta,\phi), \tag{7.3}$$

where u is the Bondi time and ${}_{-2}Y_{(\ell,m)}$ are the spin-weighted $s=-2$ spherical harmonics. We model this data with two different QNM Ansätze, valid between times $u\in[u_0,u_f]$. The first model, which is typically used in the literature, involves purely linear QNMs,

$$h^{{\rm model},\,L}_{(\ell,m,N)}(u) = \sum_{n=0}^{N} A_{(\ell,m,n)}\, e^{-i\omega_{(\ell,m,n)}(u-u_{\rm peak})}. \tag{7.4}$$

Here $A_{(\ell,m,n)}$ is the peak amplitude of the linear QNM with frequency $\omega_{(\ell,m,n)}$, N is the total number of overtones considered in the model, and $u_{\rm peak}$ is the time at which the L^2 norm of the strain over the two-sphere achieves its maximum value (a proxy for the merger time), which we take to be $u_{\rm peak}=0$ without loss of generality. Note that here we have suppressed the spheroidal-spherical decomposition (which we include as in Eq. (6) of [17]).

We will use Eq. (7.4) to model both the $(2,2)$ and $(4,4)$ modes of the strain.[3] When modeling the $(2,2)$ mode, we use $N=1$ and when modeling the $(4,4)$ mode we use $N=2$. While prior works have included more overtones in their models [10–14, 17], we restrict ourselves to no more than two overtones because we find that the amplitudes of higher overtones tend to vary with the model start time u_0 and hence are not very robust. Moreover, their inclusion does not affect considerably the best-fit amplitude of the modes in which we are interested.

The novel QNM model, which includes second-order effects and highlights our main result, only changes how the $(4,4)$ mode is described, compared to Eq. (7.4). It is

[2] The $(\ell,m,n)=(2,2,0)$ can excite other quadratic QNMs with frequency $\omega=\omega_{(2,2,0)}-\overline{\omega_{(2,2,0)}}$. These will instead be related to the memory effect, as they are non-oscillatory. From angular selection rules they will be most prominent in the $(2,0)$ mode. While these effects could also prove interesting to study, they are much more well understood than the quadratic QNMs in the $(4,4)$ mode, so we reserve their examination for future work [17, 45].

[3] We ignore the $m<0$ modes because the binary BH simulations that we consider are non-precessing and are in quasicircular orbits, so the $m<0$ modes can be recovered from the $m>0$ modes via $h_{(\ell,m)}=(-1)^{\ell}\overline{h_{(\ell,-m)}}$

given by

$$h^{\text{model},\,Q}_{(4,4)}(u) = \sum_{n=0}^{1} A_{(4,4,n)} e^{-i\omega_{(4,4,n)}(u-u_{\text{peak}})} + A^{(2,2,0)\times(2,2,0)}_{(4,4)} e^{-i\omega_{(2,2,0)\times(2,2,0)}(u-u_{\text{peak}})}, \tag{7.5}$$

where $A^{(2,2,0)\times(2,2,0)}_{(4,4)}$ is the peak amplitude of the quadratic QNM sourced by the linear $(2,2,0)$ QNM interacting with itself. In each model, for the linear amplitudes we factor out the angular mixing coefficients, whereas for the quadratic term we absorb the angular structure (from the nonlinear mixing coefficients and the Green's function integral of the second-order source terms) into the amplitude $A^{(2,2,0)\times(2,2,0)}_{(4,4)}$. We emphasize that the two models $h^{\text{model},\,L}_{(4,4,2)}(u)$ and $h^{\text{model},\,Q}_{(4,4)}(u)$ contain the same number of free parameters.

In these ringdown models, we fix the QNM frequencies to the values predicted by GR in vacuum and fit the QNM amplitudes to NR simulations, which cannot be predicted from first principles as they depend on the merger details. From the quadratic sourcing by the linear $(2,2,0)$ mode, we expect $A^{(2,2,0)\times(2,2,0)}_{(4,4)} \propto (A_{(2,2,0)})^2$. We will use this theoretical expectation as one main test to confirm the presence of quadratic QNMs. To perform this check we need a family of systems with different linear amplitudes, which is easily accomplished by varying the binary mass ratio $q \equiv m_1/m_2 \geq 1$.

The proportionality coefficient between $(A_{(2,2,0)})^2$ and $A^{(2,2,0)\times(2,2,0)}_{(4,4)}$ (which we expect to be order unity [31, 43]) comes from the spacetime dependence of the full quadratic source as well as the Green's function. While, in principle, this can be computed, we use the fact that it should only depend on the dimensionless spin χ_f of the remnant BH.

We consider a family of 17 simulations (listed in Table 7.1) of binary BH systems in the range $q \in [1, 8]$. To control the dependence on χ_f, six are in the range $\chi_f = 0.5 \pm 0.035$, and ten have $\chi_f = 0.7 \pm 0.035$. The final simulation, SXS:BBH:0305, is consistent with GW150914 [47]. These simulations were produced using the Spectral Einstein Code (SpEC) and are available in the SXS catalog [46, 48, 49]. For each simulation, the strain waveform has been extracted using Cauchy characteristic extraction and has then been mapped to the superrest frame at $250M$ after u_{peak} [50–54] using the techniques presented in [54] and the code `scri` [55–58].

Table 7.1: List of simulations used (ID is shorthand for SXS:BBH:ID from the SXS catalog [46] where the full list of binary parameters can be found) with their mass ratios q and dimensionless remnant spins χ_f. All of these binaries are nonprecessing and are in quasicircular orbits.

ID	1502	1476	1506	1508	1474	1505	1504	1485	1486	1441
q	1.00	1.00	1.00	1.28	1.28	1.33	1.98	3.09	3.72	8.00
χ_f	0.73	0.68	0.71	0.73	0.73	0.71	0.71	0.68	0.70	0.72

ID	1500	1492	1465	1458	1438	1430
q	1.00	1.00	1.71	3.80	5.87	8.00
χ_f	0.53	0.48	0.48	0.47	0.47	0.50

ID	0305
q	1.22
χ_f	0.69

7.4 Quadratic fitting

In order to fit the ringdown models to the NR waveforms, using the least-squares implementation from SciPy v1.6.2 [59], we minimize the L^2 norm of the residual

$$\langle R, R\rangle \quad \text{for} \quad R \equiv h^{\rm NR}_{(\ell,m)} - h^{\rm model}_{(\ell,m)}, \tag{7.6}$$

where the inner product between modes a and b is

$$\langle a, b\rangle \equiv \int_{u_0}^{u_f} du\, \overline{a(u)} b(u), \tag{7.7}$$

with $\overline{a(u)}$ being the complex conjugate of $a(u)$. We will fix $u_f = 100M$ and vary the value of u_0. In Eq. (7.6), $h^{\rm model}$ is given by Eq. (7.4) with $N = 1$ for the $(2, 2)$ mode and Eq. (7.5) for the $(4, 4)$ mode by default, unless explicitly mentioned that we use the purely linear model, Eq. (7.4), with $N = 2$. We fix the frequencies and perform a spheroidal-to-spherical angular decomposition of the linear terms in our QNM models using the open-source `Python` package `qnm` [60].

We show the main result of the fits in Fig. 7.1 for a range of initial times u_0 with which we find the best-fit amplitudes to be stable (shown later). In the top panel, we see that $A_{(2,2,0)}$ and $A^{(2,2,0)\times(2,2,0)}_{(4,4)}$ are consistent with a quadratic relationship, illustrated by the shaded blue region that is obtained by combining the fitted quadratic curves for $u_0 \in [15M, 30M]$. In this region, we find the ratio $A^{(2,2,0)\times(2,2,0)}_{(4,4)}/(A_{(2,2,0)})^2$ to range between 0.20 and 0.15.[4] Again we emphasize that here $A_{(2,2,0)}$ has the mixing coefficients factored out, while $A^{(2,2,0)\times(2,2,0)}_{(4,4)}$ contains whatever angular structure arises through nonlinear effects. There is no noticeable difference in the quadratic

[4] In addition to the amplitudes, we can also check the consistency of the phases of the quadratic $(4, 4)$ QNM and the linear $(2, 2, 0)$ QNM. We find that the phase of $A^{(2,2,0)\times(2,2,0)}_{(4,4)}/A^2_{(2,2,0)}$ is always within 0.4 radians of 0, for each simulation, for start times in the range $u_0 \in [15M, 30M]$.

relationship followed by the 0.7 and 0.5 spin families of waveforms, compared to the variations that are observed in the best-fit $A^{(2,2,0)\times(2,2,0)}_{(4,4)}$ due to the choice of the model start time u_0.

We emphasize that this quadratic behavior is unique to the $A^{(2,2,0)\times(2,2,0)}_{(4,4)}$ mode, as can be seen in the bottom panel of Fig. 7.1, where we show the best-fit linear amplitude $A_{(4,4,0)}$ as a function of $A_{(2,2,0)}$. These two modes are not related quadratically (for more on their scaling with mass ratio, see [61]), which confirms the distinct physical origin of $A_{(4,4,0)}$ and $A^{(2,2,0)\times(2,2,0)}_{(4,4)}$. The best-fit amplitudes of $A_{(4,4,0)}$ and $A_{(2,2,0)}$ are nearly constant across these values of u_0, which is why the four bottom figures look the same. A key result of Fig. 7.1 is that $A^{(2,2,0)\times(2,2,0)}_{(4,4)}$ is comparable to or larger (by a factor of ~ 4 in cases with $q \approx 1$) than $A_{(4,4,0)}$ at the time of the peak. Given that the exponential decay rates of $A^{(2,2,0)\times(2,2,0)}_{(4,4)}$ and $A_{(4,4,0)}$ for a BH with $\chi_f = 0.7$ are $\mathrm{Im}[M\omega_{(2,2,0)\times(2,2,0)}] = -0.16$ and $\mathrm{Im}[M\omega_{(4,4,0)}] = -0.08$, respectively, even beyond $10M$ after $u_{\rm peak}$ the quadratic mode will be larger than the linear mode for equal mass ratio binaries.[5] Thus, for large SNR events in which the $(4,4)$ mode is detectable, the quadratic QNM could be measurable.

7.5 Comparisons

Figure 7.2 shows the GW150914 simulation (SXS:BBH:0305) and its fitting at $u_0 = 20M$, the time at which the residual in the $(4,4)$ mode reaches its minimum. The top panel shows the waveform fit with the $(4,4)$ quadratic model $h^{\mathrm{model},Q}_{(4,4)}$ as a function of time, where we find that it can fit rather well the amplitude and phase evolution of the numerical waveform at late times. The bottom panel shows the residual of the NR waveform with the linear and quadratic $(4,4)$ QNM models, $h^{\mathrm{model},L}_{(4,4,2)}$ and $h^{\mathrm{model},Q}_{(4,4)}$, and a conservative estimate for the numerical error obtained by comparing the highest and second highest resolution simulations for SXS:BBH:0305. We see that even though the linear and quadratic $(4,4)$ models have the same number of free parameters, the residual of $h^{\mathrm{model},Q}_{(4,4)}$ is nearly an order of magnitude better, which confirms the importance of including quadratic QNMs. Since, in general, the quadratic mode decays in time slower than the $(4,4,2)$ QNM, the quadratic model generally better describes the late time behavior of the waveform. In addition, the best-fit value of $A_{(4,4,0)}$—which is the most important QNM in the $(4,4)$ mode at late times—differs in the linear and quadratic models, which causes the residuals

[5] We also find the peak amplitude $A_{(4,4,1)}$ to be comparable or sometimes larger than $A^{(2,2,0)\times(2,2,0)}_{(4,4)}$ (see bottom panel of Fig. 7.3) but, since $\mathrm{Im}[M\omega_{(4,4,1)}] = -0.25$, this $(4,4,1)$ mode decays fast enough that it will be comparable or smaller than the quadratic $(4,4)$ mode after $u = 10M$.

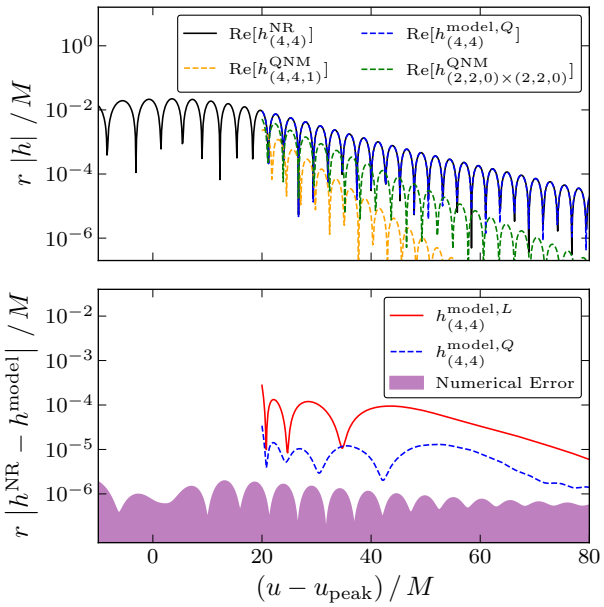

Figure 7.2: Top: in black, the NR waveform for the SXS:BBH:0305 simulation and its comparison to the quadratic $(4,4)$ QNM model with start time $u_0 = 20M$ (total is dashed blue; yellow and green are contributions from individual QNMs, respectively the linear $(4,4,1)$ and the quadratic $(2,2,0)\times(2,2,0)$). Bottom: residual in the $(4,4)$ mode when using the linear (solid red) or the quadratic (dashed blue) $(4,4)$ model. We also show a conservative estimate of the numerical error.

to be rather different even beyond $u = 50M$ when we expect the overtones and quadratic mode to be subdominant.

In addition to the residuals, we quantify the goodness of fit by our models through the mismatch

$$\mathcal{M} = 1 - \mathrm{Re}\left[\frac{\langle h^{\mathrm{NR}}_{(\ell,m)}|h^{\mathrm{model}}_{(\ell,m)}\rangle}{\sqrt{\langle h^{\mathrm{NR}}_{(\ell,m)}|h^{\mathrm{NR}}_{(\ell,m)}\rangle\langle h^{\mathrm{model}}_{(\ell,m)}|h^{\mathrm{model}}_{(\ell,m)}\rangle}}\right]. \tag{7.8}$$

The top panel of Fig. 7.3 shows the mismatch in the $(4,4)$ mode between the NR waveform and the QNM model as a function of u_0. The red and blue lines show the results for the SXS:BBH:0305 simulation when the $(4,4)$ mode was modeled with $h^{\mathrm{model},L}_{(4,4,2)}$ and $h^{\mathrm{model},Q}_{(4,4)}$, respectively. As a reference, we also show the numerical error calculated for SXS:BBH:0305.[6] We see that the numerical error is below the fitted model mismatches for $u_0 \lesssim 40M$, but will cause the mismatch to worsen at

[6]The numerical error for the other simulations tends to be worse since they were not run with as fine of a resolution, but the errors are nonetheless comparable to that of SXS:BBH:0305.

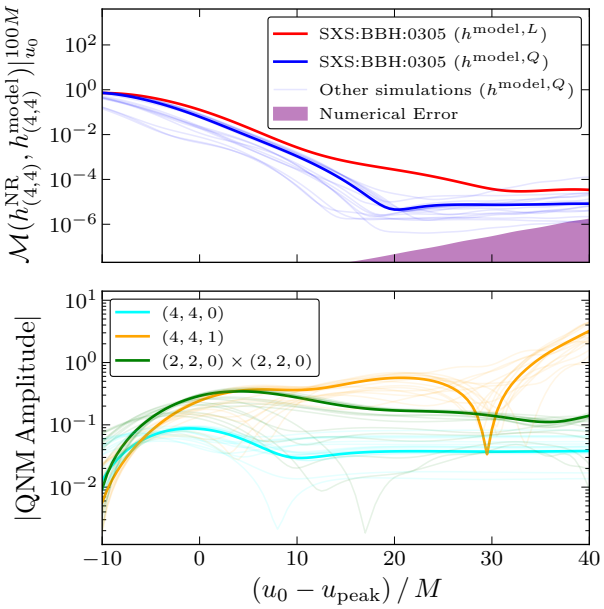

Figure 7.3: Top: mismatch in the $(4,4)$ mode for SXS:BBH:0305, as well as for every other simulation examined, and a comparison to the numerical error floor. Bottom: amplitudes of the three QNM terms in the quadratic $(4,4)$ QNM model as a function of the model start time u_0.

later times. We also see that the linear model performs worse than the quadratic model for any u_0, confirming that the residual difference shown in the bottom panel of Fig. 7.2 was not a coincidence of the particular fitting time chosen there. At times $u_0 \approx 20M$, we see that the mismatch is about 2 orders of magnitude better in the quadratic model. We find similar results for all of the simulations analyzed in this Letter[7] (light blue thin curves show the mismatch of the $h^{\mathrm{model},Q}_{(4,4)}$ in those simulations), although the mismatch difference becomes more modest for simulations with $q \approx 8$ since the relative amplitude of the quadratic mode decreases (cf. bottom panel of Fig. 7.1 where we see that amplitude of the $(2,2,0)$ mode decreases with q, while the amplitude of the $(4,4,0)$ mode increases with q). When comparing the mismatches to the error, we find that every simulation remains above the numerical error floor until $u_0 \gtrsim 40M$.[8]

In the bottom panel of Fig. 7.3, we show the best-fit amplitudes of the QNMs in

[7]Except for a few simulations at early times $0 \lesssim u_0 \lesssim 10M$, for which the linear model can have a marginally better mismatch.

[8]We emphasize that the reason the numerical error curve increases with u_0 is because of the normalization factor in Eq. (7.8); i.e., with higher u_0 the integral of the numerical error becomes more comparable to the strain's amplitude.

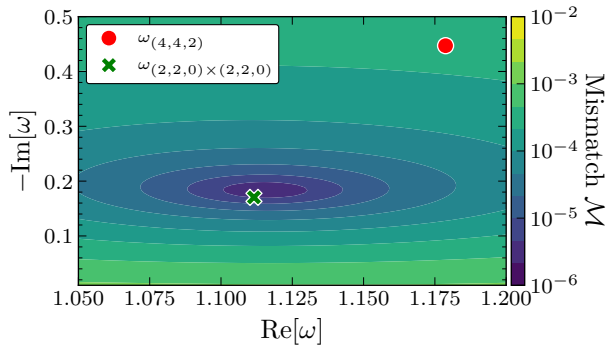

Figure 7.4: Contour plot of the mismatch between the SXS:BBH:0305 waveform and a $(4,4)$ model with three QNMs, in which two frequencies are fixed to the GR predictions of the linear $(4,4,0)$ and $(4,4,1)$ QNMs, but the third is varied. The contour lines are logarithmically spaced in $\mathcal{M}$ between 10^{-6} and 10^{-2}. The start time of the model is taken to be $u_0 = 20M$.

the $(4,4)$ mode as functions of u_0. We show the results for SXS:BBH:0305 (thick lines) as well as the rest of the simulations (thin lines). We see that at $u_0 \gtrsim 10M$ the amplitude of $A_{(4,4,0)}$ is extremely stable, but the faster the additional QNM decays, the more variations that are seen. Nevertheless, the $A^{(2,2,0)\times(2,2,0)}_{(4,4)}$ exhibits only $\sim 20\%$ variations for $u_0 \in [15M, 30M]$, whereas $A_{(4,4,1)}$ varies by $\sim 90\%$ in the same range. Before and near $u_0 \approx 10M$ every amplitude shows considerable variations, which is why we use $u_0 \geq 15M$ in this Letter. This suggests a need to improve the QNM model, either by including more overtones as in [10], modifying the time dependence of the linear [62] and quadratic terms, or considering more nonlinear effects.

Finally we check which frequency is preferred by the $(4,4)$ mode of the numerical strain. For this, we fix two frequencies to be the linear $\omega_{(4,4,0)}$ and $\omega_{(4,4,1)}$ frequencies, and keep one frequency free. We vary the frequency of that third term and fit every amplitude to minimize the residual in Eq. (7.6). Figure 7.4 shows contours of the mismatch over the real and imaginary parts of the unknown frequency for the SXS:BBH:0305 simulation using $u_0 = 20M$. We confirm that the data clearly prefers the frequency $\omega_{(2,2,0)\times(2,2,0)} = 2\omega_{(2,2,0)}$ over $\omega_{(4,4,2)}$.

7.6 Conclusions

We have shown that second-order effects are present in the ringdown phase of binary BH mergers for a wide range of mass ratios, matching theoretical expectations and helping improve ringdown modeling at late times. We analyzed 17 NR sim-

ulations and in every one of them we found that, in the $(\ell, m) = (4, 4)$ mode, the quadratic QNM analyzed has a peak amplitude that is comparable to or larger than the $(\ell, m, n) = (4, 4, 0)$ fundamental linear QNM. Because of the relatively slow decay of this quadratic QNM, we find that for nearly equal-mass systems this QNM will be larger than the corresponding linear fundamental mode even $10M$ after $u_{\rm peak}$.

These results highlight that we may be able to observe this nonlinear effect in future high-SNR GW events with a detectable $(4, 4)$ harmonic. A quantitative analysis, and a generalization to other harmonics, will be performed in the future to assess in detail the detectability of quadratic QNMs and how well they can be distinguished from linear QNMs, for current GW detectors at design sensitivity as well as next-generation GW detectors. It would also be interesting to study how the linear/quadratic relationship of these nonlinearities varies with the spin of the remnant, especially as one approaches maximal spin.

The confirmation of quadratic QNMs opens new possibilities for more general understanding of the role of nonlinearities in the ringdown of perturbed black holes. It is now clear that we can readily improve the basic linear models that have been used previously in theoretical and observational ringdown analyses. Quadratic QNMs provide new opportunities to maximize the science return of GW detections, by increasing the likelihood of detecting multiple QNM frequencies. One of these key science goals is performing high-precision consistency tests of GR with GW observations. Fulfilling this aim will require a correct ringdown model, which incorporates the nonlinear effects that we have shown to be robustly present.

7.7 Acknowledgments

We thank Max Isi and the Flatiron Institute for fostering discourse, and Vishal Baibhav, Emanuele Berti, Mark Cheung, Matt Giesler, Scott Hughes, and Max Isi for valuable conversations. Computations for this work were performed with the Wheeler cluster at Caltech. This work was supported in part by the Sherman Fairchild Foundation and by NSF Grants No. PHY-2011961, No. PHY-2011968, and No. OAC-1931266 at Caltech, as well as NSF Grants No. PHY-1912081, No. PHY-2207342, and No. OAC-1931280 at Cornell. The work of L.C.S. was partially supported by NSF CAREER Grant No. PHY-2047382. M.L. was funded by the Innovative Theoretical Cosmology Fellowship at Columbia University. L.H. was funded by the DOE DE-SC0011941 and a Simons Fellowship in Theoretical Physics. M.L. and L.C.S. thank the Benasque Science Center and the organizers of the 2022

workshop "New frontiers in strong gravity," where some of this work was performed; and M.L. acknowledges NSF Grant No. PHY-1759835 for supporting travel to this workshop.

Note added.–Recently, we learned that Cheung *et al.* conducted a similar study, whose results are consistent with ours [63].

References

[1] H. Stephani, D. Kramer, M. A. H. MacCallum, C. Hoenselaers, and E. Herlt, *Exact solutions of Einstein's field equations*, Cambridge Monographs on Mathematical Physics (Cambridge Univ. Press, Cambridge, 2003), 10.1017/CBO9780511535185.

[2] J. B. Griffiths and J. Podolsky, *Exact Space-Times in Einstein's General Relativity*, Cambridge Monographs on Mathematical Physics (Cambridge University Press, Cambridge, 2009), 10.1017/CBO9780511635397.

[3] T. Regge and J. A. Wheeler, Phys. Rev. **108**, 1063 (1957) 10.1103/PhysRev.108.1063.

[4] F. J. Zerilli, Phys. Rev. D **2**, 2141 (1970) 10.1103/PhysRevD.2.2141.

[5] S. A. Teukolsky, Astrophys. J. **185**, 635 (1973) 10.1086/152444.

[6] R. Penrose, Riv. Nuovo Cim. **1**, 252 (1969) 10.1023/A:1016578408204.

[7] P. T. Chrusciel, J. Lopes Costa, and M. Heusler, Living Rev. Rel. **15**, 7 (2012) 10.12942/lrr-2012-7.

[8] L. Blanchet, Living Rev. Rel. **17**, 2 (2014) 10.12942/lrr-2014-2.

[9] E. Berti, V. Cardoso, and A. O. Starinets, Class. Quant. Grav. **26**, 163001 (2009) 10.1088/0264-9381/26/16/163001.

[10] M. Giesler, M. Isi, M. A. Scheel, and S. Teukolsky, Phys. Rev. X **9**, 041060 (2019) 10.1103/PhysRevX.9.041060.

[11] S. Bhagwat, X. J. Forteza, P. Pani, and V. Ferrari, Phys. Rev. D **101**, 044033 (2020) 10.1103/PhysRevD.101.044033.

[12] G. B. Cook, Phys. Rev. D **102**, 024027 (2020) 10.1103/PhysRevD.102.024027.

[13] X. Jiménez Forteza, S. Bhagwat, P. Pani, and V. Ferrari, Phys. Rev. D **102**, 044053 (2020) 10.1103/PhysRevD.102.044053.

[14] A. Dhani, Phys. Rev. D **103**, 104048 (2021) 10.1103/PhysRevD.103.104048.

[15] E. Finch and C. J. Moore, (2022).

[16] S. A. Teukolsky, Class. Quant. Grav. **32**, 124006 (2015) 10.1088/0264-9381/32/12/124006.

[17] L. Magaña Zertuche, K. Mitman, N. Khera, L. C. Stein, M. Boyle, N. Deppe, F. Hébert, D. A. B. Iozzo, L. E. Kidder, J. Moxon, H. P. Pfeiffer, M. A. Scheel, S. A. Teukolsky, W. Throwe, and N. Vu, Physical Review D **105**, 10.1103/physrevd.105.104015 (2022) 10.1103/physrevd.105.104015.

[18] E. W. Leaver, Phys. Rev. D **34**, 384 (1986) 10.1103/PhysRevD.34.384.

[19] M. Isi, M. Giesler, W. M. Farr, M. A. Scheel, and S. A. Teukolsky, Phys. Rev. Lett. **123**, 111102 (2019) 10.1103/PhysRevLett.123.111102.

[20] R. Cotesta, G. Carullo, E. Berti, and V. Cardoso, (2022).

[21] M. Isi and W. M. Farr, (2022).

[22] E. Berti, A. Sesana, E. Barausse, V. Cardoso, and K. Belczynski, Phys. Rev. Lett. **117**, 101102 (2016) 10.1103/PhysRevLett.117.101102.

[23] I. Ota and C. Chirenti, Phys. Rev. D **101**, 104005 (2020) 10.1103/PhysRevD.101.104005.

[24] S. Bhagwat, C. Pacilio, E. Barausse, and P. Pani, Phys. Rev. D **105**, 124063 (2022) 10.1103/PhysRevD.105.124063.

[25] E. Berti, K. Yagi, H. Yang, and N. Yunes, General Relativity and Gravitation **50**, 10.1007/s10714-018-2372-6 (2018) 10.1007/s10714-018-2372-6.

[26] R. Abbott et al. (LIGO Scientific, VIRGO, KAGRA), (2021).

[27] B. P. Abbott et al. (KAGRA, LIGO Scientific, Virgo, VIRGO), Living Rev. Rel. **21**, 3 (2018) 10.1007/s41114-020-00026-9.

[28] L. S. Team, (2018).

[29] M. Maggiore et al., JCAP **03**, 050 (2020) 10.1088/1475-7516/2020/03/050.

[30] M. Evans et al., (2021).

[31] L. London, D. Shoemaker, and J. Healy, Phys. Rev. D **90**, [Erratum: Phys.Rev.D 94, 069902 (2016)], 124032 (2014) 10.1103/PhysRevD.90.124032.

[32] S. Ma, K. Mitman, L. Sun, N. Deppe, F. Hébert, L. E. Kidder, J. Moxon, W. Throwe, N. L. Vu, and Y. Chen, (2022).

[33] R. J. Gleiser, C. O. Nicasio, R. H. Price, and J. Pullin, Phys. Rev. Lett. **77**, 4483 (1996) 10.1103/PhysRevLett.77.4483.

[34] R. J. Gleiser, C. O. Nicasio, R. H. Price, and J. Pullin, Class. Quant. Grav. **13**, L117 (1996) 10.1088/0264-9381/13/10/001.

[35] R. J. Gleiser, C. O. Nicasio, R. H. Price, and J. Pullin, Phys. Rept. **325**, 41 (2000) 10.1016/S0370-1573(99)00048-4.

[36] K. Ioka and H. Nakano, Phys. Rev. D **76**, 061503 (2007) 10.1103/PhysRevD.76.061503.

[37] H. Nakano and K. Ioka, Phys. Rev. D **76**, 084007 (2007) 10.1103/PhysRevD.76.084007.

[38] S. Okuzumi, K. Ioka, and M.-a. Sakagami, Phys. Rev. D **77**, 124018 (2008) 10.1103/PhysRevD.77.124018.

[39] D. Brizuela, J. M. Martin-Garcia, and M. Tiglio, Phys. Rev. D **80**, 024021 (2009) 10.1103/PhysRevD.80.024021.

[40] E. Pazos, D. Brizuela, J. M. Martin-Garcia, and M. Tiglio, Phys. Rev. D **82**, 104028 (2010) 10.1103/PhysRevD.82.104028.

[41] J. L. Ripley, N. Loutrel, E. Giorgi, and F. Pretorius, Phys. Rev. D **103**, 104018 (2021) 10.1103/PhysRevD.103.104018.

[42] N. Loutrel, J. L. Ripley, E. Giorgi, and F. Pretorius, Phys. Rev. D **103**, 104017 (2021) 10.1103/PhysRevD.103.104017.

[43] M. Lagos and L. Hui, (2022).

[44] M. Campanelli and C. O. Lousto, Phys. Rev. D **59**, 124022 (1999) 10.1103/PhysRevD.59.124022.

[45] K. Mitman, J. Moxon, M. A. Scheel, S. A. Teukolsky, M. Boyle, N. Deppe, L. E. Kidder, and W. Throwe, Phys. Rev. D **102**, 104007 (2020) 10.1103/PhysRevD.102.104007.

[46] M. Boyle et al., Class. Quant. Grav. **36**, 195006 (2019) 10.1088/1361-6382/ab34e2.

[47] B. P. Abbott et al. (LIGO Scientific, Virgo), Phys. Rev. D **93**, 122003 (2016) 10.1103/PhysRevD.93.122003.

[48] https://www.black-holes.org/code/SpEC.html.

[49] *SXS Gravitational Waveform Database*, http://www.black-holes.org/waveforms.

[50] J. Moxon, M. A. Scheel, and S. A. Teukolsky, Phys. Rev. D **102**, 044052 (2020) 10.1103/PhysRevD.102.044052.

[51] J. Moxon, M. A. Scheel, S. A. Teukolsky, N. Deppe, N. Fischer, F. Hébert, L. E. Kidder, and W. Throwe, (2021).

[52] N. Deppe, W. Throwe, L. E. Kidder, N. L. Fischer, C. Armaza, G. S. Bonilla, F. Hébert, P. Kumar, G. Lovelace, J. Moxon, E. O'Shea, H. P. Pfeiffer, M. A. Scheel, S. A. Teukolsky, I. Anantpurkar, M. Boyle, F. Foucart, M. Giesler, D. A. B. Iozzo, I. Legred, D. Li, A. Macedo, D. Melchor, M. Morales, T. Ramirez, H. R. Rüter, J. Sanchez, S. Thomas, and T. Wlodarczyk, *SpECTRE*, version 2020.12.07, Dec. 2020, 10.5281/zenodo.4290405.

[53] K. Mitman et al., Phys. Rev. D **104**, 024051 (2021) 10.1103/PhysRevD.104.024051.

[54] K. Mitman et al., (2022).

[55] M. Boyle, D. Iozzo, and L. C. Stein, *Moble/scri: v1.2*, version v1.2, Sept. 2020, 10.5281/zenodo.4041972.

[56] M. Boyle, Phys. Rev. D **87**, 104006 (2013) 10.1103/PhysRevD.87.104006.

[57] M. Boyle, L. E. Kidder, S. Ossokine, and H. P. Pfeiffer, (2014).

[58] M. Boyle, Phys. Rev. D **93**, 084031 (2016) 10.1103/PhysRevD.93.084031.

[59] P. Virtanen, R. Gommers, T. E. Oliphant, M. Haberland, T. Reddy, D. Cournapeau, E. Burovski, P. Peterson, W. Weckesser, J. Bright, S. J. van der Walt, M. Brett, J. Wilson, K. J. Millman, N. Mayorov, A. R. J. Nelson, E. Jones, R. Kern, E. Larson, C. J. Carey, İ. Polat, Y. Feng, E. W. Moore, J. VanderPlas, D. Laxalde, J. Perktold, R. Cimrman, I. Henriksen, E. A. Quintero, C. R. Harris, A. M. Archibald, A. H. Ribeiro, F. Pedregosa, P. van Mulbregt, and SciPy 1.0 Contributors, Nature Methods **17**, 261 (2020) 10.1038/s41592-019-0686-2.

[60] L. C. Stein, J. Open Source Softw. **4**, 1683 (2019) 10.21105/joss.01683.

[61] S. Borhanian, K. G. Arun, H. P. Pfeiffer, and B. S. Sathyaprakash, Class. Quant. Grav. **37**, 065006 (2020) 10.1088/1361-6382/ab6a21.

[62] L. Sberna, P. Bosch, W. E. East, S. R. Green, and L. Lehner, Phys. Rev. D **105**, 064046 (2022) 10.1103/PhysRevD.105.064046.

[63] M. H.-Y. Cheung, V. Baibhav, E. Berti, V. Cardoso, G. Carullo, R. Cotesta, W. Del Pozzo, F. Duque, T. Helfer, E. Shukla, and K. W. K. Wong, (2022).